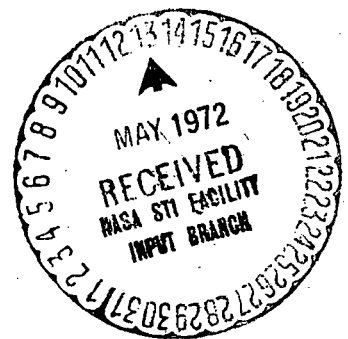


SOLUTIONS FOR REACTING AND NONREACTING
VISCOUS SHOCK LAYERS WITH MULTICOMPONENT
DIFFUSION AND MASS INJECTION

By

James Norvel Moss



Thesis submitted to the Graduate Faculty of the
Virginia Polytechnic Institute and State University
in candidacy for the degree of

DOCTOR OF PHILOSOPHY

in

Aerospace Engineering

October 1971

(NASA-TM-X-67708) SOLUTIONS FOR REACTING
AND NONREACTING VISCOUS SHOCK LAYERS WITH
MULTICOMPONENT DIFFUSION AND MASS INJECTION
Ph.D. Thesis - Virginia Polytechnic J.N.
Moss (NASA) Oct. 1971 222 p CACL 20D G3/12 26893
N72-23243
Unclas

SOLUTIONS FOR REACTING AND NONREACTING
VISCOUS SHOCK LAYERS WITH MULTICOMPONENT
DIFFUSION AND MASS INJECTION

by

James Norvel Moss

ABSTRACT

This study presents numerical solutions of the viscous shock-layer equations where the chemistry is treated as being either frozen, equilibrium, or nonequilibrium. Also the effects of the diffusion model, surface catalyticity, and mass injection on surface transport and flow parameters are considered. The equilibrium calculations for air species using multicomponent diffusion provide solutions previously unavailable. The same can also be said for the downstream nonequilibrium calculations where the diffusion is multicomponent.

The viscous shock-layer equations are solved by using an implicit finite-difference scheme. The flow is treated as a mixture of inert and thermally perfect species. Also the flow is assumed to be in vibrational equilibrium.

All calculations are for a 45° hyperboloid. The flight conditions are those for various altitudes and velocities in the earth's atmosphere. Data are presented showing the effects of the chemical models; diffusion models; surface catalyticity; and mass injection of air, water, and ablation products on heat transfer; skin friction; shock stand-off distance; wall pressure distribution; and tangential velocity, temperature, and species profiles.

SOLUTIONS FOR REACTING AND NONREACTING VISCOUS SHOCK LAYERS
WITH MULTICOMPONENT DIFFUSION AND MASS INJECTION

by

James Norvel Moss

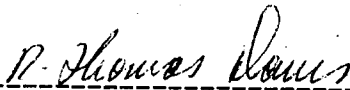
Thesis submitted to the Graduate Faculty of the
Virginia Polytechnic Institute and State University
in partial fulfillment of the requirement for the degree of

DOCTOR OF PHILOSOPHY

in

Aerospace Engineering

APPROVED:



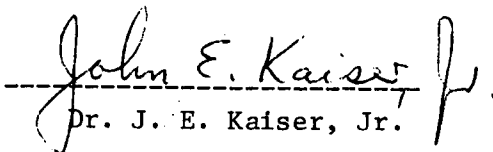
Dr. R. T. Davis, Chairman



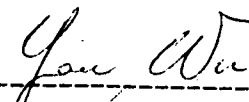
Dr. G. C. Debney, Jr.



Dr. C. H. Lewis



Dr. J. E. Kaiser, Jr.



Dr. Yau Wu

October 1971

Blacksburg, Virginia

ACKNOWLEDGMENTS

The author wishes to express his appreciation to Dr. R. T. Davis for his suggestions and criticisms throughout this effort and to the entire committee for their review and comments on this thesis.

Further, the author is indebted to the National Aeronautics and Space Administration for permitting material obtained from research conducted at the Langley Research Center to be used in this thesis. In particular, thanks are due to Mr. Robert T. Swann and Mr. Marvin B. Dow for their support and encouragement during this effort.

Thanks are also due to the following people for their assistance in the preparation of this thesis: Mrs. Kay L. Brinkley who programmed the computer plotting routine, Mrs. Carol M. Lockett who typed the rough draft, and Mrs. Joanne H. Halvorson who typed the final draft of this thesis.

TABLE OF CONTENTS

	Page
TITLE	i
ACKNOWLEDGEMENTS.	ii
TABLE OF CONTENTS	iii
LIST OF FIGURES	v
LIST OF TABLES.	xii
LIST OF SYMBOLS	xiv
CHAPTER	1
I. INTRODUCTION	1
II. DEVELOPMENT OF THE GOVERNING EQUATIONS	4
Flow Field Equations	4
Boundary Conditions.	24
Surface Transport.	29
III. THERMODYNAMIC AND TRANSPORT PROPERTIES	31
Thermodynamic Properties	31
Transport Properties	32
IV. CHEMICAL REACTION MODELS	37
Equilibrium Chemistry	37
Finite Rate Chemistry.	41
V. METHOD OF SOLUTION	45
Stagnation Streamline Equations.	45
Finite-Difference Expressions.	52
Solution Procedure	53

VI. RESULTS AND DISCUSSION	57
Introduction	57
Comparison With Previous Analyses.	58
Chemical Models.	63
Catalytic Wall Effects	70
Diffusion Models	71
Mass Injection	73
VII. CONCLUDING REMARKS	84
REFERENCES.	87
TABLES.	90
FIGURES	109 - 201
VITA.	202

LIST OF FIGURES

FIGURE	Page
1. Coordinate system	109
2. Surface boundary conditions for mass and energy transfer	110
(a) Mass balance at gas-solid interface	110
(b) Energy balance at gas-solid interface	110
3. Flow chart for shock solution procedure	111
(a) Shock in chemical equilibrium	111
(b) Shock frozen at free stream chemistry	112
4. Flow chart for solution sequence of viscous shock-layer equations	113
(a) Equilibrium chemistry	113
(b) Frozen and nonequilibrium chemistry	114
5. Comparison of the present calculations with the results of Whitehead for frozen air	115
(a) Shock stand-off variation with distance along body surface	115
(b) Skin friction variation with distance along body surface	116
(c) Heat transfer variation with distance along body surface	117
6. Comparison of the present calculations with the results of Whitehead for equilibrium air.	118
(a) Shock stand-off variation with distance along body surface	118
(b) Skin friction variation with distance along body surface	119
(c) Heat transfer variation with distance along body surface	120

FIGURE	Page
7. Comparison of the present calculations with the stagnation results of Edelman and Hoffman for equilibrium air	121
(a) Stagnation temperature profiles for alt = 280,000 ft, $U_{\infty}^* = 26,000$ ft/sec, and $a^* = 12$ in.	121
(b) Stagnation species profiles for alt = 280,000 ft, $U_{\infty}^* = 26,000$ ft/sec, and $a^* = 12$ in.	122
(c) Stagnation temperature profiles for alt = 150,000 ft, $U_{\infty}^* = 22,520$ ft/sec, and $a^* = 0.5$ in.	123
(d) Stagnation species profiles for alt = 150,000 ft, $U_{\infty}^* = 22,520$ ft/sec, and $a^* = 0.5$ in.	124
8. Comparison of the present calculations with the stagnation results of Blottner for nonequilibrium air.	125
(a) Stagnation temperature profiles	125
(b) Stagnation velocity ratio profiles	126
(c) Stagnation species profiles	127
9. Velocity profiles for reacting and nonreacting air with multicomponent diffusion and no mass injection.	128
(a) Nonequilibrium chemistry.	128
(b) Equilibrium chemistry	129
(c) Frozen chemistry.	130
10. Temperature profiles for air with multicomponent diffusion and no mass injection	131
(a) Nonequilibrium chemistry.	131
(b) Equilibrium chemistry	132
(c) Frozen chemistry.	133
11. Species profiles for nonequilibrium air with multicomponent diffusion and no mass injection	134

FIGURE	Page
(a) $s = 0.0$	134
(b) $s = 1.0$	135
(c) $s = 2.0$	136
(d) $s = 3.0$	137
12. Species profiles for equilibrium air with multi- component diffusion and no mass injection	138
(a) $s = 0.0$	138
(b) $s = 1.0$	139
(c) $s = 2.0$	140
(d) $s = 3.0$	141
13. Stagnation equilibrium and frozen air species and temperature profiles.	142
14. Stagnation equilibrium air results for an alt = 100,000 ft, $U_{\infty}^* = 20,000$ ft/sec, and $a^* = 1.0$ in	143
(a) Temperature profile	143
(b) Species profiles.	144
15. Effect of chemistry model on tangential velocity profiles with multicomponent diffusion and no mass injection	145
(a) $s = 0.0$	145
(b) $s = 2.0$	146
16. Effect of chemistry model on temperature profiles with multicomponent diffusion and no mass injection	147
(a) $s = 0.0$	147
(b) $s = 2.0$	148
17. Effect of chemistry model on shock stand-off distance with multicomponent diffusion and no mass injection.	149

FIGURE	Page
18. Effect of chemistry model on nondimensional heat transfer with multicomponent diffusion and no mass injection	150
19. Effect of chemistry model on Stanton number with multicomponent diffusion and no mass injection	151
20. Effect of chemistry model on skin friction coefficient with multicomponent diffusion and no mass injection.	152
21. Effect of chemistry model on wall pressure distribution with multicomponent diffusion and no mass injection	153
22. Effect of wall catalyticity on species profiles	154
(a) $s = 0.0$	154
(b) $s = 1.0$	155
(c) $s = 3.0$	156
23. Effect of wall catalyticity on shock stand-off distance . .	157
24. Effect of wall catalyticity on nondimensional heat transfer	158
25. Effect of wall catalyticity on Stanton number	159
26. Effect of wall catalyticity on skin friction coefficient. .	160
27. Effect of diffusion model on species profiles for equilibrium air	161
(a) $s = 0.0$	161
(b) $s = 1.0$	162
28. Effect of diffusion model on species profiles for nonequilibrium air	163
(a) $s = 0.0$	163
(b) $s = 1.0$	164

FIGURE	Page
29. Nondimensional mass injection distributions	165
30. Comparison of nonequilibrium species profiles with and without mass injection of equilibrium air	166
(a) $s = 0.0$	166
(b) $s = 1.0$	167
(c) $s = 3.0$	168
31. Stagnation tangential velocity ratio profiles for different injection rates of equilibrium air into reacting non- equilibrium air	169
32. Stagnation temperature profiles for different injection rates of equilibrium air into reacting nonequilibrium air	170
33. Comparison of shock stand-off distances for different injection rates of equilibrium air into reacting nonequilibrium air	171
34. Comparison of nondimensional heat transfer distributions for different injection rates of equilibrium air into reacting nonequilibrium air.	172
35. Comparison of Stanton number distributions for different injection rates of nonequilibrium air into reacting non- equilibrium air	173
36. Comparison of skin friction coefficient distributions for different injection rates of equilibrium air into reacting nonequilibrium air.	174
37. Comparison of wall pressure ratio distributions for different injection rates of equilibrium air into reacting non- equilibrium air	175
38. Stagnation heat transfer as influenced by injecting equi- librium air into reacting equilibrium air	176
39. Stagnation shock stand-off distance as influenced by injec- tion of equilibrium air into reacting equilibrium air	177
40. Stagnation shock stand-off distance as influenced by large mass injection rates of equilibrium air into reacting equilibrium air	178

FIGURE	Page
41. Equilibrium composition of H ₂ O	179
(a) Pressure = 0.1 atm	179
(b) Pressure = 0.01 atm	180
42. Stagnation elemental profiles for injecting H ₂ O into equilibrium air.	181
43. Species profiles for a 0.1 injection rate of H ₂ O into equilibrium air.	182
(a) s = 0.0.	182
(b) s = 0.4.	183
(c) s = 1.0.	184
44. Species profiles for a 0.05 injection rate of H ₂ O into equilibrium air.	185
(a) s = 0.0.	185
(b) s = 0.4.	186
(c) s = 1.0.	187
45. Stagnation temperature profiles for different injection rates of H ₂ O into equilibrium air.	188
46. Stagnation velocity profiles for different injection rates of H ₂ O into equilibrium air	189
47. Equilibrium composition of ablation products	190
(a) Pressure = 0.1 atm	190
(b) Pressure = 0.01 atm	191
48. Stagnation elemental profiles for injecting ablation species into equilibrium air	192
49. Species profiles for a 0.1 injection rate of ablation species into equilibrium air	193
(a) s = 0.0.	193
(b) s = 0.4.	194

FIGURE	Page
50. Species profiles for a 0.05 injection rate of ablation species into equilibrium air	195
(a) $s = 0.0$	195
(b) $s = 0.4$	196
51. Stagnation temperature profiles for different injection rates of ablation products	197
52. Stagnation velocity profiles for different injection rates of ablation products	198
53. Comparison of nondimensional heat transfer distributions for different injection rates of air, H_2O , and ablation species into equilibrium air	199
54. Comparison of Stanton number distributions for different injection rates of air, H_2O , and ablation species into equilibrium air.	200
55. Comparison of skin friction coefficient distributions for different injection rates of air, H_2O , and ablation species into equilibrium air	201

LIST OF TABLES

TABLE	Page
I. Thermodynamic properties	90
II. Molecular constants.	92
III. Third body efficiencies relative to argon	93
IV. Reaction rate coefficients	94
V. Free stream conditions	95
VI. Summary of computing time and iteration requirements for various cases	96
VII. Frozen air stagnation shock and wall values [alt = 200,000 ft; $U^* = 20,000$ ft/sec; $a^* = 1.0$ in.; $Re_\infty =$ 2.597×10^3 ; $Re_s = 1.914 \times 10^2$].	97
VIII. Equilibrium air stagnation shock and wall values [alt = 200,000 ft; $U^* = 20,000$ ft/sec; $a^* = 1.0$ in.; $Re_\infty =$ 2.597×10^3 ; $Re_s = 3.37 \times 10^2$]	98
IX. Equilibrium air stagnation shock and wall values [alt = 280,000 ft; $U^* = 26,000$ ft/sec; $a^* = 12.0$ in.; $Re_\infty =$ 1.482×10^3 ; $Re_s = 1.498 \times 10^2$].	99
X. Equilibrium air stagnation shock and wall values [alt = 150,000 ft; $U^* = 22,520$ ft/sec; $a^* = 0.5$ in.; $Re_\infty =$ 9.236×10^3 ; $Re_s = 1.134 \times 10^3$].	100
XI. Nonequilibrium air stagnation shock and wall values [alt = 200,000 ft; $U^* = 20,000$ ft/sec; $a^* = 1.0$ in.; $Re_\infty =$ 2.597×10^3 ; $Re_s = 1.914 \times 10^2$].	101
XII. Equilibrium air stagnation shock and wall values [alt = 100,000 ft; $U^* = 20,000$ ft/sec; $a^* = 1.0$ in.; $Re_\infty =$ 1.791×10^5 ; $Re_s = 1.876 \times 10^4$].	102
XIII. Summary of dimensional heat transfer rates at different body stations [alt = 200,000 ft; $U^* = 20,000$ ft/sec; $a^* =$ 1.0 in.; $Re_\infty = 2.597 \times 10^3$].	103
XIV. Nonequilibrium stagnation wall conditions for a non- catalytic wall and mass injection of equilibrium air [alt = 200,000 ft; $U^* = 20,000$ ft/sec; $a^* = 1.0$ in.; $Re_\infty = 2.597 \times 10^3$; $Re_s = 1.914 \times 10^2$; multicomponent diffusion]	104

TABLE

Page

XV. Stagnation equilibrium wall conditions for mass injection of water and ablation species [alt = 200,000 ft; $U^* = 20,000$ ft/sec; $a^* = 12$ in.; $Re_\infty = 3.1164 \times 10^4$; $Re_s = 2.297 \times 10^3$; binary diffusion] 105

XVI. Nondimensional heat transfer rate, skin friction coefficient, Stanton number, wall pressure ratio, and shock stand-off distance values for no injection and injection of air, water, and ablation products at different body stations 107

LIST OF SYMBOLS

a^*	body nose radius of curvature
a_1, a_2, a_3, a_4	coefficients used in equation for specific heats (eq. (3.1))
B_{jk}	quantity defined by equation (2.18b)
C_f	skin friction coefficient (eq. (2.55))
C_i	mass fraction of species i , ρ_i/ρ
\tilde{C}_ℓ	mass fraction of element ℓ (eq. (2.9))
C_p	frozen specific heat of mixture, $\sum_i C_i C_{p_i}$
C_{p_i}	constant pressure specific heat of species i , $C_{p_i}^* / C_{p_\infty}^*$
\mathcal{D}_{ij}	binary diffusion coefficients
D_{ij}	multicomponent diffusion coefficients
F	free energy of mixture
F_i	free energy of species i
h	enthalpy of mixture, $\sum_i C_i h_i$
h_i	enthalpy of species i , h_i^* / U_∞^{*2}
H	total enthalpy of mixture (eq. (2.8)) H^* / U_∞^{*2}
J_i	diffusion mass flux of species i , $J_i^* a^* / \mu_{ref}^*$
\tilde{J}_ℓ	diffusion mass flux of element ℓ , (eq. (2.11))
$k_{b,r}$	backward rate constant
$k_{f,r}$	forward rate constant
K	thermal conductivity of mixture, $K^* / \mu^* (U_\infty^{*2} / C_{p_\infty}^*) C_{p_\infty}^*$
K_i	thermal conductivity of species i

L	Lewis number defined by equation (2.18 c)
L_i	Lewis number defined by equation (2.17 c)
L_{ik}	multicomponent Lewis number, $\frac{\rho^* C_p^* D_{ij}^*}{K^*}$
\dot{m}	mass injection rate, $m^*/\rho_\infty^* U_\infty^*$
M_i^*	molecular weight of species i
\bar{M}^*	molecular weight of mixture
M_∞	free stream Mach number
n	coordinate measured normal to the body, n^*/a^*
P	pressure, $P^*/(\rho_\infty^* U_\infty^{*2})$
P_i	partial pressure of species i
PL	parameter defined by equations (2.29 e) and (2.29 g)
PM	parameter defined by equations (2.29 f) and (2.29 h)
$\tilde{P}L$	parameter defined by equations (2.30 e) and (2.30 g)
$\tilde{P}M$	parameter defined by equations (2.30 f) and (2.30 h)
Pr	Prandtl number defined by equation (2.22 a)
q	wall heat transfer rate, $q^*/(\rho_\infty^* U_\infty^{*3})$
r	radius measured from axis of symmetry to a point on the body surface, r^*/a^*
R	universal gas constant
Re_s	shock Reynolds number, $\rho_\infty^* U_\infty^* a^*/\mu_s^*$
Re_∞	free stream Reynolds number, $\rho_\infty^* U_\infty^* a^*/\mu_\infty^*$
s	coordinate measured along the body surface, s^*/a^*
S_i	entropy of species i
St	Stanton number defined by equation (2.54)

t	time
T	temperature, $T^*/(U_\infty^{*2}/C_{p\infty}^*)$
T^+	reduced temperature defined by equation (3.8)
u	velocity component tangent to body surface, u^*/U_∞^*
U_∞^*	free stream velocity
v	velocity component normal to body surface, v^*/U_∞^*
\dot{w}_i	mass rate of formation of species i , $\dot{w}_i^*\rho_\infty^*U_\infty^*/a^*$
x_i	mole fraction of species i
X_i	concentration of species i , moles/volume
α	shock angle defined in figure 1
$\alpha_{i,r}$	stoichiometric coefficients for reactants
$\alpha_1, \alpha_2, \alpha_3, \alpha_4$	coefficients in equation (2.25)
β_1, β_2	coefficients in equation (2.45)
$\beta_{i,r}$	stoichiometric coefficients for products
γ_i	mole mass ratio of species i (eq. (4.11))
γ_∞	free stream ratio of specific heats, $(C_p^*/C_v^*)_\infty$
$\delta_{i\ell}$	number of atoms of the ℓ th element in species i
ϵ	Reynolds number parameter
ϵ_i	maximum energy of attraction of colliding i molecules
ϵ_{ij}	maximum energy of attraction of colliding unlike molecules
Δb_{ik}	mass diffusion-parameter defined by equation (2.17 b)
$\widetilde{\Delta b}_{ik}$	mass diffusion parameter defined by equation (2.18 c)
θ	body angle defined in figure 1

ζ_{ij}	binary Lewis number
η	transformed n coordinate, n/n_s
κ	body curvature, K^*a^*
μ	viscosity of mixture, $\mu^*/\mu^*(U_\infty^{*2}/C_{p\infty}^*)$
ξ	transformed s coordinate, $\xi = s$
ρ	density of mixture, ρ^*/ρ_∞^*
σ_i	collision diameter of species i
σ_{ij}	collision diameter for unlike species (eq. (3.9))
Φ_{ij}	quantity defined by equation (3.5 b)
Ψ	quantity defined by equation (2.28 e)
$\Omega^{(1,2)}$	collision integral for diffusion
$\Omega^{(2,2)}$	collision integral for viscosity

Subscripts

i	ith species
l	lth element
s	shock value
w	wall value
0	stagnation point value
∞	free stream condition

Superscripts

0	standard state (pure substance at one atmosphere of pressure)
j	zero for plane flow and one for axisymmetric flow
-	quantity divided by its corresponding shock value

- * dimensional quantity
- ' total differential
- " shock oriented velocity components (See figure 1.)

I. INTRODUCTION

Analysis of the flow about a hypersonic vehicle must account for the interactions that occur between the reacting outer flow and the vehicle surface. This problem is complicated in many cases because the vehicle surface is either an ablative or transpiration-cooled surface. In such instances, gaseous species that may have a wide spectrum of molecular weights are injected into the external flow. Consequently, assumptions concerning the chemistry and diffusion models may significantly affect the accuracy of an analysis for such a problem.

Numerical solutions to the aforementioned problem have been either that of the inviscid-boundary-layer solutions (refs. 1 through 6, for example) or the viscous shock-layer solution (refs. 6 through 16, for example). The viscous shock-layer solution as originally suggested by Cheng (ref. 16) and later modified by Davis (ref. 17) is a most appealing method because one set of equations uniformly valid throughout the shock layer is used. Furthermore, the viscous-inviscid interactions are accounted for in a straightforward manner with or without mass injection.

The most recent numerical solutions of the viscous shock-layer equations have been those of Davis (ref. 8), Whitehead (ref. 9), Dellinger (ref. 10), Blottner (ref. 11), and Adams (ref. 6). References 8 and 9 used the most extensive shock-layer equations since the solutions are not restricted to the thin shock-layer approximations as in the other stated references. The solutions of references 8, 9, and 10

are for the stagnation and downstream flow, whereas those of references 6 and 11 are for the stagnation streamline only. However, the above viscous shock-layer solutions considered rather simple chemical systems of species. For example, reference 8 considered atomic and molecular oxygen species using finite-rate chemistry; reference 9 considered the effects of injecting argon, air, and helium into air where air was treated as one species and the chemistry was either frozen or equilibrium; reference 10 considered nonequilibrium air as a reacting mixture of seven chemical species with constant but arbitrary Prandtl and Lewis numbers; and references 6 and 11, which presented stagnation solutions, considered the same chemical species as reference 10, but reference 6, in addition, considered multicomponent diffusion and the effects of inert gas injection. Yet, none of the above viscous shock-layer solutions for either equilibrium or nonequilibrium chemistry has all of the following features: downstream solution capability, mass injection, multicomponent diffusion, and second-order terms in the normal momentum equation. However, this study presents numerical solutions of the viscous shock-layer equations where all the above features are accounted for. The chemistry is treated as being either frozen, equilibrium, or nonequilibrium. The equilibrium air calculations that treat the diffusion as multicomponent provide solutions previously unavailable. The same can also be said for the downstream nonequilibrium air calculations where the diffusion is multicomponent.

The viscous shock-layer equations and the implicit finite-difference scheme used to solve the equations are essentially those given by

Davis in reference 8. The flow is treated as a mixture of inert and thermally perfect species. Also, the flow is assumed to be in vibrational equilibrium.

All calculations are for a 45° hyperboloid. The flight conditions are those for various altitudes and velocities in the earth's atmosphere. Data are presented showing the effects of the chemical models; diffusion models; surface catalyticity; and mass injection of air, water, and ablation products on heat transfer; skin friction; shock stand-off distance; wall pressure distribution; and tangential velocity, temperature, and species profiles.

II. DEVELOPMENT OF THE GOVERNING EQUATIONS

The conservation equations and their associated boundary conditions are presented for the laminar viscous shock layer about an axisymmetric or two-dimensional body. These equations account for mass injection and treat the diffusion as either multicomponent or binary. Equations convenient for solving frozen, equilibrium, and nonequilibrium flow are presented. Also, the non-dimensionalizing quantities are given, along with the transformation used to facilitate the numerical solution of the equations.

Flow Field Equations

The conservation equations that describe a reacting multicomponent gas mixture can be found, for example, in reference 18 or 19. The viscous shock-layer equations as used herein are obtained by expressing the conservation equations in the body-oriented coordinate system shown in figure 1. Then these equations are nondimensionalized in each of two flow regions. That is, the equations are nondimensionalized with variables which are of order one in the region near the body surface (boundary layer for large Reynolds numbers), and then the same set of equations is nondimensionalized with variables which are of order one in the essentially inviscid region outside the boundary layer. Terms in each of the two resulting sets of equations are retained up to second order in the inverse square root of a Reynolds number. By combining these two sets of equations such that terms up to second

order in both the inner and outer regions are retained, a set of equations uniformly valid to second order in the entire shock layer is obtained.

The resulting equations are of a hyperbolic-parabolic nature. However, if the thin-shock-layer approximation is made (an approximation to the normal momentum equation), the equations are parabolic. The parabolic equations can be solved by using numerical methods similar to those used in solving boundary-layer problems. Then, an iteration procedure is used to remove the thin-shock-layer approximation, as will be discussed in a later section.

The derivation described above and the subsequent equations are the same as given by Davis (ref. 8) except that the energy equation, in addition to being formulated in terms of temperature, is formulated in terms of total enthalpy and the species equations are also formulated as elemental equations. The viscous shock-layer equations for a chemically reacting multicomponent mixture are:

Global Continuity

$$\frac{\partial}{\partial s} [(r + n \cos \theta)^j \rho u] + \frac{\partial}{\partial n} [(1 + n\kappa)(r + n \cos \theta)^j \rho v] = 0, \quad (2.1)$$

s-momentum

$$\rho \left[\frac{u}{1+n\kappa} \frac{\partial u}{\partial s} + v \frac{\partial u}{\partial n} + \frac{uv\kappa}{1+n\kappa} \right] + \frac{1}{1+n\kappa} \frac{\partial P}{\partial s} =$$

$$\epsilon^2 \left[\frac{\partial}{\partial n} \left(\mu \left\{ \frac{\partial u}{\partial n} - \frac{u\kappa}{1+n\kappa} \right\} \right) + \mu \left(\frac{2\kappa}{1+n\kappa} + \frac{j \cos \theta}{r+n \cos \theta} \right) \left(\frac{\partial u}{\partial n} - \frac{u\kappa}{1+n\kappa} \right) \right], \quad (2.2)$$

n-momentum

$$\rho \left[\frac{u}{1+n\kappa} \frac{\partial v}{\partial s} + v \frac{\partial v}{\partial n} - \frac{u^2 \kappa}{1+n\kappa} \right] + \frac{\partial P}{\partial n} = 0, \quad (2.3a)$$

which becomes

$$\frac{\partial P}{\partial n} = \frac{\rho u^2 \kappa}{1+n\kappa} \quad (2.3b)$$

if the thin-shock-layer approximation is made,

Energy (temperature)

$$\begin{aligned} & \rho C_p \left[\frac{u}{1+n\kappa} \frac{\partial T}{\partial s} + v \frac{\partial T}{\partial n} \right] - \left[\frac{u}{1+n\kappa} \frac{\partial P}{\partial s} + v \frac{\partial P}{\partial n} \right] = \\ & \epsilon^2 \left[\frac{\partial}{\partial n} \left(\kappa \frac{\partial T}{\partial n} \right) + \left(\frac{\kappa}{1+n\kappa} + \frac{j \cos \theta}{r+n \cos \theta} \right) \kappa \frac{\partial T}{\partial n} - \sum_{i=1}^{NS} J_i C_{pi} \frac{\partial T}{\partial n} \right. \\ & \left. + \mu \left(\frac{\partial u}{\partial n} - \frac{\kappa u}{1+n\kappa} \right)^2 \right] - \sum_{i=1}^{NS} h_i \dot{w}_i, \quad (2.4) \end{aligned}$$

Species Continuity

$$\rho \left[\frac{u}{1+n\kappa} \frac{\partial C_i}{\partial s} + v \frac{\partial C_i}{\partial n} \right] = \dot{w}_o - \frac{\epsilon^2}{(1+n\kappa)(r+n \cos \theta)^j} \left[\right.$$

$$\frac{\partial}{\partial n} \left(\{1 + n\kappa\} \{r + n\cos\theta\} j_{J_i} \right) , \tag{2.5}$$

Where J_i is the diffusion mass flux of species i , and

State

$$p = \rho T \left[\frac{R^*}{\bar{M}^* C^*_{p\infty}} \right] . \tag{2.6}$$

The above equations are in a form that is convenient to apply when the flow-field chemistry is nonequilibrium. In the energy equation and the species continuity equations, the term \dot{w}_i appears. This term represents the rate of production of species i due to chemical reactions. For frozen flow the rate of production terms is zero. However, when the gas is assumed to be in chemical equilibrium, the production terms cannot be obtained from the chemical kinetics. Thus, the production terms in the energy equation are eliminated by formulating this equation in terms of enthalpy.

The energy equation in terms of total enthalpy becomes

$$\rho \left[\frac{u}{1+n\kappa} \frac{\partial H}{\partial s} + v \frac{\partial H}{\partial n} \right] - v \frac{\partial p}{\partial n} + \frac{\rho \kappa u^2 v}{1+n\kappa} = \epsilon^2 \left[\frac{\partial}{\partial n} \left(\frac{\mu}{Pr} \frac{\partial H}{\partial n} \right) - \frac{\mu}{Pr} \sum_{i=1}^{NS} h_i \frac{\partial C_i}{\partial n} - \sum_{i=1}^{NS} h_i J_i + \frac{\mu}{Pr} \{ Pr - 1 \} u \frac{\partial u}{\partial n} - \frac{\mu \kappa u^2}{1+n\kappa} \right]$$

$$\begin{aligned}
& + \left(\frac{\kappa}{1+n\kappa} + \frac{j\cos\theta}{r+n\cos\theta} \right) \left(\frac{\mu}{Pr} \frac{\partial H}{\partial n} - \frac{\mu}{Pr} \sum_{i=1}^{NS} h_i \frac{\partial C_i}{\partial n} - \sum_{i=1}^{NS} h_i J_i \right. \\
& \left. + \frac{\mu}{Pr} \left\{ Pr - 1 \right\} u \frac{\partial u}{\partial n} - \frac{\mu \kappa u^2}{1+n\kappa} \right) \Bigg], \quad (2.7)
\end{aligned}$$

where the total enthalpy as used in the above equation is given by

$$H \equiv h + \frac{u^2}{2} \quad (2.8)$$

This particular formulation of the energy equation reduces the coupling between the energy and species continuity equations (ref. 20) over that of equation (24).

The production terms that appear in the species continuity equations are eliminated by introducing the concept of elemental mass fractions as expressed by Lees in reference 21. As long as no nuclear reactions occur, the elemental mass fractions remain fixed and unchanged during chemical reactions. The relation between the elemental and species mass fractions is given by

$$\tilde{C}_\ell = \sum_{i=1}^{NS} \delta_{i\ell} \frac{M_\ell^*}{M_i^*} C_i \quad (2.9)$$

where

- $\delta_{i\ell}$ is the number of atoms of the ℓ th element in species i ,
- M_ℓ is the molecular weight of the ℓ th element,
- M_i is the molecular weight of the i th species,

and

C_i is the mass fraction of species i .

The elemental continuity equations for the elements can be obtained by multiplying equation (25) by $\delta_{i\ell} M_\ell^* C_i / M_i^*$ and summing over i . The resulting elemental continuity equations are.

$$\rho \left[\frac{u}{1+n\kappa} \frac{\partial \tilde{C}_\ell}{\partial s} + v \frac{\partial \tilde{C}_\ell}{\partial n} \right] = - \frac{\epsilon^2}{(1+n\kappa)(r+n\cos\theta)^j} \left[\frac{\partial}{\partial n} \left((1+n\kappa) \{r+n\cos\theta\}^j \tilde{J}_\ell \right) \right], \quad (2.10)$$

where

$$\tilde{J}_\ell = \sum_{i=1}^{NS} \delta_{i\ell} \frac{M_\ell^*}{M_i^*} J_i \quad (2.11)$$

Introducing the elemental mass fraction not only eliminates the production terms in equations (2.4) and (2.5) but also reduces the number of equations to be solved, since there is one equation (eq. (2.10)) for each element rather than one equation (eq. (2.5)) for each species.

In addition to the above system of equations, additional equations are required to specify the mixture thermodynamic quantities and the diffusion mass flux quantities. The thermodynamic relations are as follows:

Mass Fractions

$$C_i = \rho_i / \rho \quad , \quad (2.12)$$

Frozen Specific Heat

$$C_p = \sum_{i=1}^{NS} C_i C_{pi} \quad , \quad (2.13)$$

Molecular Weight

$$\bar{M}^* = 1 / \sum_{i=1}^{NS} \frac{C_i}{M_i^*} \quad , \quad (2.14)$$

and

Enthalpy

$$h = \sum_{i=1}^{NS} h_i C_i \quad , \quad (2.15)$$

where h_i includes the enthalpy of formation of the i th species.

The mass flux relative to the mass average velocity when thermal and pressure diffusion are neglected can be written in terms of the multi-component Lewis numbers, L_{ij} , (ref. 22) as

$$J_i = \frac{\mu}{Pr} \sum_{\substack{j=1 \\ \neq i}}^{NS} \frac{M_i^* M_j^*}{M^{*2}} L_{ij} \frac{\partial x_j}{\partial n} \quad (2.16)$$

or as given in reference 1 as

$$J_i = -\frac{\mu}{Pr} \sum_{k=1}^{NS} \Delta b_{ik} \frac{\partial C_k}{\partial n}, \quad (2.17a)$$

where

$$\Delta b_{ik} = \begin{cases} L_i & \text{for } i = k \\ L_i - \left[\frac{M^*_i}{\bar{M}^*} L_{ik} + \left(1 - \frac{M^*_i}{M^*_k} \right) \sum_{j=1}^{NS} L_{ij} C_j \right] & \text{for } i \neq k, \end{cases} \quad (2.17b)$$

and

$$L_i = \frac{\sum_{\substack{j=1 \\ \neq i}}^{NS} C_j / M^*_j}{\sum_{\substack{j=1 \\ \neq i}}^{NS} C_j / \zeta_{ij} M^*_j}, \quad (2.17c)$$

and ζ_{ij} are the binary Lewis numbers. The relative mass flux for the elements can be written as

$$\tilde{J}_\ell = -\frac{\mu}{Pr} \left[L_\ell \frac{\partial \tilde{C}_\ell}{\partial n} + \sum_{k=1}^{NS} B_{\ell k} \frac{\partial C_k}{\partial n} \right], \quad (2.18a)$$

where

$$B_{\ell k} = \sum_{i=1}^{NS} \delta_{i\ell} \frac{M^*_\ell}{M^*_i} \tilde{\Delta b}_{ik}, \quad (2.18b)$$

$$\tilde{\Delta}b_{ik} = \begin{cases} L_i - L & \text{for } i = k \\ L_i - \left[\frac{M^*_i}{\bar{M}^*} L_{ik} + \left(1 - \frac{M^*_i}{M^*_k} \right) \sum_{j=1}^{NS} L_{ij} C_j \right] & \text{for } i \neq k \end{cases}, \quad (2.18c)$$

and L is an arbitrary constant. When the diffusional mass flux for the elements is written as indicated, the elemental continuity equation can be arranged in a convenient form for numerical solution. Equations (2.17) and (2.18) can be simplified to

$$J_i = - \frac{\mu}{Pr} \zeta \frac{\partial C_i}{\partial n} \quad (2.19)$$

and

$$\tilde{J}_\ell = - \frac{\mu}{Pr} \zeta \frac{\partial \tilde{C}_\ell}{\partial n} \quad (2.20)$$

respectively, when the binary Lewis numbers, ζ_{ij} , are all equal to ζ or an "effective" Lewis number is used that is equal to ζ .

The previous equations have been nondimensionalized by using the following relations:

$$u^* = uU^*_\infty, \quad (2.21a)$$

$$v^* = vU^*_\infty, \quad (2.21b)$$

$$T^* = TU_{\infty}^{*2} / C_{p_{\infty}}^* , \quad (2.21c)$$

$$p^* = p_{\infty}^* U_{\infty}^{*2} , \quad (2.21d)$$

$$\rho^* = \rho_{\infty}^* , \quad (2.21e)$$

$$\mu^* = \mu_{\text{ref}}^* \left(U_{\infty}^{*2} / C_{p_{\infty}}^* \right) = \mu_{\text{ref}}^* , \quad (2.21f)$$

$$K^* = K_{\text{ref}}^* C_{p_{\infty}}^* , \quad (2.21g)$$

$$C_p^* = C_p C_{p_{\infty}}^* , \quad (2.21h)$$

$$h^* = h U_{\infty}^{*2} \quad (2.21i)$$

$$\dot{w}_i^* = \dot{w}_i \rho_{\infty}^* U_{\infty}^* / a^* , \quad (2.21j)$$

$$J_i^* = J_i \mu_{\text{ref}}^* / a^* , \quad (2.21k)$$

$$s^* = s a^* , \quad (2.21l)$$

$$n^* = n a^* , \quad (2.21m)$$

Q

$$\kappa^* = \kappa a^* , \quad (2.21n)$$

and

$$r^* = ra^* \quad (2.21o)$$

Also, four dimensionless parameters appear in the shock-layer equations.

They are

$$Pr = C_p^* \mu^*/K^* \quad (2.22a)$$

$$\epsilon = \sqrt{\frac{\mu_{ref}^*}{\rho_{\infty}^* U_{\infty}^* a^*}} \quad (2.22b)$$

$$\zeta = \rho^* C_p^* \delta_{ij}^*/K^* \quad (2.22c)$$

and

$$L_{ij} = \rho^* C_p^* D_{ij}^*/K^* \quad (2.22c)$$

To simplify the numerical computations, a transformation is applied to the foregoing equations. This is accomplished by normalizing the independent and dependent variables with their local shock values. When the normal coordinate is normalized with respect to the local shock stand-off distance, a constant number of finite-difference grid points between the body and shock are used. Also, the need for interpolating to determine shock shape and the addition of grid points in the normal direction is eliminated.

The transformed independent and dependent variables are

$$\eta = n/n_s \quad (2.23a)$$

$$\xi = s, \quad (2.23b)$$

$$\bar{u} = u/u_s, \quad (2.23c)$$

$$\bar{v} = v/v_s, \quad (2.23d)$$

$$\bar{p} = p/p_s, \quad (2.23e)$$

$$\bar{\rho} = \rho/\rho_s, \quad (2.23f)$$

$$\bar{T} = T/T_s, \quad (2.23g)$$

$$\bar{H} = H/H_s, \quad (2.23h)$$

$$\bar{\mu} = \mu/\mu_s, \quad (2.23i)$$

$$\bar{K} = K/K_s, \quad (2.23j)$$

and

$$\bar{c}_p = c_p/c_{p_s}. \quad (2.23k)$$

The transformations relating the differential quantities are

$$\frac{\partial}{\partial s} = \frac{\partial}{\partial \xi} - \frac{n'_s}{n_s} \eta \frac{\partial}{\partial \eta} , \quad (2.24a)$$

$$\frac{\partial}{\partial n} = \frac{1}{n_s} \frac{\partial}{\partial \eta} , \quad (2.24b)$$

and

$$\frac{\partial^2}{\partial n^2} = \frac{1}{n_s^2} \frac{\partial^2}{\partial \eta^2} \quad (2.24c)$$

where

$$n'_s = \frac{dn_s}{d\xi} . \quad (2.24d)$$

The s-momentum, energy (temperature and enthalpy), species continuity, and elemental continuity equations (eqs. (2.2), (2.4), (2.7), (2.5) and (2.10), when written in the transformed ξ, η plane, can be put into the following standard form for a parabolic partial differential equation:

$$\frac{\partial^2 W}{\partial \eta^2} + \alpha_1 \frac{\partial W}{\partial \eta} + \alpha_2 W + \alpha_3 + \alpha_4 \frac{\partial W}{\partial \xi} = 0 \quad (2.25)$$

where W equals \bar{u} in the s-momentum equation, \bar{T} in the temperature energy equation, \bar{H} in the enthalpy energy equation, C_i in the species continuity equations, and \tilde{C}_ℓ in the elemental continuity equation. The coefficients α_1 through α_4 may be written as follows:

s-momentum

$$\alpha_1 = \frac{1}{\bar{\mu}} \frac{\partial \bar{\mu}}{\partial \eta} + \frac{n_s \kappa}{1+n_s \eta \kappa} + \frac{j n_s \cos \theta}{r+n_s \eta \cos \theta} + \frac{n_s \rho_s u_s n'_s}{\epsilon^2 \mu_s (1+n_s \eta \kappa)} \frac{\bar{\rho} u \eta}{\bar{\mu}} - \frac{n_s \rho_s v_s}{\epsilon^2 \mu_s} \frac{\bar{\rho} v}{\bar{\mu}}, \quad (2.26a)$$

$$\alpha_2 = -\frac{\kappa n_s}{(1+n_s \eta \kappa)} \frac{1}{\bar{\mu}} \frac{\partial \bar{\mu}}{\partial \eta} - \frac{\kappa^2 n_s^2}{(1+n_s \eta \kappa)^2} - \frac{j \cos \theta n_s^2 \kappa}{(r+n_s \eta \cos \theta) (1+n_s \eta \kappa)} - \frac{\rho_s n_s^2 u'_s}{\epsilon^2 \mu_s (1+n_s \eta \kappa)} \frac{\bar{u} \rho}{\bar{\mu}} - \frac{n_s^2 \rho_s v_s \kappa}{\epsilon^2 \mu_s (1+n_s \eta \kappa)} \frac{\bar{\rho} v}{\bar{\mu}}, \quad (2.26b)$$

$$\alpha_3 = -\frac{p_s n_s^2}{\epsilon^2 \mu_s (1+n_s \eta \kappa)} \frac{\bar{p}}{\bar{\mu}} \left[\frac{\partial \bar{p}}{\partial \xi} + \frac{p'_s \bar{p}}{p_s} - \frac{n'_s \eta}{n_s} \frac{\partial \bar{p}}{\partial \eta} \right], \quad (2.26c)$$

$$\alpha_4 = -\frac{\rho_s u_s n_s^2}{\epsilon^2 \mu_s (1+n_s \eta \kappa)} \frac{\bar{\rho} u}{\bar{\mu}}, \quad (2.26d)$$

Energy (temperature)

$$\alpha_1 = \frac{1}{\bar{K}} \frac{\partial \bar{K}}{\partial \eta} + n_s \left[\frac{\kappa}{1+n_s \eta \kappa} + \frac{j \cos \theta}{r+n_s \eta \cos \theta} \right] - \frac{n_s \sum_{i=1}^{NS} J_i^C p_i}{K_s \bar{K}} - \frac{n_s \rho_s C_p \bar{\rho} C_p}{\epsilon^2 K_s \bar{K}} \left[v_s \bar{v} - \frac{u_s n'_s \bar{u} \eta}{1+n_s \eta \kappa} \right], \quad (2.27a)$$

$$\alpha_2 = \frac{\alpha_4 T'_s}{T_s} - \frac{n_s^2 \dot{w}_s^2}{\epsilon^2 K_s} \frac{\bar{w}_2}{\bar{K}}, \quad (2.27b)$$

$$\begin{aligned}
\alpha_3 = & -\frac{n_s^2 \dot{w}_s \bar{1}}{\epsilon^2 T_s K_s \bar{K}} + \frac{n_s^2 \mu_s \bar{\mu}}{T_s K_s \bar{K}} \left[\frac{u_s}{n_s} \frac{\partial \bar{u}}{\partial \eta} - \frac{\kappa u_s \bar{u}}{1+n_s \eta \kappa} \right]^2 \\
& + \frac{n_s^2 u_s P_s \bar{u}}{\epsilon^2 T_s K_s \bar{K} (1+n_s \eta \kappa)} \left[\frac{P'_s \bar{P}}{P_s} - \frac{\partial \bar{P}}{\partial \xi} - \frac{n'_s \eta}{n_s} \frac{\partial \bar{P}}{\partial \eta} \right] \\
& + \frac{n_s v_s P_s}{\epsilon^2 T_s K_s \bar{K}} \bar{v} \frac{\partial \bar{P}}{\partial \eta} ,
\end{aligned} \tag{2.27c}$$

$$\alpha_4 = -\frac{n_s^2 p_s C_p u_s}{\epsilon^2 K_s (1+n_s \eta \kappa)} \frac{\bar{\rho} \bar{C} \bar{u}}{\bar{K}} , \tag{2.27d}$$

Energy (enthalpy)

$$\begin{aligned}
\alpha_1 = & \frac{1}{\bar{\mu}} \frac{\partial \bar{\mu}}{\partial \eta} - \frac{1}{\bar{Pr}} \frac{\partial \bar{Pr}}{\partial \eta} + n_s \left[\frac{\kappa}{1+n_s \eta \kappa} + \frac{j \cos \theta}{r+n_s \eta \cos \theta} \right] \\
& + \frac{\rho_s Pr_s \bar{Pr} n_s}{\epsilon^2 \mu_s \bar{\mu}} \left[\frac{n'_s u_s \eta \bar{\rho}}{1+n_s \eta \kappa} - v_s \bar{\rho} \bar{v} \right]
\end{aligned} \tag{2.28a}$$

$$\alpha_2 = \frac{\alpha_4 H'_s}{H_s} \tag{2.28b}$$

$$\alpha_3 = \frac{Pr_s \bar{Pr} n_s^2}{\mu_s \bar{\mu} H_s} \left[\frac{1}{n_s} \frac{\partial \Psi}{\partial \eta} + \left(\frac{\kappa}{1+n_s \eta \kappa} + \frac{j \cos \theta}{r+n_s \eta \cos \theta} \right) \Psi \right] \tag{2.28c}$$

$$\alpha_4 = -\frac{Pr_s n_s^2 \rho_s u_s \bar{Pr} \bar{\rho}}{\epsilon^2 \mu_s (1+n_s \eta \kappa) \bar{\mu}} \tag{2.28d}$$

where

$$\Psi = \frac{\mu_s}{n_s \bar{Pr}_s} \left[-\frac{\bar{\mu}}{\bar{Pr}} \sum_{i=1}^{NS} h_i \frac{\partial C_i}{\partial \eta} + \frac{u^2 \bar{\mu} \bar{u}}{\bar{Pr}} \left(\bar{Pr}_s \bar{Pr} - 1 \right) \frac{\partial \bar{u}}{\partial \eta} \right] - \sum_{i=1}^{NS} h_i J_i - \frac{\mu_s u^2 \kappa \bar{\mu} \bar{u}^2}{1+n_s \eta \kappa} \quad (2.28e)$$

The above relations are for the thin shock-layer approximation. When equation (2.3a) is used for the n-momentum equation, the following terms must be added to α_3 :

$$- \frac{\bar{Pr}_s v_s n_s^2 \rho_s \bar{Pr} \bar{\rho} v}{\epsilon^2 \mu_s H_s \bar{\mu}} \left[\frac{u \bar{u}}{1+n_s \eta \kappa} \left(-v v'_s + v_s \frac{\partial \bar{v}}{\partial \xi} - \frac{n'_s \eta v_s}{n_s} \frac{\partial \bar{v}}{\partial \eta} \right) + \frac{v_s^2 \bar{v}}{n_s} \frac{\partial \bar{v}}{\partial \eta} \right] \quad (2.28f)$$

Species continuity

$$\alpha_1 = \frac{1}{PL} \frac{\partial PL}{\partial \eta} + n_s \left[\frac{\kappa}{1+n_s \eta \kappa} + \frac{j \cos \theta}{r+n_s \eta \cos \theta} \right] - \frac{\rho_s v_s n_s \bar{\rho} v}{\epsilon^2 PL} + \frac{n_s \rho_s u_s n'_s \bar{\rho} u \eta}{\epsilon^2 PL (1+n_s \eta \kappa)} \quad (2.29a)$$

$$\alpha_2 = - \frac{n_s \dot{w}_i}{\epsilon^2 PL} \quad (2.29b)$$

$$\alpha_3 = \frac{1}{PL} \left[\frac{\partial PM}{\partial \eta} + n_s PM \left(\frac{\kappa}{1+n_s \eta \kappa} + \frac{j \cos \theta}{r+n_s \eta \cos \theta} \right) + \frac{\dot{w}_i^0 n_s^2}{\epsilon^2} \right] \quad (2.29c)$$

$$\alpha_4 = - \frac{n_s^2 \rho_s u_s \bar{\rho} u}{\epsilon^2 PL (1+n_s \eta \kappa)} \quad (2.29d)$$

where

$$PL = \frac{\mu_s \bar{\mu} L_i}{Pr_s \bar{Pr}} \quad (2.29e)$$

and

$$PM = \frac{\mu_s \bar{\mu}}{Pr_s \bar{Pr}} \sum_{\substack{NS \\ k=1 \\ \neq i}} \Delta b_{i,k} \frac{\partial C_k}{\partial \eta} \quad (2.29f)$$

for multicomponent diffusion and

$$PL = \frac{\mu_s \bar{\mu} \zeta}{Pr_s \bar{Pr}} \quad (2.29g)$$

and

$$PM = 0 \quad (2.29h)$$

for binary diffusion.

Elemental Continuity

$$\alpha_1 = \frac{1}{\tilde{PL}} \frac{\partial \tilde{PL}}{\partial \eta} + n_s \left[\frac{\kappa}{1+n_s \eta \kappa} + \frac{j \cos \theta}{r+n_s \eta \cos \theta} \right] - \frac{\rho_s v_s n_s \bar{\rho} \bar{v}}{\epsilon^2 \tilde{PL}} + \frac{n_s \rho_s u_s n'_s \bar{\rho} \bar{u} \eta}{\epsilon^2 \tilde{PL} (1+n_s \eta \kappa)} \quad (2.30a)$$

$$\alpha_2 = 0 \quad (2.30b)$$

$$\alpha_3 = \frac{1}{\tilde{PL}} \left[\frac{\partial}{\partial \eta} \tilde{PM} + n_s \tilde{PM} \left(\frac{\kappa}{1+n_s \eta \kappa} + \frac{j \cos \theta}{r+n_s \eta \cos \theta} \right) \right] \quad (2.30c)$$

$$\alpha_4 = - \frac{n_s^2 \rho_s u_s}{\epsilon^2 (1+n_s \eta \kappa)} \frac{\bar{\rho u}}{\bar{P L}} \quad (2.30d)$$

where

$$\tilde{P L} = \frac{\mu_s \bar{\mu L}}{Pr_s \bar{P r}} \quad (2.30e)$$

and

$$\tilde{P M} = \frac{NS}{\sum_{i=1}^{NS} \delta_{i\ell}} \frac{M^*_\ell}{M^*_i} \frac{NS}{\sum_{k=1}^{NS} \Delta b_{ik}} \frac{\partial C_k}{\partial \eta} \quad (2.30f)$$

≠i

for multicomponent diffusion and

$$\tilde{P L} = \frac{\mu_s \bar{\mu \zeta}}{Pr_s \bar{P r}} \quad (2.30g)$$

and

$$\tilde{P M} = 0 \quad (2.30h)$$

for binary diffusion.

The remaining equations may be written as follows:

Global Continuity

$$\frac{\partial}{\partial \xi} \left[n_s (r + n_s \eta \cos \theta)^j \rho_s u_s \bar{\rho u} \right] + \frac{\partial}{\partial \eta} \left[(r + n_s \eta \cos \theta)^j \left\{ (1 + n_s \eta \kappa) \right. \right. \\ \left. \left. \rho_s v_s \bar{\rho v} - n'_s \eta \rho_s u_s \bar{\rho u} \right\} \right] = 0, \quad (2.31)$$

n-momentum

$$\frac{\bar{\rho} \bar{u}}{1+n_s \eta \kappa} \left[\frac{v'_s}{v_s} \bar{v} + \frac{\partial \bar{v}}{\partial \xi} - \frac{n'_s \eta}{n_s} \frac{\partial \bar{v}}{\partial \eta} \right] + \frac{v_s}{u_s} \frac{\bar{\rho} \bar{v}}{n_s} \frac{\partial \bar{v}}{\partial \eta}$$

$$- \frac{u_s}{v_s} \frac{\kappa}{(1+n_s \eta \kappa)} \bar{\rho} \bar{u}^2 + \frac{P_s}{\rho_s u_s n_s v_s} \frac{\partial \bar{P}}{\partial \eta} = 0, \quad (2.32a)$$

which becomes

$$\frac{\partial \bar{P}}{\partial \eta} = \frac{n_s \rho_s u_s^2 \kappa}{P_s (1+n_s \eta \kappa)} \bar{\rho} \bar{u}^2 \quad (2.32b)$$

if the thin shock-layer approximation is made, and

State

$$\bar{P} = \bar{\rho} \bar{T} \frac{M^*}{M^*_s} \quad (2.33)$$

The terms \dot{w}_1 and \dot{w}_2 which appear in the temperature form of the energy equation and the terms w_i^0 and w_i^1 which appear in the species continuity equations are quantities that involve the rate of production terms \dot{w}_i . As discussed in reference 1, 8, and 11, the way the production terms are written is very important to achieve convergence of the iteration procedure. Consequently, for the energy equation, the production terms were written as given in reference 8 as

$$\left(\frac{\dot{w}_i}{\rho}\right)_{k+1} = \left(\frac{\dot{w}_i}{\rho}\right)_k + \left[\frac{\partial}{\partial T}\left(\frac{\dot{w}_i}{\rho}\right)\right]_k [T_{k+1} - T_k] \quad (2.34)$$

where k denotes the iteration for which the solution is known and $k + 1$ the iteration for which a solution is required. Accordingly, the term $\sum_{i=1}^{NS} h_i \dot{w}_i$ which appears in equation (2.4) was written as follows:

$$\sum_{i=1}^{NS} h_i \dot{w}_i = \dot{w}_{s1} \bar{w}_1 + T_s w_{s2} \bar{T} \dot{w}_2 \quad (2.35)$$

and appears in equations (2.27b) and (2.27c). As for the species continuity equations, the production term was written as

$$\frac{\dot{w}_i}{\rho} = \dot{w}_i^o - C_i \dot{w}_i^1 \quad (2.36)$$

and appears in equations (2.29b) and (2.29c). Hence, equations (2.34) and (2.36) express the production terms in terms of temperature for the energy equation and species mass fraction for the species equations. Blottner in reference 1 comments on the necessity of using expressions like equations (2.34) and (2.36).

For frozen, equilibrium, and nonequilibrium chemistry, equations (2.25) through (2.33), along with appropriate boundary conditions and relations for the thermodynamic and transport properties, are the governing relations that will be used to describe the viscous shock layer.

Boundary Conditions

Conditions at the body surface.-The no-slip boundary conditions are used in this study. The surface conditions for $\eta = 0$ (see fig. 2) are

$$\bar{u} = 0, \quad (2.37)$$

$$\bar{v} = \dot{m}/\bar{\rho}, \quad (2.38)$$

where the mass injection rate,

$$\dot{m} = (\bar{\rho}\bar{v}), \quad (2.39a)$$

is specified. The mass injection distribution along the body surface is assumed to be

$$\dot{m} = \dot{m}_0 e^{-3.47 r^2}, \quad (2.39b)$$

where \dot{m}_0 is the stagnation mass injection rate. This injection distribution is the same as that used in reference 9.

The wall temperature is assumed to be

$$T_w = \text{constant}. \quad (2.40)$$

Also, the surface total enthalpy is given as

$$\bar{H} = \sum_{i=1}^{NS} h_i C_i \quad (2.41)$$

Finally, consider the boundary conditions for the elemental and species equations (see fig. 2) at the gas-solid interface. The species i are transported away from the surface at the rate J_i by diffusion and at the rate $\bar{\rho}v C_i$ by convection. At the same time, the species i are being convected to the surface at the rate $(\bar{\rho}v C_i)_-$. This flux may be considered that from an ablating surface or the injectant from a porous solid. The surface species concentrations are given (ref. 20) by

$$\bar{\rho}v C_i + \epsilon^2 J_i = (\bar{\rho}v C_i)_- \quad (2.42)$$

Since

$$\bar{\rho}v = (\bar{\rho}v)_- = \dot{m} \quad (2.43)$$

equation (2.42) may be written as

$$(C_i - C_{i-}) \dot{m} = -\epsilon^2 J_i \quad (2.44a)$$

and in terms of elemental boundary conditions as

$$(\tilde{C}_\ell - \tilde{C}_{\ell-}) \dot{m} = -\epsilon^2 \tilde{J}_\ell \quad (2.44b)$$

For the numerical computations, the surface elemental and species boundary conditions are written in the following form:

$$\frac{\partial w}{\partial \eta} + \beta_1 w + \beta_2 = 0 \quad (2.45)$$

where w equals \tilde{C}_ℓ for the elemental equations and C_i for the species equations. For the elemental surface boundary conditions, the coefficients β_1 and β_2 are defined as follows:

Multicomponent Diffusion

$$\beta_1 = - \frac{\rho_s v_s \dot{m}_s \text{Pr}_s \bar{\text{Pr}}}{\epsilon^2 \mu_s \bar{\mu} L} \quad (2.46a)$$

$$\beta_2 = -\beta_1 \tilde{C}_{\ell-} + n_{sL}^2 \sum_{i=1}^{NS} \frac{\delta_{i\ell} M_i^*}{M_i^*} \sum_{\substack{k=1 \\ \neq i}}^{NS} \Delta b_{ik} \frac{\partial C_k}{\partial \eta} \quad (2.46b)$$

Binary Diffusion

$$\beta_1 = - \frac{\rho_s v_s \dot{m}_s}{\epsilon^2 \mu_s \bar{\mu} \zeta} \text{Pr}_s \bar{\text{Pr}} \quad (2.46c)$$

$$\beta_2 = -\beta_1 \tilde{C}_{\ell-} \quad (2.46d)$$

Accordingly, for the species boundary conditions, the coefficients β_1 and β_2 are defined as follows:

Multicomponent Diffusion

$$\beta_1 = - \frac{\rho_s v_s \dot{m}_s \text{Pr}_s \bar{\text{Pr}}_s}{\epsilon^2 L_i \mu_s \bar{\mu}} \quad (2.47a)$$

$$\beta_2 = - \beta_1 C_{i-} + \frac{1}{L_i} \sum_{\substack{\text{NS} \\ k=1 \\ \neq i}} \Delta b_{ik} \frac{\partial C_k}{\partial \eta} \quad (2.47b)$$

Binary Diffusion

$$\beta_1 = - \frac{\rho_s v_s \dot{m}_s \text{Pr}_s \bar{\text{Pr}}_s}{\epsilon^2 \mu_s \bar{\mu} \zeta} \quad (2.47c)$$

$$\beta_2 = -\beta_1 C_{i-} \quad (2.47d)$$

When the diffusion is binary and no injection occurs, the elemental concentrations are constant and equal to the free-stream value. For this case, the elemental equations are superfluous and the surface conditions become

$$\tilde{C}_{l_w} = \tilde{C}_{l_\infty} \quad (2.48)$$

However, when the diffusion is multicomponent the elemental distribution along the normal to the surface is not constant and the element conservation equations must be used to calculate the elemental distribution.

Conditions at the Shock.-The conditions imposed at the shock were calculated by using the Rankine-Hugoniot relations where the flow was assumed to be in chemical equilibrium or frozen at the free-stream composition. The nondimensional shock relations are as follows:

$$\rho_s v_s'' = -\sin \alpha, \quad (2.49a)$$

$$u_s'' = \cos \alpha, \quad (2.49b)$$

$$P_s = \frac{1}{\gamma_\infty M_\infty^2} + \sin^2 \alpha \left[1 - \frac{1}{\rho_s} \right], \quad (2.49c)$$

$$h_s = \frac{1}{M_\infty^2 (\gamma_\infty - 1)} + \frac{\sin^2 \alpha}{2} \left[1 - \frac{1}{\rho_s^2} \right], \quad (2.49d)$$

$$P_s = \frac{\rho_s T_s R^*}{\bar{M}_s^* C_p^* P_\infty} \quad (2.49e)$$

$$h_s = \sum_{i=1}^{NS} h_i C_i, \quad (2.49f)$$

and

$$\tilde{C}_{\lambda_s} = \tilde{C}_{\lambda_\infty}. \quad (2.49g)$$

Also, for the calculations where the chemistry was frozen across the shock,

$$C_{i_s} = C_{i_\infty} \quad (2.49h)$$

When the flow field chemistry is equilibrium, additional relations are required to relate the species compositions to the state variables. This is accomplished by using a free-energy minimization equilibrium program that will be discussed later.

The transformations used to express the shock-oriented velocities u''_s and v''_s in terms of the body-oriented coordinate system (fig. 1) are

$$u_s = u''_s \sin(\alpha + \beta) + v''_s \cos(\alpha + \beta) \quad (2.50)$$

and

$$v_s = -u''_s \cos(\alpha + \beta) + v''_s \sin(\alpha + \beta). \quad (2.51)$$

The normalized shock conditions become

$$\bar{u} = \bar{T} = \bar{H} = \bar{v} = \bar{\rho} = \bar{P} = 1 \quad (2.52)$$

at $\eta = 1$. Note that the elemental and species mass fractions are not normalized with their respective shock values.

Surface Transport

The rate at which heat is transferred to the surface boundary, q , is given by the sum of the convective, conductive, and diffusion contributions. This is true if radiation and surface reactions such as sublimation, vaporization, oxidation, and melting are neglected, as was

the case for this study. The net nondimensional heat transfer to the solid interior is given by

$$q = - \left[\epsilon^2 \left(K \frac{\partial T}{\partial n} + \sum_{i=1}^{NS} J_i h_i \right) + \dot{m} \sum_{i=1}^{NS} \left(C_i h_i - C_{i-} h_{i-} \right) \right]_w \quad (2.53)$$

The Stanton number is given by

$$St = - \frac{q}{H_\infty - H_w} \quad (2.54)$$

and the skin friction coefficient is given by

$$C_f = 2\epsilon^2 \left[\mu \frac{\partial u}{\partial n} \right]_w \quad (2.55)$$

III. THERMODYNAMIC AND TRANSPORT PROPERTIES

The thermodynamic properties C_{pi} and h_i and the transport properties μ_i , K_i , and \mathcal{D}_{ij} are required for each species considered. Also, for the equilibrium calculations, the free energies, F_i , are required. Since the multicomponent gas mixtures are considered to be mixtures of thermally perfect gases, the thermodynamic and transport properties for each species are calculated by using the local temperature and pressure. Then the properties for the gas mixtures are determined in terms of the individual species properties. The methods used to calculate the thermodynamic and transport properties are given in this chapter. Since all the expressions presented are in terms of dimensional quantities, the starred superscript will not be used to denote a dimensional quantity.

Thermodynamic Properties

Data for thermodynamic properties were obtained from references 23 and 24. Reference 23 presents thermodynamic properties for 210 substances for temperatures up to 6000°K. Reference 24 presents thermodynamic properties for a smaller number of species than reference 23 but for temperatures up to 15000°K. The specific heats are expressed in terms of temperature according to the following polynomial equation:

$$\frac{C_{pi}}{R} = a_1 + a_2T + a_3T^2 + a_4T^3 + a_5T^4 . \quad (3.1)$$

The coefficients a_1 through a_5 are given in table I for each species considered in this study. In addition to specific heat data, the following quantities are required: $(h_i^o)_o$, $(h_i^o)_{298} - (h_i^o)_o$, and $-\left[\left(F_i^o\right)_{298} - \left(h_i^o\right)_o\right]$. Values for these quantities are also given in table I. The enthalpy for species i is obtained from the relation

$$h_i = \int_{298}^T C_{P_i} dT + h_{i,298}^o \quad (3.2)$$

where $h_{i,298}^o$ is the enthalpy of formation. Development of the expressions for the free energies, F_i , will be given in Chapter IV. The mixture frozen specific heat and the mixture enthalpy are given by equations (2.13) and (2.15), respectively.

Transport Properties

The gas mixtures considered in this work were assumed to be mixtures of thermally perfect gases. Accordingly, the expressions for calculating the transport properties of the pure species will be presented first, followed by the expressions for calculating the transport properties of the mixture.

To a first approximation (first-order kinetic theory), the viscosity for a perfect gas (ref. 22) is given as

$$\mu_i = \frac{2.6693 \times 10^{-5} \sqrt{T M_i}}{\sigma_i^2 \Omega(2,2)}, \quad (3.3)$$

and the thermal conductivity for a monotonic gas is given as

$$K_{i \text{ mono}} = \frac{1.9891 \times 10^{-4} \sqrt{T/M_i}}{\sigma_i^2 \Omega(2,2)}, \quad (3.4a)$$

or

$$K_{i \text{ mono}} = \frac{15}{4} \frac{\mu_i}{M_i} R, \quad (3.4b)$$

whereas the thermal conductivity for a polyatomic gas has an additional contribution due to the transfer of energy between translational and internal degrees of freedom. Consequently, the expression for the thermal conductivity of polyatomic molecules is given (ref. 25) as

$$K_i = \frac{R}{M_i} \mu_i \left[\frac{15}{4} + 1.32 \left(\frac{C_{P_i}}{R} - \frac{5}{2} \right) \right]. \quad (3.4c)$$

In the foregoing equations

T = temperature in °K,

M_i = molecular weight,

σ_i = collision diameter in Å

μ_i = viscosity in g/cm sec,

K_i = thermal conductivity in cal/sec-°K,

and

$\Omega(2,2)$ = collision integral for viscosity.

Expressions for the multicomponent viscosity and thermal conductivity according to rigorous kinetic theory are given in reference 22. However, these expressions are cumbersome and computationally time consuming.

Consequently most studies use approximate techniques for evaluating the mixture viscosity and thermal conductivity.

The mixture viscosity is obtained by using the semiempirical formula of Wilke (from ref. 18)

$$\mu = \frac{\sum_{i=1}^{NS} x_i \mu_i}{\sum_{j=1}^{NS} x_j \phi_{ij}} \quad (3.5a)$$

where

$$\phi_{ij} = \frac{\left[1 + (\mu_i/\mu_j)^{1/2} (M_j/M_i)^{1/4} \right]^2}{\frac{1}{8} \left[1 + \frac{M_i}{M_j} \right]^{1/2}} \quad (3.5b)$$

The mixture thermal conductivity is obtained by a method analogous to that used for viscosity. The relation used (ref. 18) for calculating the mixture conductivity is

$$K = \frac{\sum_{i=1}^{NS} x_i K_i}{\sum_{j=1}^{NS} x_j \phi_{ij}} \quad (3.6)$$

where the ϕ_{ij} coefficients are identical with those that appear in the viscosity equation (eq. (3.5b)).

The binary diffusion coefficients are obtained by using the relation given in reference 22

$$D_{ij} = \frac{2.628 \times 10^{-3} T^{3/2} \sqrt{\frac{M_i + M_j}{2M_i M_j}}}{P \sigma_{ij}^2 \Omega^{(1,1)}}, \quad (3.7)$$

where $\Omega^{(1,1)}$ is the collision integral for diffusion. The collision integrals $\Omega^{(1,1)}$ and $\Omega^{(2,2)}$ are functions of the nondimensional reduced temperature,

$$T^+ = \frac{T}{\epsilon_{ij}/k}, \quad (3.8)$$

where ϵ_{ij} is the maximum energy of attraction between colliding molecules and k is Boltzmann's constant. The parameters σ_{ij} and ϵ_{ij} are estimated satisfactorily by combining as

$$\sigma_{ij} = \frac{1}{2} [\sigma_i + \sigma_j] \quad (3.9)$$

and

$$\epsilon_{ij} = \sqrt{\epsilon_i \epsilon_j}. \quad (3.10)$$

The force constants σ_i and ϵ_i/k for each species considered in this study are given in table II. The force constants are those given in references 25 and 26. The collision integrals were obtained from reference 22, pages 1126-1127, where they are tabulated as a function of reduced temperature T^+ . These collision integrals are based on the

Lennard Jones (12-6) potential for the interaction of colliding molecules.

The multicomponent diffusion coefficients are dependent on the concentration of the species whereas the binary coefficients are concentration independent. The multicomponent coefficients are obtained by using the relations given in reference 1, which may be written as:

$$D_{ij} = \bar{K}_{ij} - \frac{M_i}{M_j} \bar{K}_{ii} \quad (3.11a)$$

where the quantities \bar{K}_{ij} are coefficients in a matrix which is the inverse of the matrix with the following coefficients:

$$K_{ij} = \left\{ \begin{array}{ll} \frac{C_i}{D_{ij}} + M_j \sum_{\substack{\ell=1 \\ \ell \neq i}}^{NS} \frac{C_\ell}{M_\ell} D_{i\ell} & \text{for } i \neq j \\ 0 & \text{for } i = j \end{array} \right\} \quad (3.11b)$$

For the binary calculations, it is assumed that all species have diffusion coefficients that are equal to an effective binary coefficient. The effective binary coefficients are determined for a pre-assigned diffusing pair of species. For example, the effective binary diffusion coefficients for air will be that of atomic oxygen diffusing into molecular nitrogen evaluated at the local temperature and pressure according to equation (3.7). However, for the calculations with multicomponent diffusion, the diffusion coefficients, D_{ij} , are evaluated according to equation (3.11).

IV. CHEMICAL REACTION MODELS

Analyses of chemically reacting flows are frequently simplified by considering the limiting cases of frozen and equilibrium chemical behavior. However, the question naturally arises: Which of these two limiting cases is more descriptive of reality? Of course, to answer this question the detailed finite-rate behavior of the chemical reactions must be accounted for. Yet, an analysis of a complex chemically reacting gas mixture, where the chemistry is nonequilibrium, presents problems that are not associated with either frozen or equilibrium treatments. These problems are primarily those of defining a realistic reactions model, of obtaining the appropriate rate constants, and of obtaining a numerical solution. In general, it is the latter problem that precludes a non-equilibrium treatment of reacting flows.

In this study, the finite-rate treatment of the chemical reactions will be applied only to a system of neutral air species (O, O₂, N, N₂, and NO). However, the equilibrium treatment includes neutral air species as well as the complex chemical systems that result from injection of water or ablation products into a reacting air stream. The methods used to make the equilibrium and finite rate calculations will presently be discussed.

Equilibrium Chemistry

The mixture equilibrium composition is determined for a given temperature and pressure by the free-energy minimization technique.

Reference 27 describes the free-energy minimization computer program used in this study.

In the free-energy minimization method, the equilibrium constants are not used. In fact, specification of the various reactions is not required. However, the species for which the equilibrium composition is to be determined must be specified and the elemental composition must be known. Also, the free energy for each species is calculated from which the total free energy of the mixture is determined. This total free energy is then made a minimum with respect to any possible change in composition for the given temperature and pressure. Since the criterion for equilibrium at constant temperature and pressure is that the change in free energy be zero, $dF = 0$, the equilibrium composition is determined when the total free energy of the mixture is a minimum.

The free energy for a mixture of thermally perfect gases is obtained by using the following definition for free energy of species i :

$$F_i = h_i - TS_i, \quad (4.1)$$

where S_i is the entropy of species i . The standard state (pure substance at one atmosphere of pressure) free energies,

$$F_i^0 = h_i^0 - TS_i^0, \quad (4.2)$$

are a function of temperature only. The enthalpies are obtained relative to a base state, taken as the elements in their most natural form at 298°K and one atmosphere (ref. 23). For a constant pressure, an expression for the entropies in terms of specific heats is obtained from the combined first and second laws of thermodynamics as

$$dS_i^o = \frac{C_{P_i} dT}{T} \quad (4.3)$$

or

$$S_i^o = S_{i,298}^o + \int_{298}^T \frac{C_{P_i} dT}{T} \quad (4.4)$$

With

$$h_i^o = \int_{298}^T C_{P_i} dT + h_{i,298}^o \quad (4.5)$$

equation (4.2) may be written as

$$F_i^o = F_{i,298}^o - \left[\frac{T - 298}{298} \right] \left[h_{i,298}^o - F_{i,298}^o \right] + \int_{298}^T C_{P_i} dT - T \int_{298}^T \frac{C_{P_i} dT}{T} \quad (4.6)$$

For constant temperature, the change in free energy of a thermally perfect gas is given by the expression

$$dF_i = RTd\ln p_i \quad (4.7)$$

By integrating equation (4.7) at constant temperature from a standard state where the free energy and pressure are F_i^0 and one atmosphere, respectively, to some other state F_i and p_i , the following is obtained:

$$F_i = F_i^0 + RT\ln p_i \quad (4.8a)$$

or

$$F_i = F_i^0 + RT \left[\ln p + \ln x_i \right] \quad (4.8b)$$

since

$$p_i = p x_i \quad (4.9)$$

and x_i denotes the mole fractions. The expression for the free energy of the mixture becomes

$$F = \sum_{i=1}^{NS} x_i \left[F_i^0 + RT (\ln p + \ln x_i) \right] \quad (4.10)$$

where the free energies in the standard state are given by equation (4.6).

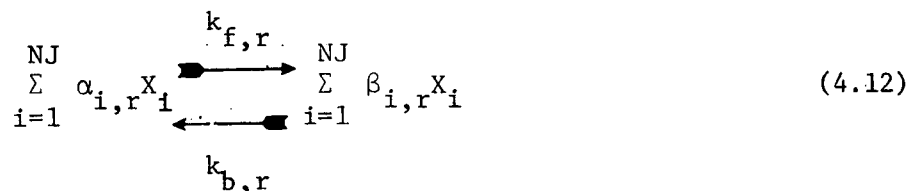
By minimizing the above equation subject to the constraint equations

$$\sum_{i=1}^{NS} \delta_{i\ell} \frac{M_\ell}{\bar{M}} x_i = \tilde{C}_\ell \quad (4.11)$$

the equilibrium composition is obtained. Details of the solution procedure are given in reference 27.

Finite Rate Chemistry

When chemical reactions proceed at a finite rate, the rate of production terms, \dot{w}_i , are required. The production terms appear in the energy equation (eq.(2.4)) when formulated in terms of temperature and in the species continuity equations (eq. (2.5)). For a multicomponent gas with NS chemical species and NR chemical reactions, the chemical equation describing the overall change from reactants to products may be written in the general form



where $r = 1, 2, \dots, NR$ and NJ is equal to the sum of the species and the catalytic bodies. The quantities $\alpha_{i,r}$ and $\beta_{i,r}$ are the stoichiometric coefficients for reactants and products respectively whereas $k_{f,r}$ and $k_{b,r}$ are the forward and backward rate constants. Also, the quantities X_i denote the concentrations in moles per volume of the distinct chemical species NS and the catalytic bodies. The

catalytic bodies (NJ-NS) may be chemical species or linear combinations of species that do not undergo a chemical change during the reaction. The rate of change of any species as a result of a particular reaction (ref. 28) is

$$\left(\frac{dX_i}{dt}\right)_r = \left[\beta_{i,r} - \alpha_{i,r}\right] \left[k_{f,r} \prod_{j=1}^{NJ} X_j^{\alpha_{j,r}} - k_{b,r} \prod_{j=1}^{NJ} X_j^{\beta_{j,r}} \right] \quad (4.13)$$

The above equation may be rewritten as

$$\left(\dot{w}_i\right)_r = M_i \left[\beta_{i,r} - \alpha_{i,r}\right] \left[k_{f,r} \prod_{j=1}^{NJ} (\gamma_j \rho)^{\alpha_{j,r}} - k_{b,r} \prod_{j=1}^{NJ} (\gamma_j \rho)^{\beta_{j,r}} \right] \quad (4.14)$$

where the mole-mass ratio, γ_j , is defined as

$$\gamma_j = \frac{X_j}{\rho_i} = \frac{C_j}{M_j} \quad (4.15)$$

and

$$\dot{w}_i = \frac{1}{M_i} \frac{dX_i}{dt} = \frac{d\rho_i}{dt} \quad (4.16)$$

In order to find the net mass rate of production of the i^{th} species per unit volume, equation (4.14) must be summed over all reactions r . Thus, one obtains

$$\dot{w}_i = M_i \sum_{r=1}^{NR} \left[\beta_{i,r} - \alpha_{i,r}\right] \left[k_{f,r} \prod_{j=1}^{NJ} (\gamma_j \rho)^{\alpha_{j,r}} - k_{b,r} \prod_{j=1}^{NJ} (\gamma_j \rho)^{\beta_{j,r}} \right] \quad (4.17)$$

which is the general rate equation for a gas mixture.

The mole-mass ratios for the NS species are

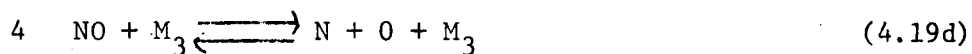
$$\gamma_j = C_j/M_j \quad j = 1, 2, \dots, NS, \quad (4.18a)$$

whereas for the catalytic bodies, the following expressions (ref. 2) are used:

$$\gamma_j = \sum_{i=1}^{NS} Z_{(j-NS),i} \gamma_i \quad j = NS + 1, \dots, NJ. \quad (4.18b)$$

The constants $Z_{(j-NS),i}$ are determined from the linear dependence of the catalytic bodies upon the NS species. Values of these constants are given in reference 11 and in table III.

The chemical reactions used in the study are as follows:



The reaction constants for these equations are expressed in the modified Arrhenius form, where the forward rate is given as

$$k_{f,r} = T^{C2_r} \exp \left[\ln CO_r - C1_r \times 10^3/T \right] \quad (4.20a)$$

and the backward rate is given as

$$k_{b,r} = T^{D2_r} \exp \left[\ln DO_r - D1_r \times 10^3/T \right] \quad (4.20b)$$

The experimentally determined coefficients for these equations are those given in reference 29 and are tabulated in table IV. Therefore, for a specified temperature, density, and species composition, equation (4.19) along with equations (4.18), (4.19), and (4.20) are used to determine the rates of production for a multicomponent gas. The manner in which the production terms are written for numerical solution was discussed in Chapter II. (See equations (2.34) and (2.36)).

V. METHOD OF SOLUTION

In this chapter the procedure for solving the viscous shock-layer equations is presented. Development of the stagnation streamline equations is presented first where the nonlinear set of partial differential equations is reduced to ordinary differential equations by using a truncated series method. Then the finite-difference expressions used to transform the differential expressions to algebraic expressions are presented. The solution procedure is then discussed. This procedure is essentially that developed by Blottner and Flugge-Lotz (ref. 30) for compressible boundary layer solutions and applied by Davis (refs. 7 and 8) to the viscous shock-layer problem.

Basically, the solution procedure is to assume an initial stagnation profile for all dependent variables, do iterative calculations locally until the solution converges, advance to the next body station using the previous station profiles as an initial guess, and repeat the procedure until around the body solution is obtained. Once this is accomplished, the solution may be iterated in ξ to remove the assumptions (thin shock-layer form of the n-momentum equation and assumptions regarding the shock geometry) that were used in the first approximation.

Stagnation Streamline Equations

When downstream numerical solutions are required, it is necessary to have an accurate solution for the flow along the stagnation

streamline. A truncated series, which has the same form as that used by Kao in reference 31, is used to develop the stagnation streamline equations. The flow variables are expanded about the axis of symmetry with respect to the nondimensional distance ξ along the body as follows:

$$P(\xi, \eta) = P_1(\eta) + P_2(\eta)\xi^2 + \dots, \quad (5.1a)$$

$$u(\xi, \eta) = u_1(\eta)\xi + \dots, \quad (5.1b)$$

$$v(\xi, \eta) = v_1(\eta) + \dots, \quad (5.1c)$$

$$\rho(\xi, \eta) = \rho_1(\eta) + \dots, \quad (5.1d)$$

$$T(\xi, \eta) = T_1(\eta) + \dots, \quad (5.1e)$$

$$h(\xi, \eta) = h_1(\eta) + \dots, \quad (5.1f)$$

$$\mu(\xi, \eta) = \mu_1(\eta) + \dots, \quad (5.1g)$$

$$K(\xi, \eta) = K_1(\eta) + \dots, \quad (5.1h)$$

$$C_p(\xi, \eta) = C_{p1}(\eta) + \dots, \quad (5.1i)$$

$$\tilde{C}_\ell(\xi, \eta) = \tilde{C}_{\ell j}(\eta) + \dots, \quad (5.1j)$$

and

$$C_i(\xi, \eta) = C_{i_1}(\eta) + \dots \quad (5.1k)$$

The shock stand-off distance is written as

$$n_s = n_{1s} + n_{2s} \xi^2 + \dots \quad (5.2)$$

Furthermore, ξ is small and the curvature, κ , is approximately one in the stagnation region. Consequently, the geometric relations (see figure 1) including terms of order ξ can be written as

$$\beta \approx \xi \quad (5.3)$$

and

$$\alpha \approx \frac{\pi}{2} + \xi \left[\frac{2n_{2s}}{1+n_{1s}} - 1 \right] \quad (5.4)$$

Therefore,

$$\sin(\alpha + \beta) \approx 1 \quad (5.5)$$

and

$$\cos(\alpha + \beta) \approx \frac{2n_{2s} \xi}{1+n_{1s}} \quad (5.6)$$

The shock relations (equations (2.49) in terms of expanded variables) become

$$v_s = v_{1s} + \dots \sim -\frac{1}{\rho_{1s}}, \quad (5.7a)$$

$$u_s = u_{1s} \xi + \dots \sim \xi \left[1 - \frac{2n_{2s}}{1+n_{1s}} \left(1 - \frac{1}{\rho_{1s}} \right) \right], \quad (5.7b)$$

$$P_s = P_{1s} + P_{2s} \xi^2 + \dots \sim \frac{1}{\gamma M_\infty^2} + \left(1 - \frac{1}{\rho_{1s}} \right) - \xi^2 \left[\left(1 - \frac{1}{\rho_{1s}} \right) \left(1 - \frac{2n_{2s}}{1+n_{1s}} \right) \right], \quad (5.7c)$$

and

$$h_s = h_{1s} + \dots \sim \frac{1}{M_\infty^2 (\gamma_\infty - 1)} + \frac{1}{2} \left(1 - \frac{1}{\rho_{1s}} \right) \quad (5.7d)$$

along with equations (2.49f) through (2.49h).

By examining the above equations it is seen that the equations for u_s and P_s contains n_{2s} . This term cannot be determined from the stagnation solutions since it is a function of the downstream flow. Consequently, a value must be assumed for n_{2s} . In this study, it was assumed to be zero to start the solution but this assumption is then removed by iterating on the solution by using the previous shock stand-off distances to define n_{2s} . The effect of the downstream shock shape on the stagnation point solution is elliptic rather than parabolic.

By substituting the above relations into the governing viscous shock-layer equations, the following relations are obtained:

$$\frac{d^2 w}{d\eta^2} + \alpha_1 \frac{dw}{d\eta} + \alpha_2 w + \alpha_3 = 0 \quad (5.8)$$

where w assumes the values of \bar{u}_1 , \bar{H}_1 , \bar{T}_1 , C_{i1} , and $\bar{C}_{\lambda 1}$ for the s-momentum, energy (enthalpy and temperature), species continuity, and elemental continuity equations, respectively. The coefficients are defined as

s-momentum

$$\alpha_1 = \frac{1}{\bar{\mu}_1} \frac{d\bar{\mu}_1}{d\eta} + [j + 1] \frac{n_{1s}}{1+n_{1s}\eta} - \frac{n_{1s}\rho_{1s}v_{1s}}{\epsilon^2\mu_{1s}} \frac{\bar{\rho}_1\bar{v}_1}{\bar{\mu}_1} \quad (5.9a)$$

$$\alpha_2 = -\frac{n_{1s}}{1+n_{1s}\eta} \left[\frac{1}{\bar{\mu}_1} \frac{d\bar{\mu}_1}{d\eta} + \frac{n_{1s}}{1+n_{1s}\eta} (j + 1) + \frac{\rho_{1s}n_{1s}u_{1s}}{\epsilon^2\mu_{1s}} \frac{\bar{u}_1\bar{\rho}_1}{\bar{\mu}_1} - \frac{n_{1s}\rho_{1s}v_{1s}}{\epsilon^2\mu_{1s}} \frac{\bar{\rho}_1\bar{v}_1}{(1+n_{1s}\eta)\bar{\mu}_1} \right] \quad (5.9b)$$

$$\alpha_3 = \frac{-2P_{1s}n_{1s}^2}{\epsilon^2\mu_{1s}(1+n_{1s}\eta)u_{1s}\bar{\mu}_1} \left[\bar{P}_2 + \frac{P_{2s}\bar{P}_1}{P_{1s}} - \frac{n_{1s}\eta}{n_{1s}} \frac{d\bar{P}_1}{d\eta} \right] \quad (5.9c)$$

Energy (temperature)

$$\alpha_1 = \frac{1}{K_1} \frac{d\bar{K}_1}{d\eta} + (j + 1) \frac{n_{1s}}{1+n_{1s}\eta} - \frac{n_{1s}}{K_{1s}\bar{K}_1} \sum_{i=1}^{NS} J_{i1} C_{p_{i1}} - \frac{n_{1s}\rho_{1s}C_{p_{1s}}v_s}{\epsilon^2K_{1s}} \frac{\bar{\rho}_1\bar{C}_{p_1}\bar{v}_1}{\bar{K}_1} \quad (5.10a)$$

$$\alpha_2 = - \frac{n_{1s}^2 \dot{w}_{s2} \bar{w}_2}{\epsilon^2 K_{1s} \bar{K}_1} \quad (5.10b)$$

$$\alpha_3 = \frac{n_{1s} v_{1s} p_{1s} \bar{v}_1}{\epsilon^2 T_{1s} K_{1s} \bar{K}_1} \frac{d\bar{p}_1}{d\eta} - \frac{n_{1s}^2 \dot{w}_{s1}}{\epsilon^2 T_{1s} K_{1s} \bar{K}_1} \bar{w}_1 \quad (5.10c)$$

Energy (enthalpy)

$$\alpha_1 = \frac{1}{\bar{\mu}_1} \frac{d\bar{\mu}_1}{d\eta} - \frac{1}{\bar{p}_{r1}} \frac{d\bar{p}_{r1}}{d\eta} + \frac{(j+1)n_{1s}}{1+\eta n_{1s}} - \frac{n_{1s} \rho_{1s} p_{r1s} v_{1s}}{\epsilon^2 \mu_{1s}} \frac{\bar{\rho}_1 \bar{p}_{r1} \bar{v}_1}{\bar{\mu}_1} \quad (5.11a)$$

$$\alpha_2 = 0 \quad (5.11b)$$

$$\alpha_3 = \frac{p_{r1s} n_{1s}^2}{\mu_{1s} H_{1s}} \frac{\bar{p}_{r1}}{\bar{\mu}_1} \left[\frac{1}{n_{1s}} \frac{d\psi}{d\eta} + \frac{(j+1)\psi}{1+\eta n_{1s}} \right] \quad (5.11c)$$

Species Continuity

$$\alpha_1 = \frac{1}{PL} \frac{dPL}{d\eta} + (j+1) \frac{n_{1s}}{1+\eta n_{1s}} - \frac{\rho_{1s} v_{1s} n_{1s} \bar{\rho}_1 \bar{v}_1}{\epsilon^2 PL} \quad (5.12a)$$

$$\alpha_2 = - \frac{n_{1s}^2 \dot{w}_i^1}{\epsilon^2 PL} \quad (5.12b)$$

$$\alpha_3 = \frac{1}{PL} \left[\frac{dPM}{d\eta} + (j+1) \frac{PM n_{1s}}{(1+\eta n_{1s})} + \frac{\dot{w}_i^0 n_{1s}^2}{\epsilon^2} \right] \quad (5.12c)$$

and

Elemental Continuity

$$\alpha_1 = \frac{1}{\widetilde{PL}} \frac{d\widetilde{PL}}{d\eta} + (j+1) \frac{n_{1s}}{1+\eta n_{1s}} - \frac{n_{1s} c_{1s} v_{1s} \bar{\rho}_1 \bar{v}_1}{\epsilon^2 \widetilde{PL}} \quad (5.13a)$$

$$\alpha_2 = 0 \quad (5.13b)$$

$$\alpha_3 = \frac{1}{\widetilde{PL}} \left[\frac{d\widetilde{PM}}{d\eta} + (j+1) \frac{n_{1s} \widetilde{PM}}{1+\eta n_{1s}} \right] \quad (5.13c)$$

The remaining equations may be written as follows:

Global Continuity

$$\begin{aligned} \frac{d}{d\eta} \left[\left(1 + n_{1s} \eta \right)^{j+1} \rho_{1s} v_{1s} \bar{\rho}_1 \bar{v}_1 \right] = \\ - (j+1) n_{1s} \left(1 + n_{1s} \eta \right)^j \rho_{1s} u_{1s} \bar{\rho}_1 \bar{u}_1 \end{aligned} \quad (5.14a)$$

n-momentum

$$\frac{d\bar{P}_1}{d\eta} = - \frac{v_{1s}^2 \rho_{1s}}{P_{1s}} \bar{\rho}_1 \bar{v}_1 \frac{d\bar{v}_1}{d\eta} \quad (5.15a)$$

When the thin shock-layer approximation is made, the n-momentum equation becomes

$$\frac{d\bar{P}_1}{d\eta} = 0 \quad (5.15b)$$

Also, the \bar{P}_2 term that appears in equation (5.9c) can be expressed in terms of "one" quantities by using the following equation:

$$\frac{d\bar{P}_2}{d\eta} = \frac{\rho_{1s} u_{1s}^2}{P_{1s}} \frac{\bar{\rho}_1 \bar{u}_1^2}{1 + \eta n_{1s}} \quad (5.15c)$$

The above equations along with the equation of state constitute the nonlinear ordinary differential equations that are solved along the stagnation streamline.

Finite-Difference Expressions

The ordinary and partial differential equations were solved by using the same techniques. The derivatives in equations (2.25) and (5.8) are expressed as difference quotients using Taylor series expansions. A variable grid spacing is used in the direction, η , normal to the surface so that the grid spacing can be made small in the region of large gradients. The implicit representation of the derivatives is given in reference 7. When the difference quotients are substituted in equation (2.25), the following difference equation results:

$$A W_{n,m,n-1} + B W_{n,m,n} + C W_{n,m,n+1} = D_n \quad (5.16)$$

The subscript n denotes the grid points along a line normal to the body surface, whereas the subscript m denotes the grid stations along the body surface. Equations (5.16) along with the boundary conditions constitute a system of the tridiagonal form, for which efficient computational procedures are available (ref. 32).

Solution Procedure

Once the free stream conditions and body geometry are specified, initial profile values for the dependent variables are assumed along with a guess value for the stagnation shock stand-off distance. Then the shock quantities are calculated by using the shock equations previously described. For the equilibrium shock calculations, initial guess values for the density and mixture molecular weight are made. Then a double iteration scheme is used (see figure 3(a)) to obtain a converged solution. For the shock calculations where the chemical composition is frozen at the free stream value, only a guess value for the nondimensional shock density is made (see figure 3(b)). Then iterative calculations are made until convergence is achieved.

With the shock conditions established, the viscous shock-layer equations are solved in the sequence shown in figure 4(a) for the equilibrium calculations and the sequence shown in figure 4(b) for the frozen and nonequilibrium calculations. Finite difference methods are used to integrate the equations. Along the stagnation streamline, equations (5.8) through (5.15) are used, whereas for the downstream equations (2.25) through (2.33) are used.

First consider the equilibrium calculations. As shown in figure 4(a), the elemental continuity equations are integrated to determine elemental profiles. Next, the energy equation in terms of total enthalpy is integrated to determine a total enthalpy profile. Then a temperature profile is calculated iteratively such that is consistent

with the enthalpy values resulting from the energy equation. This is accomplished by converting the total enthalpy to static enthalpy values, then performing the following procedure at each grid point across the flow field: With local values of pressure, elemental composition, and an assumed value of temperature, an equilibrium calculation is made, whereby new values for species composition and static enthalpy are obtained for the assumed temperature value. Additional iterations are made until the temperature corresponding to the local enthalpy is determined. Once the temperature profile is calculated, the species profiles are also known.

For the frozen and chemical nonequilibrium calculations, the above procedure is somewhat simpler (see figure 4(b)). That is, the species continuity equations are integrated to determine species profiles for nonequilibrium flow. For frozen flow, the species continuity equations are not required. For both nonequilibrium and frozen flow, a temperature profile is determined directly by integrating the energy equation that is written in terms of temperature.

The procedure for solving the remaining equations is identical for all three chemistry models. With new values for species and temperature profiles, a density profile is calculated by using the equation of state. Next, thermodynamic and transport properties are calculated. Then the s-momentum equation is integrated to determine the tangential velocity profile. Thereafter, the continuity equation is integrated to determine first the shock stand-off distance and second the v

component of velocity. Next, the n-momentum equation is integrated to determine the pressure profile, and the equation of state is used once again to update the density profile. This procedure is repeated until the differences between values of quantities for the current iteration and the previous iteration satisfy the convergence criteria. Once the solution has converged, the computation advances to the next body station using as initial profiles those computed for the previous station. Again, iterative computations are made until convergence is achieved. Hence, the computation advances in ξ until the desired body station is reached.

The foregoing procedure provides a first approximation to the flow field solution since the following assumptions are used:

- a. The thin shock-layer form of the n-momentum equation (2.32b) was used.
- b. The stagnation streamline solution was independent of downstream influence (approximation of local similarity where $n_{2s} = 0$).
- c. The term $\frac{dn_s}{d\xi}$ was equated to zero at each body station.
- d. The shock angle α was assumed to be the same as the body angle θ .

These assumptions are then removed by making a second approximation to the flow field solution whereby the v components of velocity from the first approximation are retained and averaged with the local and current v velocities and then used in the n-momentum equation (eq. 2.32a) for determining the pressure profile. Furthermore, the shock stand-off values from the first approximation are used to evaluate $dn_s/d\xi$

which is then used in the subsequent approximation. If necessary, additional iterations are performed until the total solution converges. Hence, the viscous shock-layer equations are solved as parabolic equations, yet retaining effects, the nature of which are elliptic and hyperbolic.

V. RESULTS AND DISCUSSION

Introduction

In this chapter numerical solutions to the previously discussed viscous shock-layer equations are presented and discussed. The solutions are those for flow about a 45° hyperboloid at zero-degree angle of attack. First, comparisons of present results are made with data in the literature. Second, results are presented which demonstrate the effects of chemistry model, diffusion model, surface catalyticity, and mass injection on flow parameters and surface transport.

All computations, unless otherwise indicated, were made by using a constant step size of 0.2 in the ξ -direction and a variable step size in the η -direction where a total of fifty grid points were used. Also, two iterations were made in the ξ -direction. Table V summarizes the altitude, velocity, and free stream properties used. The free stream properties are those given by the U. S. Standard Atmosphere (ref. 33).

All computations were made by using a Control Data Corporation (CDC) 6600 computer. The program language was FORTRAN IV. The maximum storage requirement of the different programs was 147000 core locations, and the program was dimensioned to accommodate fifty grid points along the normal to the body, fifty grid points along the body surface, four chemical elements, and twenty chemical species. A plotting routine was also included in the program. Table VI summarizes the total time required to calculate various cases and the number of iterations

required at the stagnation station and a representative downstream station. For purposes of comparison, time and iterations required for an ideal gas calculation are also included.

For each body station, the convergence criteria was that the relative difference be less than 0.001 for both the temperature and tangential velocity derivatives at the wall. This criteria was used for all calculations except for those where the temperature gradient was approaching zero due to mass injection. In addition, a minimum of four iterations was required at each body station.

The equilibrium flow solutions require large computing times because of the time required to make a chemical equilibrium calculation. For equilibrium flow calculations where the diffusion is binary, a major reduction in computing time can be realized by using tabulated or curve fitted data for the chemical composition. This is also applicable for mass injection provided the injectant has the same elemental composition as the free stream. However, this approach was not used in the present study since most of the equilibrium calculations were for multicomponent diffusion or binary diffusion with an injectant whose elemental composition was not the same as the free stream composition.

Comparison With Previous Analyses

In order to assess the results obtained for the present analyses, comparisons were made of the results for each of the three chemistry models with data reported in the literature. No attempt was made to

obtain exact comparisons since the solution is dependent upon step size, values of transport and thermodynamic quantities, details of the given chemistry model, etc.

Frozen and equilibrium calculations were compared with the data of Whitehead as reported in ref. 9. The comparisons were for the following conditions: a free stream velocity of 20,000 ft/sec, an altitude of 200,000 ft in the earth's atmosphere, a 45° hyperboloid with a one-inch nose radius, and a surface temperature of 1800°R. Even though the solution procedure used herein is essentially the same as used by Whitehead, several differences exist. Whitehead results accounted for shock slip at the outer boundary condition and slip and temperature jump at the surface, whereas the present analyses use the Rankine-Hugoniot relations to describe the shock conditions and assumes no slip or temperature jump at the wall. Furthermore, the expressions used to calculate the thermodynamic and transport properties are not the same as used by Whitehead.

Figure 5(a) through (c) show comparisons of the present analysis with that of Whitehead's for shock stand-off, skin friction coefficient, and nondimensional heat transfer rate where the chemistry is frozen at the free stream composition. Table VII presents a detailed listing of the shock and wall values that result from the present calculation. The heat transfer results are in excellent agreement; however, the agreement is not as good for shock stand-off distances or skin friction coefficients.

Figures 6(a) through (c) show the same comparisons for equilibrium air where the Lewis number is assumed to be one. Table VIII presents a detailed listing of the stagnation shock and wall values for the present calculation. Whitehead's equilibrium results were obtained assuming air to be represented as one "effective" species with a constant molecular weight equal to the free stream value whereas the present analysis treated air as a multicomponent mixture of five species. The present calculation predicts greater values for shock stand-off distance (as would be expected due to Whitehead's assumption concerning the molecular weight), skin friction coefficient, and heat transfer.

Results of the equilibrium air calculations were also compared with the data of Edelman and Hoffman (ref. 14) which was for the stagnation station only. Comparisons of stagnation temperature and species concentration profiles are presented in figures 7(a) through (d). Figures 7(a) and (b) show a comparison of the temperature and species profiles, respectively, for a 280,000-ft altitude, a 26,000-ft/sec free stream velocity, a 12-inch nose radius, a 2430°R wall temperature, and a Lewis number of 1.4. Table IX presents a detailed listing of the stagnation shock and wall values for the present calculation. Figure 7(c) and (d) show the same comparisons for a 150,000-ft altitude, a 22,520-ft/sec free stream velocity, a 2657°R wall temperature, a 0.5-inch nose radius, and a Lewis number of 1.4. Table X presents the stagnation shock and wall values corresponding to the above conditions for the present calculation.

When the results of the two calculations for both sets of conditions are compared, two differences are apparent: first, the shape of the temperature profiles, and second, the shock-layer thickness. The curvature of the temperature profiles as calculated by reference 14 decreases monotonically with increasing distance from the surface. Temperature profiles resulting from the present equilibrium calculations are not smooth, especially at the higher altitude (lower pressure) conditions. However, it is believed that the temperature profiles resulting from the present calculations can be substantiated by considering the chemical reactions that occur within the shock layer. A more detailed discussion of this assessment is given in the next section of this chapter.

The differences in shock layer thickness are expected since the results presented in reference 14 were for the stagnation streamline only and, therefore, did not account for the downstream influence on shock stand-off distance. However, when the downstream influence on shock shape is accounted for as in the present analysis, a larger shock layer thickness results. This effect was shown in reference 7 for an ideal gas.

Results of the nonequilibrium calculation were compared with the stagnation viscous shock-layer results of Blottner (ref. 11). Comparisons were made of temperature, tangential velocity, and species concentration profiles.

For the chemical kinetics model, Blottner considered two additional species (NO^+ and e^-) and one additional reaction equation ($\text{N} + \text{O} \rightleftharpoons \text{NO}^+ + e^-$);

however, for the remaining reactions, identical rate expressions were used. The calculations are for a 200,000 ft altitude, a 20,000 ft/sec free stream velocity, a 1800°R wall temperature, and a catalytic wall. Both analyses use the Rankine-Hugoniot relations to describe the shock conditions and use the no-slip or temperature jump conditions at the wall. Also, for purposes of comparison, the present calculation was made with a constant Lewis number of 1.4.

For two reasons, differences in shock-layer thickness are expected. First, the results of reference 11 do not account for the downstream influence on the stagnation shock stand-off distance as does the present analysis. When the downstream effect is neglected, a significant underprediction of stagnation shock stand-off distance can occur (refs. 7 and 34). Second, the analysis of reference 11 did not include the effect of the shock-layer thickness on the shock radius of curvature as did the present analysis. Reference 34 (p. 91) found that when the shock-layer thickness contribution to the radius of curvature is neglected, an underprediction of the stagnation shock stand-off distance occurs.

Table XI presents a detailed listing of stagnation shock and wall conditions for the present calculation (a constant Lewis number of 1.4). Figure 8(a) shows a comparison of temperature profiles. The most apparent difference is in the shock stand-off distance. Nevertheless, near the wall the temperature profiles are in good agreement. The same can also be said for the tangential velocity profiles as evidenced

by figure 8(b) where the agreement is good near the wall.

Figure 8(c) shows a comparison of the species concentration profiles for the two analyses. Appreciable differences exist. However, it is believed that these differences are due primarily to differences in shock stand-off distance. The shock stand-off distance for the present analysis is approximately 22 percent greater than that of reference 11. Consequently a larger distance is available for reactions to occur - in particular the dissociation reactions. This is evident in figure 8(c) which shows that, for a given value of n , the amount of dissociated flow predicted by the present calculation is greater than that predicted by reference 11.

Chemistry Models

In this section results of calculations for a free-stream velocity of 20,000 ft/sec, an altitude of 200,000 ft in the earth's atmosphere, a one-inch nose radius, and a surface temperature of 2700°R using frozen, equilibrium, and nonequilibrium chemistry are presented. Multi-component diffusion, no mass injection, and a noncatalytic wall are assumed. Surface catalyticity effects are discussed in the next section. First, velocity, temperature, and species concentration profiles are presented for each chemistry model. Next, the equilibrium temperature profiles are shown and their dependence on chemical reactions and pressure variations are discussed. Then the effect of each chemistry model on tangential velocity, temperature, and chemical species profiles, heat transfer, Stanton number, skin friction, shock stand-off distance, and wall pressure is shown.

Figures 9 through 12 show the velocity, temperature, and species profiles at various body stations for each chemistry model. There are several features of these profiles that are of interest. The tangential velocity profiles are practically linear in the outer region of the shock layer, that is, the flow has an outer region of essentially uniform vorticity. This is in marked contrast to the classical velocity boundary-layer profile that is derived with a zero velocity gradient imposed at the outer boundary. However, the flow considered here is in the viscous-layer regime (ref. 35) where the viscous effects extend over an appreciable fraction of the shock layer, thereby invalidating the boundary-layer concept.

The equilibrium temperature profiles are shown in figure 10(b). Near the wall, the equilibrium temperature profiles do not show the monotonically decreasing curvature associated with frozen and non-equilibrium profiles. The equilibrium temperature profiles have two distinct inflection points. From the body to the shock, the profiles are characterized by concave, convex, and concave segments. The curvature of the convex segment diminishes as the flow moves downstream. To the author's knowledge, this complex shape of the equilibrium air temperature profiles has not been observed previously.

The bulges appearing in the temperature profiles can be explained in terms of chemical reactions. This is demonstrated in figure 13, where stagnation temperature profiles and species concentration profiles are shown. Temperature profiles for an equilibrium chemistry solution

and a frozen chemistry solution (where the chemistry is frozen at the equilibrium shock composition) are shown. The temperature profile for the equilibrium calculation is much fuller than the profile for the frozen calculation. This should be, of course, because exothermic reactions occur near the wall. Essentially all chemical reactions occur within that half of the shock layer which is adjacent to the wall; that is, essentially all the atom recombinations occur near the wall. The recombinations also occur over two distinct and separate regions. The oxygen recombines between the wall and $\eta = 0.11$. This causes the inner bulge in the temperature profile. Then there is a small region (η of 0.11 to 0.16) where the recombination process is negligible. Finally, practically all the atomic nitrogen recombines between η values of 0.16 and 0.5. This causes the outer bulge in the temperature profile.

The extent to which the equilibrium temperature profiles differ from smooth profiles will depend upon the pressure, hence the altitude for a given free stream velocity. This is demonstrated by Hansen in figure 1 of reference 36. The data of Hansen show that the recombination reactions occur over narrow temperature intervals at low pressures (0.0001 to 0.1 atm); however, the temperature intervals required for nitrogen and oxygen recombination increase significantly with increasing pressure. Furthermore, the temperature interval between the completion of nitrogen recombination and the onset of oxygen recombination decreases with increasing pressure. Consequently, as the

pressure increases, the chemical composition experiences a more gradual change with temperature. The pressures were 0.1 atmosphere or less for the temperature profiles shown in figure 10(b), therefore, recombinations over narrow temperature intervals would be expected.

To demonstrate the effect of the recombination reactions on the equilibrium temperature profiles at higher pressures, an equilibrium calculation was made for an altitude of 100,000 ft and a velocity of 20,000 ft/sec (a detailed listing of the shock and wall values resulting from this calculation are presented in table XII.) The stagnation pressure was approximately 5.2 atmospheres. Figure 14(a) shows the stagnation temperature profile, while figure 14(b) shows the stagnation species profiles. From figure 14(a), it is seen that the curvature of the equilibrium temperature profile is essentially monotonic, decreasing with increasing η . Hence, the results of the higher pressure calculation agree qualitatively with the aforementioned effect of pressure on equilibrium temperature.

Figures 11(a) through 11(d) show the nonequilibrium species profiles at different body stations for a noncatalytic wall. The chemistry across the shock is frozen at the free stream composition ($C_0 = 0.24$; $C_{N_2} = 0.76$). The figures show that most of the dissociation occurs in the outermost portion of the shock layer. Furthermore, only a small amount of recombination occurs near the wall. This is due to the low density flow conditions which reduce the effectiveness of recombination reactions; consequently, the amount of dissociated flow

at the wall is significant (approximately one-fifth of the total mass). This is important because the energy invested in dissociation is not recovered at the wall in nonequilibrium flow.

Figures 12(a) through (c) show the equilibrium concentration profiles at different body stations. It is seen that a large percentage of flow is dissociated in the outer portion of the shock layer. The amount of dissociation decreases rapidly downstream. Also, essentially all the dissociated species recombine in a relatively small region near the wall with the wall composition being approximately that of the free stream composition. This, of course, means that the energy of dissociation is recovered. The significance of this in terms of heat transfer rate will be discussed later.

Comparisons of results using the three chemistry models are shown in figures 15 through 21. The effect on tangential velocity and temperature profiles, shock stand-off distance, heat transfer rate, Stanton number, skin friction and wall pressure are shown. Note that all the aforementioned quantities are significantly influenced by the chemistry model with the exception of the tangential velocity profiles (fig. 15) and the wall pressure distribution (fig. 21). Of particular significance are the large differences in shock-layer temperatures for the different chemistry models. Figures 16(a) and (b) show the temperature profiles at an ξ of 0.0 and 2.0, respectively, for each chemistry model. The conditions at the shock were identical for the frozen and nonequilibrium calculation since the chemical composition

was assumed to be frozen across the shock at the free stream composition. For the stagnation streamline (fig. 16(a)), the frozen shock temperature is more than twice that of the equilibrium shock temperature. Moreover, the equilibrium temperatures across the shock layer are much less than those of the frozen or nonequilibrium values except in the region near the wall. This is due to the large amount of energy invested in dissociation rather than static temperature. Also, the nonequilibrium temperatures are less than the frozen values because some dissociation occurs within the nonequilibrium shock layer. Also at the downstream (fig. 16(b)) station, $\xi = 2.0$, the temperature differences are noticeably less than those at the stagnation station because the equilibrium and nonequilibrium compositions are more nearly like the frozen composition at the lower temperatures.

Figure 17 shows how the chemistry model influences shock stand-off distance. The shock stand-off distances corresponding to the equilibrium calculation are considerably less than those for frozen and nonequilibrium calculations. Also, the shock stand-off distances for the nonequilibrium calculations are somewhat less than those for the frozen calculations. These results are expected since the shock-layer densities for the nonequilibrium and especially the equilibrium calculations are greater than the frozen flow densities.

Consider next the effect that the chemistry model has on heat transfer rate distribution. As is shown in figure 18, the chemistry model has a very pronounced effect on nondimensional heat transfer. Both the frozen and equilibrium chemistry models significantly

over-predict the heat transfer for a noncatalytic wall. This is especially so in the stagnation region where the frozen and equilibrium values are approximately 50 percent greater than the nonequilibrium values. This is particularly significant because the entry corridor for manned entry vehicles includes the altitude-velocity conditions used in the present calculations. Furthermore, the heating rates are significant at these conditions, and therefore, the need for nonequilibrium analyses is clearly evident from these results.

When the heat transfer rate is expressed in terms of Stanton number (fig. 19), the results for the three chemistry models are in closer agreement than were the nondimensional heat transfer rates (fig. 18). As was pointed out previously (fig. 11), a significant amount of energy is invested in dissociation at the wall in nonequilibrium flow. Consequently, the enthalpy at the wall is larger for the nonequilibrium and noncatalytic wall calculation and necessarily the enthalpy potential is smaller. The maximum difference between the equilibrium and nonequilibrium Stanton numbers is about 13 percent and occurs at the stagnation point.

The effect of the chemistry model on skin friction distribution is shown in figure 20. This figure shows that the skin friction distributions for the equilibrium and nonequilibrium calculations are about the same. The values for the frozen calculation are greater than the nonequilibrium values, but the differences never exceed 9 percent.

The effect of chemistry model on wall pressure distribution is shown in figure 21. Also shown is the Newtonian pressure distribution.

The nonequilibrium and frozen pressure distributions are identical. Also, the equilibrium and Newtonian pressure values are in close agreement, yet less than the nonequilibrium pressure. At $\xi = 3.0$, the nonequilibrium pressure is 10.8 percent greater than the equilibrium and the Newtonian pressures.

Catalytic Wall Effects

Results presented in the previous section demonstrated how the flow field chemistry can influence flow parameters and surface transport. This section demonstrates how surface catalyticity influences the same flow parameters and surface transport. Either noncatalytic or equilibrium catalytic walls are assumed. For the equilibrium catalytic wall, the gas composition at the wall is the equilibrium composition for the wall temperature and pressure. The elemental composition at the wall is governed by multicomponent diffusion and is, therefore, not necessarily equal to the free stream elemental composition.

Comparison of the noncatalytic and equilibrium catalytic wall calculations is made for a 2700°R wall temperature, a 20,000 ft/sec free stream velocity, and a 200,000 ft altitude. The diffusion for both calculations is multicomponent. Table XI provides a detailed listing of the stagnation shock and wall values for the noncatalytic and equilibrium catalytic calculations.

The wall catalyticity has negligible effect on temperature and velocity profiles, and therefore, comparisons are not presented. However, the species profiles for the flow configuration examined were

necessarily influenced by the wall catalyticity. This is shown in figures 22(a) through (c) where comparisons are made at an ξ of 0, 1.0, and 3.0, respectively, of nonequilibrium species profiles with noncatalytic and equilibrium catalytic wall conditions. It is seen that the species profiles for the innermost 70 percent of the shock layer is influenced by the wall catalyticity.

Figures 23 through 26 show how wall catalyticity influences shock stand-off distance, heat transfer, Stanton number, and skin friction. With the exception of heat transfer, the wall catalyticity has little effect. The maximum relative difference between the catalytic and non-catalytic calculations were: 3.5 percent for shock stand-off, 4.9 percent for skin friction, and 9.2 percent for Stanton number. The maximum relative difference in heat transfer was 48 percent.

For purposes of comparison, figure 24 also includes the heat transfer distribution where equilibrium flow field chemistry was used. It is seen that the nonequilibrium equilibrium catalytic wall results and the equilibrium noncatalytic wall results are in close agreement. For both of these calculations, the energy invested in dissociation is recovered. However, in the nonequilibrium noncatalytic wall calculation, an appreciable amount of dissociation is present at the wall (see fig. 11), and, hence, the wall heat transfer is substantially reduced.

Diffusion Models

Prior to this study, stagnation and downstream viscous shock-layer results that treated the diffusion as multicomponent were not available.

In this section, comparisons are shown between multicomponent and binary diffusion models. The effects on flow parameters and surface transport are presented for both equilibrium and nonequilibrium air.

The binary approximation, as indicated previously, is that all species have the same diffusion coefficient, which is assumed to be the coefficient for molecular nitrogen diffusing into atomic oxygen. This approach is used to evaluate the binary diffusion coefficient because atomic oxygen and molecular nitrogen are the dominant species in the shock layer. (See figures 11 and 12.) The multicomponent diffusion coefficients are determined according to equation (3.11).

The flow conditions were as indicated previously that is, a 200,000-ft altitude, a 20,000-ft/sec velocity, a one-inch nose radius, and a surface temperature of 2700°R. No mass injection and a noncatalytic wall are assumed. With the exception of the species profile, essentially no effect of diffusion model was observed. Even the effect on species profiles was small as shown in figures 27 and 28.

Figure 27(a) and (b) show comparisons of binary and multicomponent species profiles for equilibrium air at an ξ of 0.0 and 1.0 respectively. More molecular nitrogen and less molecular oxygen are present at the wall for multicomponent diffusion.

The elemental composition is not a constant for multicomponent diffusion as is the case for binary diffusion. However, the departure from elemental invariance is small for the equilibrium air calculation. The elemental composition at the wall was $\tilde{C}_O = 0.278$ and $\tilde{C}_N = 0.722$

at $\xi = 0.0$, and $\tilde{C}_O = 0.279$ and $\tilde{C}_N = 0.721$ at $\xi = 1.0$, as opposed to the free stream values of $\tilde{C}_O = 0.24$ and $\tilde{C}_N = 0.76$.

Figures 28(a) and (b) show comparisons of species profiles for multicomponent and binary diffusion models at ξ values of 0 and 1.0 respectively. The flow chemistry is nonequilibrium. Once again the diffusion model has a small effect on species profiles. The elemental wall concentrations were $\tilde{C}_O = 0.221$ and $\tilde{C}_N = 0.778$ at $\xi = 0$, and $\tilde{C}_O = 0.222$ and $\tilde{C}_N = 0.779$ at $\xi = 1.0$.

The other flow parameters and surface transport values were essentially the same for both diffusion models, and therefore, comparisons of results are not presented. However, table XIII, which presents dimensional heating rates for various body stations, illustrates this point. It can be seen from the table that the heat transfer rates for the flow conditions considered were about the same for both diffusion models.

Mass Injection

In the following, the results of computations with mass injection are considered. In all cases the mass injection rate distribution is given by equation (2.39). Figure 29 shows the injection distribution for different values of the nondimensional stagnation injection parameter \dot{m}_0 . It is seen that the injection rate approaches zero at a ξ of about 1.5.

Injecting air into air.-Figures 30 through 37 and table XIV show how injecting equilibrium air into nonequilibrium air influences flow

parameters and surface transport. Multicomponent diffusion and a non-catalytic wall are assumed. Stagnation mass injection rates as large as 0.4 are considered.

Figures 30(a) through (c) show comparisons of species profiles for no injection and an injection rate of 0.2. These comparisons are made at a ξ of 0., 1.0, and 3.0. At the stagnation station, the shock-layer chemical composition is altered substantially due to mass injection (fig. 30(a)). At the wall, the mass of dissociated flow is 6 percent for a 0.2 injection rate and 24 percent for no injection. Downstream the effect of mass injection on chemical composition decreases (fig. 30(b)) because the injection rate is smaller (eq. (2.39)). At $\xi = 3.0$, which is beyond the body station where mass injection is zero, the chemical composition of the two shock layers (fig. 30(c)) is about the same.

Figures 31 and 32 show the stagnation tangential velocity and temperature profiles, respectively. These results qualitatively are as one would expect. That is, the shock-layer thickness increases and the tangential velocity and temperature gradients decrease with increasing mass injection rate.

Figure 33 shows the effect of mass injection on shock stand-off distance. For stagnation injection rates of 0.2 or greater, the injectant increases the shock stand-off distance as far downstream as the calculations are made ($\xi = 3.0$).

Figure 34 shows the effect of injecting equilibrium air into non-equilibrium air on nondimensional heat transfer distribution. As the

injection rate increases, the heat transfer rate near the stagnation point approaches zero for an \dot{m}_0 of 0.4. Downstream, however, the effect of injection rate on heat transfer rate decreases rapidly. These results also show that the smaller injection rates are more effective in reducing the surface heating. Figure 35 shows that the same conclusions apply to Stanton number distributions.

Figure 36 shows the effect of mass injection on skin friction coefficient distributions. In the mass injection region, large reductions in skin friction occur. Downstream, however, the skin friction values with injection are approaching the no injection values. For example, for a stagnation mass injection rate of 0.4, the skin friction at $\xi = 0.4$ is 90 percent less than the no injection value, but at $\xi = 3.0$ the reduction is only 9 percent.

The effect of mass injection on wall pressure distribution is shown in figure 37. An almost negligible effect was obtained. The wall pressure is less with mass injection but the pressure differences never exceed 4 percent for the mass injection rates considered. This result is due primarily to the way that the injected mass alters the shock shape and, consequently, the shock pressure. This is evident in figure 33, where the shock slope decreases with increasing injection rate. Hence, the local shock angle, α , (fig. 1) is less and so is the shock pressure. Obviously, the way mass injection alters the shock shape and shock pressure will depend on the mass injection distribution which is assumed.

For some hypersonic flow conditions, in particular hypervelocity planetary entries where radiant heating is very large, the mass injection rates can be large enough so that the convective heating is reduced to zero. Calculations were made to demonstrate the present capability to predict the effect of mass injection on stagnation heat transfer and shock shape at such injection rates. Figures 38 through 40 show such an effect for the injection of equilibrium air into reaching equilibrium air. Figure 38 shows how the stagnation wall heat transfer rate decreases with increasing mass injection - becoming zero at a mass injection rate of about 0.4. Figure 39 shows the influence of injection on stagnation shock stand-off distance. For the range of injection rates shown, the shock stand-off distance increases linearly with increasing injection rate. Figure 40 shows the effect of even larger injection rates on shock stand-off distance. (The results for injection rates greater than 0.4 did not consider the downstream influence on the stagnation solution.) For injection rates greater than 0.4, the shock stand-off distance continues to increase with increasing injection rate but the slope of the curve decreases with increasing injection rate.

Injecting water into air.-Injecting water either as a liquid or as a gas into a reacting flow is an example of transpiration cooling. A current study (ref. 37) shows water to be one of the most efficient transpiration system fluids for limiting surface temperatures. This result was contingent on the transpiration cooling design being such that the water vaporizes at the wall-flow field interface.

Since water is an effective transpiration coolant, calculations were made to determine the effect of injecting water into reacting equilibrium air. The calculations were made for a 200,000 ft altitude, a 20,000 ft/sec velocity, a 45° hyperboloid with a 12-inch nose radius, and a wall temperature of 2700°R. The large nose radius (12 inches vs 1 inch) was used so that the equilibrium flow approximation would be more realistic. That is, previous results have shown that the equilibrium flow approximation is not valid for the above free stream conditions and a one-inch nose radius calculation.

The injected water (gas phase) was in equilibrium with the wall temperature and pressure and consisted of a total of six possible chemical species. These species were H, O, H₂, O₂, OH, and H₂O. Figures 41 (a) through (c) show the equilibrium composition of water for the aforementioned six species over a temperature range of 1800° to 5400° R and for pressures of 0.1 and 0.01 atmosphere, respectively. Since the calculations were for a wall temperature of 2700°R and wall pressures of 0.1 atmosphere or less, the injectant was essentially all H₂O. (See figure 41(a)).

The equilibrium flow is assumed to consist of nine species, the six previously mentioned plus N, N₂, and NO. Since the larger number of chemical species increases the computational requirements, downstream solutions are presented only as far as $\xi = 1.6$, and the solutions are iterated in ξ only once. Also the diffusion is binary where the diffusion coefficient is taken as the coefficient for molecular nitrogen diffusing into atomic oxygen.

Figure 42 shows how the stagnation elemental profiles are influenced by H_2O (gas) injection rates. Note that for an injection rate of 0.1, the elemental hydrogen mass fraction at the wall is 0.11, the same as that for H_2O . For the 0.05 injection rate, the hydrogen elemental mass fraction at the wall is 0.095. Figure 42 also shows the distance that the elemental hydrogen is transported away from the wall. The elemental hydrogen mass fraction is 0.001 at $\eta = 0.24$ ($n = 0.014$) and at $\eta = 0.31$ ($n = 0.019$) for 0.05 and 0.1 injection rates, respectively.

Species profiles for H_2O injection rate of 0.1 are shown in figures 43(a) through (c) for ξ values of 0, 0.4, and 1.0. Figures 44(a) through (c) show the species profiles for a 0.05 injection rate at the same ξ values. For the range of ξ considered, the wall mass fraction of H_2O is approximately 1.0 for the 0.1 injection rate and approximately 0.85 for the 0.05 injection rate. (A detailed listing of the stagnation wall species mass fractions is included in table XV.) Dissociation occurs as the H_2O (gas) is transported into the higher temperature flow. The dissociation of H_2O is strongly endothermic and substantially reduces the flow field temperature.

Figure 45 shows the stagnation temperature profiles for H_2O injection rates of 0.0, 0.05, and 0.1. At the wall, the temperature gradients decrease with increasing injection rate. As a result of the H_2O injection, the temperature profiles experience a marked reduction in temperature for about one-third of the shock-layer thickness adjacent to the wall. This temperature reduction occurs because energy is

absorbed as the sensible enthalpy of the H_2O is increased and as the H_2O undergoes endothermal reactions.

Dissociation of H_2O is highly endothermic. For example, the dissociation of one gram of H_2O at $4500^\circ R$ ($2500^\circ K$), forming H and O, requires 12.7 kcal/gram. In contrast, the dissociation of one gram of O_2 at the same temperature requires only 3.8 kcal/gram.

Figure 46 shows the effect of H_2O injection on stagnation tangential velocity profiles. Note that the velocity profiles have a distinct boundary-layer region. The effects of H_2O injection on heat transfer, Stanton number and skin friction coefficient are compared with the results for air and ablation injection in a subsequent section.

Injecting ablation products into air.—When an ablator is used to protect the surface of a vehicle from a high-temperature environment, gaseous species are injected into the flow field as the ablator is thermally degraded. The ablative products injected into the flow field have the same qualitative effect as that obtained with transpiration cooling. For an ablating surface, however, the number of gaseous species injected into the flow field is generally much larger than that for a transpiration cooled surface. Consequently, analyses for reacting flows adjacent to ablating surfaces must account for a large number of reacting species.

To determine the effect of injecting ablation species on flow parameters and surface transport, calculations were made for a low-density phenolic-nylon ablator. Gaseous ablation products in chemical

equilibrium at the wall temperature and pressure were injected into equilibrium air. Results are presented for injection rates of 0.0, 0.05, and 0.1. The calculations were made for the same free stream and wall temperature conditions as that for the H₂O injection calculations.

The elemental composition used for the low-density phenolic nylon ablator is that given by reference 38 and is $\tilde{C}_C = 0.699$, $\tilde{C}_O = 0.163$, $\tilde{C}_H = 0.0812$ and $\tilde{C}_N = 0.0568$. For equilibrium calculations, the elemental composition completely specifies the material. A total of nineteen possible species are assumed to be injected into the equilibrium flow field. The species are those listed in table II with the exception of OH and H₂O. The equilibrium species mass fractions for the aforementioned elemental composition and assumed species are shown as a function of temperature in figures 47(a) and (b) for pressures of 0.1 and 0.01 atm, respectively.

The possible flow field species are assumed to be the same as those that are injected at the wall. For this system of species, the computational time required to obtain solutions become quite large as indicated in table VI. Consequently, downstream solutions are presented only as far as $\xi = 0.6$, and the solutions are iterated in ξ only once. The diffusion is binary where the diffusion coefficient is taken as the coefficient for molecular nitrogen diffusing into atomic oxygen.

Since the wall temperature is 2700°R (1500°K), the injected ablation species are predominantly C₂H₂ and CO, as shown in figures 47(a) and (b). Also, the species at the wall are essentially C₂H₂ and CO. A detailed listing of the stagnation species mass fractions and other wall properties are included in table XV.

Figure 48 presents the stagnation elemental profiles for ablation injection rates of 0.05 and 0.1. For these injection rates, the carbon and hydrogen elements are confined to about one third or less of the shock-layer thickness adjacent to the wall.

For the 0.1 injection rate, figures 49(a) through (b) show the species profiles at ξ values of 0.0 and 0.4. The species profiles for the same ξ values and a mass injection rate of 0.05 are shown in figures 50(a) and (b). These results show that a large number of chemical reactions occur near the wall.

The chemical reactions that remove C_2H_2 are rather important because the chemical process is highly endothermic and C_2H_2 is the major species at the wall. At the stagnation point, the mass fraction of C_2H_2 is 0.574 for a 0.1 injection rate and 0.446 for a 0.05 injection rate. However, the mass fraction of C_2H_2 decreases rapidly with increasing η . At an η of 0.15, the mass fraction is 0.015 for the 0.1 injection rate and zero for the 0.05 injection rate.

The second most abundant species at the wall is CO. For the temperature interval in which the carbon element is available (fig. 48), CO dissociation does not occur (see figures 47(a) and (b)). In fact, additional CO is formed as some of the hydrocarbons are chemically degraded at the higher temperatures.

The effect of injecting ablation products on stagnation temperatures is shown in figure 51. Results for 0.0, 0.05, and 0.1 injection rates are shown. Near the wall, the temperatures are substantially reduced by injection of ablation products. For example, 35 percent of the shock

layer adjacent to the wall experiences a temperature reduction for a 0.1 injection rate and 30 percent of the shock layer experiences a temperature reduction for a 0.05 injection rate.

The effects of injecting ablation species on stagnation velocity profiles are shown in figure 52. The effect of ablation injection on heat transfer, Stanton number, and skin friction coefficient is compared in the following section.

Comparison of results for mass injection of air, H₂O (gas), and abalation species.-In this section, comparisons of the effects of injecting air, H₂O, and ablation species on heat transfer rate, Stanton number, and skin friction distributions are presented. The equilibrium air calculations were made by using the same free stream and wall temperature conditions stated in the two previous sections. For the equilibrium air results, multicomponent diffusion was used, and the solutions were iterated twice in ξ . (See table XVI for a listing of wall pressure ratio, shock stand-off distance, and the aforementioned quantities at ξ values of 0, 0.2, 0.4 and 0.6.)

Figure 53 shows the heat transfer rate distributions for injection rates of 0.0, 0.05, and 0.1. These results show that the mass injection in the stagnation region of any of the three injectants significantly reduces the heat transfer rates. Downstream of the mass injection region (see fig. 53), the H₂O injectant provides a larger reduction in heating than the air injectant (for ablation injection, the solutions presented are only within the injection region). The heat transfer

rates with air injection approach the no injection values a short distance down stream of the injection region. This agrees with the previously discussed effect of air injection for a one-inch nose radius body. For the 0.05 injection rate, H_2O effects the largest reduction in heating followed by ablation products and finally air. For the 0.1 injection rate, the H_2O and ablation injectants effect about the same reduction in heating and both injectants give more reduction than air injection.

Figure 54 shows the effect of each of the three injectants on Stanton number distribution. Most of the conclusions concerning the effect of mass injection on heat transfer distribution are also applicable to Stanton number distribution. However, the relative effectiveness of the three injectants in reducing Stanton number is not the same for the 0.05 injection rate as that for reducing the heat transfer. This effect is due to large variations in wall enthalpy (see table XV) for the three injectants.

Figure 55 shows the effect of mass injection on skin friction coefficient and how this effect differs for air, H_2O and ablation injection. Large skin friction reductions occur in the mass injection region. Downstream of the injection region, the skin friction values approach the no injection values. In the mass injection region, the three injectants effect about the same reduction in skin friction. Downstream of the injection region, the H_2O injectant provides a larger reduction in skin friction than does the air injectant.

VII. CONCLUDING REMARKS

Equations describing reacting and nonreacting viscous shock layers about an axisymmetric body at zero angle of attack were presented. These equations account for mass injection and multicomponent diffusion. An implicit finite-difference technique for solving these equations was discussed. Calculated results were described which show the effect of chemistry model, surface catalyticity, diffusion model, and mass injection on flow parameters and surface transport. Some of the solutions provide information previously unavailable for reacting air. For example, the downstream viscous shock-layer solutions that treated the diffusion as multicomponent, with or without injection of air, were previously unavailable. These results were obtained for both non-equilibrium and equilibrium flow.

Results of the study lead to the following conclusions:

1. The chemistry model substantially influences flow parameters and surface transport. Results show that the frozen and equilibrium chemistry models overpredict wall heat transfer rates for the flow conditions considered in this study. For example, the stagnation heating rate obtained with an equilibrium calculation was 54 percent greater than comparable results with a nonequilibrium and noncatalytic wall calculation.
2. Wall catalyticity significantly influences wall heat transfer rate and species composition near the wall but has little influence on the other flow parameters considered. For an equilibrium catalytic

wall, the wall heat transfer rate for nonequilibrium flow was shown to be about the same as that for equilibrium flow.

3. For reacting air, results were compared for a multicomponent and for a binary diffusion model. For the binary approximation, the diffusion coefficient was the diffusion coefficient for atomic oxygen diffusing into molecular nitrogen. Results of the comparisons show negligible differences in most flow parameters and surface transport for the two diffusion models. This result applies to both nonequilibrium and equilibrium air. For multicomponent diffusion a small amount of elemental diffusional separation was observed, and consequently, a small difference in species profiles occurred.

4. The effect that mass injection has on heat transfer rates decreases as the injection rate increases. Also, the effect that mass injected in the stagnation region has on the flow field decreases very rapidly downstream.

Results of stagnation solutions were presented for mass injection rates substantially in excess of those required to reduce the convective heating rate to zero. For the injectants considered, water was most effective in reducing wall heat transfer rates.

5. The shape of the equilibrium temperature profiles differs from the results of a previous stagnation viscous shock-layer solution; however, the shape of the present temperature profiles can be substantiated by considering the chemical reactions that occur within the shock layer.

6. Two areas for improving the present analyses are noteworthy. First, it is desirable to reduce the time required for the equilibrium flow calculations. This can be accomplished by developing improved equilibrium chemistry computer codes and by developing more efficient means for solving the energy equation. Secondly, the range of shock Reynolds numbers for which the nonequilibrium analysis can be applied needs to be extended. All the nonequilibrium results reported were for a shock Reynolds number of 191. If the shock Reynolds number is increased beyond about 500, the analysis will not converge.

7. These analyses should be appropriate for calculating radiating viscous flows with mass injection.

REFERENCES

1. Blottner, F. G.: Finite Difference Methods of Solution of the Boundary-Layer Equations. AIAA J., vol. 8, no. 2, Feb. 1970, pp. 193-205.
2. Blottner, F. G.: Nonequilibrium Laminar Boundary-Layer Flow of Ionized Air. AIAA J., vol. 2, no. 11, Nov. 1964, pp. 1921-1927.
3. Moore, Jeffrey A.: Chemical Non-Equilibrium in Viscous Flows. Ph.D. Thesis, State University of New York at Buffalo, 1967.
4. Nachtsheim, Philip R.: Multicomponent Diffusion in Chemically Reacting Laminar Boundary Layers. Proceedings of the 1967 Heat Transfer and Fluid Mechanics Institute. Ch. IV, P. A. Libby, D. B. Olfe, and C. W. Van Atta, eds., Stanford University Press, 1967, pp. 58-87.
5. Davy, William C.; Craig, Roger A.; and Lyle, Gilbert C.: An Evaluation of Approximations used in the Analysis of Chemically Reacting, Stagnation-Point Boundary Layers with Wall Injection. Proceedings of the 1970 Heat Transfer and Fluid Mechanics Institute, Ch. XV, Turgut Sarpkaya, ed., Stanford University Press, 1970, pp. 222-237.
6. Adams, J. C.; Lewis, C. H.; Brahinsky, H. S.; and Marchand, E. O.: Effects of Chemical Nonequilibrium, Mass Transfer, and Viscous Interaction on Spherically Blunted Cones at Hypersonic Conditions. (Preprint) 69-168, AIAA, Jan. 20-22, 1969.
7. Davis, R. T.: Numerical Solution of the Hypersonic Viscous Shock-Layer Equations. AIAA J., vol. 8, no. 5, May 1970, pp. 843-851.
8. Davis, R. T.: Hypersonic Flow of a Chemically Reacting Binary Mixture Past a Blunt Body. (Preprint) 70-805, AIAA, June 29-July 1, 1970.
9. Whitehead, R. E.: A Numerical Solution to the Viscous Shock-Layer Blunt-Body Problem with Inert Gas Injection Into Air. Ph.D. Thesis, Virginia Polytechnic Institute and State University, 1970.
10. Dellinger, Thomas C.: Nonequilibrium Air Ionization in Hypersonic Fully Viscous Shock Layers. (Preprint) 70-806, AIAA, June 29 - July 1, 1970.
11. Blottner, F. G.: Viscous Shock Layer at the Stagnation Point with Nonequilibrium Air Chemistry. AIAA J., vol. 7, no. 12, Dec. 1969, pp. 2281-2288.

12. Adams, J. C.: Shock Slip Analysis of Merged Layer Stagnation Point Air Ionization. AIAA J., vol. 8, no. 5, May 1970, pp. 971-973.
13. Lee, Richard H. C.; Zierten, Thomas A.: Merged Layer Ionization in the Stagnation Region of a Blunt Body. Proceedings of the 1967 Heat Transfer and Fluid Mechanics Institute, Ch. XXIII, P. A. Libby, D. B. Olfe, and C. W. Van Atta, eds., Stanford University Press, 1967, pp. 452-468.
14. Edelman, R.; Hoffman, J.: Viscous Hypersonic Flow in the Vicinity of the Stagnation Point of Axisymmetric Blunt Bodies - Calculations and Results for Equilibrium Air. TR-498, General Applied Science Lab., May 10, 1965.
15. Chen, S. Y.; Baron, J.; and Mobley, R.: Stagnation Region Gas Injection in Low Reynolds Number Hypersonic Flow. Proceeding of the 1967 Heat Transfer and Fluid Mechanics Institute, Ch. III, P. A. Libby, O. B. Olfe, and C. W. Van Atta, eds., Stanford University Press, 1967, pp. 34-57.
16. Cheng, H. K.: The Blunt-Body Problem in Hypersonic Flow at Low Reynolds Numbers. (Preprint) 63-92, IAS, Jan. 21-23, 1963.
17. Davis, R. T.; and Flugge-Lotz, I.: Second-Order Boundary Layer Effects in Hypersonic Flow Past Axisymmetric Blunt Bodies. J. Fluid Mechanics, vol. 20, part 4, 1964, pp. 593-623.
18. Bird, R. B.; Stewart, W. E.; and Lightfoot, E. N.: Transport Phenomena. John Wiley and Sons, Inc., 1960.
19. Williams, F.: Combustion Theory. Addison Wesley Book Co., Inc., 1965.
20. Chung, Paul M.: Chemically Reacting Nonequilibrium Boundary Layers. Vol. II of Advances in Heat Transfer, J. P. Hartnett and T. F. Irvine, Jr., ed., Academic Press, 1965, pp. 109-270.
21. Lees, Lester: Convective Heat Transfer With Mass Addition and Chemical Reactions. Recent Advances in Heat and Mass Transfer, J. P. Hartnett, ed., McGraw-Hill Book Co., 1961, pp. 161-207.
22. Hirschfelder, J. O.; Curtiss, C. F.; and Bird, R. B.: Molecular Theory of Gases and Liquids. John Wiley and Sons, Inc., 1954.
23. McBride, Bonnie J.; Heimel, Sheldon; Ehlers, Janet G.; Gordon, Sanford: Thermodynamic Properties to 6000°K for 210 Substances Involving the First 18 Elements. NASA SP-3001, 1963.
24. Esch, D. D.; Siripong, A.; and Pike, R. W.: Thermodynamic Properties in Polynomial Form for Carbon, Hydrogen, Nitrogen, and Oxygen Systems from 300 to 15000°K. NASA RFL-TR-70-3, 1970.

25. Svehla, Roger A.: Estimated Viscosities and Thermal Conductivities of Gases at High Temperatures. NASA TR R-132, 1962.
26. Esch, D. D.; Pike, R. W.; Engel, Carl D.; Farmer, R. C.; and Balhoff, J. F.: Stagnation Region Heating of A Phenolic-Nylon Ablator During Return from Planetary Missions. NASA NGR 19-001-059, Sept. 1971.
27. Stroud, C. W.; and Brinkley, Kay L.: Chemical Equilibrium of Ablation Materials Including Condensed Species. NASA TN D-5391, 1969.
28. Vincenti, W. G.; and Kruger, C. H.: Introduction to Physical Gas Dynamics. John Wiley and Sons, Inc., 1965.
29. Bortner, M. H.: Suggested Standard Chemical Kinetics for Flow Field Calculations - A Consensus Opinion. AMRC Proceedings, vol. 14, part. 1, 1966, pp. 569-580.
30. Blottner, F. G.; and Flugge-Lotz, I.: Finite-Difference Computation of the Boundary Layer with Displacement Thickness Interaction. Journal de Mechanique, vol. II, no. 4, 1963.
31. Kao, Hsiao C.: Hypersonic Viscous Flow Near the Stagnation Streamline of a Blunt Body. AIAA J., vol. 2, no. 11, Nov. 1964, pp. 1892-1897.
32. Conte, S. D.: Elementary Numerical Analysis. McGraw-Hill Book Co., Inc., 1965.
33. Anon: U. S. Standard Atmospheres, 1962.
34. Kaiser, J. E.; and Flugge-Lotz, I.: Viscous, Hypersonic Flow Around a Blunt Body. Stanford University TR 178, Jan. 1968.
35. Probstein, Ronald F.: Shock Wave and Flow Field Development in Hypersonic Re-entry. (Preprint) 1110-60, ARS, May 9-12, 1960.
36. Hansen, C. F.: Approximations for the Thermodynamic and Transport Properties of High Temperature Air. NASA TR R-50, 1959.
37. Gomez, A. V.; Curry, D. M.; and Johnston, C. G.: Radiative Ablative and Active Cooling Thermal Protection Studies for the Leading Edge of a Fixed-Straight Wing Space Shuttle. (Preprint) 71-495, AIAA, April 26-28, 1971.
38. Sykes, George F.: Decomposition Characteristics of a Char-Forming Phenolic Polymer Used for Ablative Composites. NASA TN D-3810, 1967.

TABLE I.-THERMODYNAMIC PROPERTIES

Species	h_o^0 , cal/mole	$h_{298}^0-h_o^0$, cal/mole	$-(F_{298}^0-h_o^0)$ cal/mole	Temperature coefficients for specific heat ^a				
				a_1	a_2	a_3	a_4	a_5
0	5.795×10^4	-1.607×10^3	9.862×10^3	2.670×10^0 ^b	-1.970×10^{-2}	7.193×10^{-6}	-8.901×10^{-10}	4.002×10^{-14}
O_2	-2.075×10^3	2.075×10^3	1.254×10^4	2.548^c	-5.952×10^{-3}	2.701×10^{-6}	-2.798×10^{-10}	9.380×10^{-15}
N	1.115×10^5	1.481×10^3	9.435×10^3	3.316	1.151×10^{-1}	-3.726×10^{-5}	6.186×10^{-9}	-3.666×10^{-13}
N_2	-2.072×10^3	2.072×10^3	1.1574×10^4	3.721	4.254×10^{-2}	-2.835×10^{-6}	6.050×10^{-11}	-5.186×10^{-16}
NO	1.940×10^4	2.197×10^3	1.281×10^4	2.474	9.097×10^{-5}	-7.814×10^{-6}	2.218×10^{-9}	-1.489×10^{-13}
C(gas)	1.697×10^5	1.562×10^3	9.696×10^3	2.746	-3.909×10^{-2}	1.338×10^{-5}	-1.191×10^{-9}	3.369×10^{-14}
C_2	1.975×10^5	2.528×10^3	1.167×10^4	3.221	9.878×10^{-2}	-2.907×10^{-5}	3.938×10^{-9}	-2.000×10^{-13}
C_3	1.873×10^6	2.319×10^3	1.279×10^4	3.727	4.684×10^{-2}	-1.140×10^{-5}	1.154×10^{-9}	-3.293×10^{-14}
CO	-2.849×10^4	2.073×10^3	1.200×10^4	3.221	1.221×10^{-1}	-4.297×10^{-5}	6.559×10^{-9}	-3.451×10^{-13}
CN	9.428×10^4	2.073×10^3	1.236×10^4	3.845	2.521×10^{-2}	-2.658×10^{-6}	2.1615×10^{-10}	-6.381×10^{-15}
C_2H	1.167×10^3	2.213×10^3	1.292×10^4	2.612	-2.030×10^{-2}	1.095×10^{-5}	1.695×10^{-9}	8.590×10^{-14}
				2.141	3.219×10^{-2}	-5.498×10^{-6}	3.604×10^{-10}	-5.564×10^{-15}
				4.443	-2.885×10^{-2}	3.036×10^{-5}	6.244×10^{-9}	3.915×10^{-13}
				4.026	4.857×10^{-2}	7.026×10^{-6}	4.666×10^{-10}	-1.142×10^{-14}
				4.002	3.541×10^{-1}	-1.318×10^{-4}	2.064×10^{-8}	-1.144×10^{-12}
				2.213	-1.759×10^0	5.565×10^{-4}	-6.758×10^{-8}	2.825×10^{-12}
				3.254	9.698×10^{-2}	-2.647×10^{-5}	3.037×10^{-9}	-1.177×10^{-13}
				3.366	8.027×10^{-2}	-1.968×10^{-5}	1.940×10^{-9}	-5.549×10^{-14}
				3.411	4.897×10^{-2}	1.005×10^{-5}	-3.473×10^{-9}	2.361×10^{-13}
				3.473	7.337×10^{-2}	-9.088×10^{-6}	4.847×10^{-10}	-1.018×10^{-14}
				3.485	3.563×10^{-2}	-1.237×10^{-4}	1.866×10^{-8}	-1.013×10^{-12}
				5.307	8.966×10^{-2}	1.378×10^{-5}	9.251×10^{-10}	-2.278×10^{-14}

^a See equation (3.1)

^b Temperature interval 1000 to 6000°K

^c Temperature interval 6000 to 15000°K

TABLE I.-THERMODYNAMIC PROPERTIES - Concluded.

Species	h_o^o , cal/mole	$h_{298}^o-h_o^o$, cal/mole	$-F(298-h_o^o)$ cal/mole	Temperature coefficients for specific heat				
				a_1	a_2	a_3	a_4	a_5
C_2H_2	5.180×10^4	2.393×10^3	1.192×10^4	3.891×10^0	5.717×10^{-1}	1.957×10^{-4}	2.931×10^{-8}	-1.585×10^{-12}
				6.789	1.503×10^{-1}	-2.295×10^{-5}	1.534×10^{-9}	-3.763×10^{-14}
C_3H	1.271×10^5	2.373×10^3	1.410×10^4	5.289	4.619×10^{-1}	-1.577×10^{-5}	2.416×10^{-8}	-1.361×10^{-12}
C_4H	1.540×10^5	3.220×10^3	1.547×10^4	7.328	5.774×10^{-2}	-2.064×10^{-4}	3.263×10^{-8}	-1.879×10^{-12}
C_4H_2	1.130×10^5	3.450×10^3	1.438×10^4	6.216	9.660×10^{-2}	-3.489×10^{-4}	5.411×10^{-8}	-2.996×10^{-12}
				1.118	2.194×10^{-2}	-3.395×10^{-5}	2.292×10^{-9}	-5.670×10^{-14}
C_6H_6	2.320×10^4	3.402×10^3	1.578×10^4	-9.311	3.584×10^{-1}	-4.174×10^{-2}	2.217×10^{-5}	-4.438×10^{-9}
H	5.062×10^4	1.481×10^3	6.686×10^3	2.500	-8.243×10^{-5}	6.421×10^{-8}	-1.720×10^{-11}	1.457×10^{-15}
				3.934	-1.776×10^{-1}	6.013×10^{-5}	-7.819×10^{-9}	3.482×10^{-13}
H_2	-2.024×10^3	2.024×10^3	7.281×10^3	3.358	2.794×10^{-2}	9.372×10^{-6}	-2.948×10^{-9}	2.141×10^{-13}
				3.363	4.656×10^{-2}	-5.127×10^{-6}	2.802×10^{-10}	-4.905×10^{-15}
HCN	2.898×10^4	2.207×10^3	1.217×10^4	3.654	3.444×10^{-1}	-1.258×10^{-4}	2.169×10^{-8}	-1.430×10^{-12}
				3.654	3.444×10^{-1}	-1.258×10^{-4}	2.169×10^{-8}	-1.430×10^{-12}
OH	7.206×10^3	2.107×10^3	1.098×10^4	3.284	5.086×10^{-2}	-2.289×10^{-6}	-1.001×10^{-9}	1.056×10^{-13}
				3.456	4.375×10^{-2}	-5.819×10^{-6}	4.187×10^{-10}	-1.104×10^{-14}
H_2O	-6.016×10^4	2.367×10^3	1.108×10^4	3.387	2.140×10^{-1}	-5.048×10^{-6}	5.269×10^{-9}	-1.999×10^{-13}
				4.339	1.035×10^{-1}	-1.545×10^{-6}	1.017×10^{-9}	-2.468×10^{-14}

TABLE II. MOLECULAR CONSTANTS

Species	$\epsilon/k,$ $^{\circ}\text{K}$	$\sigma,$ \AA	M, g/g-mole
O	106.7	3.050	16.00
O ₂	106.7	3.467	32.00
N	71.4	3.298	14.01
N ₂	71.4	3.798	28.02
NO	116.7	3.492	30.01
C	30.6	3.385	12.01
C ₂	78.8	3.913	24.02
C ₃	128.0	4.420	36.03
CO	91.7	3.690	28.01
CN	75.0	3.856	26.02
C ₂ H	218.0	3.980	25.02
C ₂ H ₂	231.8	4.033	26.04
C ₃ H	355.0	4.520	37.03
C ₄ H	503.0	5.080	49.04
C ₄ H ₂	515.0	5.120	50.04
C ₆ H ₆	412.3	5.349	78.11
H	37.0	2.708	1.01
H ₂	59.7	2.827	2.02
HCN	569.1	3.630	27.03
OH	79.8	3.147	17.01
H ₂ O	809.1	2.641	18.02

TABLE III.-THIRD BODY EFFICIENCIES RELATIVE TO ARGON

Catalytic Bodies	Z (j - NS), i	Species, i = 1, 2, --- NS					
		0	O ₂	N	N ₂	NO	
		i=1	2	3	4	5	
M ₁	1,i	25	9	1	2	1	1
M ₂	2,i	1	1	0	2.5	1	1
M ₃	3,i	20	1	20	20	20	20

TABLE IV.-REACTION RATE COEFFICIENTS

Reaction	$C0_r$	$C1_r$	$C2_r$	$D0_r$	$D1_r$	$D2_r$
r = 1	3.61×10^{18}	59.4	-1.0	3.01×10^{15}	0	-0.5
2	1.92×10^{17}	113.1	-0.5	1.09×10^{16}	0	-0.5
3	4.15×10^{22}	113.1	-1.5	2.32×10^{21}	0	-1.5
4	3.97×10^{20}	75.6	-1.5	1.01×10^{20}	0	-1.5
5	3.18×10^9	19.7	1.0	9.63×10^{11}	3.6	0.5

TABLE V.-FREE STREAM CONDITIONS

Altitude, ft	Velocity, ft/sec	Temperature, °R	Pressure, atm	Density, lbm/ft ³	Mach number	Reynolds ^a number
280,000	26,000	325.17	3.82×10^{-6}	4.66×10^{-7}	29.40	1.482×10^3
200,000	20,000	456.99	1.95×10^{-4}	1.69×10^{-5}	19.08	3.116×10^4
150,000	22,520	480.71	1.28×10^{-3}	1.06×10^{-4}	20.98	2.217×10^5
100,000	20,000	480.57	1.09×10^{-2}	1.06×10^{-3}	20.18	2.149×10^6

^a Based on a one-foot nose radius.

TABLE VI.--SUMMARY OF COMPUTING TIME AND ITERATION REQUIREMENTS FOR VARIOUS CASES^a

Case	Computational time ^c , min	Iterations per station	
		Stagnation	Downstream ^d
Ideal gas	0.43	5	4
Frozen (O ₂ , N ₂)	10.0	7	4
EQ ^b - binary - $\dot{m}_O = 0$	113.5	11	6
EQ - MCD - $\dot{m}_O = 0$	139.4	13	6
EQ - binary - $\dot{m}_O = 0.2$ Air	111.3	16	6
EQ - binary - $\dot{m}_O = 0.2$ Water	[200.0]	18	6
EQ - binary - $\dot{m}_O = 0.2$ Ablator.	[260.0]	22	6
NEQ - binary - NCW - $\dot{m}_O = 0$	23.8	10	4
NEQ - MCD - NCW - $\dot{m}_O = 0$	27.6	18	4
NEQ - binary - ECW - $\dot{m} = 0$	24.6	11	4
NEQ - MCD - ECW - $\dot{m} = 0$	27.5	14	4
NEQ - MCD - NCW - $\dot{m}_O = 0.2$ Air	30.2	18	4

^a alt = 200,000 ft.; $U_\infty^* = 20,000$ ft/sec, $T_w^* = 2700^\circ R$, and $a^* = 1.0$ in.

^b EQ = Equilibrium; MCD = multicomponent diffusion; NCW = noncatalytic wall; ECW = equilibrium catalytic wall.

^c Time based on computing to an $\xi = 3.0$ where $\Delta\xi = 0.2$; 50 grid points along η ; two iterations along ξ . Bracketed quantities are extrapolated values.

^d Typical values where a minimum of four iterations was imposed.

TABLE VII. FROZEN AIR STAGNATION SHOCK AND WALL VALUES
 [alt = 200,000 ft; $U_{\infty}^* = 20,000$ ft/sec; $a^* = 1.0$ in.;
 $Re_{\infty} = 2.597 \times 10^3$; $Re_S = 1.914 \times 10^2$]

Properties	Shock	Wall
Temperature, °R	2.396×10^4	2.700×10^{3b}
Pressure, atm	8.822×10^{-2}	9.439×10^{-2}
Density, lbm/ft ³	1.456×10^{-4}	1.381×10^{-3}
Viscosity, lbf-sec/ft ²	4.591×10^{-6}	1.106×10^{-6}
Velocity, ft/sec.	-2.328×10^3	0.0
Enthalpy, Btu/lbm	7.989×10^3	5.831×10^2
Molecular weight, g/g-mole.	2.888×10^3	2.888×10^1
Prandtl number.	7.018×10^{-1}	6.938×10^{-1}
Mass fractions:		
O ₂	2.400×10^{-1}	2.400×10^{-1}
N ₂	7.600×10^{-1}	7.600×10^{-1}

a $n_S = 9.079 \times 10^{-2}$, $q^* = 4.287 \times 10^2$ Btu/ft²-sec.

b $n_S = 9.215 \times 10^{-2}$; $q^* = 4.226 \times 10^2$ Btu/ft²-sec.

TABLE VIII.-EQUILIBRIUM AIR STAGNATION SHOCK AND WALL VALUES
 [alt = 200,000 ft; $U_{\infty}^* = 20,000$ ft/sec; $a^* = 1.0$ in.; $Re_{\infty} = 2.597 \times 10^3$; $Re_s = 3.376 \times 10^2$]

Properties	Shock	Wall			
		Binary		Multicomponent	
		3a	3b	3c	3d
Temperature, °R	1.041×10^4	1.800×10^{-2}	2.700×10^{-2}	1.800×10^{-2}	2.700×10^{-2}
Pressure, atm	9.293×10^{-2}	9.642×10^{-2}	9.655×10^{-2}	9.644×10^{-2}	9.644×10^{-2}
Density, lbm/ft ³	2.450×10^{-4}	2.104×10^{-3}	1.419×10^{-3}	2.113×10^{-3}	1.410×10^{-3}
Viscosity, lbf-sec/ft ²	2.606×10^{-6}	8.515×10^{-7}	1.104×10^{-6}	8.569×10^{-7}	1.112×10^{-6}
Velocity, ft/sec.	-1.384×10^3	0.0	0.0	0.0	0.0
Enthalpy, Btu/lbm	8.054×10^3	3.235×10^2	5.819×10^2	3.231×10^2	5.793×10^2
Molecular Weight, g/g-mole.	1.997×10^1	2.888×10^1	2.888×10^1	2.900×10^1	2.901×10^1
Lewis number	9.044×10^{-1}	1.000×10^0	1.298×10^0	-	-
Prandtl number.	6.754×10^{-1}	6.932×10^{-1}	6.957×10^{-1}	6.922×10^{-1}	6.959×10^{-1}
Mass fractions:					
O	2.381×10^{-1}	1.275×10^{-10}	2.475×10^{-8}	1.260×10^{-10}	1.809×10^{-8}
O ₂	5.035×10^{-5}	2.399×10^{-1}	2.392×10^{-1}	2.720×10^{-1}	2.759×10^{-1}
N	2.241×10^{-1}	3.962×10^{-22}	8.112×10^{-14}	3.980×10^{-22}	1.369×10^{-15}
N ₂	5.343×10^{-1}	7.600×10^{-1}	7.594×10^{-1}	7.280×10^{-1}	7.227×10^{-1}
NO	3.360×10^{-3}	3.582×10^{-5}	1.344×10^{-3}	3.722×10^{-5}	1.404×10^{-3}

a $n_s = 5.681 \times 10^{-2}$; $q^* = 4.430 \times 10^2$ Btu/ft²-sec; constant Lewis number = 1.0.
 b $n_s = 5.619 \times 10^{-2}$; $q^* = 4.443 \times 10^2$ Btu/ft²-sec.
 c $n_s = 5.636 \times 10^{-2}$; $q^* = 4.556 \times 10^2$ Btu/ft²-sec.
 d $n_s = 5.710 \times 10^{-2}$; $q^* = 4.481 \times 10^2$ Btu/ft²-sec.

TABLE IX.-EQUILIBRIUM AIR STAGNATION SHOCK AND WALL VALUES^a
 [alt = 280,000 ft; $U^* = 26,000$ ft/sec; $a^* = 12$ in.; $Re_\infty = 1.482 \times 10^3$; $Re_s = 1.498 \times 10^2$

PROPERTIES	SHOCK	WALL
Temperature, °R	1.032×10^4	2.429×10^3
Pressure, atm	4.396×10^{-3}	4.528×10^{-3}
Density, lbm/ft ³	9.274×10^{-6}	7.411×10^{-5}
Viscosity, lbf-sec/ft ²	2.513×10^{-6}	1.032×10^{-6}
Velocity, ft/sec.	-1.306×10^3	0.0
Enthalpy, Btu/lbm	1.361×10^4	5.061×10^2
Molecular weight, g/g-mole.	1.580×10^1	2.888×10^1
Lewis number	1.400×10^0	1.400×10^0
Prandtl number.	6.734×10^{-1}	6.957×10^{-1}
Mass fractions:		
O	2.398×10^{-1}	5.331×10^{-8}
O ₂	2.098×10^{-6}	2.396×10^{-1}
N	5.927×10^{-1}	5.293×10^{-15}
N ₂	1.671×10^{-1}	7.597×10^{-1}
NO	3.776×10^{-4}	6.008×10^{-4}

$$a_{n_s} = 3.801 \times 10^{-2}; q^* = 6.927 \times 10^1 \text{ Btu/ft}^2\text{-sec.}$$

TABLE X.-EQUILIBRIUM AIR STAGNATION SHOCK AND WALL VALUES^a
 [alt = 150,000 ft; $U^* = 22,520$ ft/sec; $a^* = 0.5$ in.; $Re_\infty = 9.236 \times 10^3$; $Re_s = 1.134 \times 10^3$]

PROPERTIES	SHOCK	WALL
Temperature, °R	1.221×10^4	2.657×10^3
Pressure, atm	7.729×10^{-1}	8.038×10^{-1}
Density, lbm/ft ³	1.619×10^{-3}	1.197×10^{-2}
Viscosity, lbf-sec/ft ²	2.861×10^{-6}	1.094×10^{-6}
Velocity, ft/sec	-1.547×10^3	0.0
Enthalpy, Btu/lbm	1.020×10^4	5.411×10^2
Molecular weight, g/g-mole.	1.863×10^1	2.888×10^1
Lewis number.	1.400×10^0	1.400×10^0
Prandtl number.	6.627×10^{-1}	6.958×10^{-1}
Mass fractions:		
O	2.371×10^{-1}	3.638×10^{-7}
O ₂	1.108×10^{-4}	2.397×10^{-1}
N	3.260×10^{-1}	3.983×10^{-15}
N ₂	4.310×10^{-1}	7.593×10^{-1}
NO	5.712×10^{-3}	9.205×10^{-4}

^a $n_s = 5.601 \times 10^{-2}$; $q^* = 2.375 \times 10^3$ Btu/ft²-sec.

TABLE XI.-NONEQUILIBRIUM AIR STAGNATION SHOCK AND WALL VALUES
 [alt = 200,000 ft; $U_{\infty}^* = 20,000$ ft/sec; $a^* = 1.0$ in.; $Re_{\infty} = 2.597 \times 10^3$; $Re_s = 1.914 \times 10^2$]

Properties	Shock	Wall			
		Noncatalytic		Catalytic	
		Binary	Multicomponent	Binary	Binary
Temperature, °R	2.396×10^4	2.700×10^{3a}	2.700×10^{3b}	2.700×10^{3c}	1.800×10^{3d}
Pressure, atm	8.822×10^{-2}	9.457×10^{-2}	9.457×10^{-2}	9.466×10^{-2}	9.466×10^{-2}
Density, lbm/ft ³	1.456×10^{-4}	1.116×10^{-3}	1.131×10^{-3}	1.385×10^{-3}	2.078×10^{-3}
Viscosity, lbf-sec/ft ²	4.591×10^{-6}	1.096×10^{-6}	1.091×10^{-6}	1.106×10^{-6}	8.516×10^{-7}
Velocity, ft/sec	-2.328×10^3	0.0	0.0	0.0	0.0
Enthalpy, Btu/lbm	7.989×10^3	2.586×10^3	2.558×10^3	5.849×10^2	3.283×10^2
Molecular weight, g/g-mole	2.888×10^1	2.331×10^1	2.360×10^1	2.888×10^1	2.888×10^1
Lewis number	1.338×10^0	1.040×10^0	-	-	1.400×10^0
Prandtl number	7.018×10^{-1}	6.877×10^{-1}	6.813×10^{-1}	6.962×10^{-1}	6.938×10^{-1}
Mass fractions:					
O	0.0	2.245×10^{-1}	2.052×10^{-1}	2.495×10^{-8}	1.245×10^{-16}
O ₂	2.400×10^{-1}	4.875×10^{-3}	2.935×10^{-3}	2.389×10^{-1}	2.399×10^{-1}
N	0.0	2.865×10^{-2}	3.687×10^{-2}	8.195×10^{-14}	3.453×10^{-31}
N ₂	7.600×10^{-1}	7.168×10^{-1}	7.298×10^{-1}	7.597×10^{-1}	7.600×10^{-1}
NO	0.0	3.278×10^{-2}	2.320×10^{-2}	1.343×10^{-3}	3.582×10^{-5}

^a $n_s = 8.567 \times 10^{-2}$; $q^* = 2.872 \times 10^2$ Btu/ft²-sec.
^b $n_s = 8.576 \times 10^{-2}$; $q^* = 2.891 \times 10^2$ Btu/ft²-sec.
^c $n_s = 8.291 \times 10^{-2}$; $q^* = 4.286 \times 10^2$ Btu/ft²-sec.
^d $n_s = 8.065 \times 10^{-2}$; $q^* = 4.53 \times 10^2$ Btu/ft²-sec; Lewis number was constant at 1.4.

TABLE XII.-EQUILIBRIUM AIR STAGNATION SHOCK AND WALL VALUE^a
 [alt = 100,000 ft; $U^* = 20,000$ ft/sec; $a^* = 1.0$ in.; $Re_\infty = 1.791 \times 10^5$; $Re_s = 1.876 \times 10^4$]

Properties	Shock	Wall
Temperature, °R	1.255×10^4	2.700×10^3
Pressure, atm	5.771×10^0	6.031×10^0
Density, lbm/ft ³	1.312×10^{-2}	8.913×10^{-2}
Viscosity, lbf-sec/ft ²	2.948×10^{-6}	1.110×10^{-6}
Velocity, ft/sec.	-1.627×10^3	0.0
Enthalpy, Btu/lbm	8.019×10^3	5.797×10^2
Molecular, weight, g/g-mole	2.897×10^1	2.076×10^1
Lewis number ^b	-	-
Prandtl number.	6.598×10^{-1}	6.964×10^{-1}
Mass fractions:		
O	2.305×10^{-1}	7.256×10^{-8}
O ₂	6.336×10^{-4}	2.640×10^{-1}
N	1.778×10^{-1}	1.044×10^{-14}
N ₂	5.746×10^{-1}	7.346×10^{-1}
NO	1.658×10^{-2}	1.384×10^{-3}

^a $n_s = 6.708 \times 10^{-2}$; $q^* = 2.735 \times 10^3$ Btu/ft²-sec.

^b Multicomponent diffusion.

TABLE XIII.-SUMMARY OF DIMENSIONAL HEAT TRANSFER RATES AT DIFFERENT BODY STATIONS^a
 [alt = 200,000 ft; U* = 20,000 ft/sec; a* = 1.0 in.; Re_∞ = 2.597X10³]

Conditions	ξ				
	0	0.4	1.0	2.0	3.0
Frozen chemistry at free stream composition	423	347	221	130	96
Equilibrium chemistry:					
Binary diffusion	442	376	239	135	98
Multicomponent diffusion	448	378	240	136	98
Nonequilibrium chemistry:					
Binary diffusion:					
Noncatalytic wall	287	236	157	100	76
Equilibrium catalytic wall	429	354	226	135	98
Multicomponent diffusion:					
Noncatalytic wall	289	237	158	101	77
Equilibrium catalytic wall	428	339	218	131	96

^aHeat transfer in Btu/ft²-sec; T* = 2700°R

TABLE XIV.-NONEQUILIBRIUM STAGNATION WALL CONDITIONS FOR A NONCATALYTIC WALL AND MASS INJECTION OF EQUILIBRIUM AIR [alt = 200,000 ft; $V^* = 20,000$ ft/sec; $a^* = 1.0$ in.; $Re_\infty = 2.597 \times 10^3$; $Re_s = 1.914 \times 10^2$; multicomponent diffusion]

Properties ^a	Nondimensional mass injection rate				
	0.0	0.1	0.2	0.3	0.4
Temperature, °R	2.700×10^3	2.700×10^3	2.700×10^3	2.700×10^3	2.700×10^3
Pressure, atm	9.457×10^{-2}	9.457×10^{-2}	9.457×10^{-2}	9.457×10^{-2}	9.457×10^{-2}
Density, lbm/ft ³	1.131×10^{-3}	1.233×10^{-3}	1.314×10^{-3}	1.362×10^{-3}	1.379×10^{-3}
Viscosity, lbf-sec/ft ²	1.091×10^{-6}	1.101×10^{-6}	1.105×10^{-6}	1.105×10^{-6}	1.105×10^{-6}
Velocity, ft/sec.	0.0	0.0	0.0	0.0	0.0
Enthalpy, Btu/lbm	2.558×10^3	1.607×10^3	1.034×10^3	7.191×10^2	6.104×10^2
Molecular weight, g/g-mole	2.360×10^1	2.573×10^1	2.742×10^1	2.843×10^1	2.879×10^1
Prandtl number	6.813×10^{-1}	6.876×10^{-1}	6.922×10^{-1}	6.950×10^{-1}	6.960×10^{-1}
Mass fractions:					
O	2.052×10^{-1}	1.284×10^{-1}	5.971×10^{-2}	1.839×10^{-2}	3.385×10^{-3}
O ₂	2.935×10^{-3}	8.712×10^{-2}	1.737×10^{-1}	2.232×10^{-1}	2.352×10^{-1}
N	3.687×10^{-2}	5.854×10^{-3}	6.389×10^{-4}	3.818×10^{-5}	1.089×10^{-6}
N ₂	7.298×10^{-1}	7.357×10^{-1}	7.394×10^{-1}	7.506×10^{-1}	7.583×10^{-1}
NO	2.320×10^{-2}	4.115×10^{-2}	2.622×10^{-2}	7.638×10^{-3}	3.098×10^{-3}

^aSee TABLE XI for shock properties.

TABLE XV.--STAGNATION EQUILIBRIUM WALL CONDITIONS FOR MASS INJECTION OF WATER AND ABLATION SPECIES [alt = 200,000 ft; $U_{\infty}^* = 20,000$ ft/sec; $a^* = 12$ in.; $Re_{\infty} = 3.116 \times 10^4$; $Re_s = 2.297 \times 10^3$; binary diffusion]

Properties	Water		Ablator	
	$\dot{m}_o = 0.05$	$\dot{m}_o = 0.1$	$\dot{m}_o = 0.05$	$\dot{m}_o = 0.1$
Temperature, °R	2.700×10^3	2.700×10^3	2.700×10^3	2.700×10^3
Pressure, atm	9.282×10^{-2}	9.282×10^{-2}	9.282×10^{-2}	9.282×10^{-2}
Density, lbm/ft ³	8.912×10^{-4}	8.420×10^{-4}	8.492×10^{-3}	8.903×10^{-3}
Viscosity, lbf-sec/ft ²	1.098×10^{-6}	1.095×10^{-6}	8.789×10^{-7}	8.524×10^{-7}
Velocity, ft/sec.	1.902×10^1	4.028×10^1	1.852×10^1	3.801×10^1
Enthalpy, Btu/lbm	-3.878×10^3	-4.629×10^3	2.578×10^3	3.135×10^3
Molecular weight, g/g-mole.	1.907×10^1	1.801×10^1	1.960×10^1	1.904×10^1
Lewis number	8.604×10^{-1}	8.274×10^{-1}	8.138×10^{-1}	8.195×10^{-1}
Prandtl number.	7.019×10^{-1}	7.124×10^{-1}	5.168×10^{-1}	5.196×10^{-1}
Mass fractions:				
O	1.416×10^{-6}	4.917×10^{-8}	7.471×10^{-18}	6.593×10^{-18}
O ₂	3.365×10^{-2}	3.829×10^{-5}	2.130×10^{-29}	6.107×10^{-29}
N	4.069×10^{-14}	2.355×10^{-24}	3.848×10^{-14}	8.159×10^{-17}
N ₂	1.129×10^{-1}	2.851×10^{-3}	1.038×10^{-1}	2.729×10^{-2}
NO	1.938×10^{-4}	1.039×10^{-6}	1.015×10^{-15}	4.432×10^{-16}

TABLE XV.--STAGNATION EQUILIBRIUM WALL CONDITIONS FOR MASS INJECTION
OF WATER AND ABLATION SPECIES - Concluded

Properties	Water		Ablator	
	$\dot{m}_o = 0.05$	$\dot{m}_o = 0.1$	$\dot{m}_o = 0.05$	$\dot{m}_o = 0.1$
	H			
H ₂				
H ₂ O				
OH				
HCN				
C				
C ₂				
C ₃				
CO				
CN				
C ₂ H				
C ₂ H ₂				
C ₃ H				
C ₄ H				
C ₄ H ₂				
C ₆ H ₆				
	2.149X10 ⁻⁸	1.320X10 ⁻⁷	1.699X10 ⁻⁶	1.800X10 ⁻⁶
	4.789X10 ⁻⁶	1.707X10 ⁻⁴	3.075X10 ⁻¹	3.357X10 ⁻²
	8.530X10 ⁻¹	9.969X10 ⁻¹		
	1.947X10 ⁻⁴	3.922X10 ⁻⁵		
			1.033X10 ⁻¹	6.014X10 ⁻²
			3.316X10 ⁻¹⁴	3.706X10 ⁻¹⁴
			1.362X10 ⁻¹⁷	1.652X10 ⁻¹⁷
			3.004X10 ⁻¹⁷	3.915X10 ⁻¹⁷
			3.046X10 ⁻¹	2.856X10 ⁻¹
			2.917X10 ⁻¹⁶	7.522X10 ⁻¹⁷
			1.084X10 ⁻⁵	1.356X10 ⁻⁵
			4.460X10 ⁻¹	5.744X10 ⁻¹
			7.834X10 ⁻⁴	1.064X10 ⁻³
			2.098X10 ⁻¹⁵	1.507X10 ⁻³
			1.072X10 ⁻²	1.630X10 ⁻²
			3.592X10 ⁻¹¹	9.470X10 ⁻⁶

TABLE XVI.-NONDIMENSIONAL HEAT TRANSFER-SKIN FRICTION COEFFICIENT, STANTON NUMBER, WALL PRESSURE RATIO, AND SHOCK STAND-OFF DISTANCE VALUES FOR NO INJECTION AND INJECTION OF AIR^a, WATER^b, AND ABLATION PRODUCTS^b AT DIFFERENT BODY STATIONS

\dot{m}_o	Injectant	q	C_F	St	$(P/P_o)_w$	n_s
$\xi = 0$						
0.0		2.043×10^{-2}	0.0	4.343×10^{-2}	1.0	5.825×10^{-2}
.05	air	7.027×10^{-3}	0.0	2.665×10^{-3}	1.0	6.324×10^{-2}
.05	water	5.203×10^{-3}	0.0	6.941×10^{-3}	1.0	5.732×10^{-2}
.05	ablator	6.664×10^{-3}	0.0	1.929×10^{-2}	1.0	5.881×10^{-2}
.1	air	7.127×10^{-4}	0.0	1.515×10^{-3}	1.0	6.814×10^{-2}
.1	water	3.401×10^{-4}	0.0	4.281×10^{-4}	1.0	6.221×10^{-2}
.1	ablator	2.132×10^{-4}	0.0	6.862×10^{-4}	1.0	6.385×10^{-2}
$\xi = 0.2$						
0.0		1.930×10^{-2}	6.616×10^{-3}	4.101×10^{-2}	9.588×10^{-1}	6.090×10^{-2}
.05	air	6.742×10^{-3}	2.665×10^{-3}	1.433×10^{-2}	9.584×10^{-1}	6.606×10^{-2}
.05	water	5.224×10^{-3}	2.768×10^{-3}	6.991×10^{-3}	9.469×10^{-1}	5.996×10^{-2}
.05	ablator	6.294×10^{-3}	2.277×10^{-3}	1.813×10^{-2}	9.469×10^{-1}	6.151×10^{-2}
.1	air	7.163×10^{-4}	9.562×10^{-3}	1.522×10^{-3}	9.580×10^{-1}	7.116×10^{-2}
.1	water	3.497×10^{-4}	1.058×10^{-3}	4.391×10^{-4}	9.467×10^{-1}	6.507×10^{-2}
.1	ablator	2.454×10^{-4}	8.118×10^{-4}	7.897×10^{-4}	9.467×10^{-1}	6.682×10^{-2}

^a Multicomponent diffusion

^b Binary diffusion

TABLE XVI.-NONDIMENSIONAL HEAT TRANSFER SKIN FRICTION COEFFICIENT, STANTON NUMBER, WALL PRESSURE RATIO, AND SHOCK STAND-OFF DISTANCE VALUES FOR NO INJECTION AND INJECTION OF AIR, WATER, AND ABLATION PRODUCTS AT DIFFERENT BODY STATIONS - Concluded.

\dot{m}_0	Injectant	q	C_F	St	$(P/P_0)_w$	ns
$\xi = 0.4$						
0.0		1.727×10^{-2}	1.111×10^{-2}	3.670×10^{-2}	8.608×10^{-1}	6.759×10^{-2}
.05	air	7.167×10^{-3}	5.121×10^{-3}	1.523×10^{-2}	8.594×10^{-1}	7.267×10^{-2}
.05	water	5.797×10^{-3}	5.241×10^{-3}	7.943×10^{-3}	8.207×10^{-1}	6.779×10^{-2}
.05	ablator	7.069×10^{-3}	4.433×10^{-3}	1.966×10^{-3}	8.205×10^{-1}	6.954×10^{-2}
.1	air	1.207×10^{-3}	2.006×10^{-3}	2.565×10^{-3}	8.583×10^{-1}	7.772×10^{-2}
.1	water	6.459×10^{-4}	2.121×10^{-3}	8.126×10^{-4}	8.202×10^{-1}	7.292×10^{-2}
.1	ablator	4.352×10^{-4}	1.619×10^{-3}	1.394×10^{-3}	8.199×10^{-1}	7.492×10^{-2}
$\xi = 0.6$						
0.0		1.485×10^{-2}	1.310×10^{-2}	3.156×10^{-2}	7.506×10^{-1}	7.914×10^{-2}
.05	air	7.811×10^{-3}	7.372×10^{-3}	1.660×10^{-2}	7.484×10^{-1}	8.430×10^{-2}
.05	water	6.625×10^{-3}	7.481×10^{-3}	9.491×10^{-3}	6.826×10^{-1}	8.028×10^{-2}
.05	ablator	7.798×10^{-3}	6.639×10^{-3}	2.038×10^{-2}	6.823×10^{-1}	8.233×10^{-2}
.1	air	2.408×10^{-3}	3.564×10^{-3}	5.118×10^{-3}	7.462×10^{-1}	8.930×10^{-2}
.1	water	1.069×10^{-3}	3.511×10^{-3}	1.359×10^{-3}	6.819×10^{-1}	8.523×10^{-2}
.1	ablator					

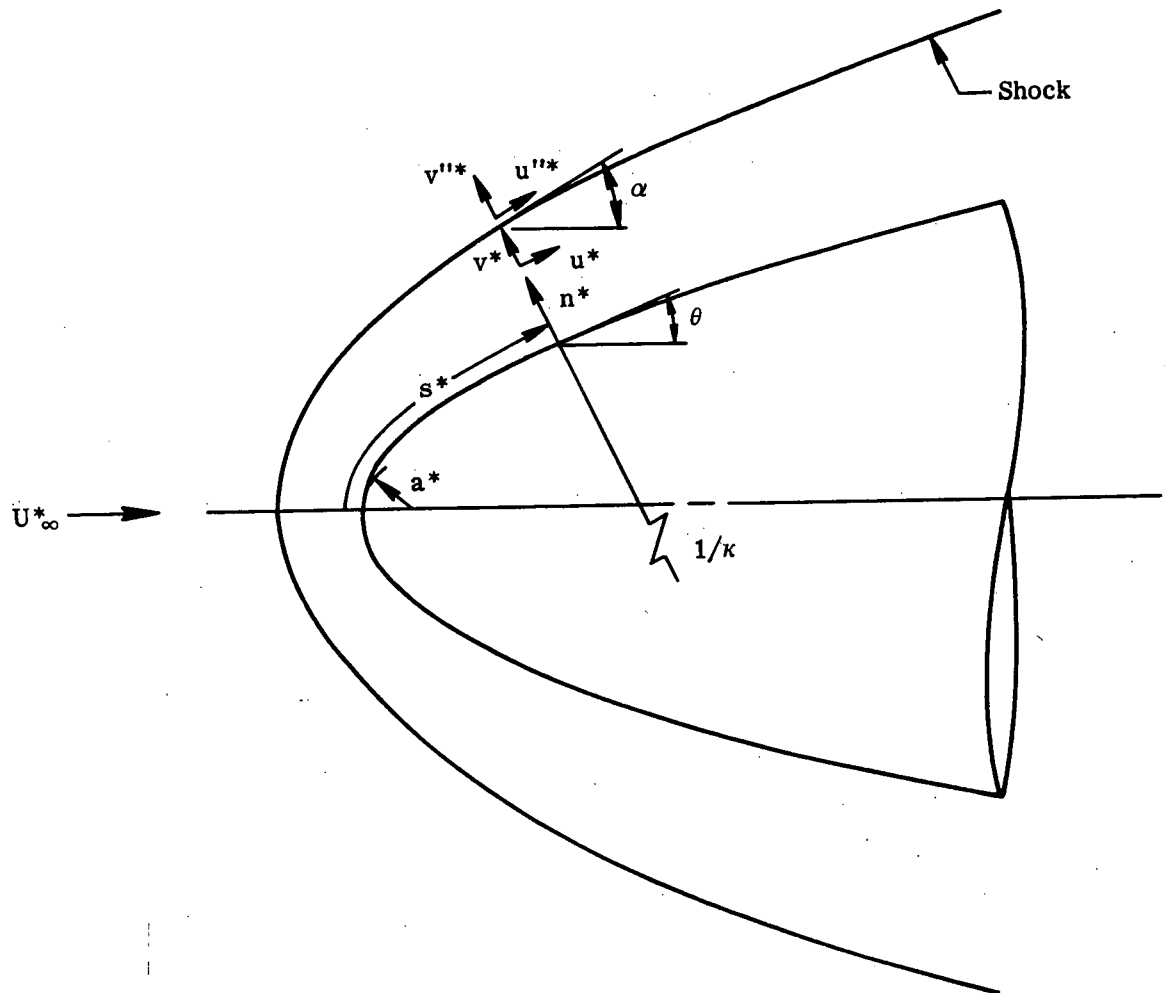
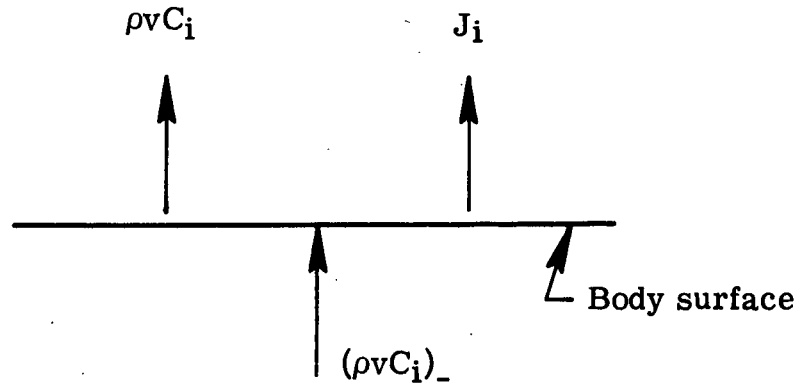
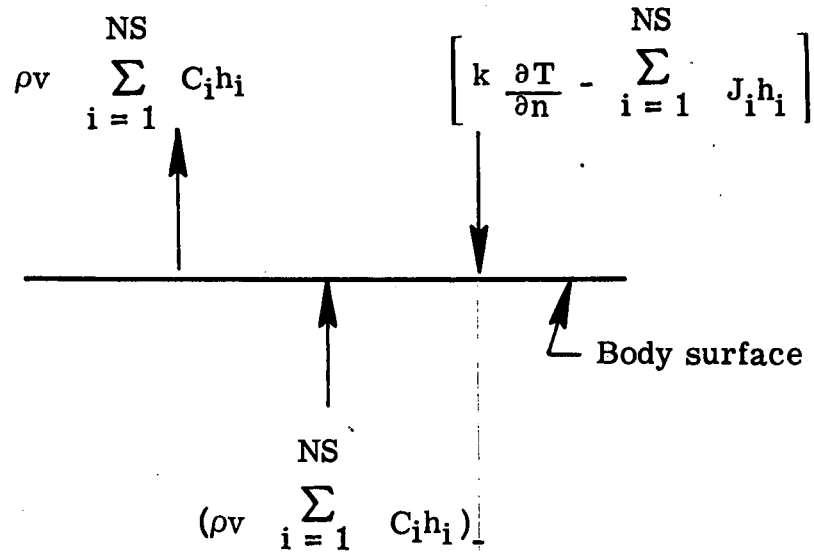


Figure 1.-Coordinate system.

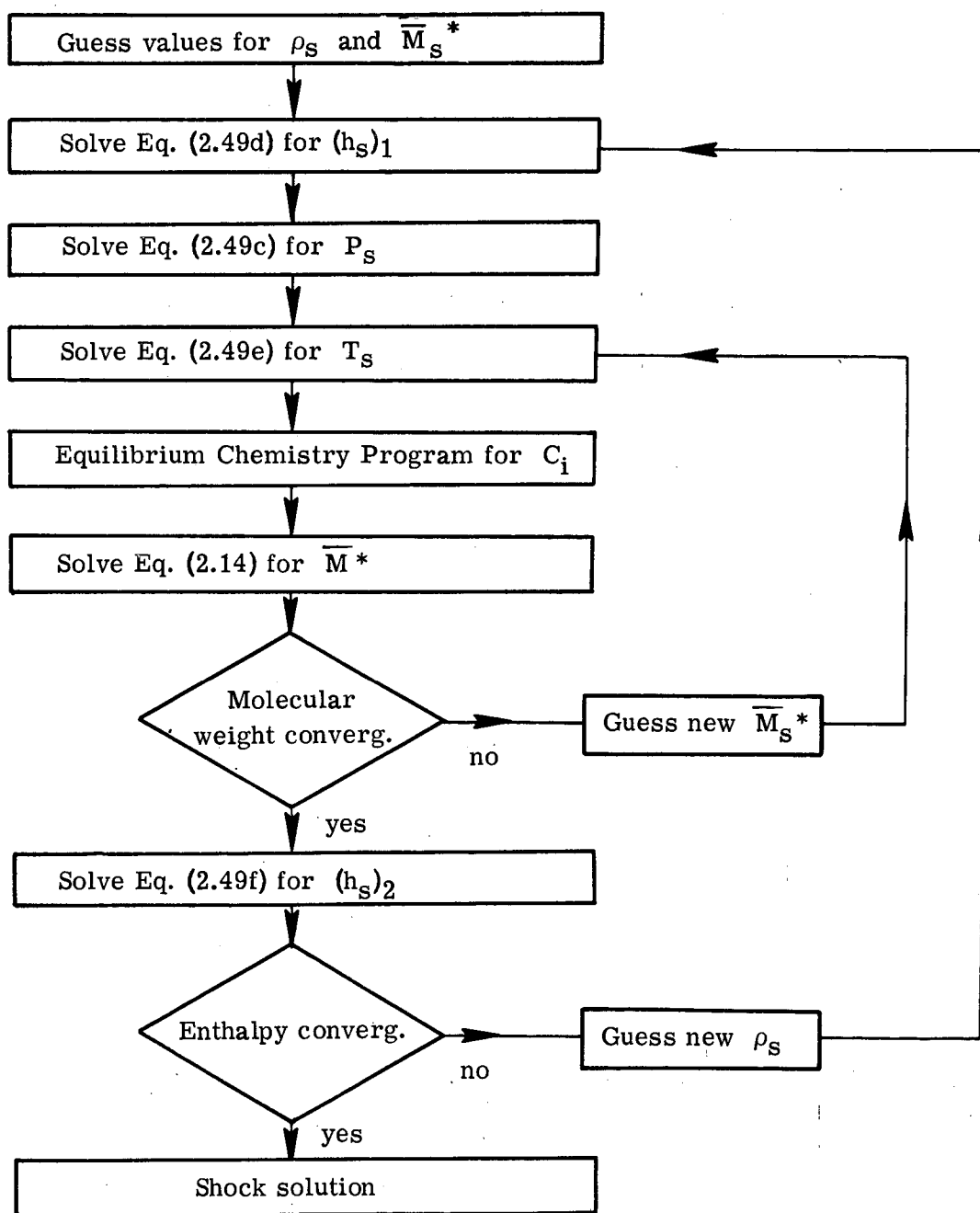


(a) Mass balance at gas-solid interface.



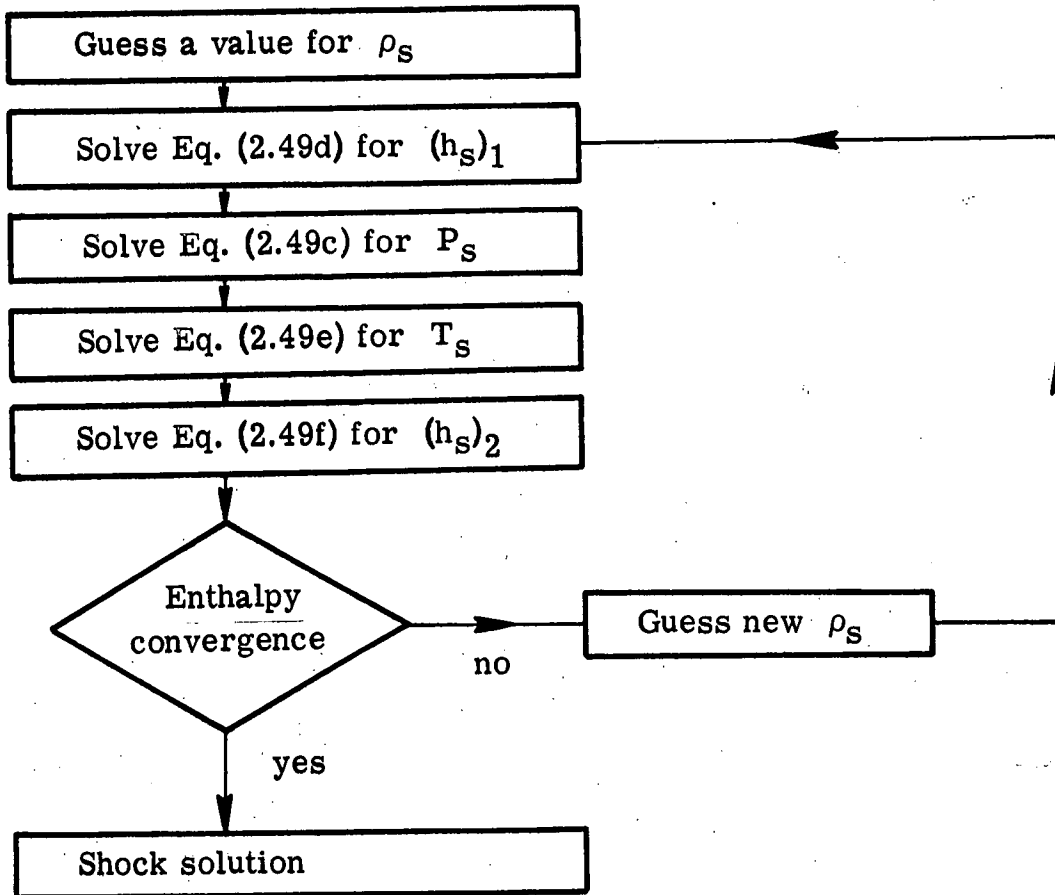
(b) Energy balance at gas-solid interface.

Figure 2.- Surface boundary conditions for mass and energy transfer.



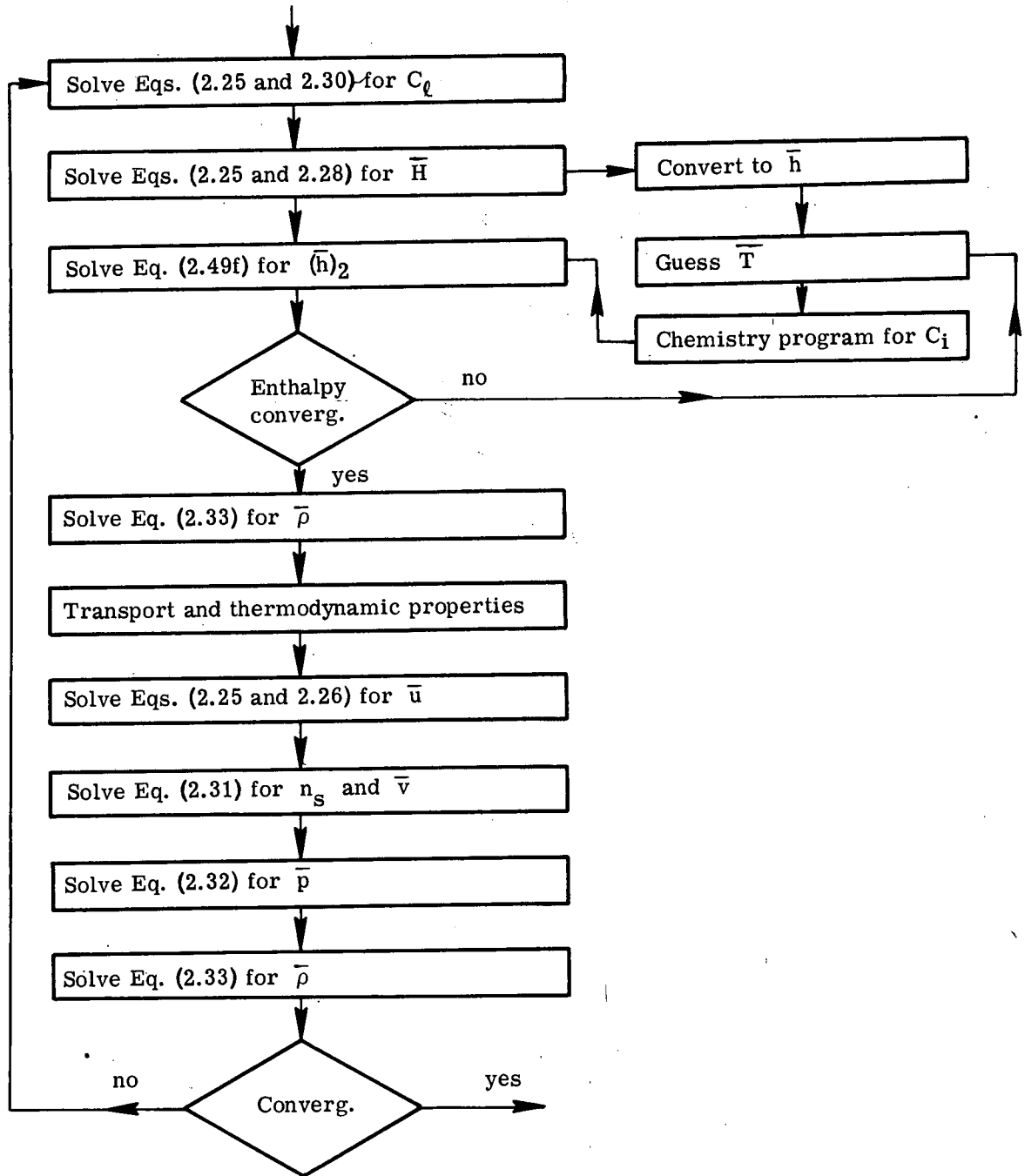
(a) Shock in chemical equilibrium

Figure 3.- Flow chart for shock solution procedure.



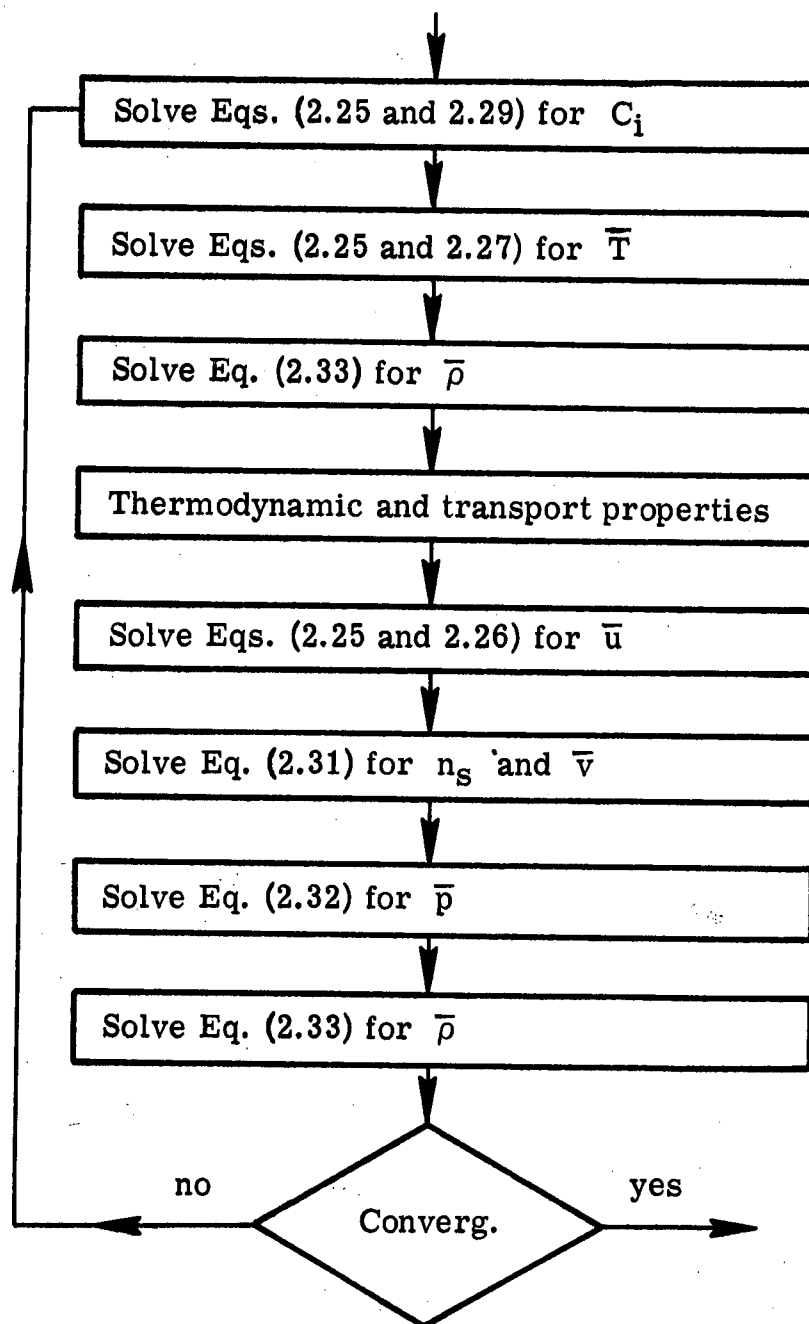
(b) Shock frozen at free stream chemistry.

Figure 3.- Concluded.



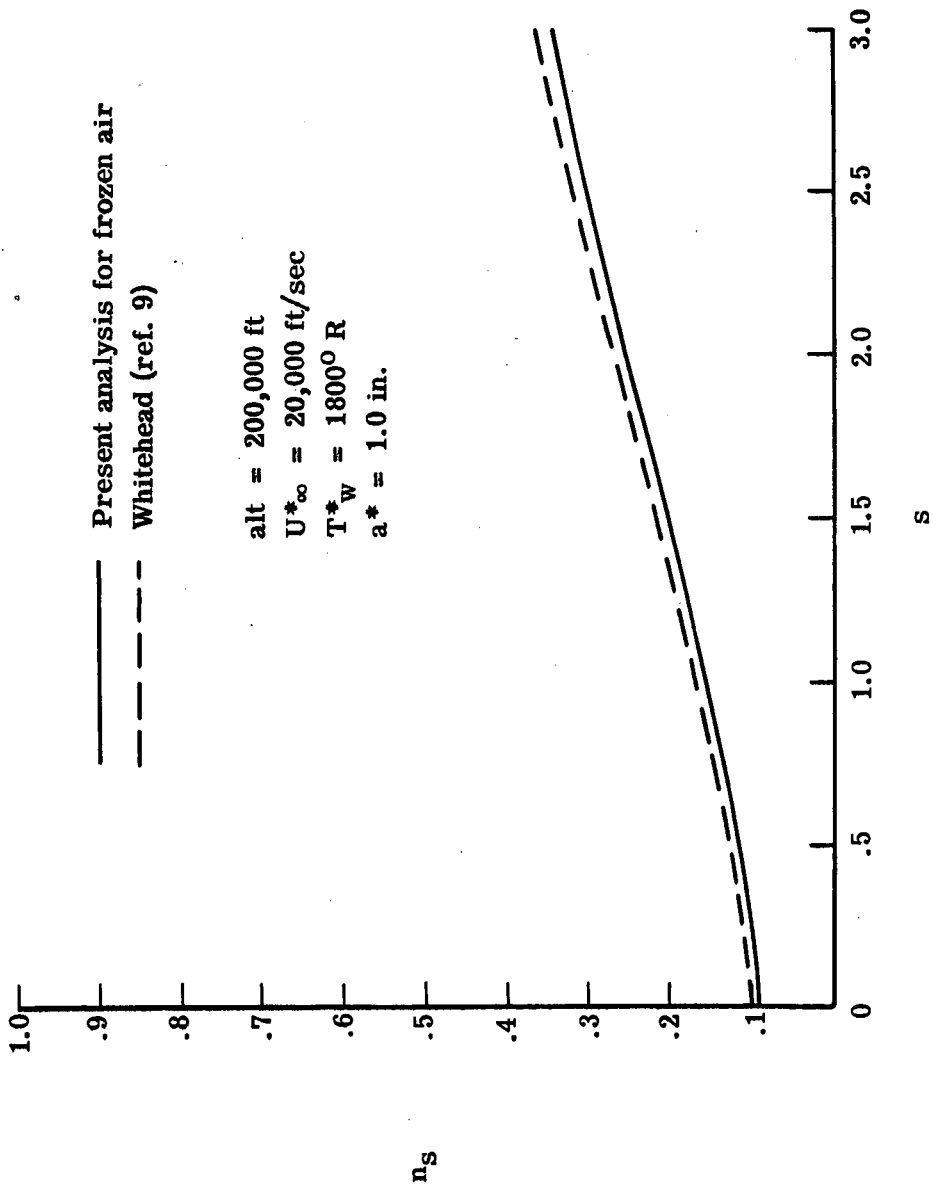
(a) Equilibrium chemistry.

Figure 4.- Flow chart for solution sequence of viscous shock-layer equations.



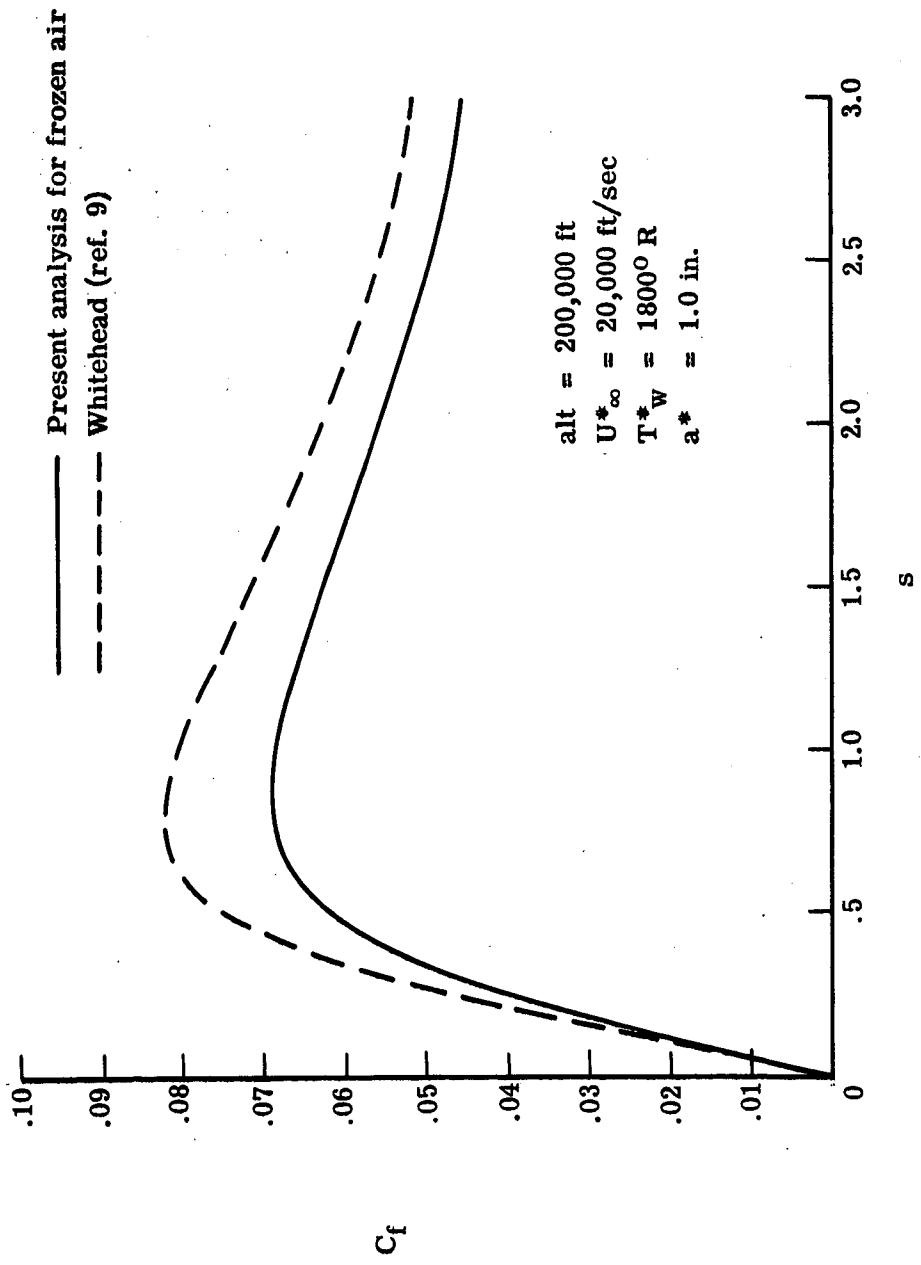
(b) Frozen and nonequilibrium chemistry.

Figure 4.- Concluded.



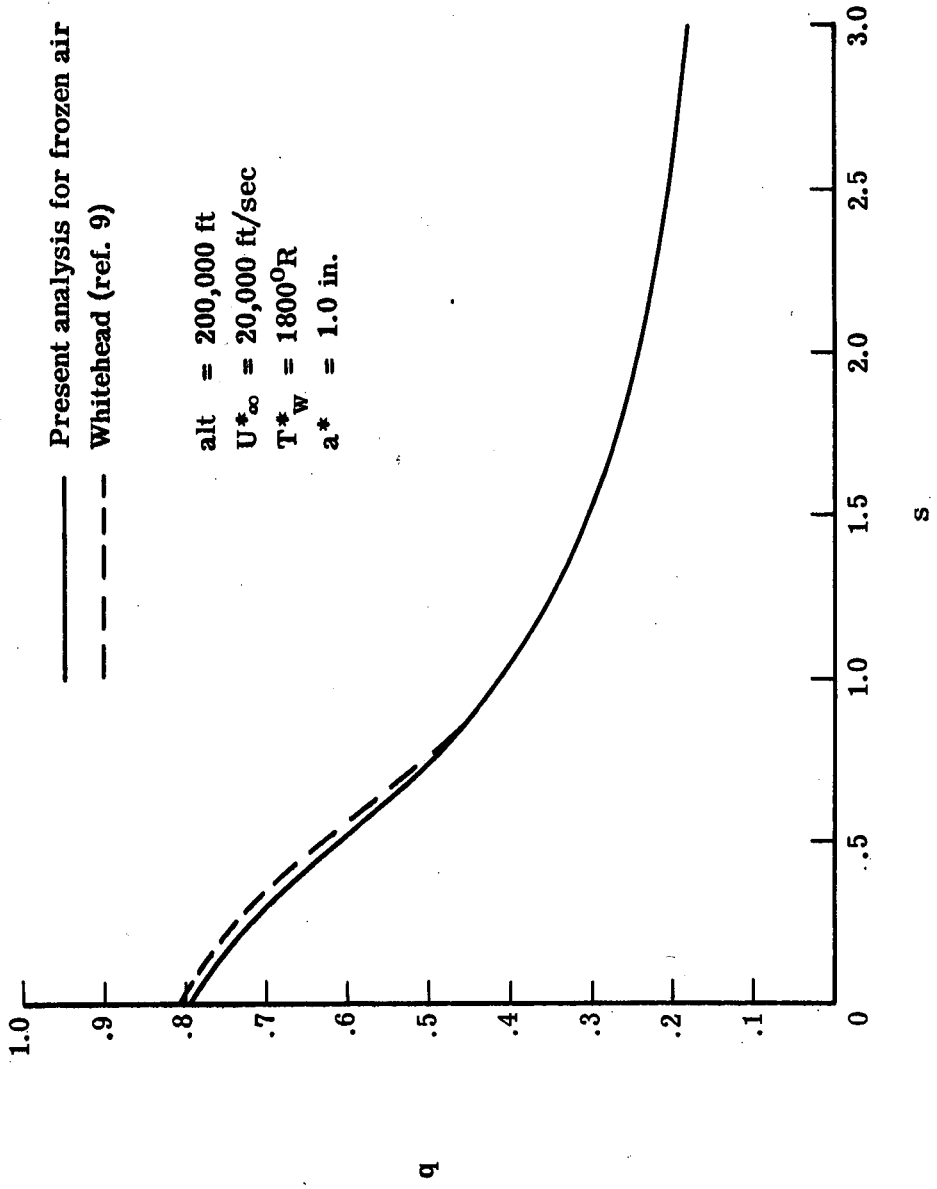
(a) Shock stand-off variation with distance along body surface.

Figure 5.- Comparison of the present calculations with the results of Whitehead for frozen air.



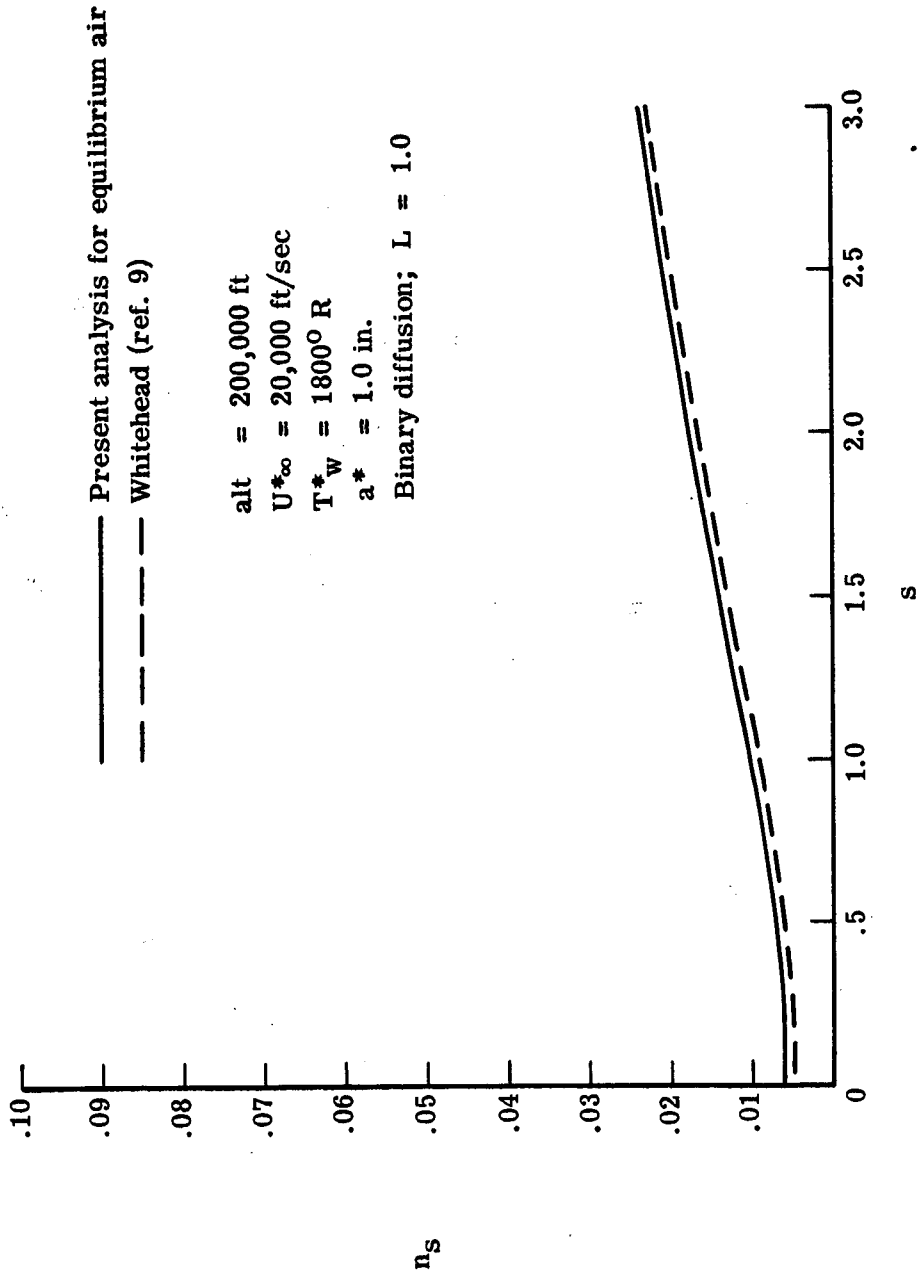
(b) Skin friction variation with distance along body surface.

Figure 5.- Continued.



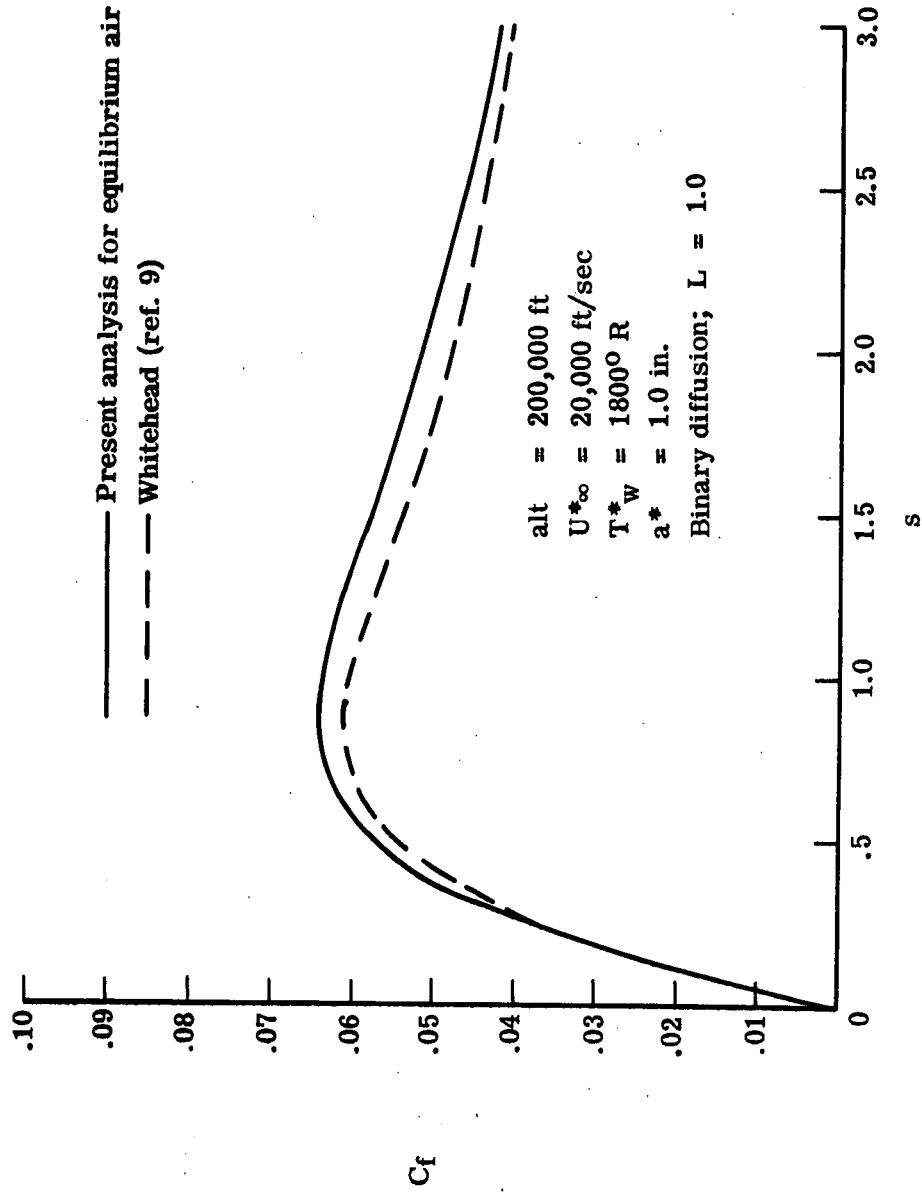
(c) Heat transfer variation with distance along body surface.

Figure 5.- Concluded.



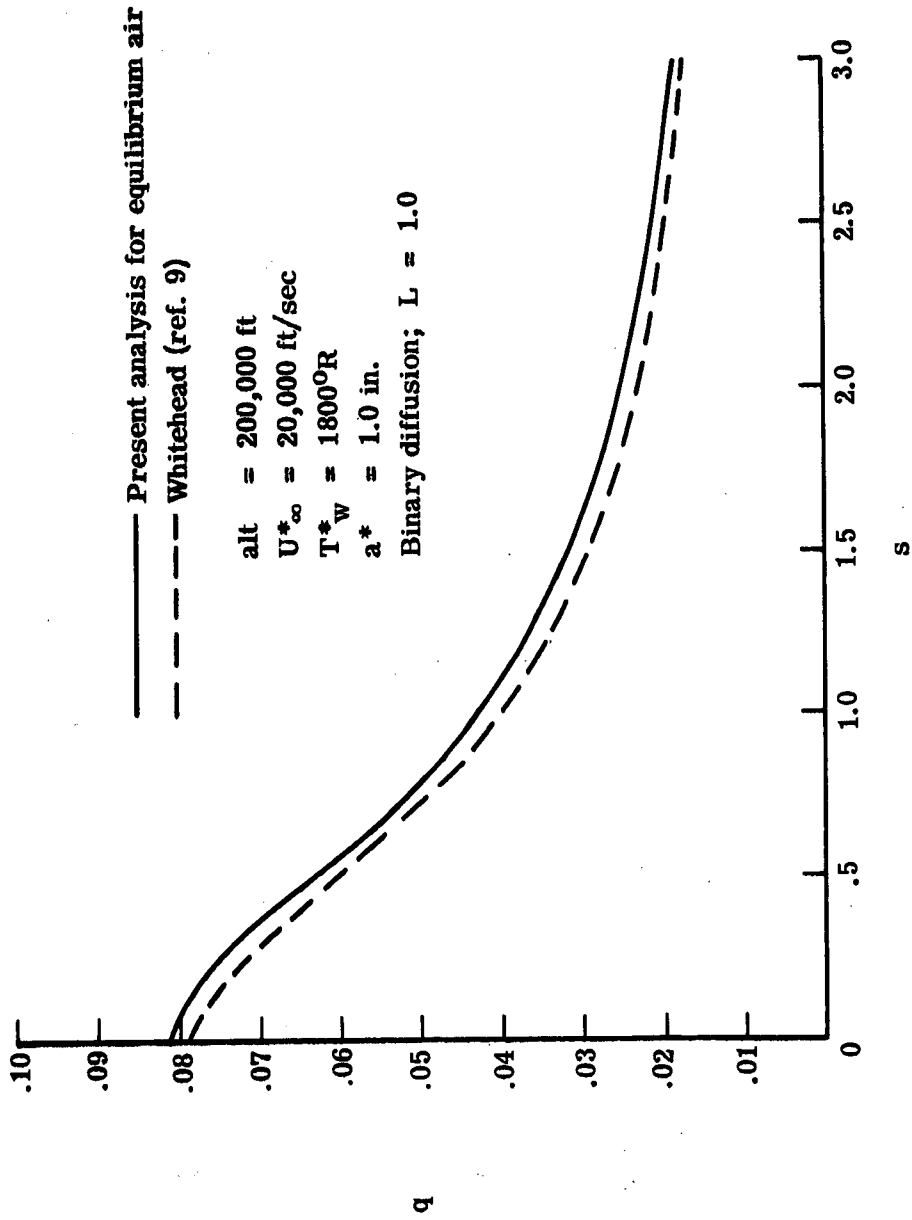
(a) Shock stand-off variation with distance along body surface.

Figure 6.- Comparison of the present calculations with the results of Whitehead for equilibrium air.



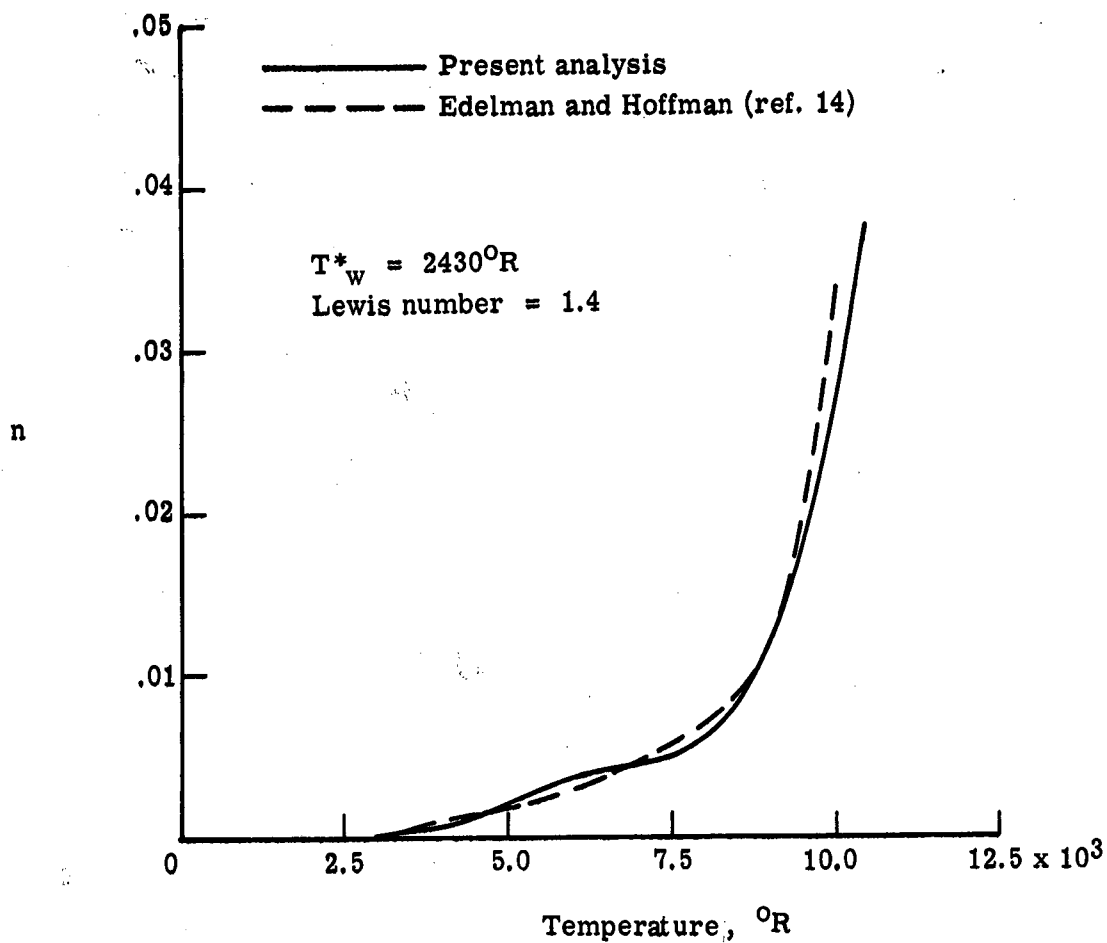
(b) Skin friction variation with distance along body surface.

Figure 6.- Continued.



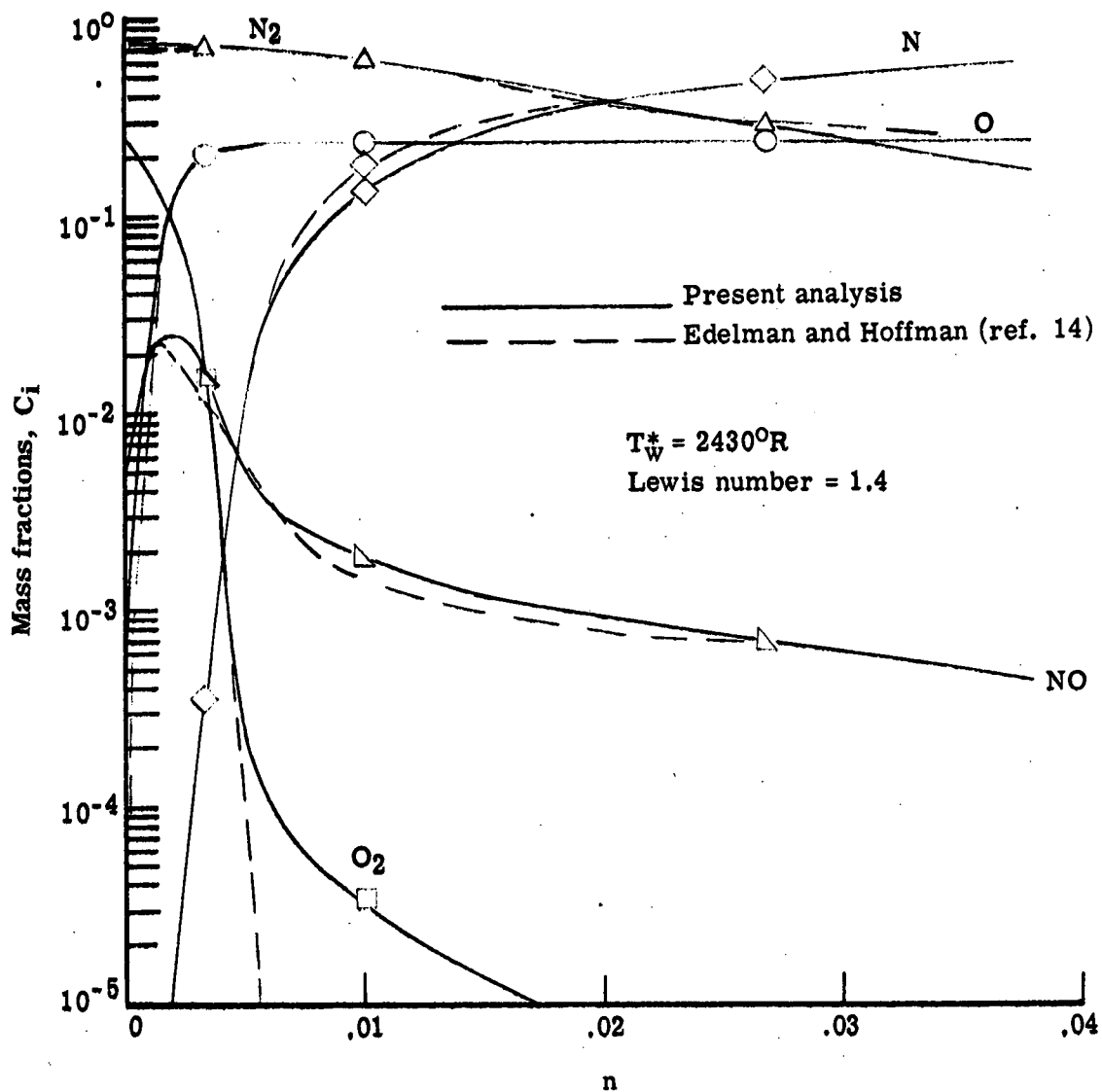
(c) Heat transfer variation with distance along body surface.

Figure 6.- Concluded.



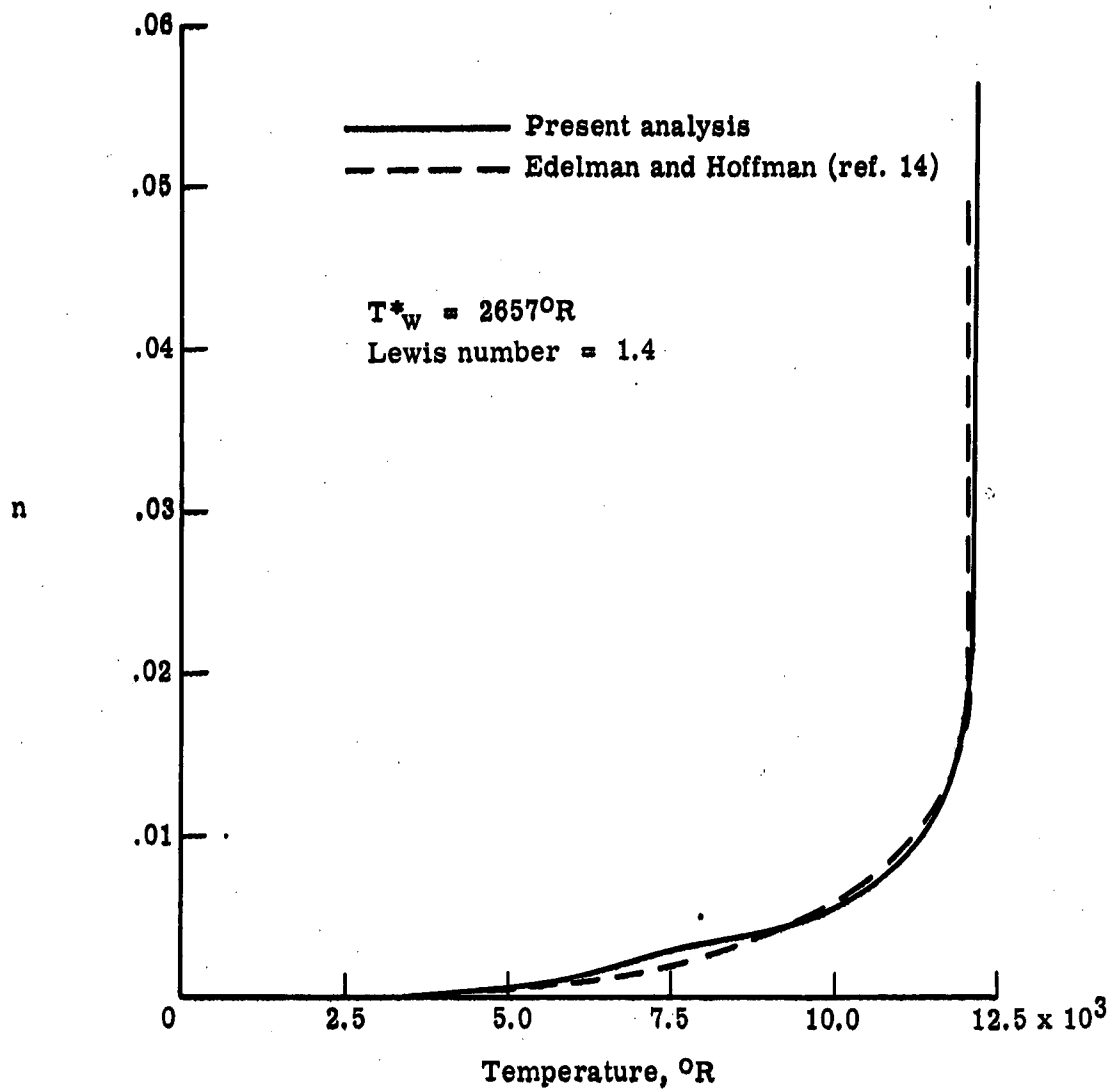
(a) Stagnation temperature profiles for alt = 280,000 ft, $U^*_{\infty} = 26,000$ ft/sec, and $a^* = 12$ in.

Figure 7.- Comparison of the present calculations with the stagnation results of Edelman and Hoffman for equilibrium air.



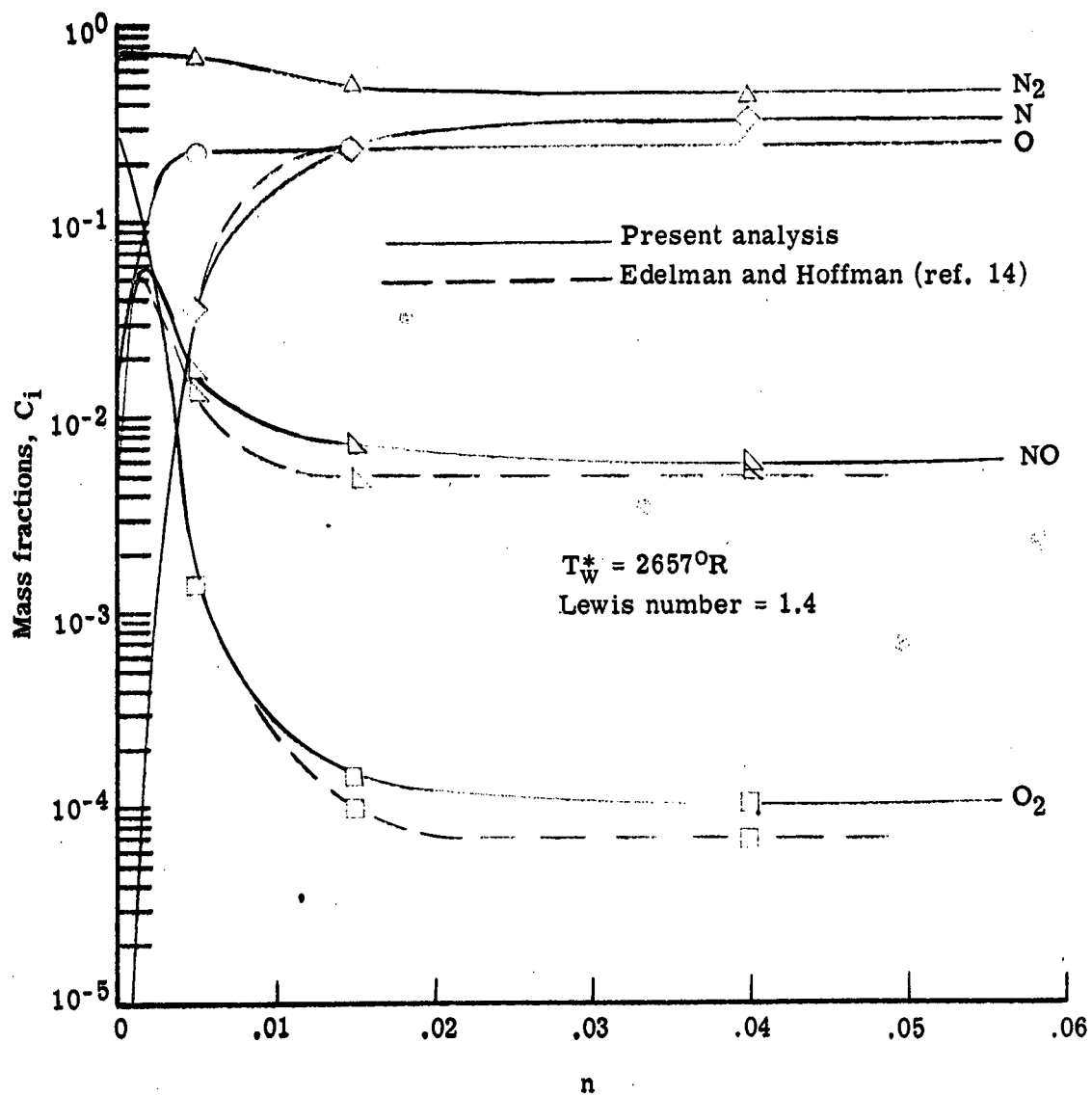
(b) Stagnation species profiles for alt = 280,000 ft,
 $U_\infty^* = 26,000$ ft/sec, and $a^* = 12$ in.

Figure 7.- Continued.



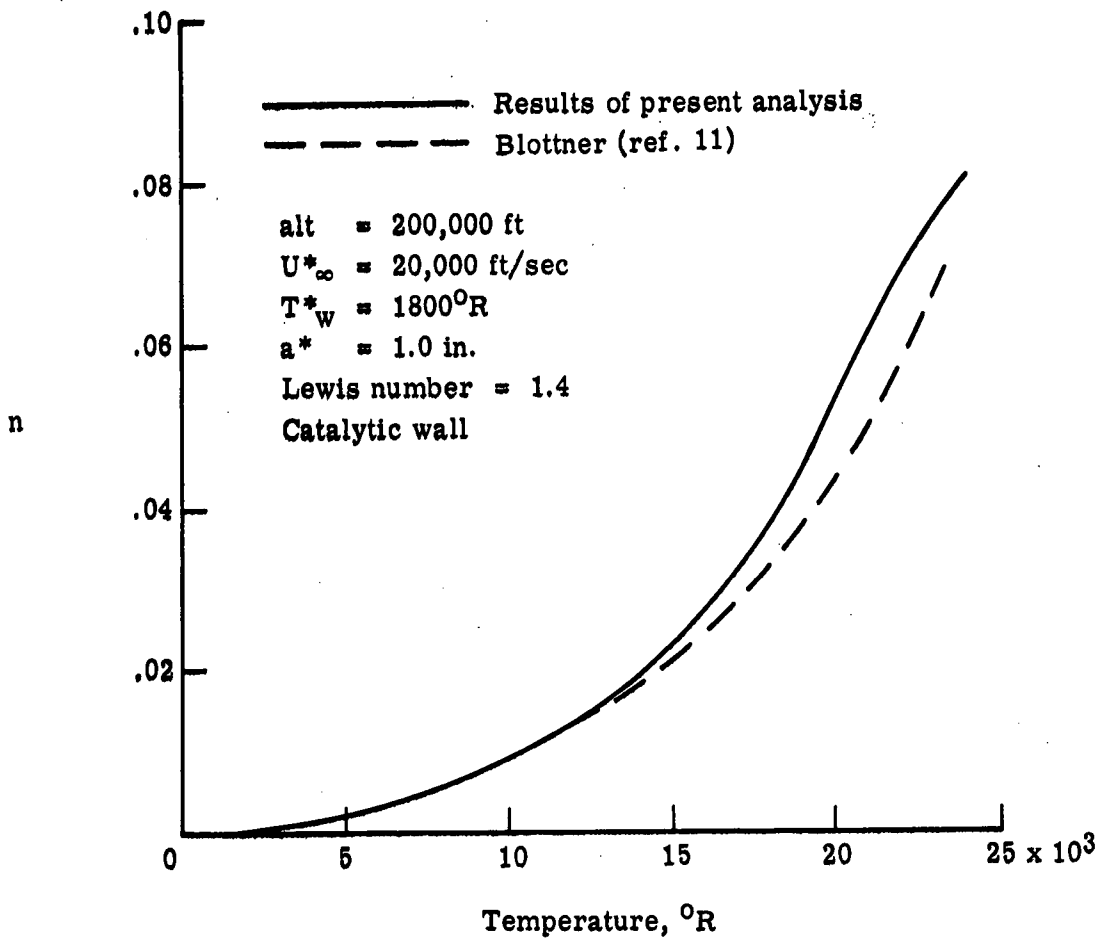
(c) Stagnation temperature profiles for alt = 150,000 ft, $U^*_\infty = 22,520$ ft/sec, and $a^* = 0.5$ in.

Figure 7.- Continued.



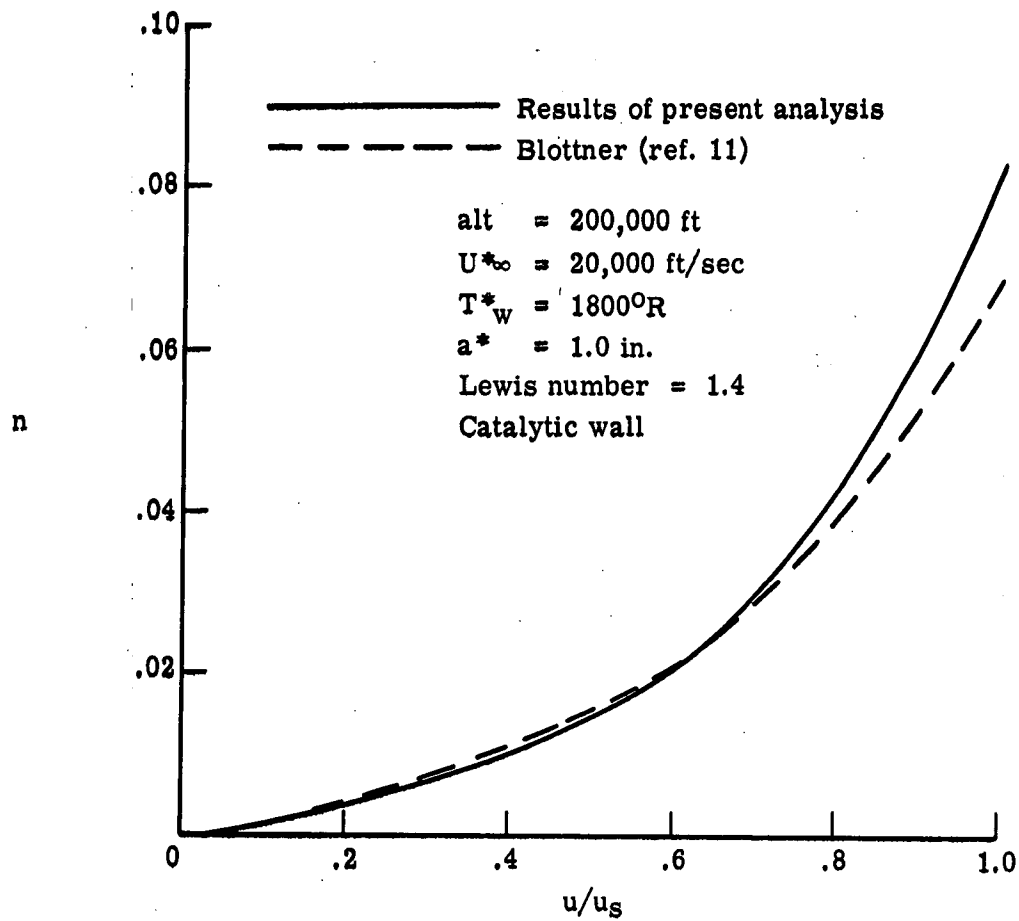
(d) Stagnation species profiles for alt = 150,000 ft,
 $U_\infty^* = 22,520$ ft/sec, and $a^* = 0.5$ in.

Figure 7. - Concluded.



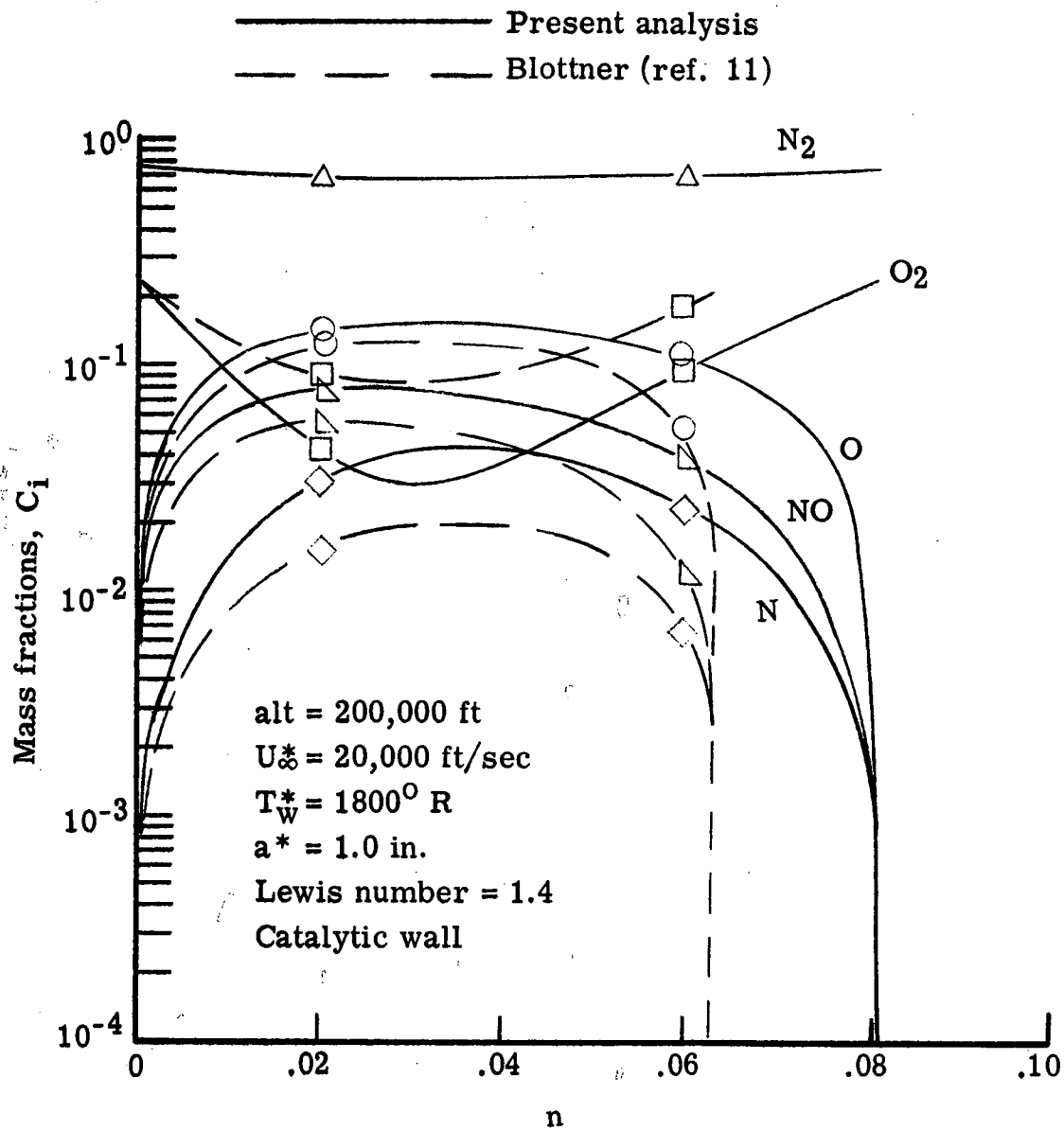
(a) Stagnation temperature profiles.

Figure 8.- Comparison of the present calculations with the stagnation results of Blottner for nonequilibrium air.



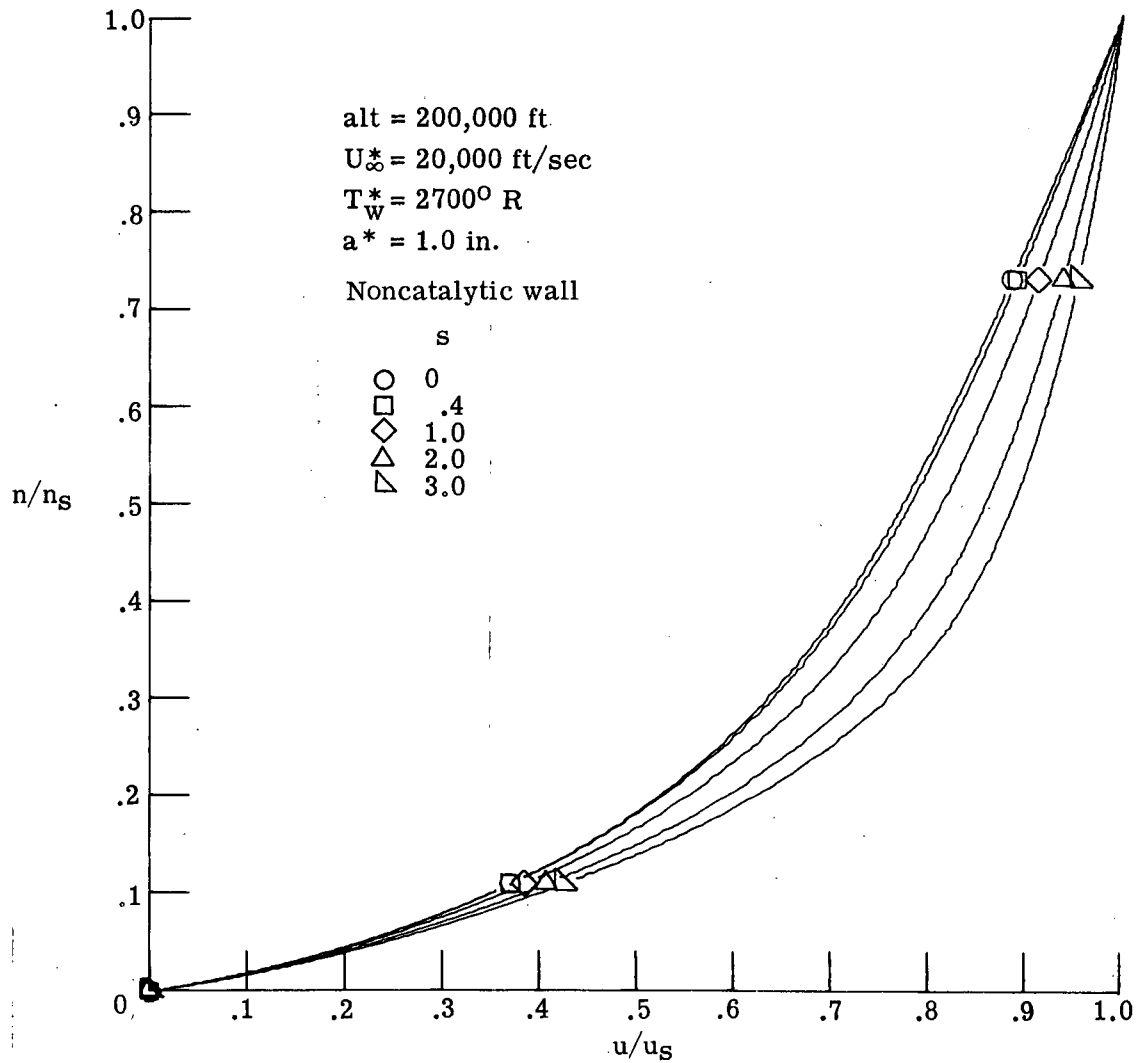
(b) Stagnation velocity ratio profiles.

Figure 8.- Continued.



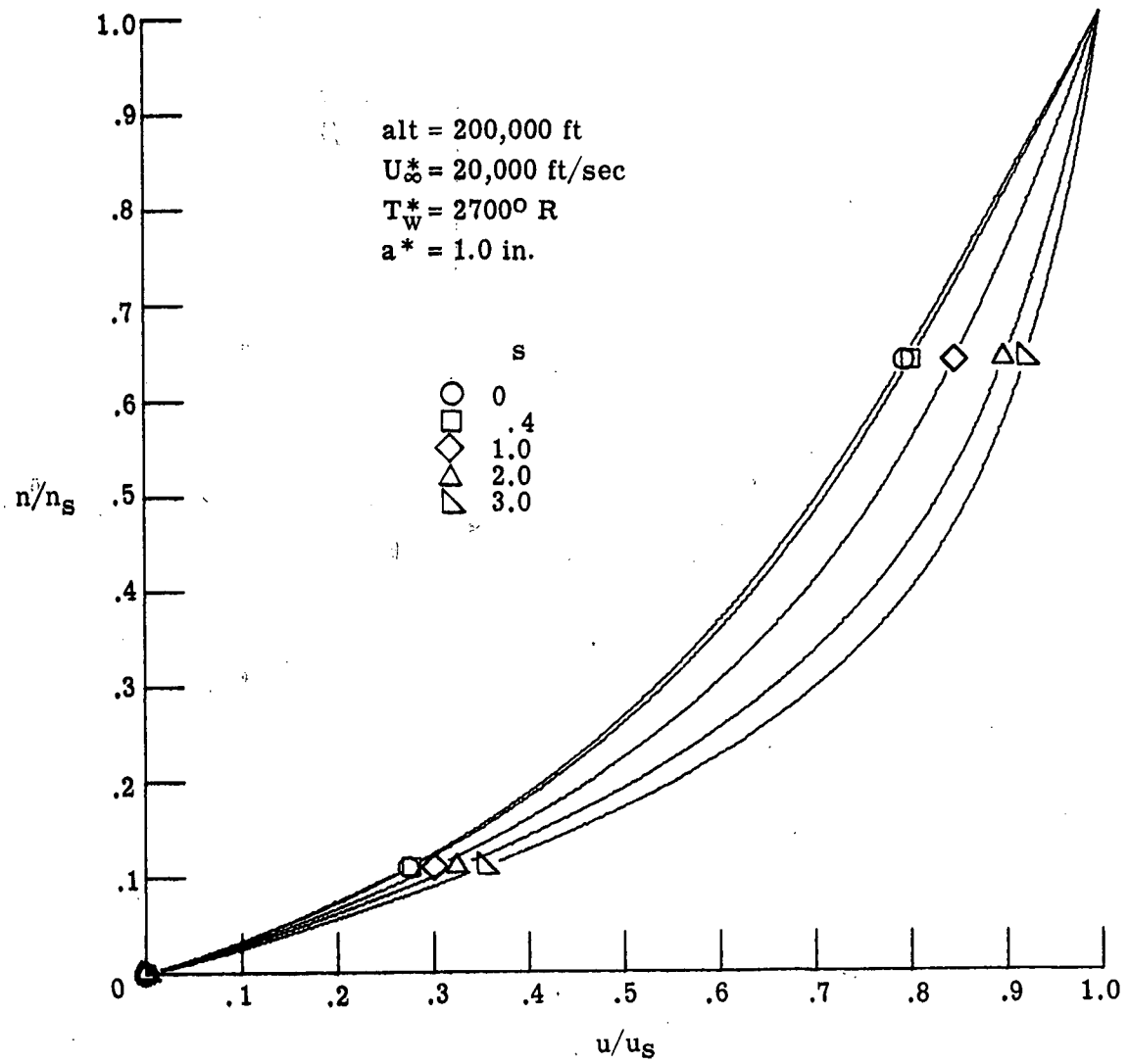
(c) Stagnation species profiles.

Figure 8.- Concluded.



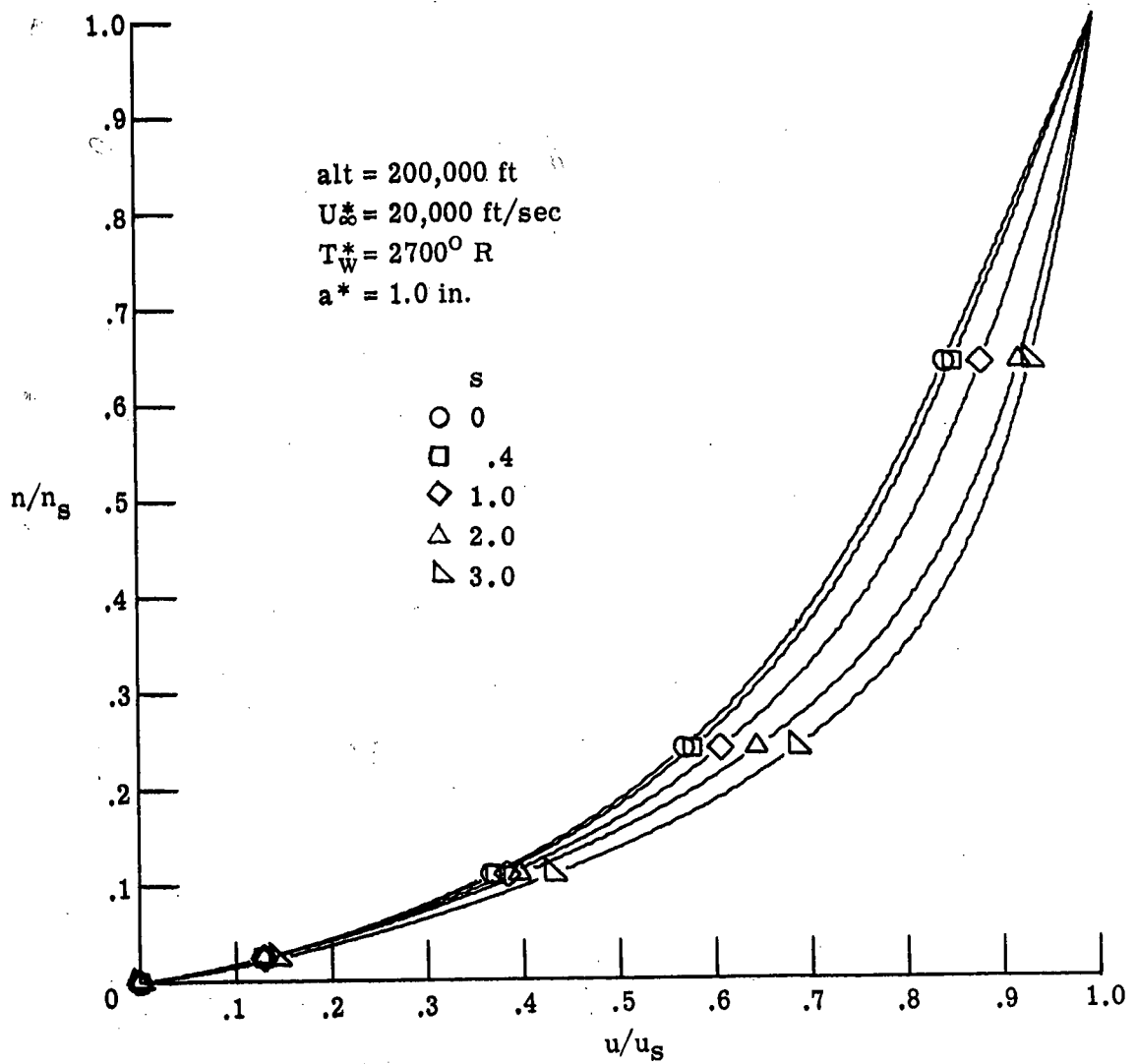
(a) Nonequilibrium chemistry.

Figure 9.- Velocity profiles for reacting and nonreacting air with multi-component diffusion and no mass injection.



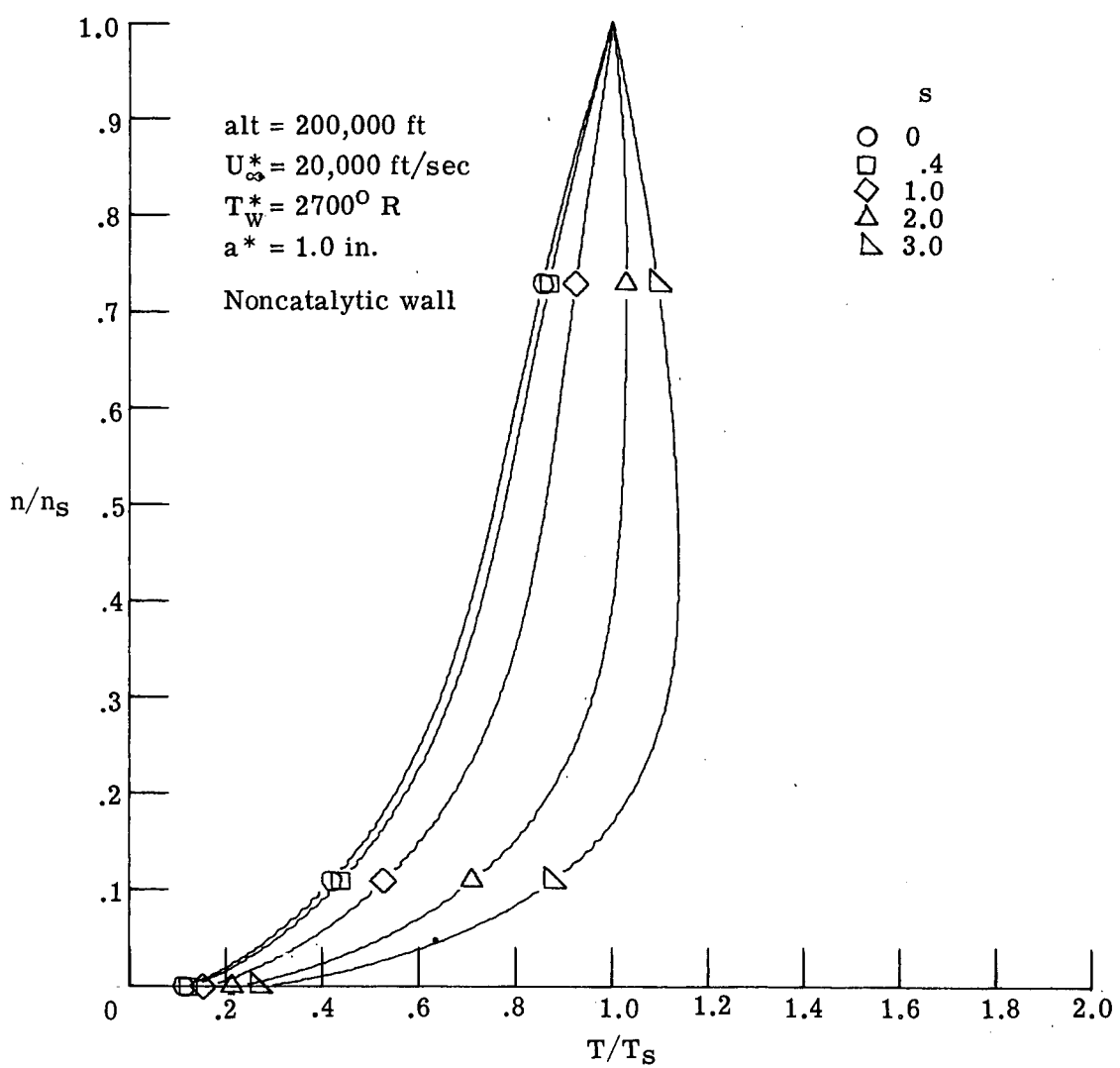
(b) Equilibrium chemistry.

Figure 9. - Continued.



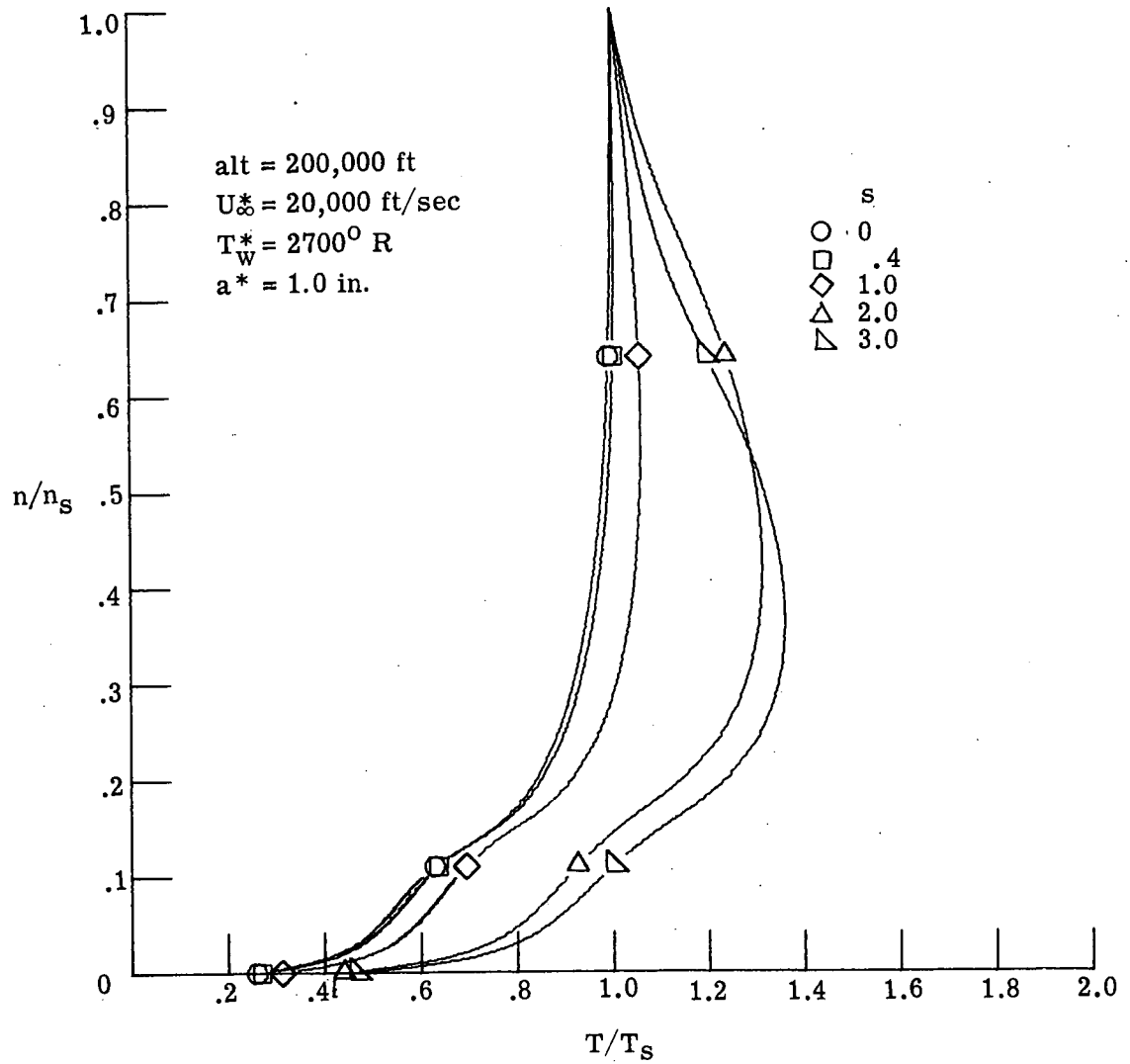
(c) Frozen chemistry.

Figure 9. - Concluded.



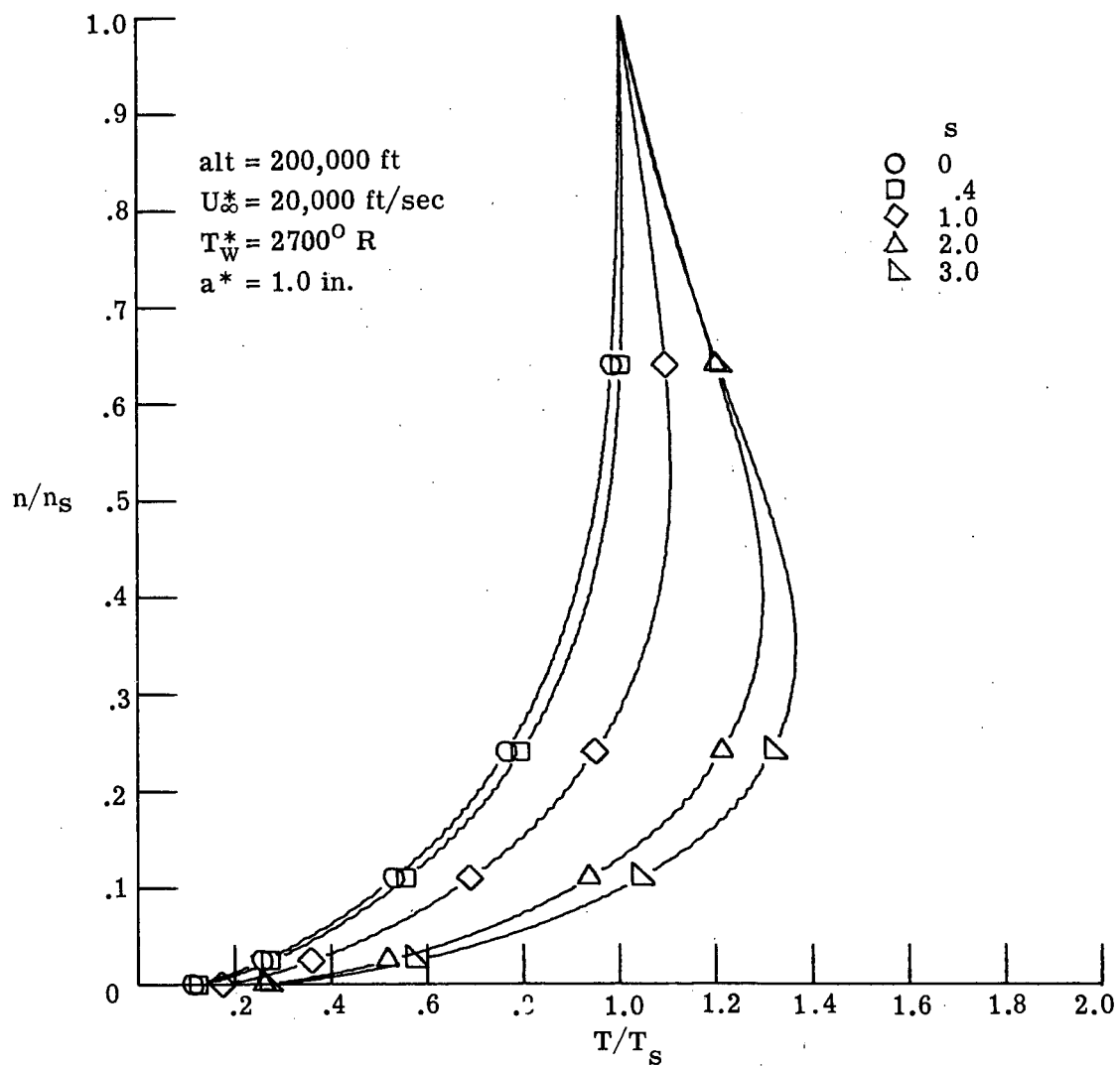
(a) Nonequilibrium chemistry.

Figure 10.- Temperature profiles for air with multicomponent diffusion and no mass injection.



(b) Equilibrium chemistry.

Figure 10.- Continued.



(c) Frozen chemistry.

Figure 10.- Concluded.

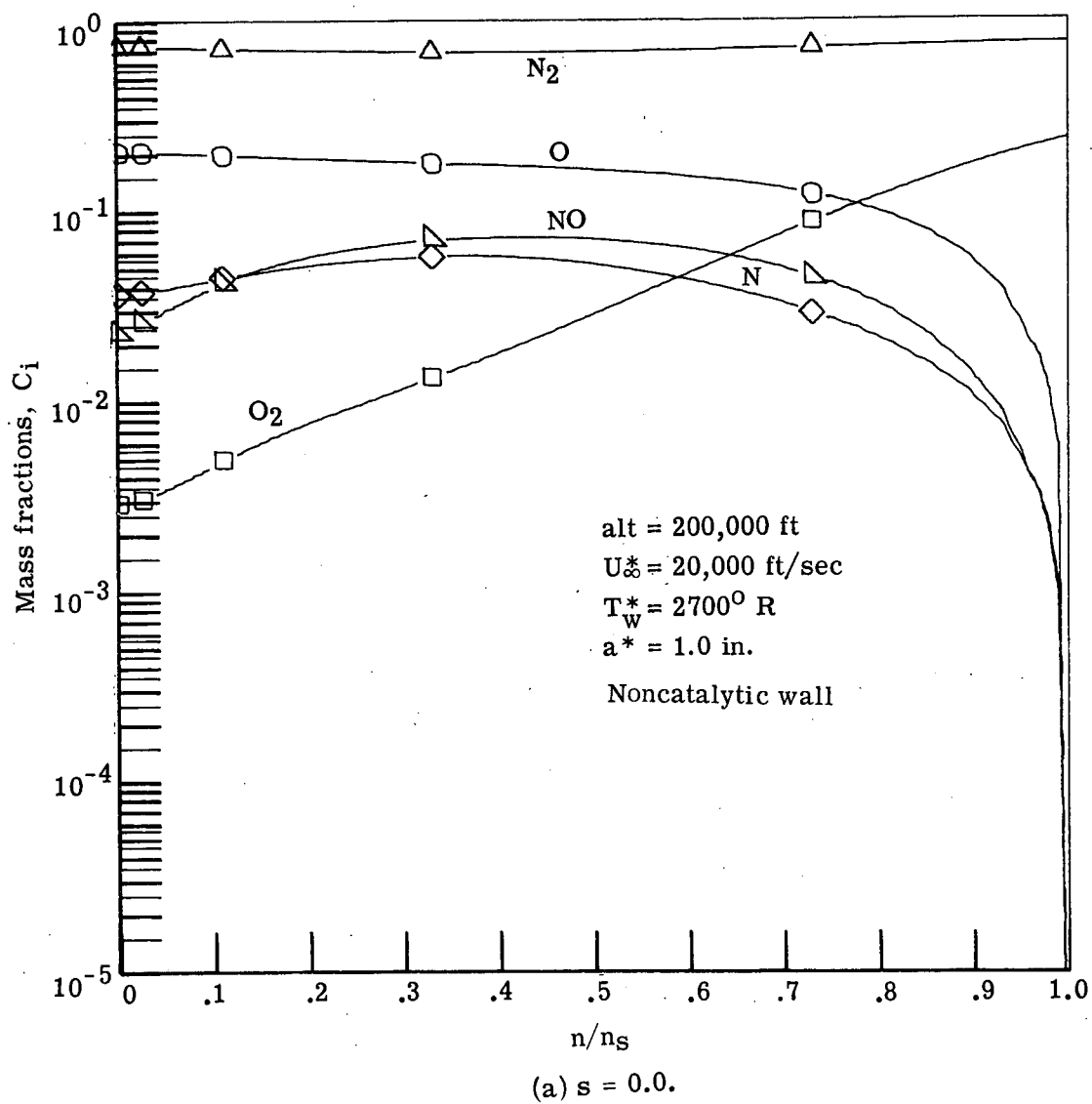


Figure 11.- Species profiles for nonequilibrium air with multi-component diffusion and no mass injection.

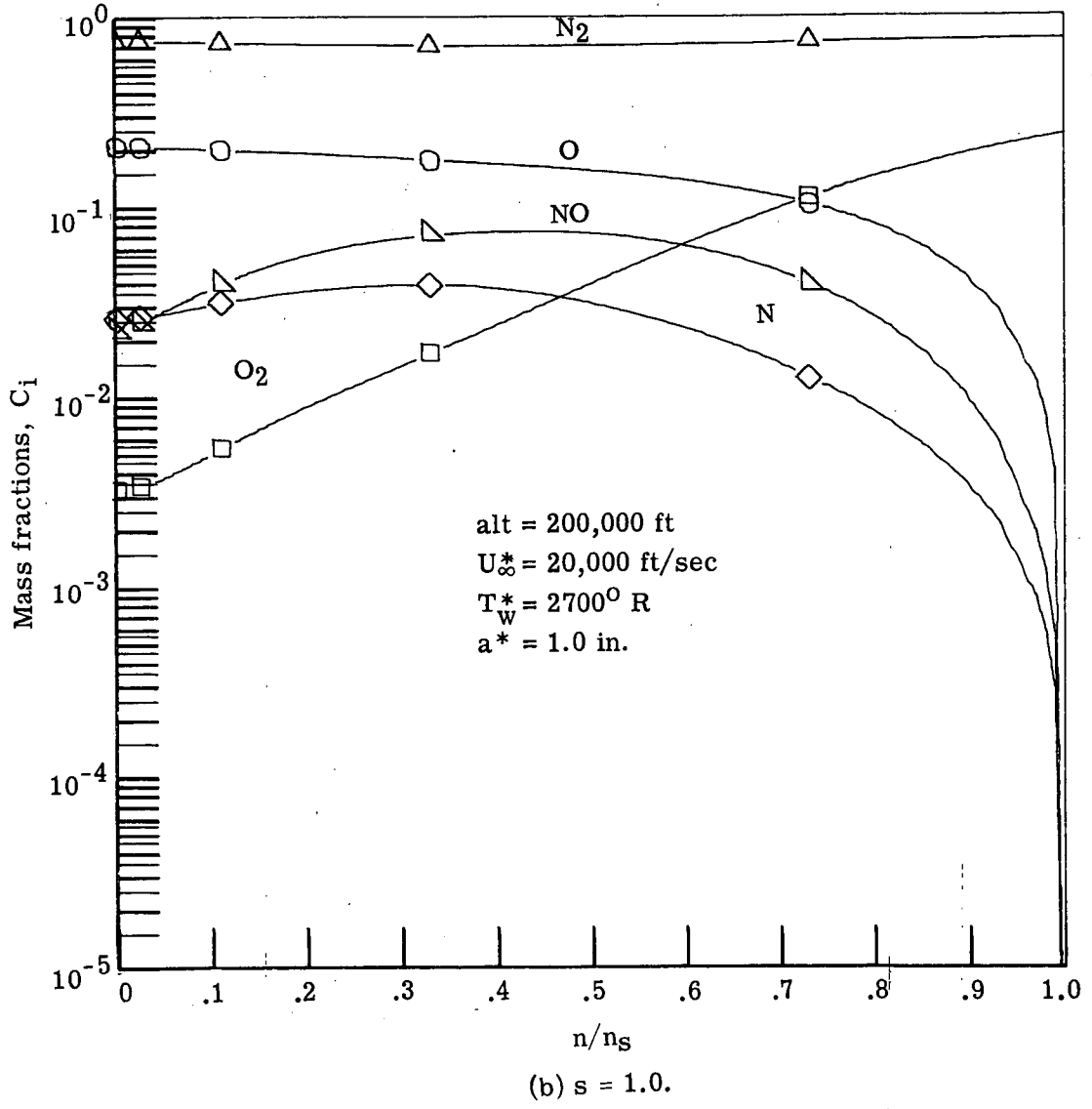


Figure 11.- Continued.

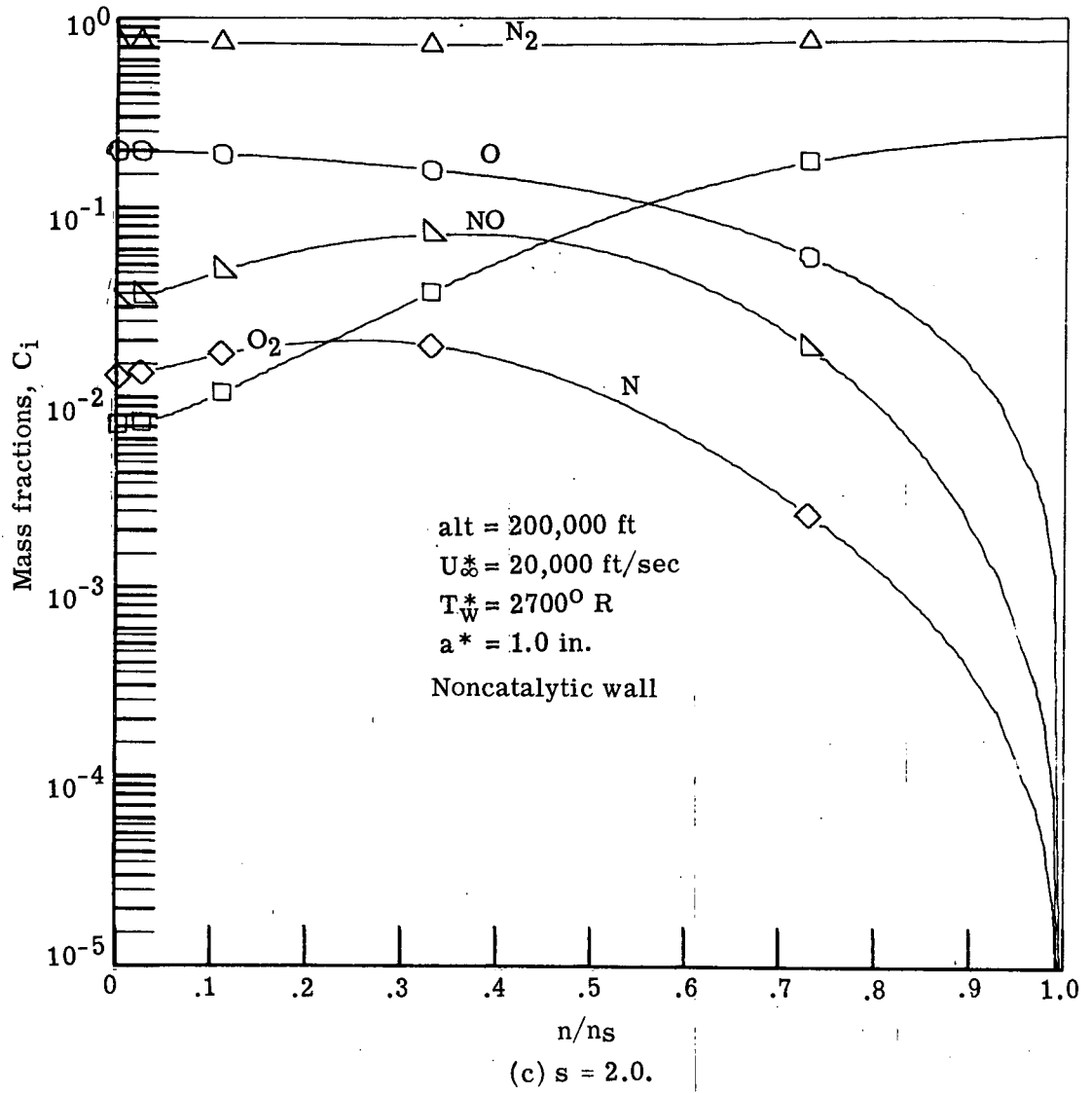
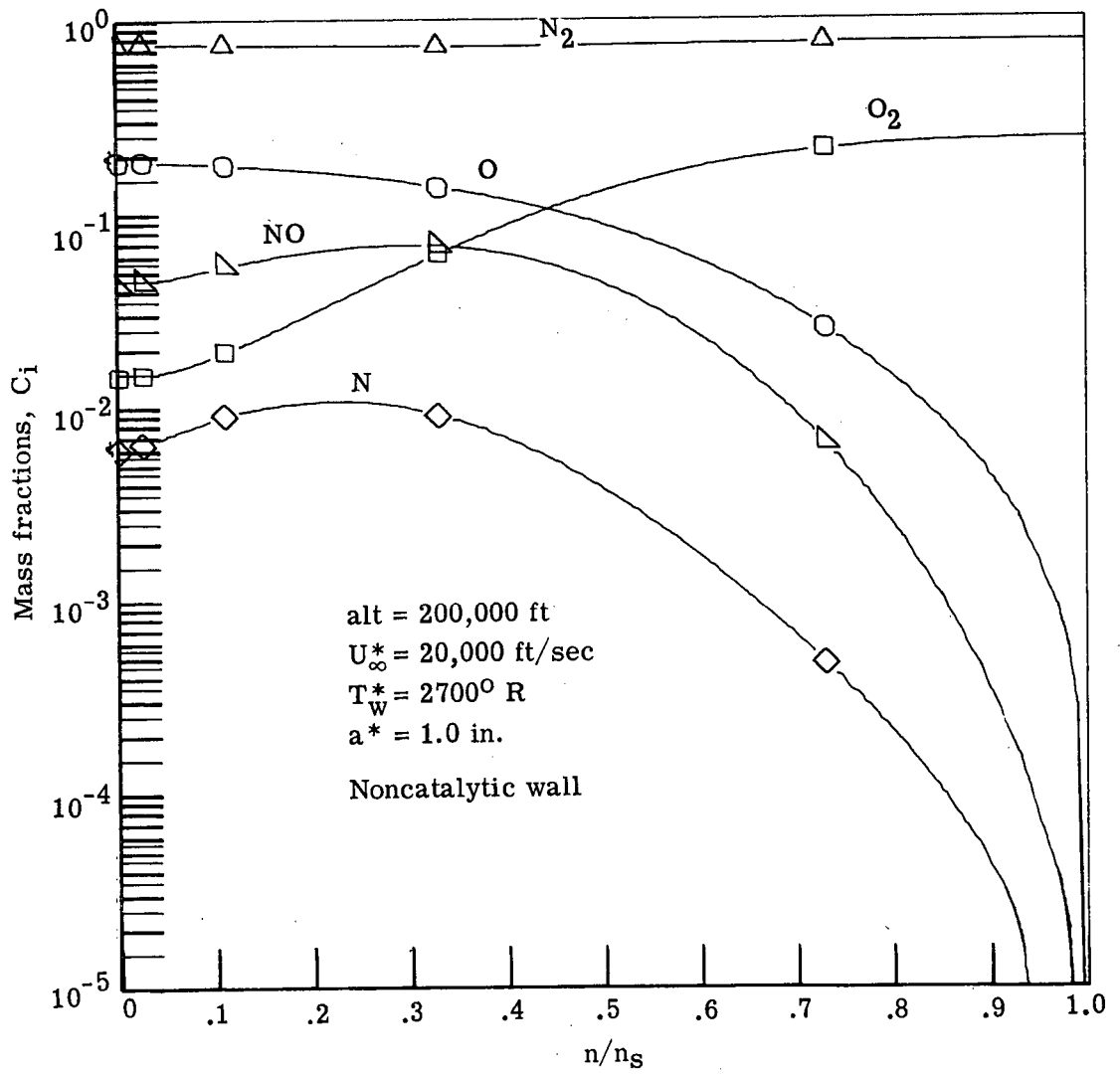


Figure 11. - Continued.



(d) $s = 3.0$.

Figure 11.- Concluded.

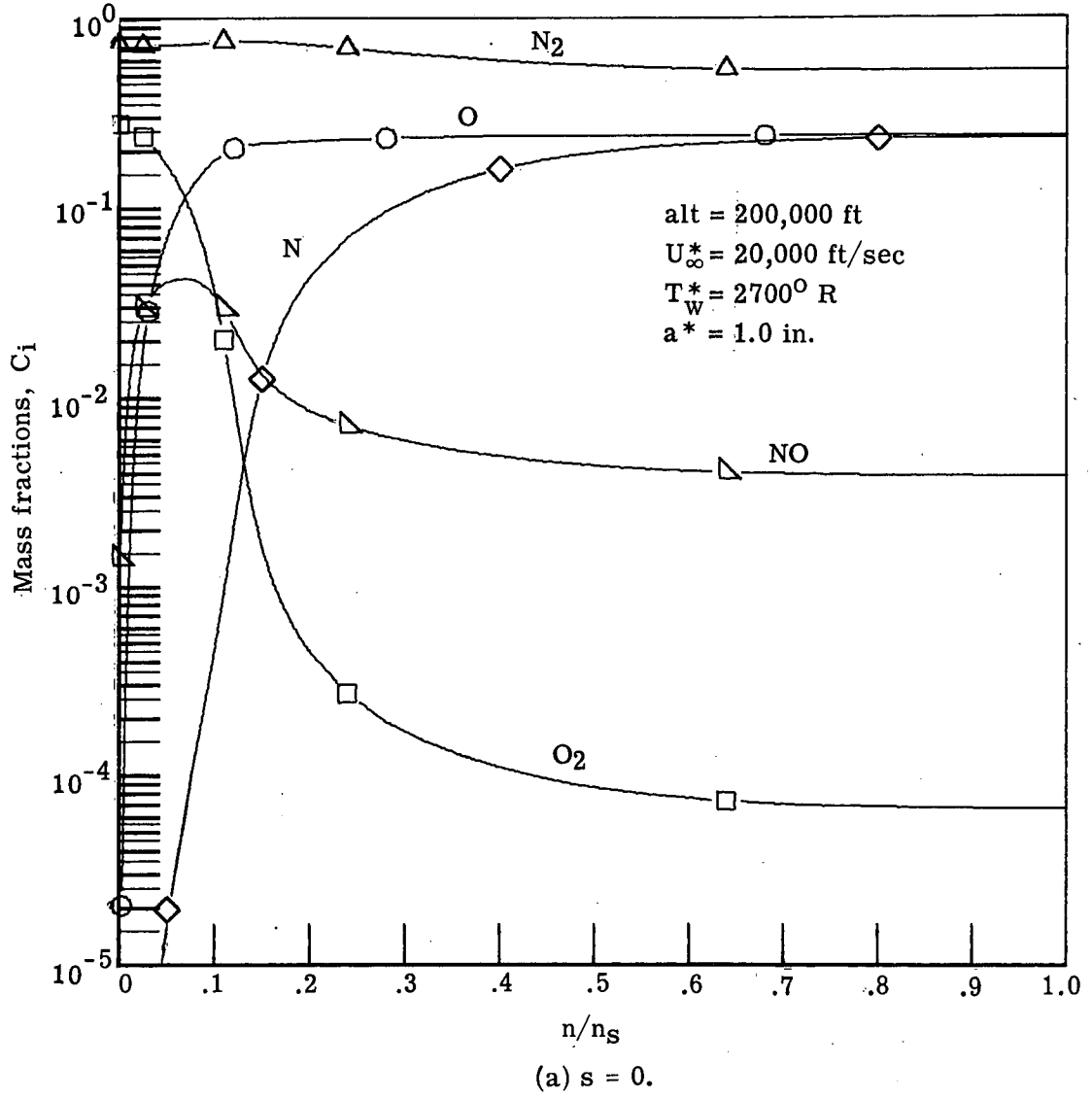


Figure 12.- Species profiles for equilibrium air with multi-component diffusion and no mass injection.

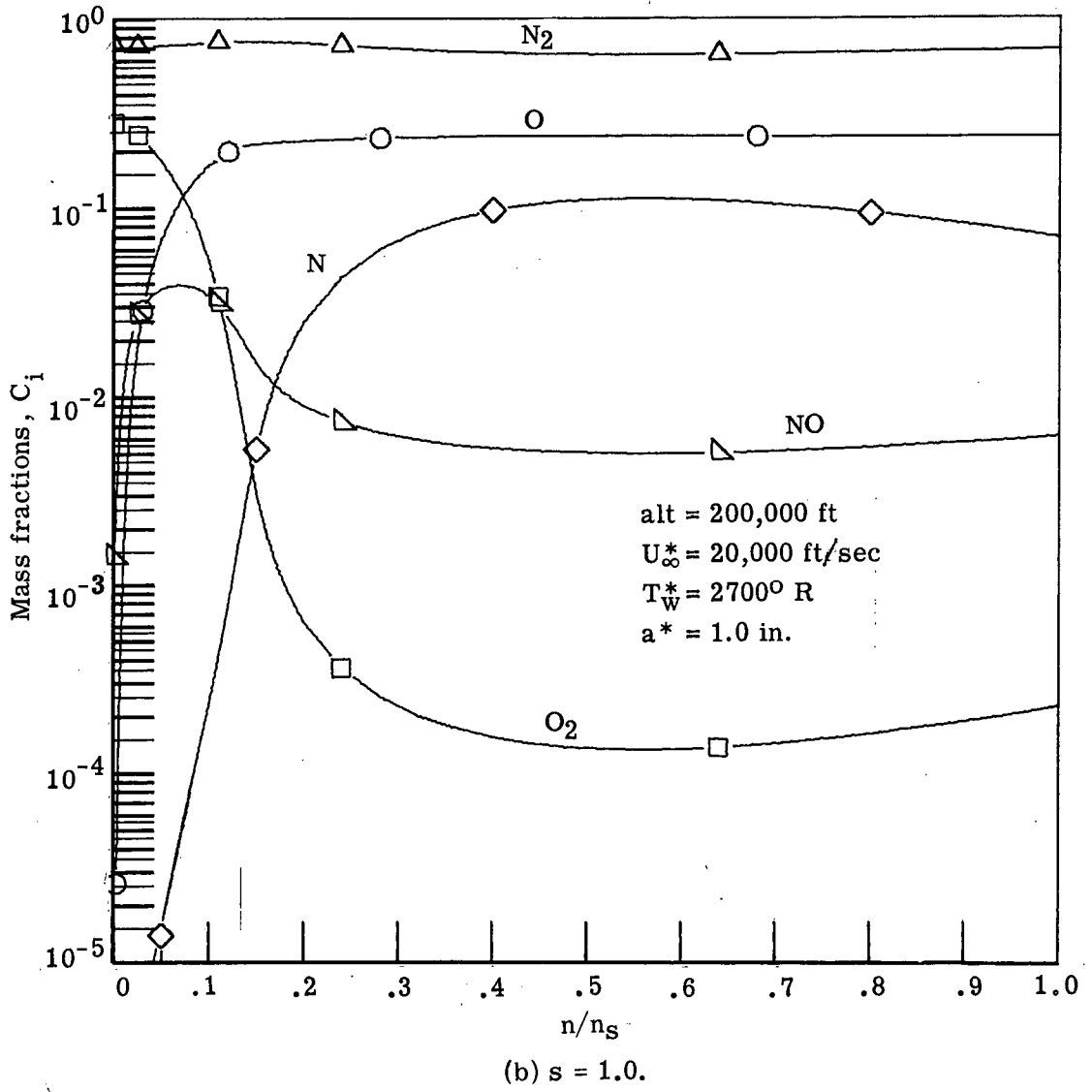
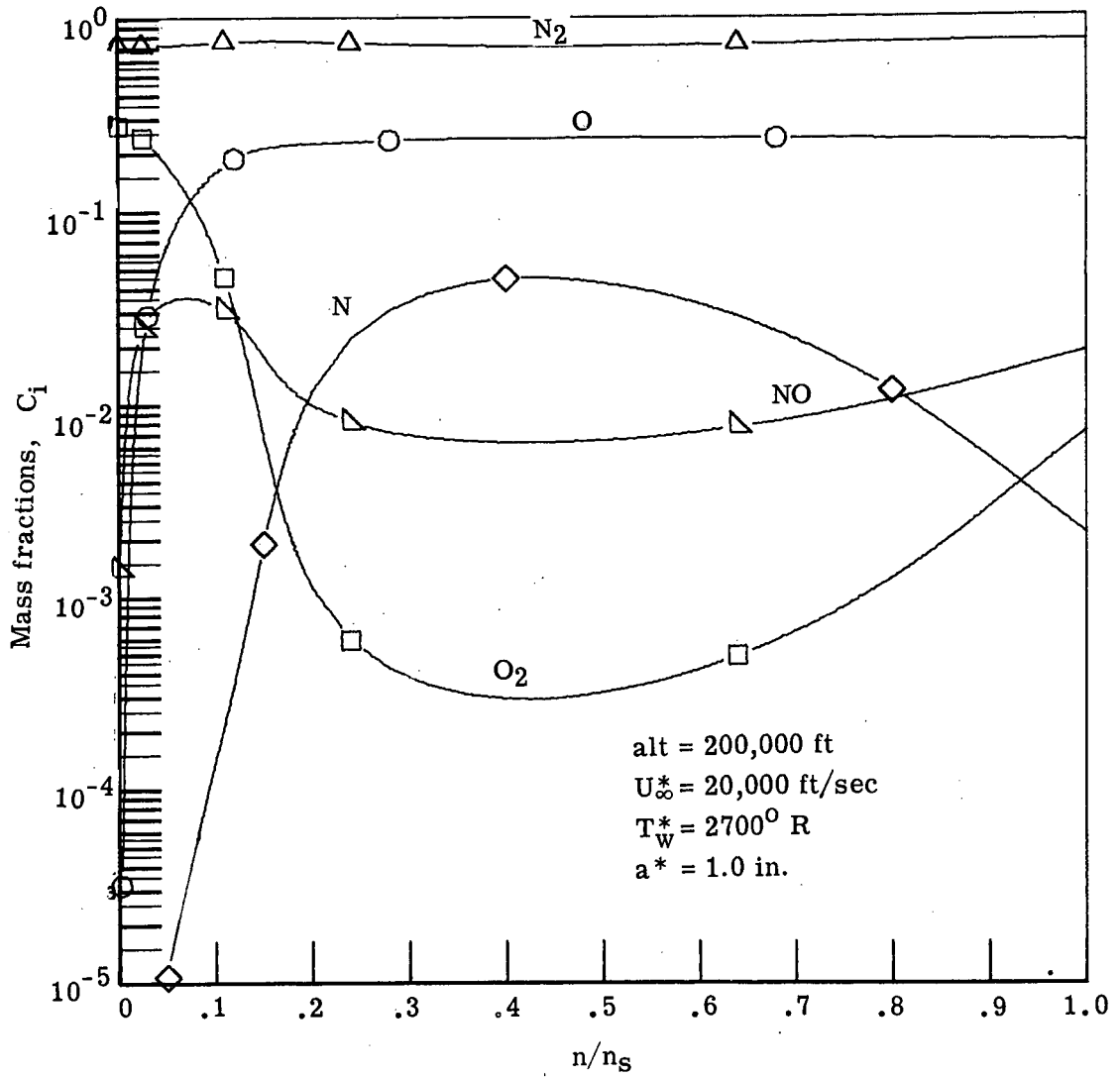
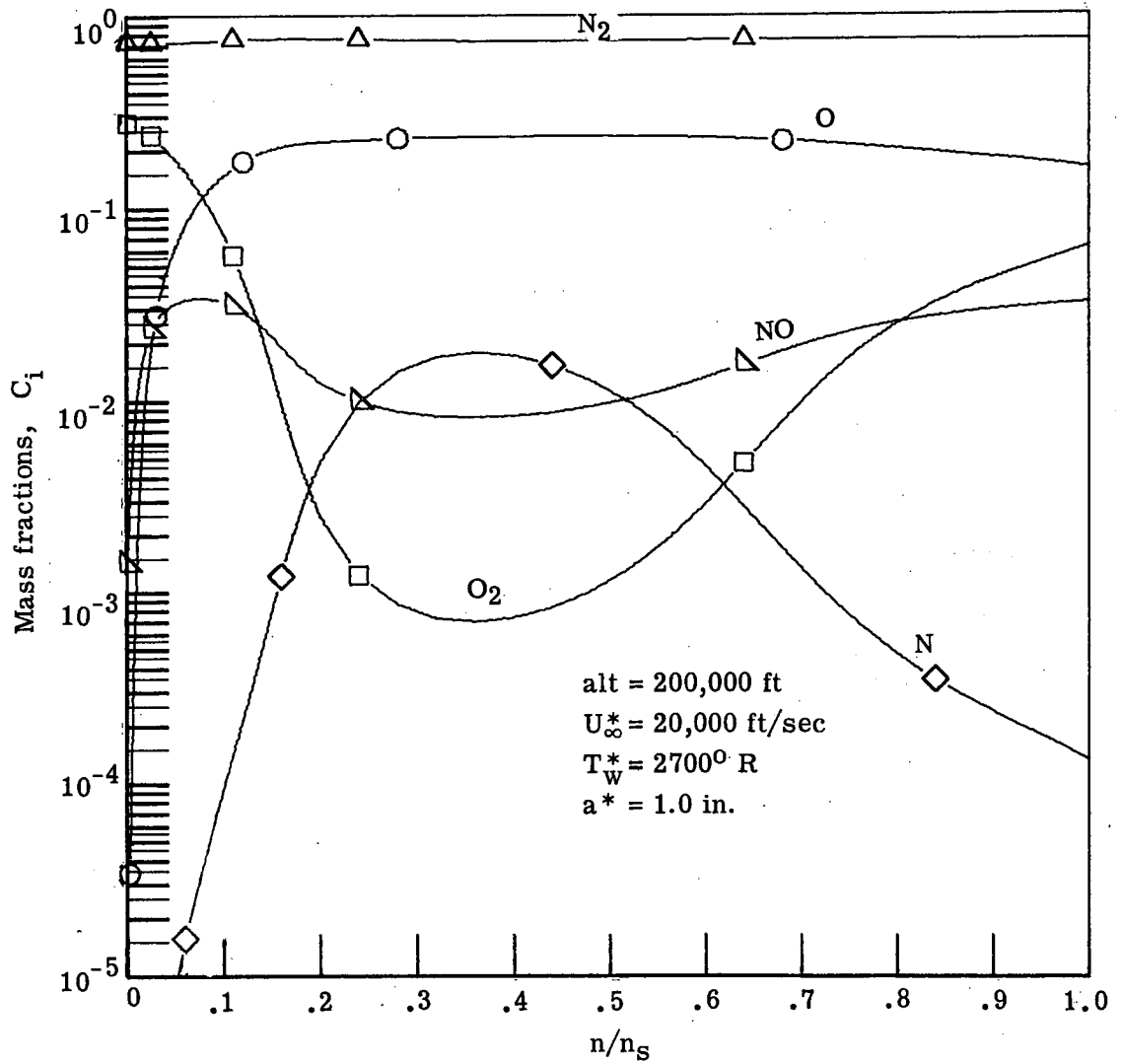


Figure 12.- Continued.



(c) $s = 2.0$

Figure 12. - Continued.



(d) $s = 3.0$.

Figure 12.- Concluded.

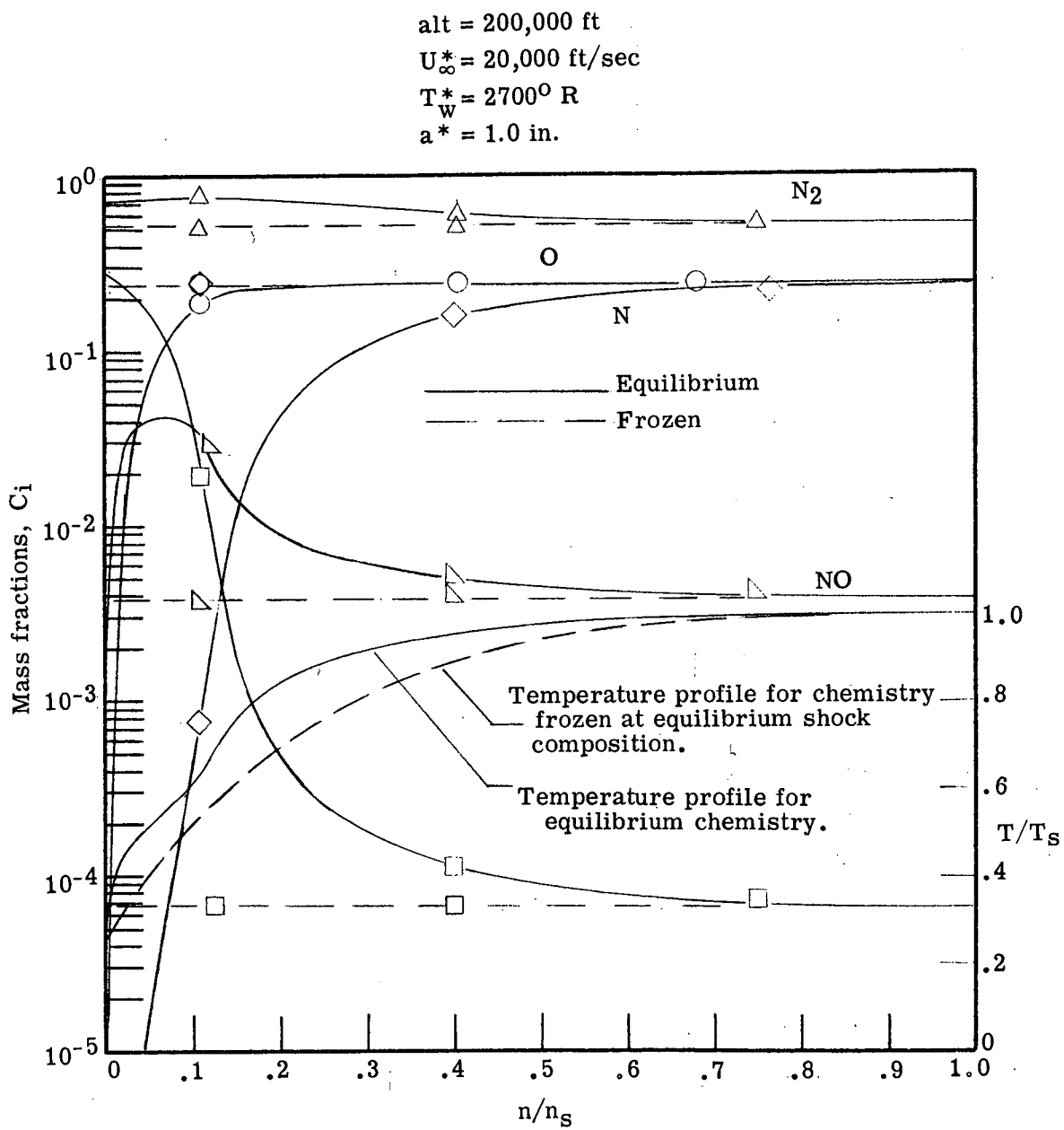
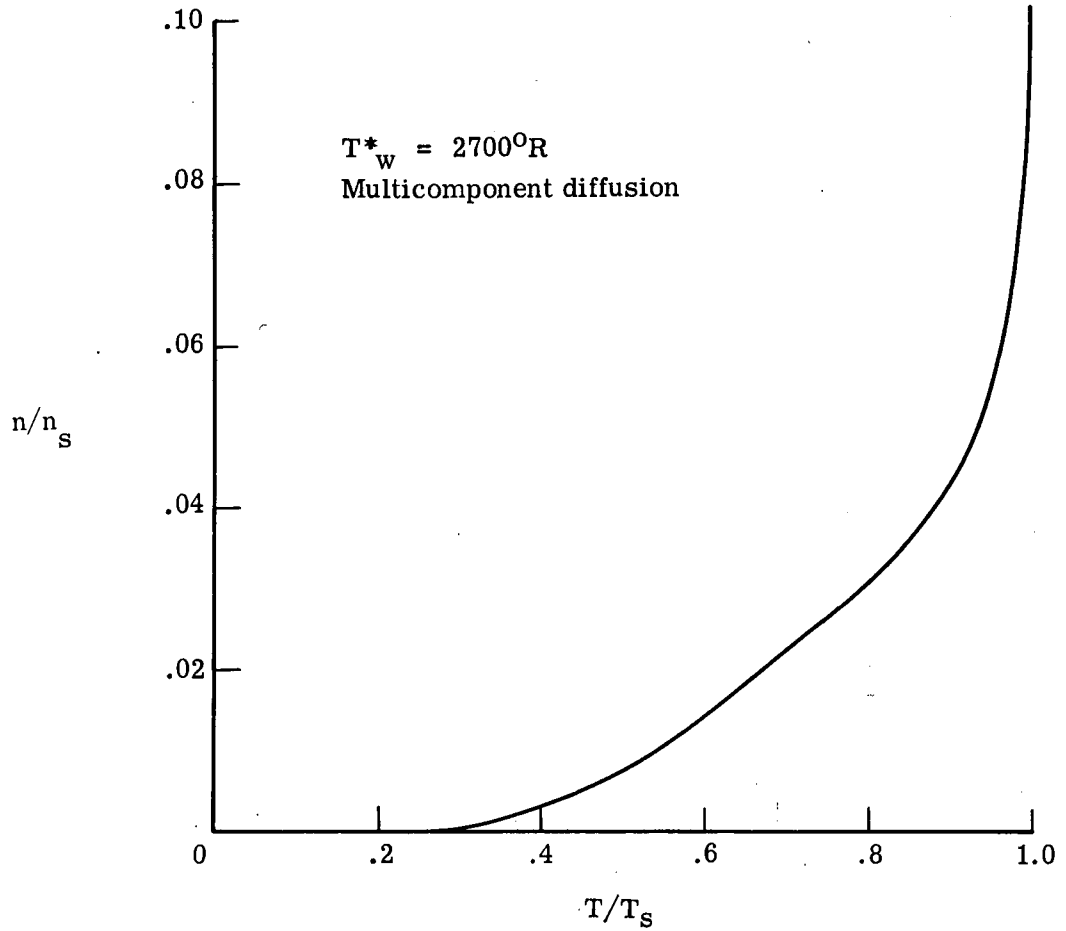
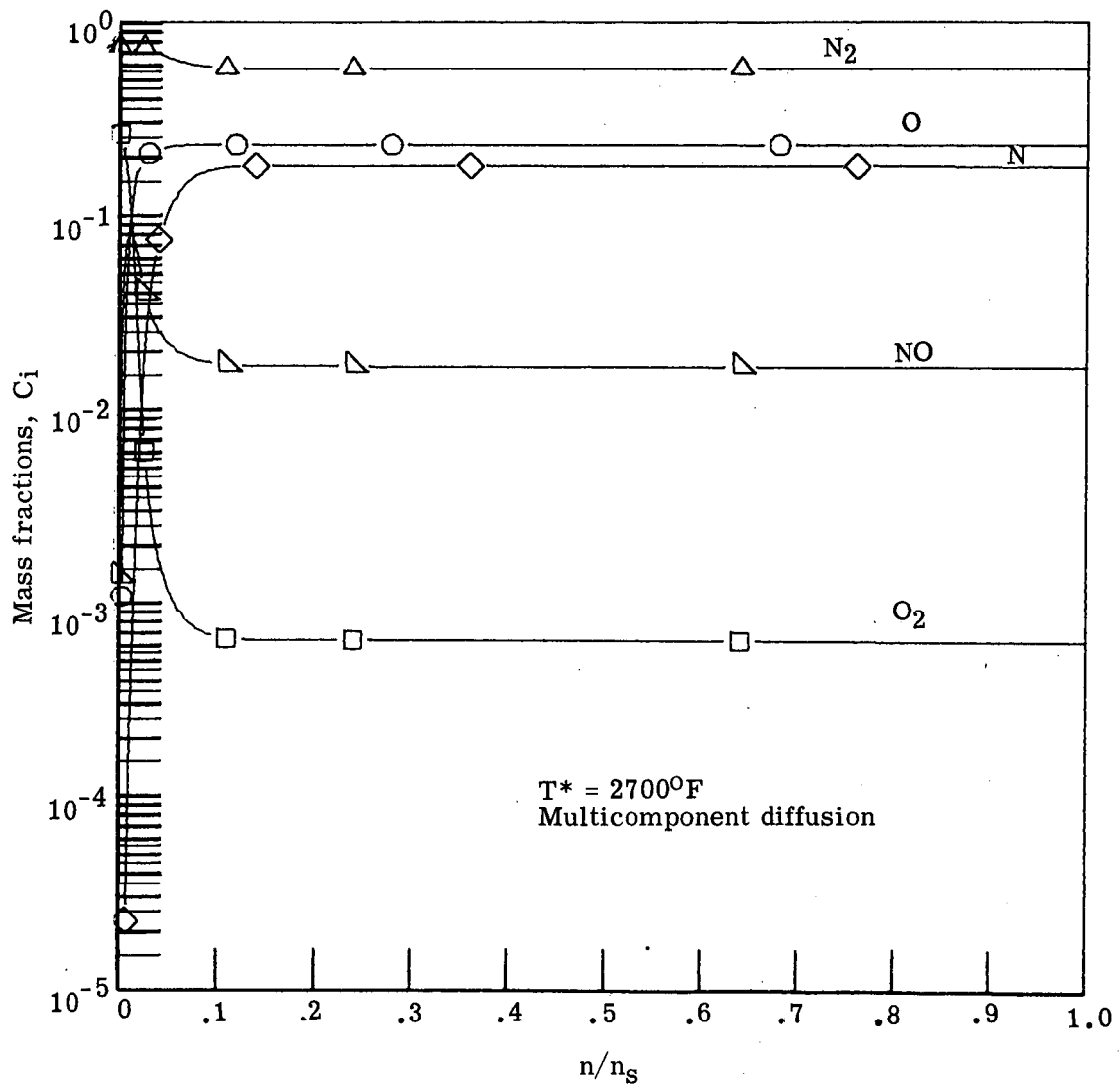


Figure 13.- Stagnation equilibrium and frozen air species and temperature profiles.



(a) Temperature profile.

Figure 14.- Stagnation equilibrium air results for an alt = 100,000 ft,
 $U_{\infty}^* = 20,000$ ft/sec, and $a^* = 1.0$ in.



(b) Species profiles

Figure 14.- Concluded.

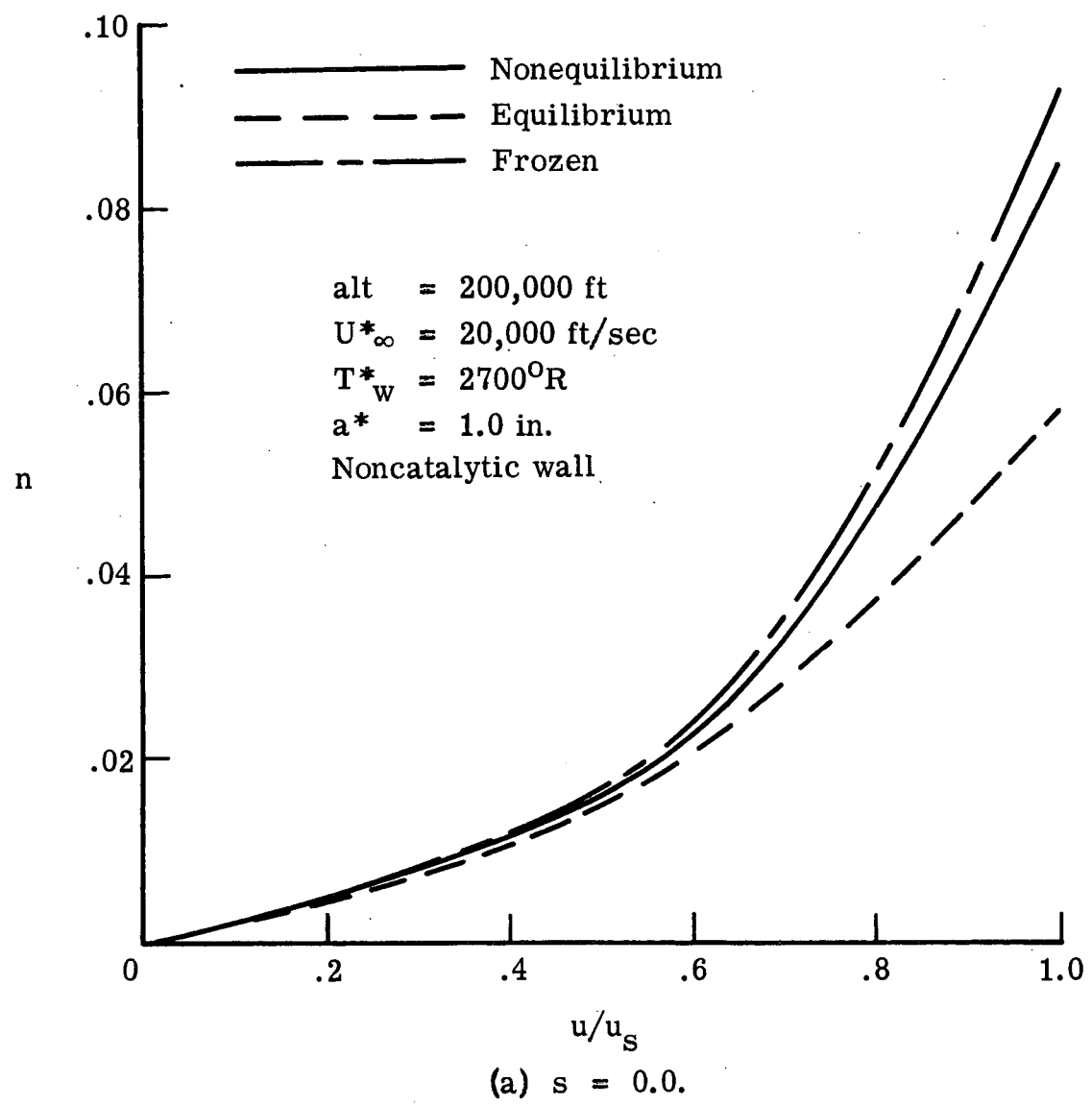
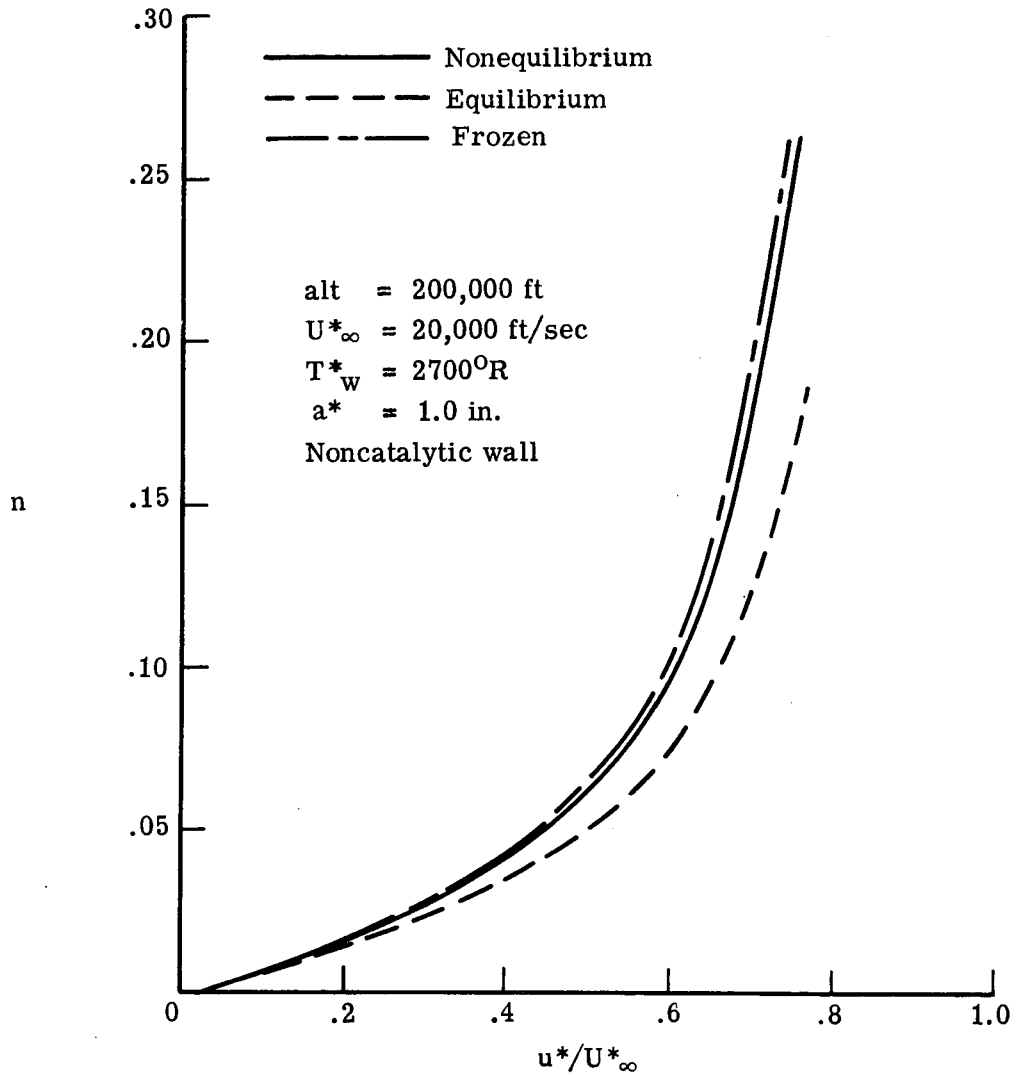


Figure 15.- Effect of chemistry model on tangential velocity profiles with multicomponent diffusion and no mass injection.



(b) $s = 2.0$.

Figure 15.- Concluded.

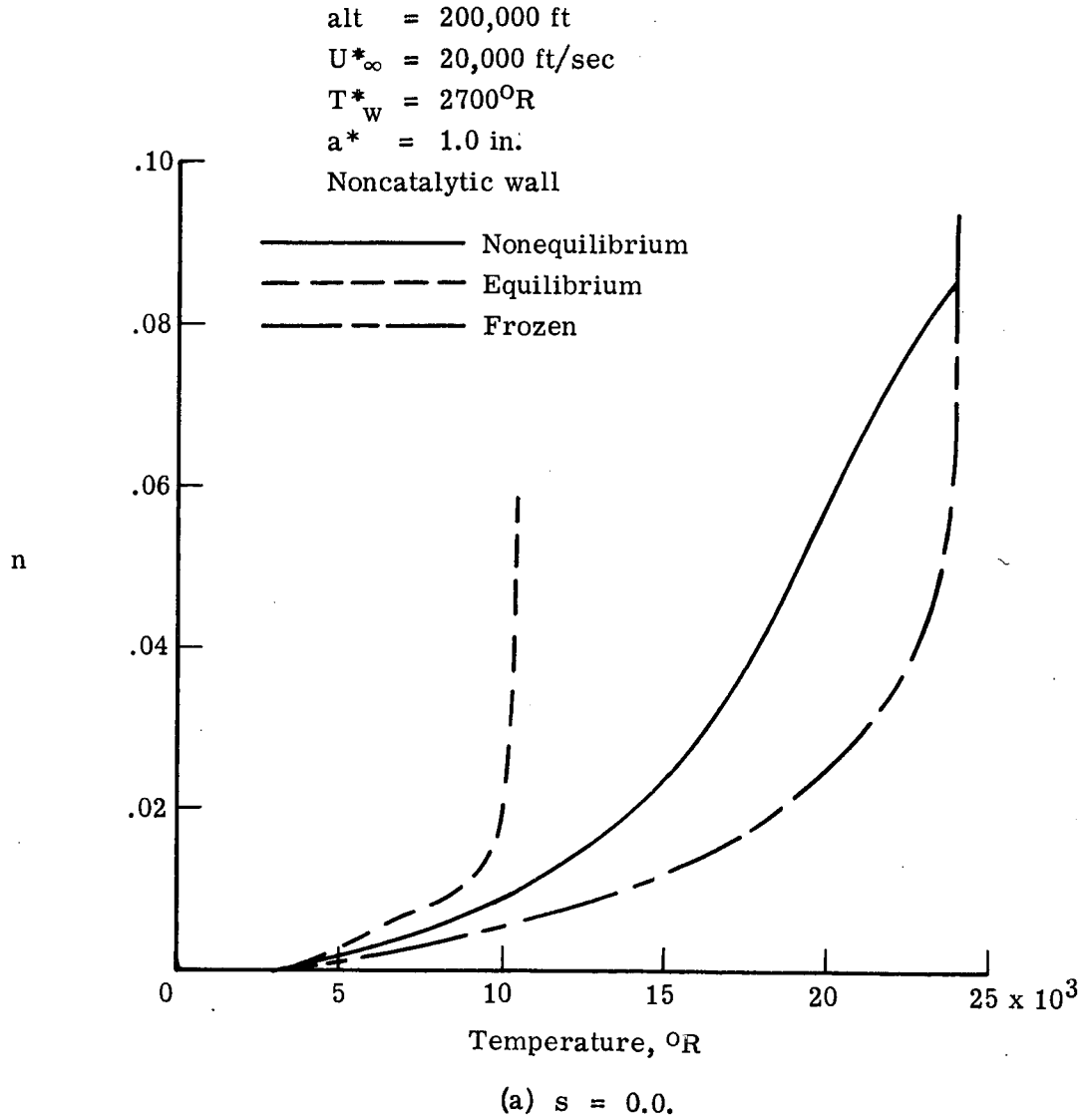
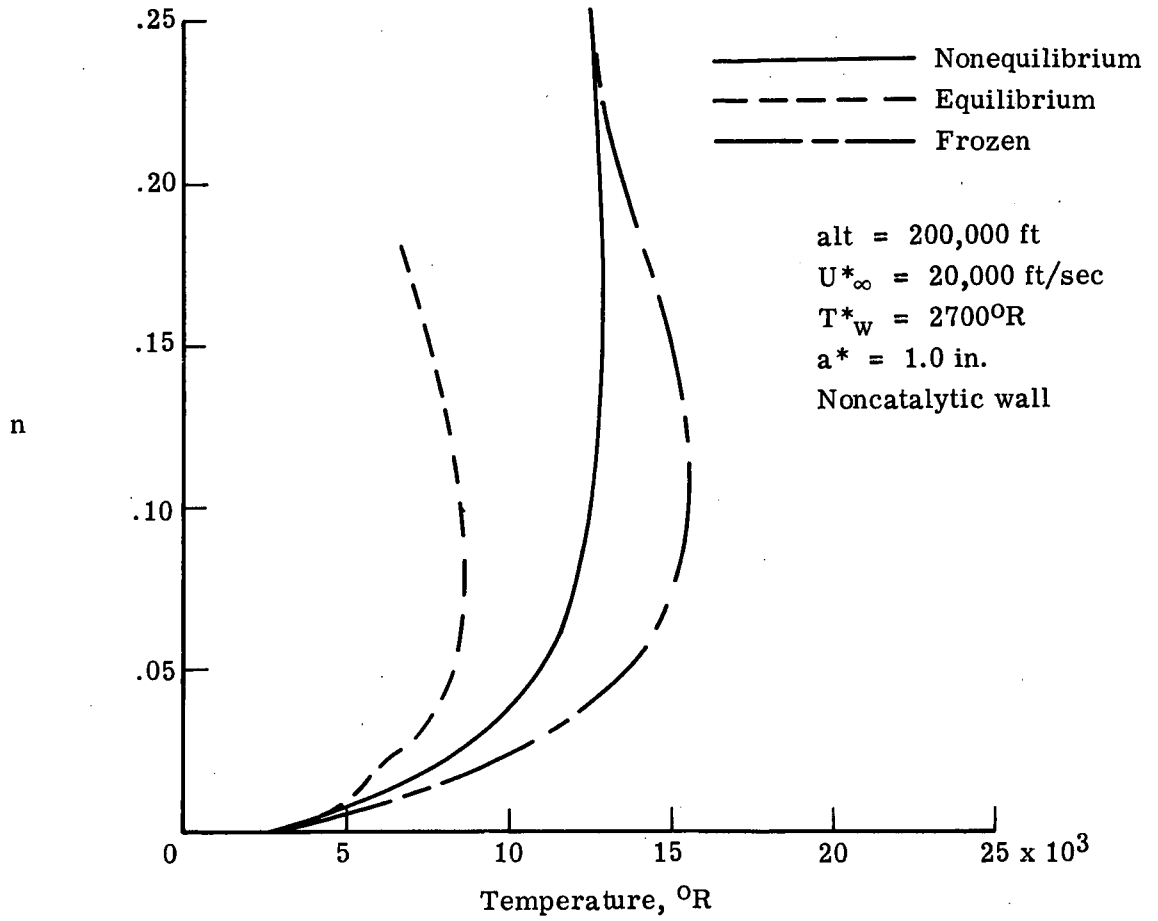


Figure 16.- Effect of chemistry model on temperature profiles with multi-component diffusion and no mass injection.



(b) $s = 2.0$.

Figure 16.- Continued.

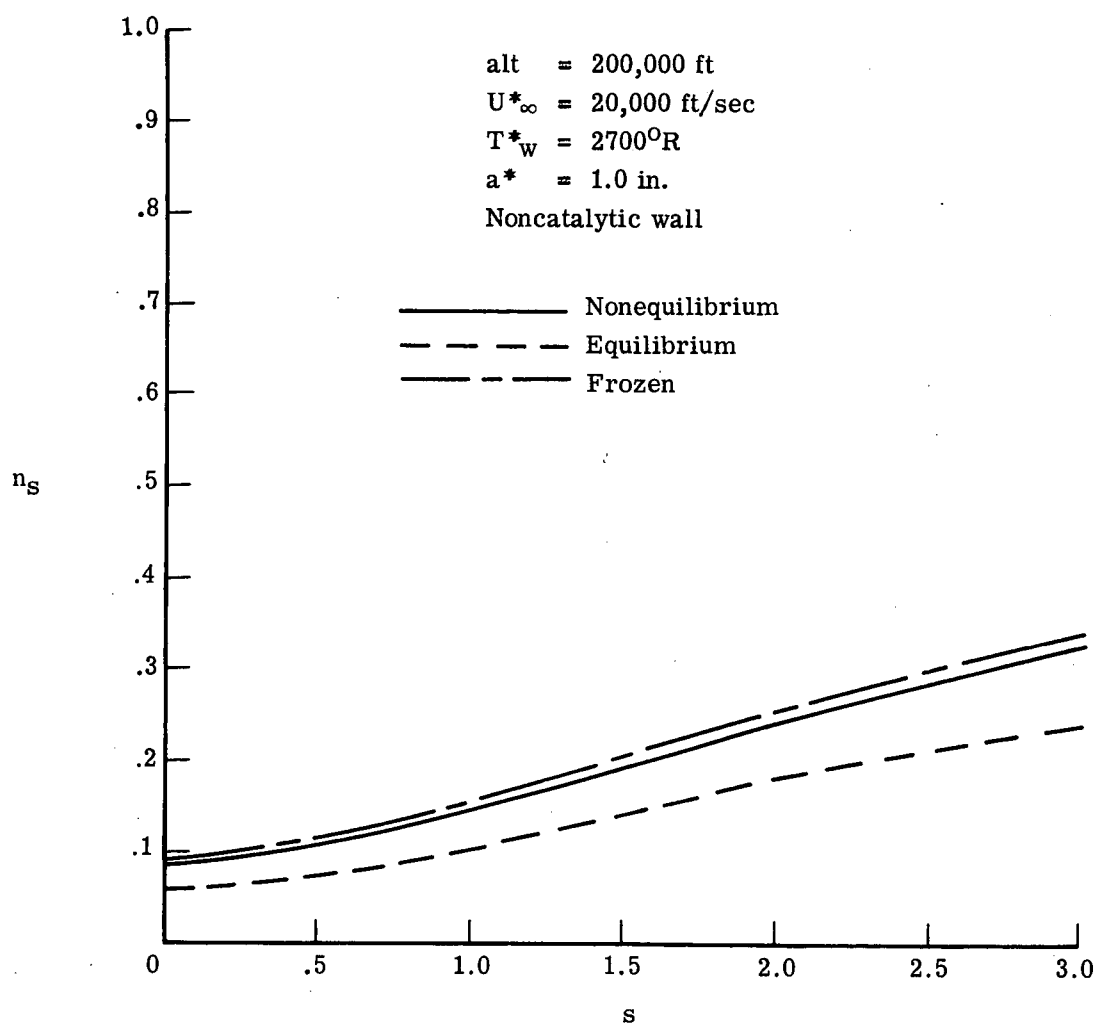


Figure 17.- Effect of chemistry model on shock stand-off distance with multicomponent diffusion and no mass injection.

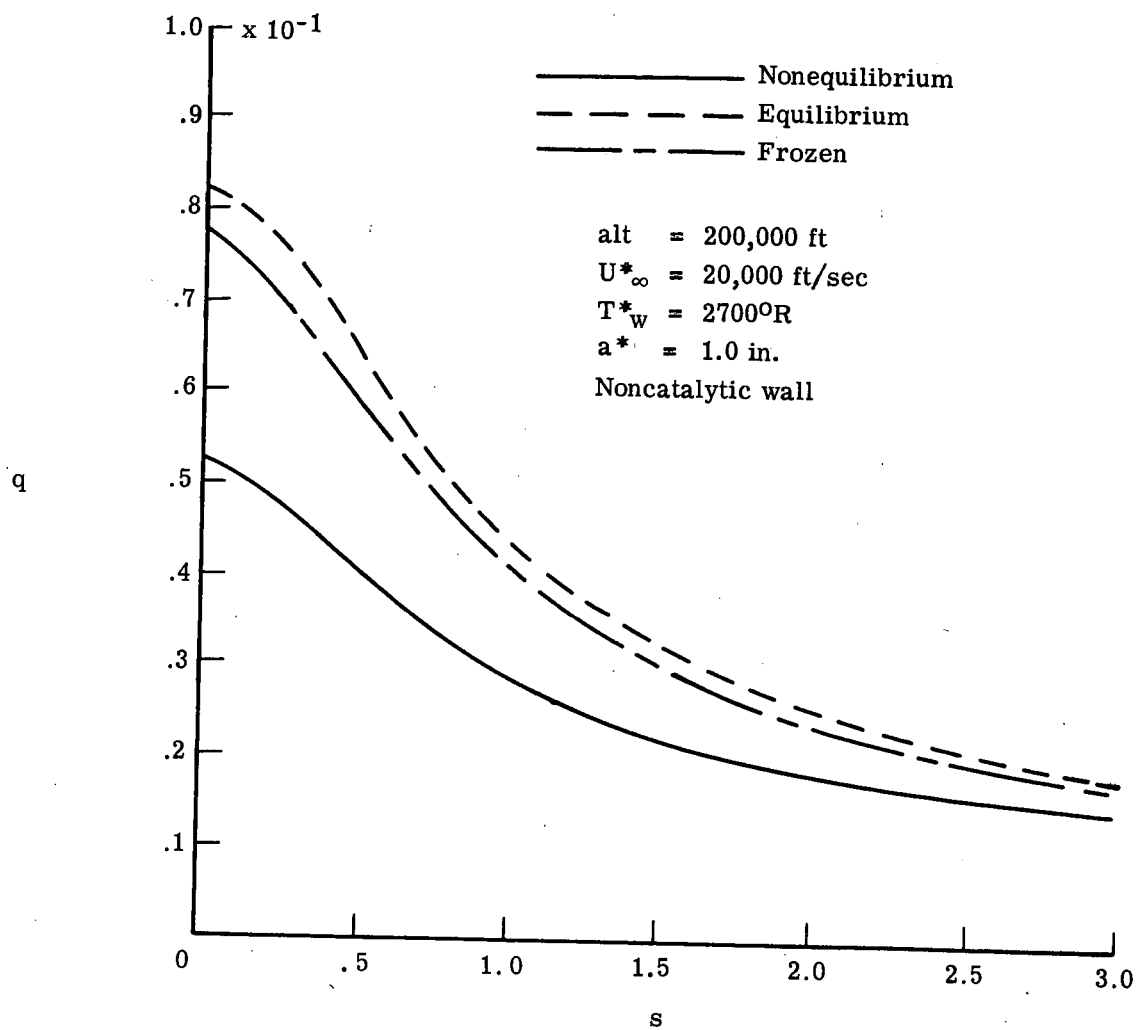


Figure 18.- Effect of chemistry model on nondimensional heat transfer with multicomponent diffusion and no mass injection.

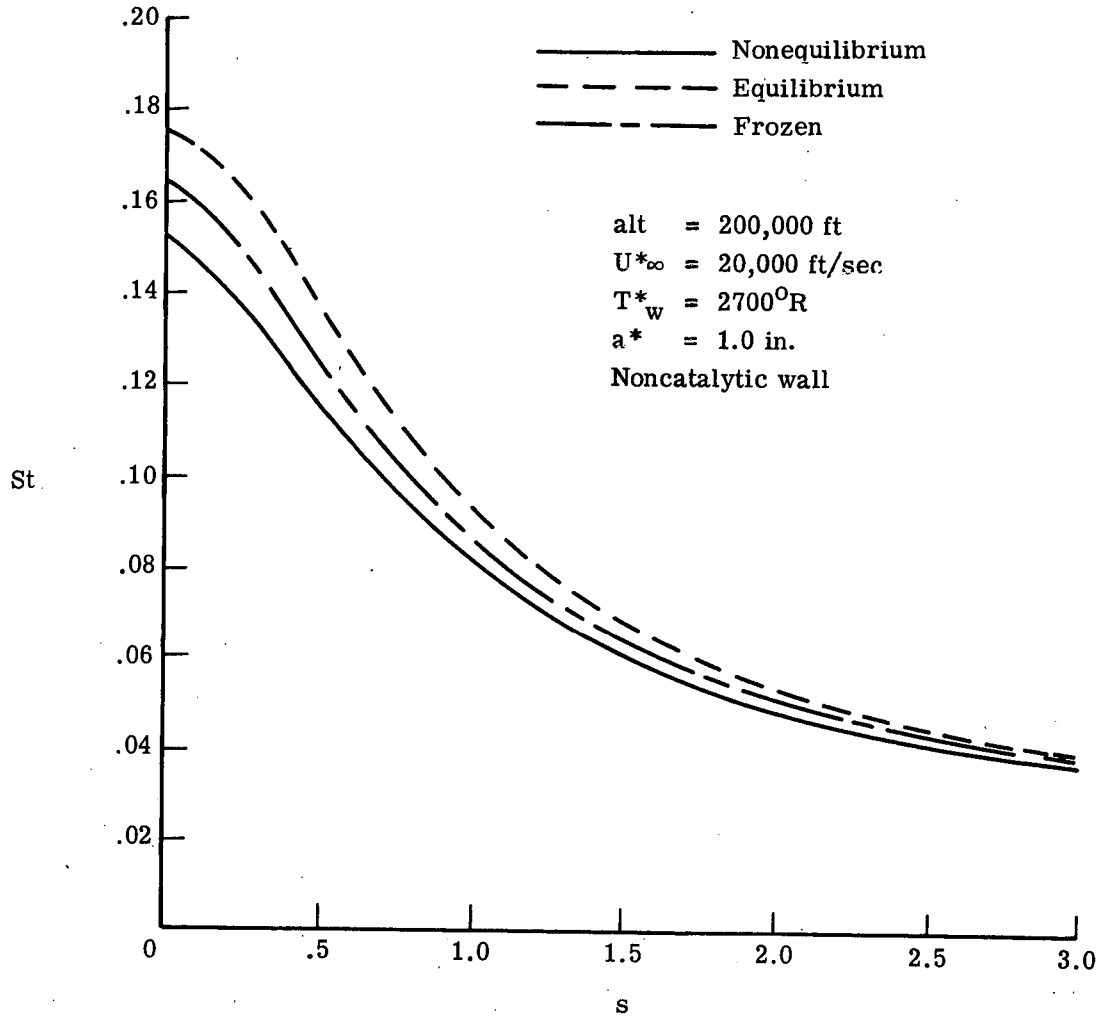


Figure 19.- Effect of chemistry model on Stanton number with multicomponent diffusion and no mass injection.

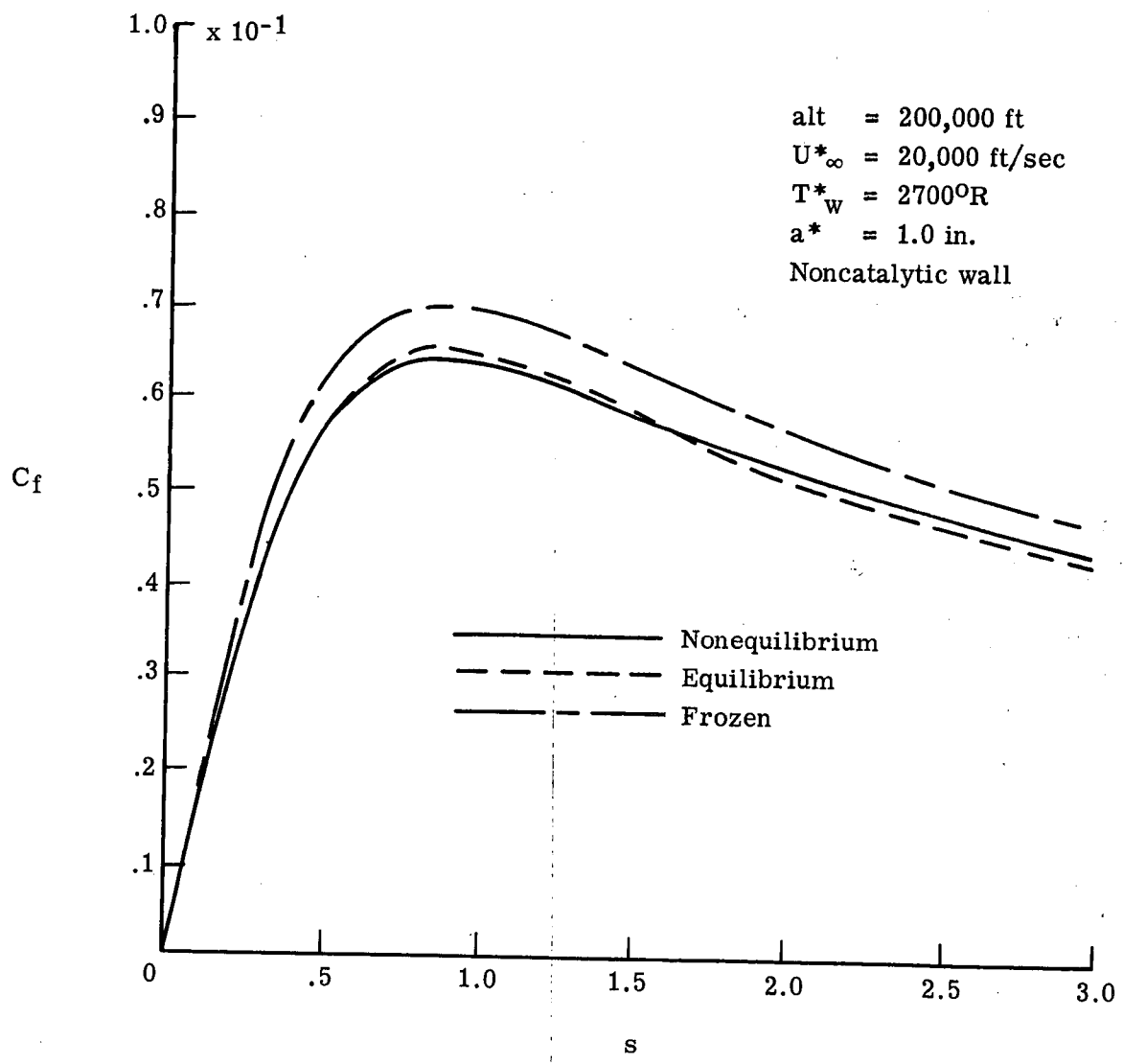


Figure 20.- Effect of chemistry model on skin friction coefficient with multicomponent diffusion and no mass injection.

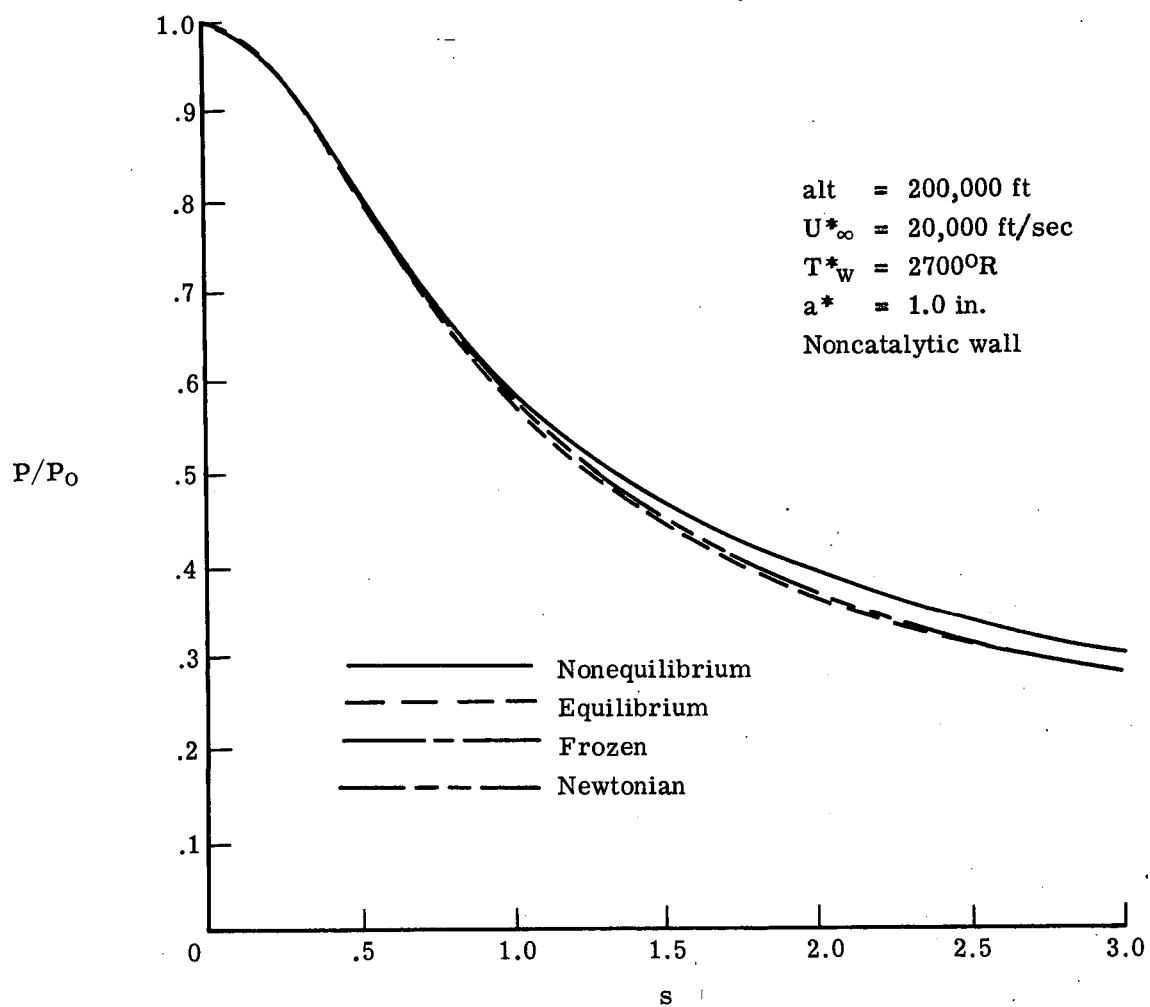


Figure 21.- Effect of chemistry model on wall pressure distribution with multicomponent diffusion and no mass injection.

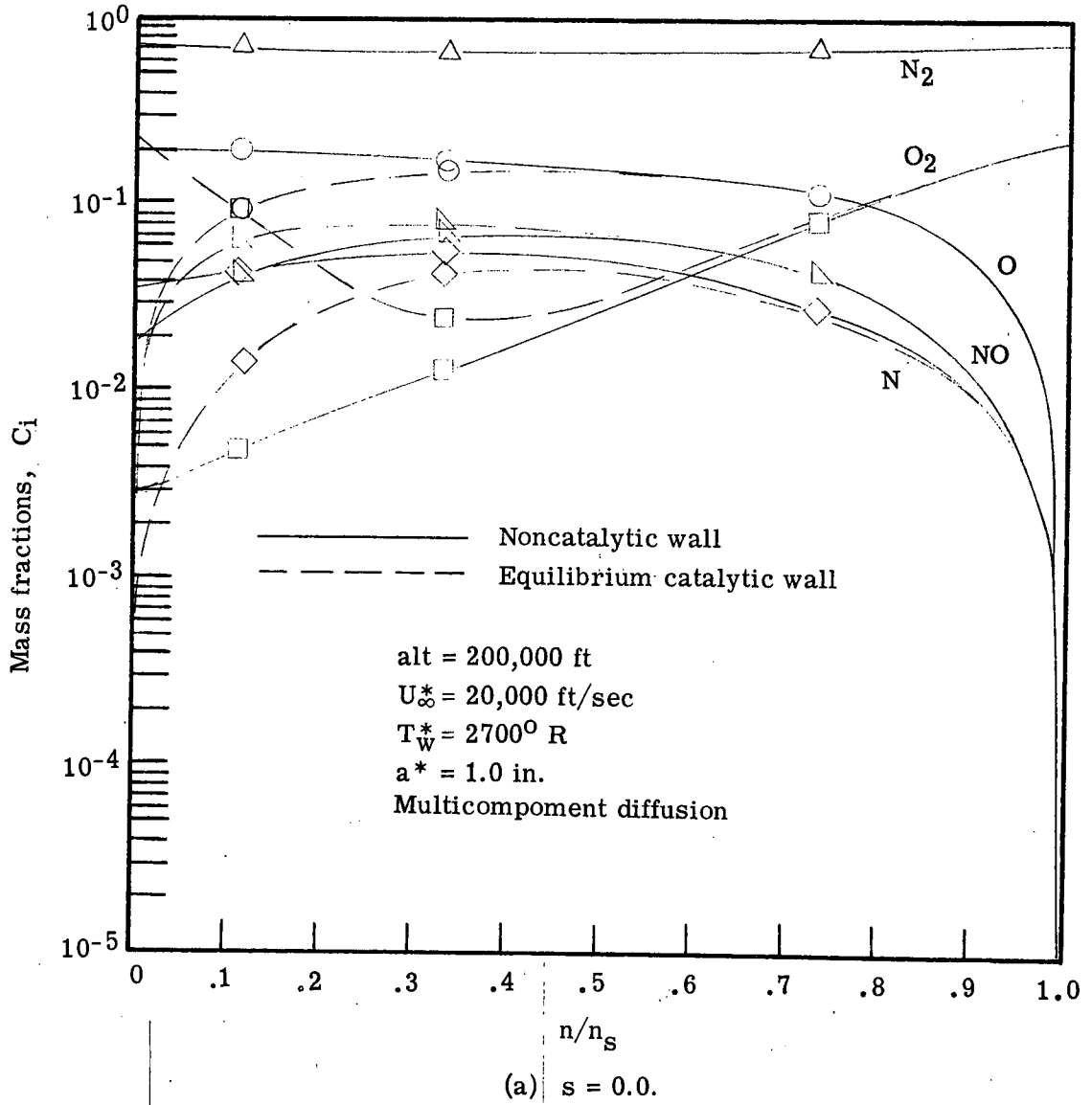


Figure 22.- Effect of wall catalyticity on species profiles.

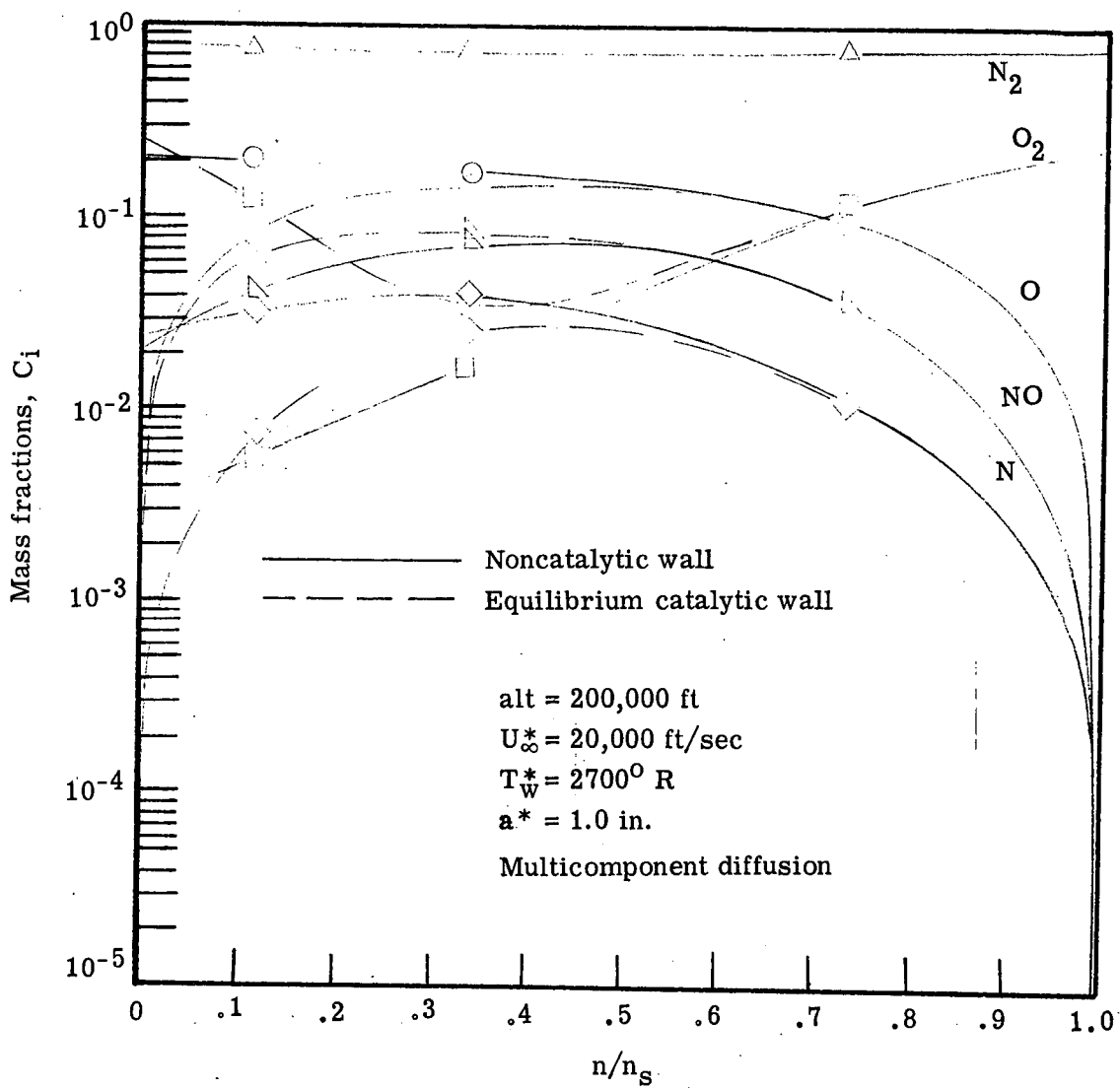
(b) $s = 1.0$.

Figure 22.- Continued.

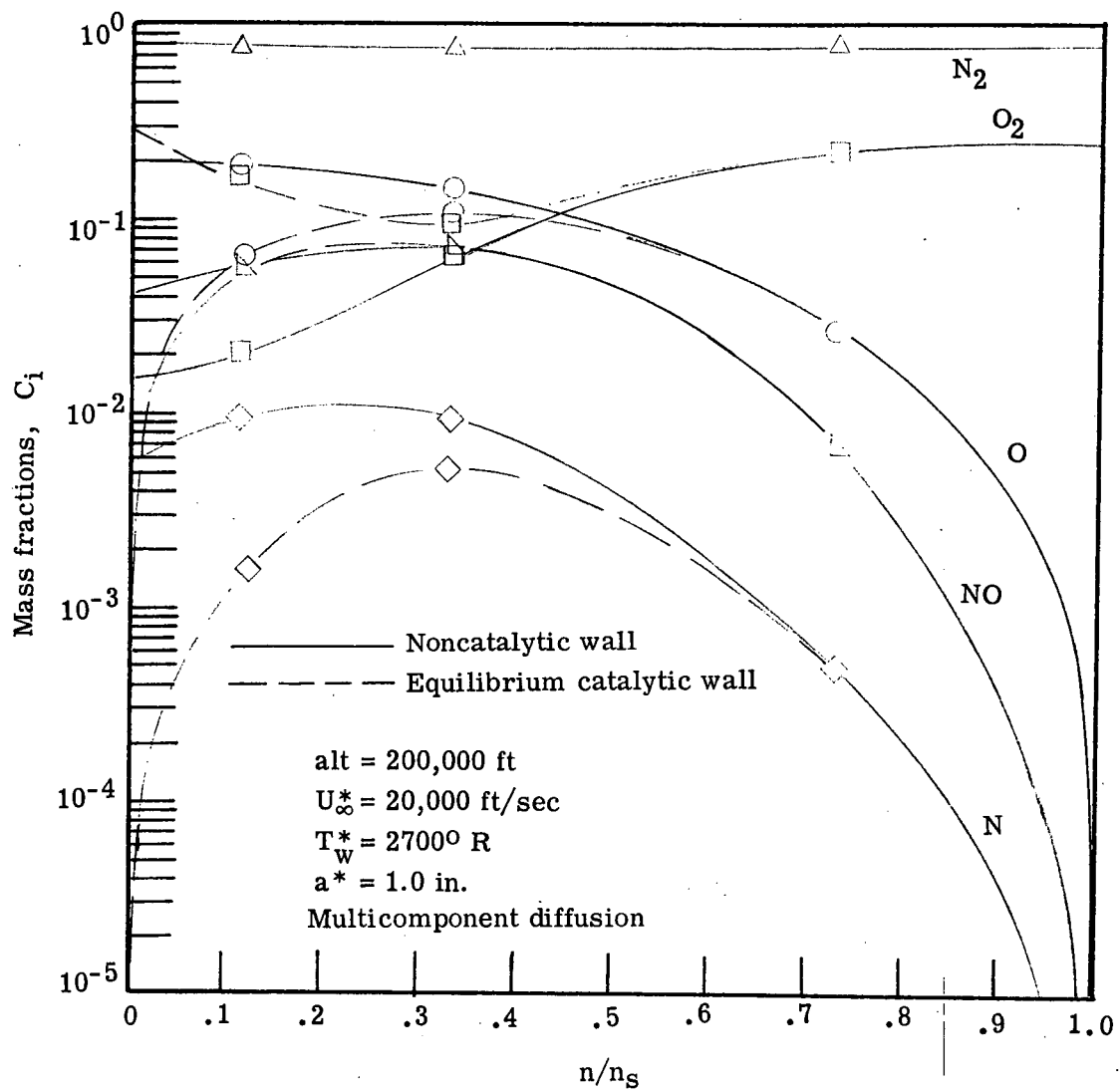
(c) $s = 3.0$

Figure 22.- Concluded.

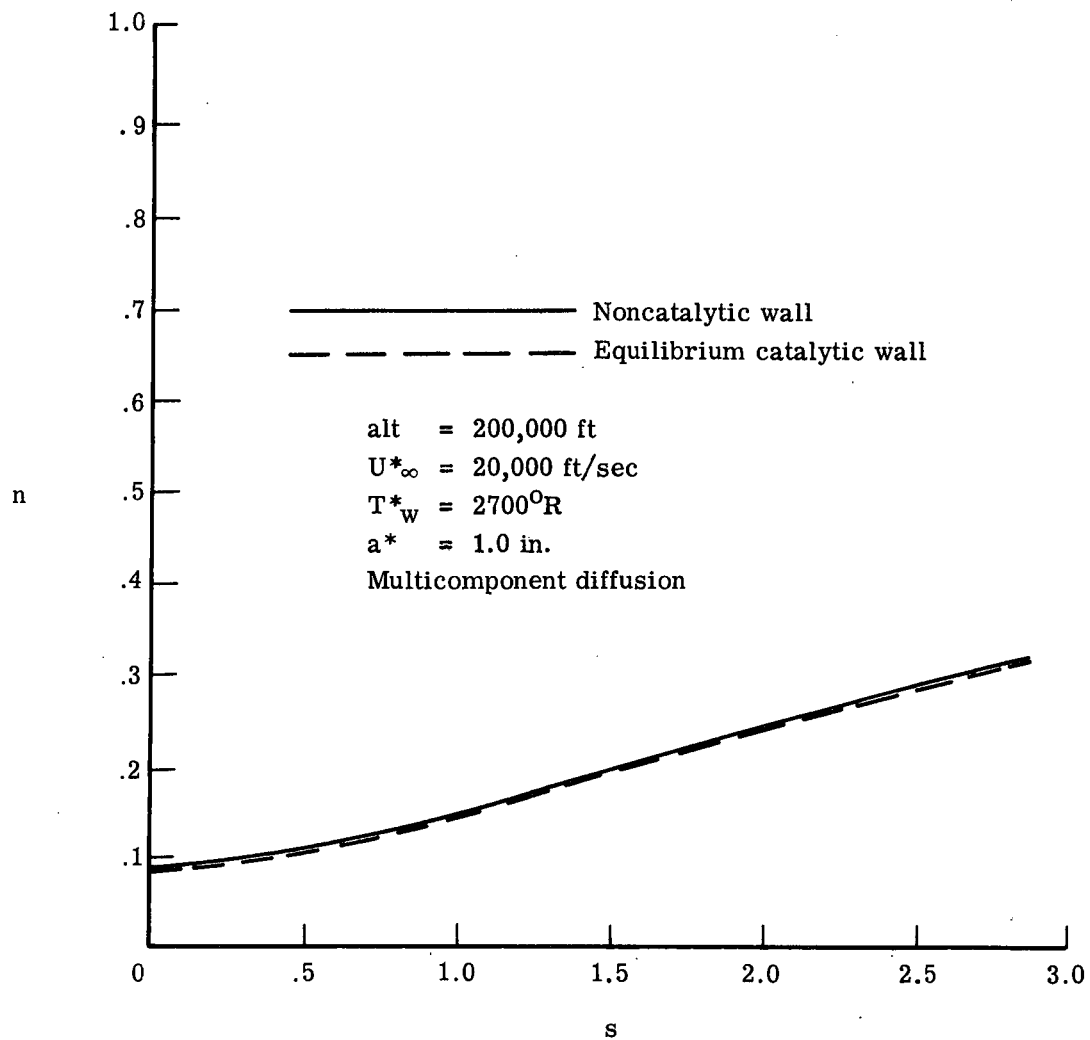


Figure 23.- Effect of wall catalyticity on shock stand-off distance.

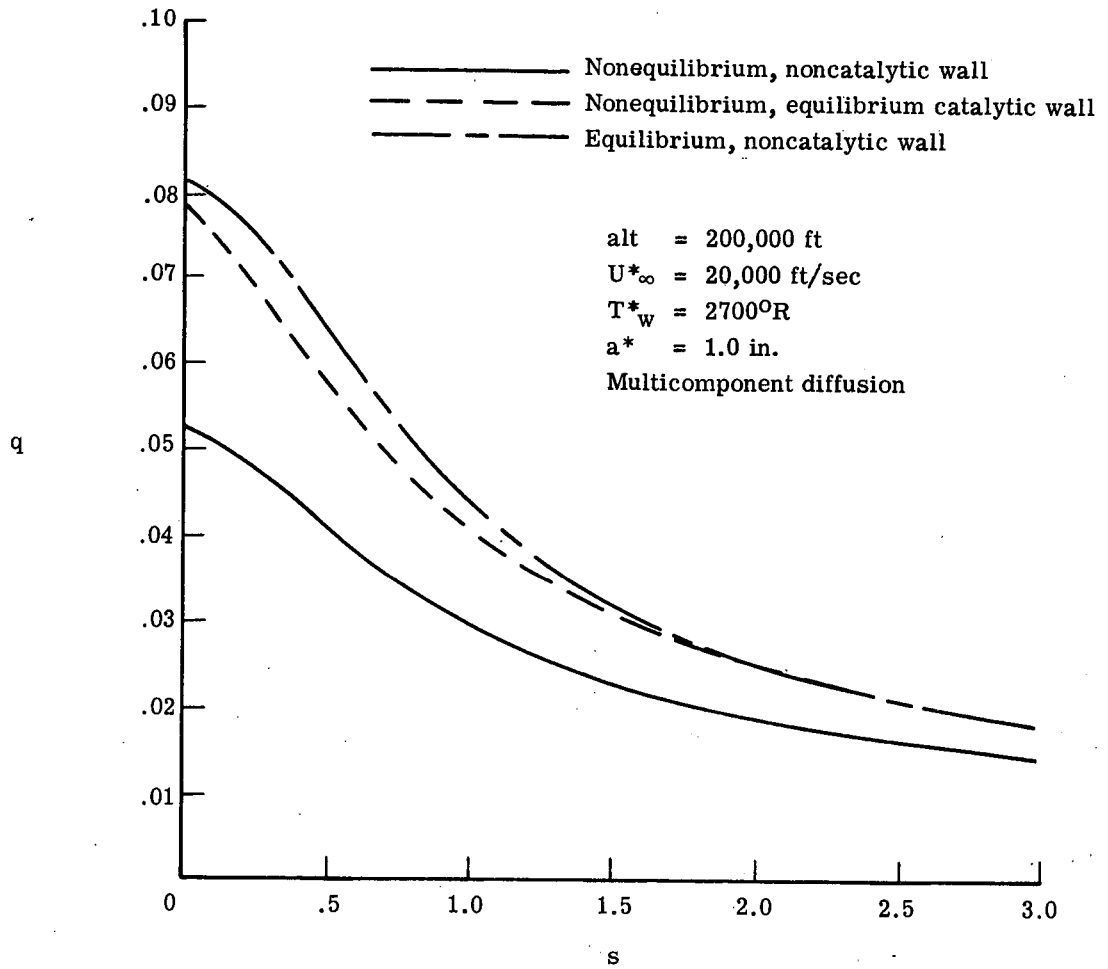


Figure 24.- Effect of wall catalyticity on nondimensional heat transfer.

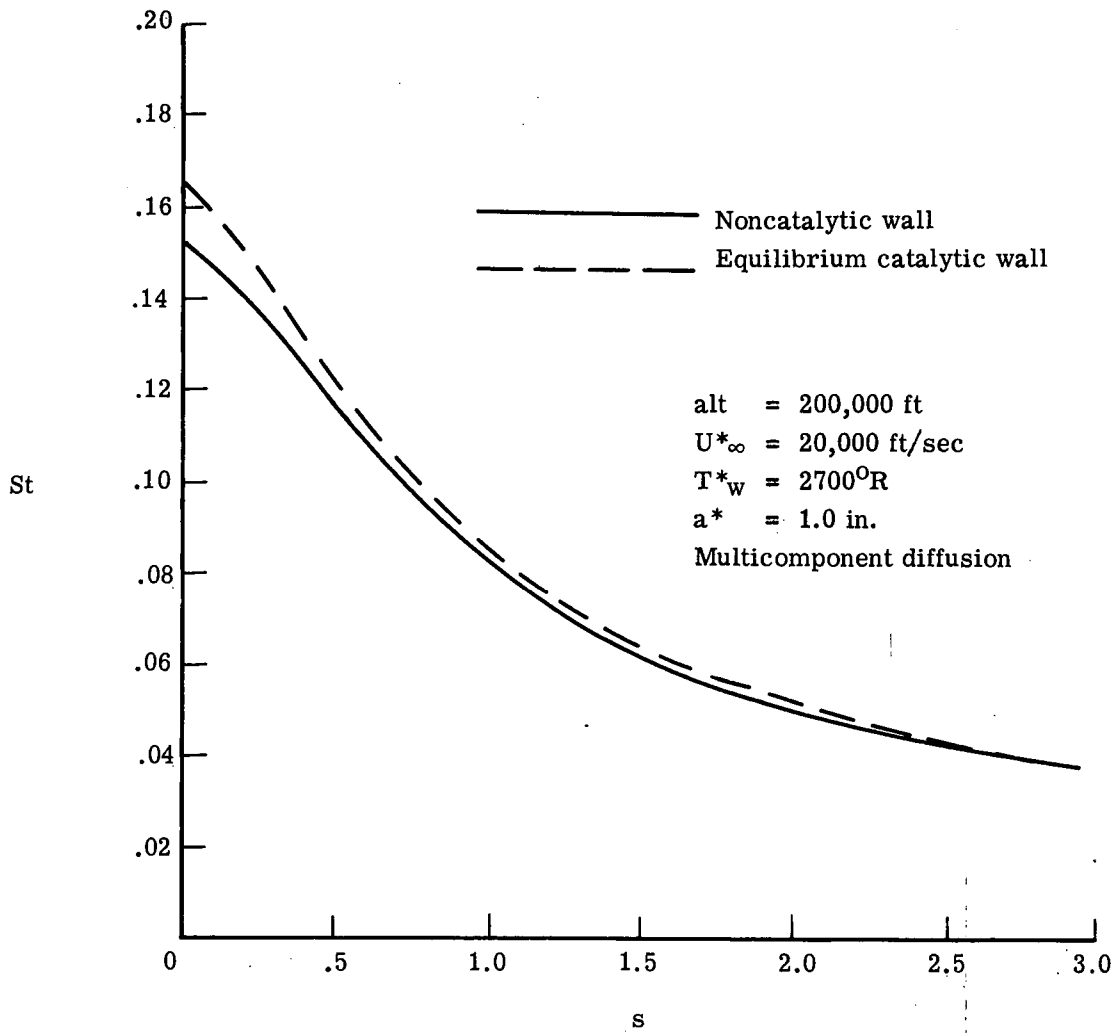


Figure 25.- Effect of wall catalyticity on Stanton number.

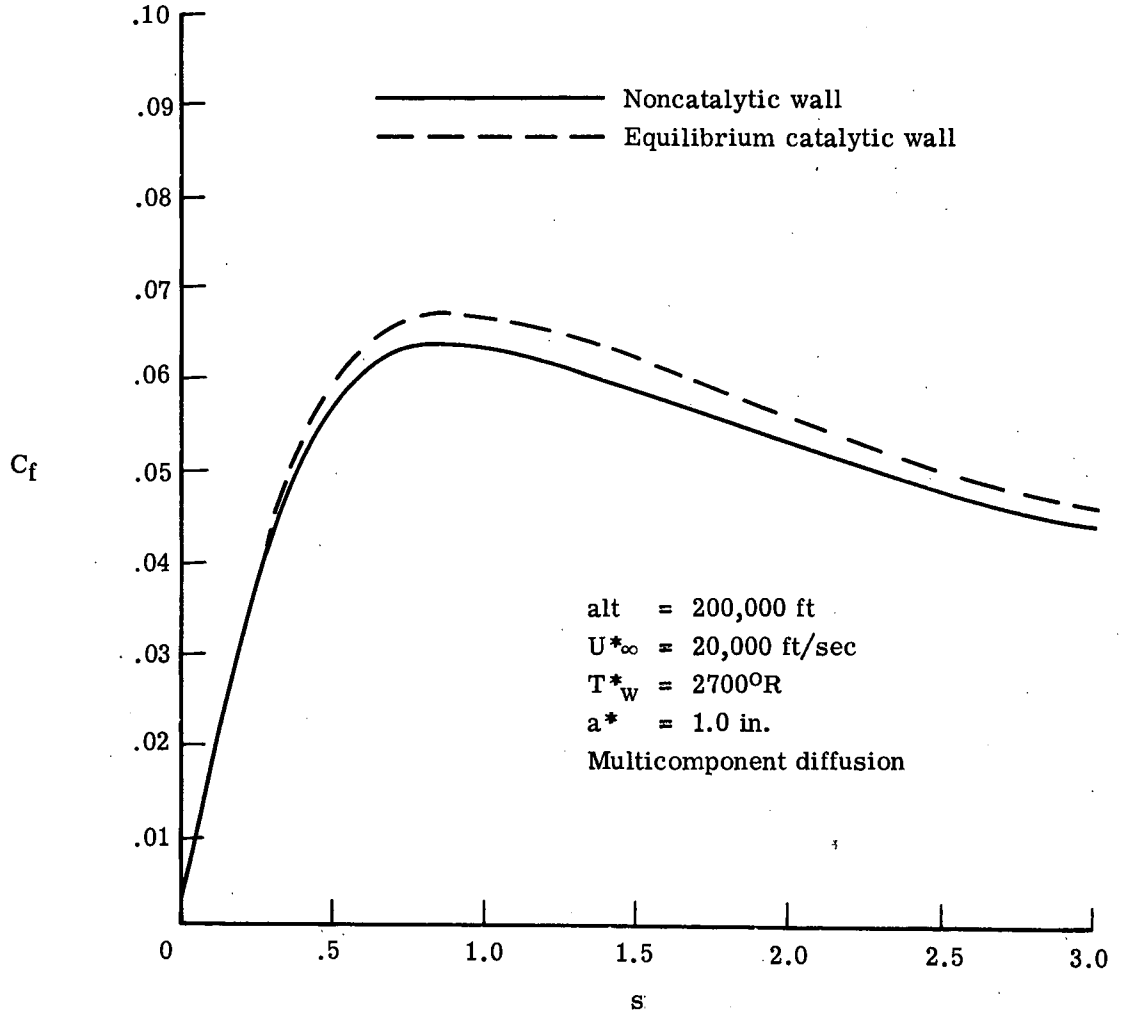


Figure 26.- Effect of wall catalyticity on skin friction coefficient.

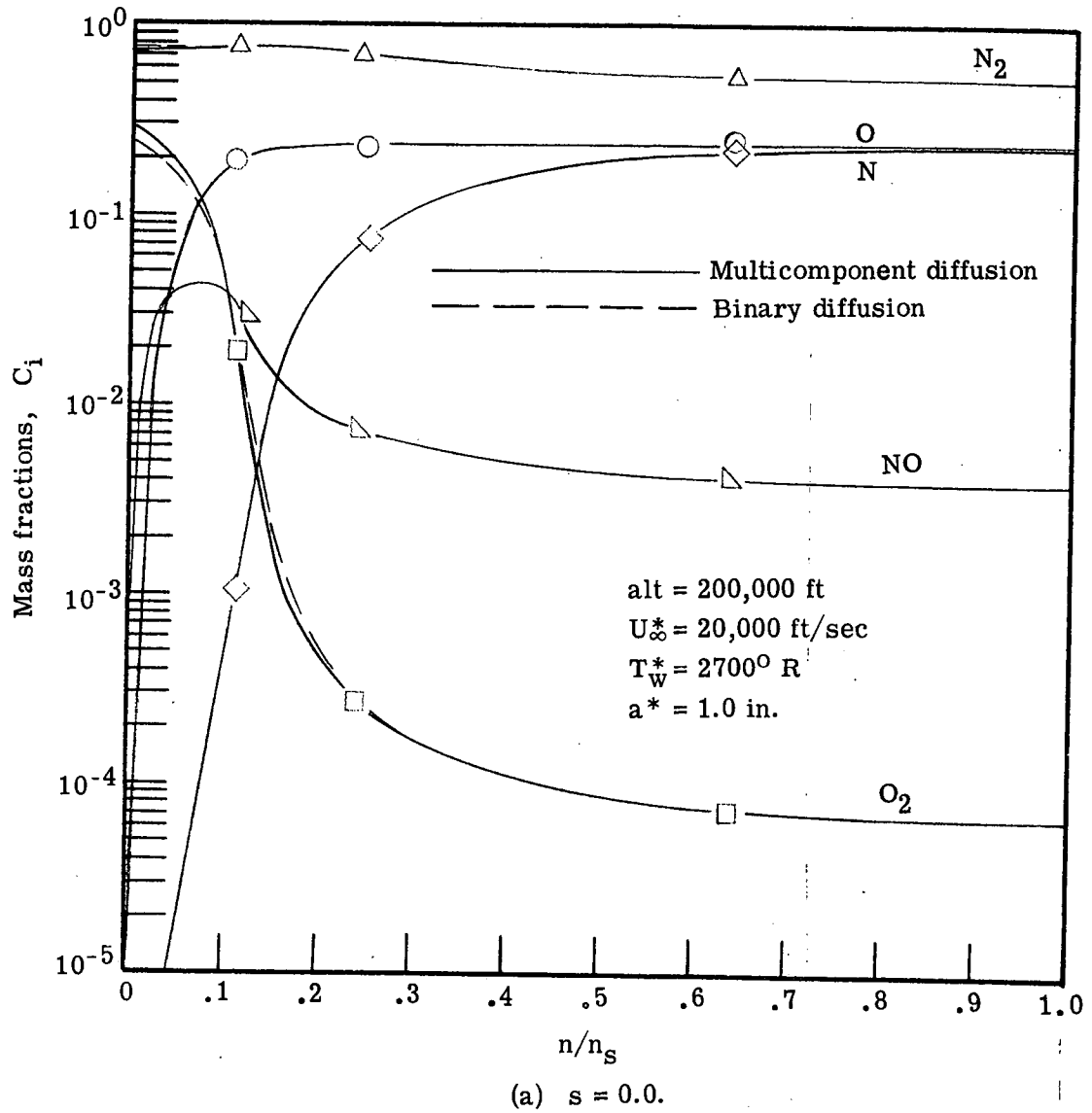


Figure 27.- Effect of diffusion model on species profiles for equilibrium air.

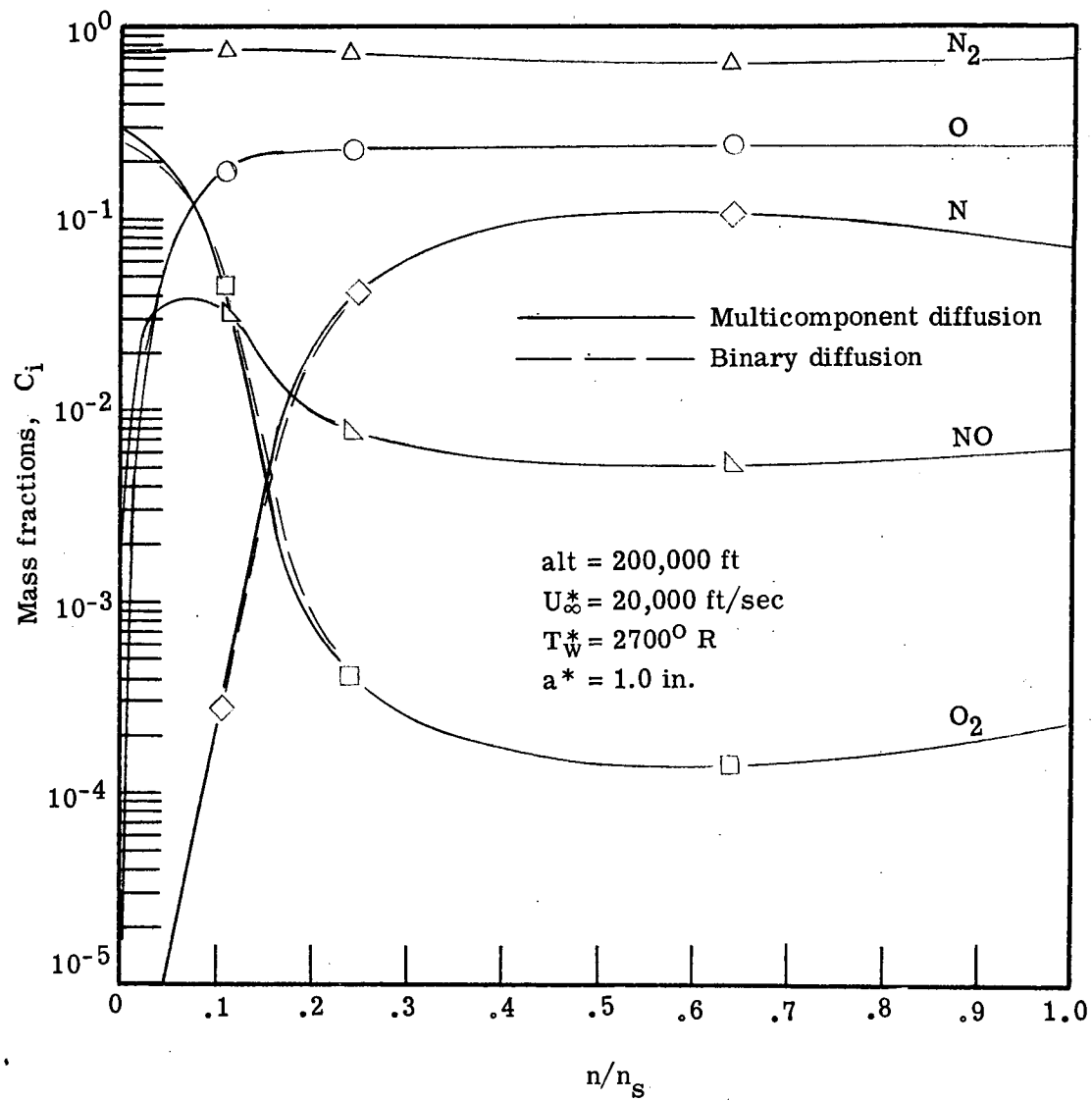
(b) $s = 1.0$.

Figure 27.- Concluded.

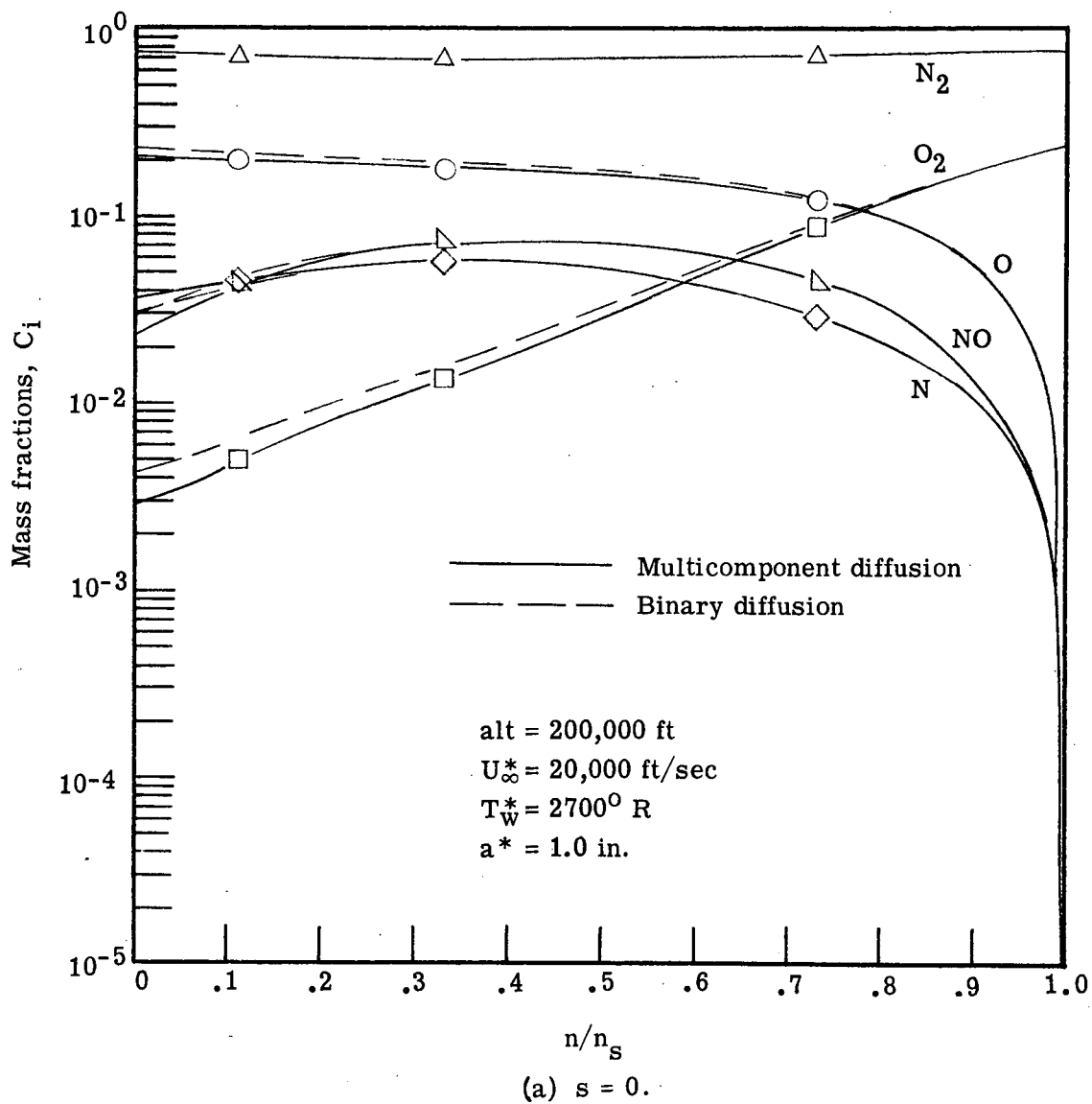
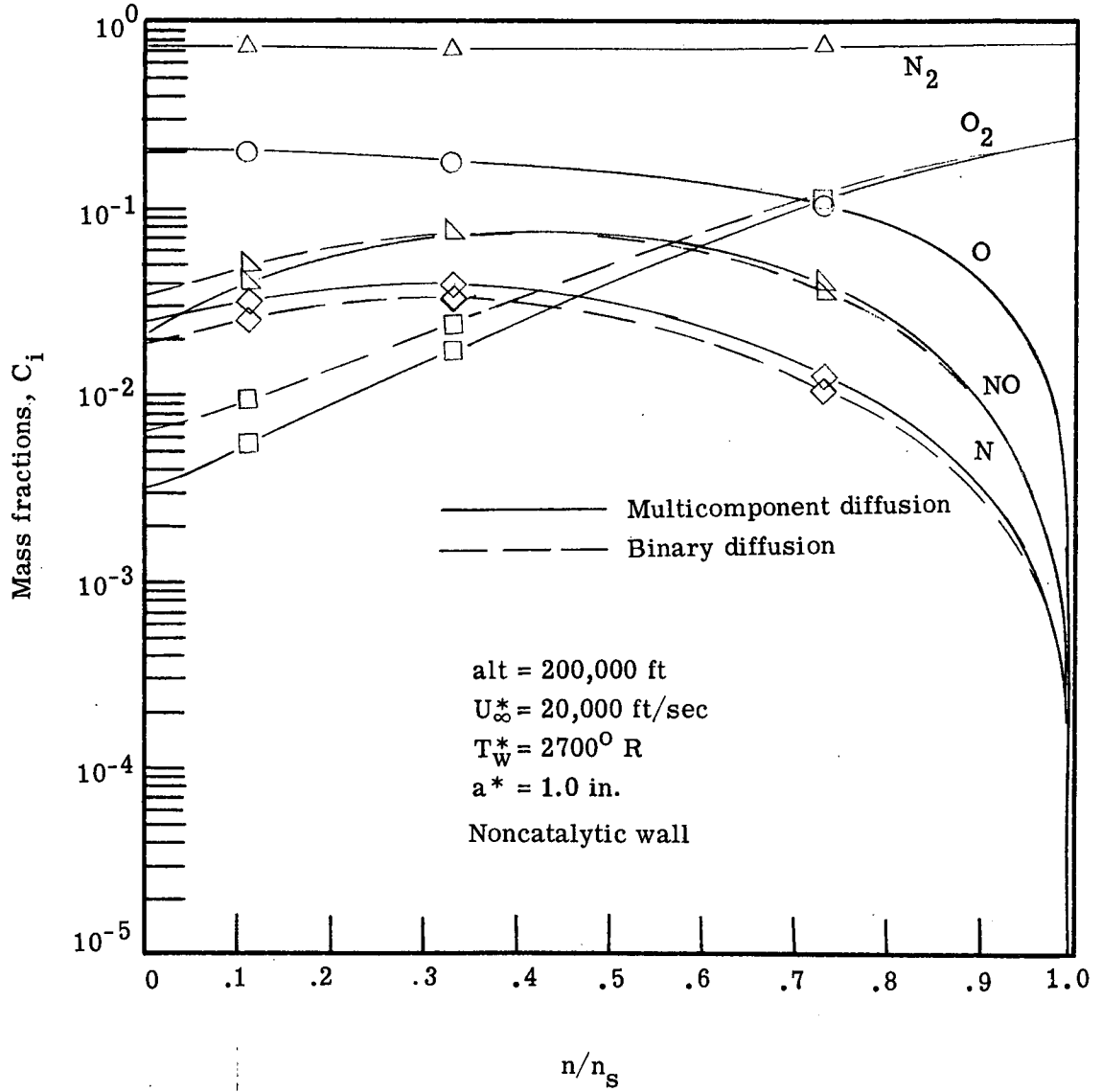


Figure 28.- Effect of diffusion model on species profiles for nonequilibrium air.



(b) $s = 1.0$.

Figure 28.- Concluded.

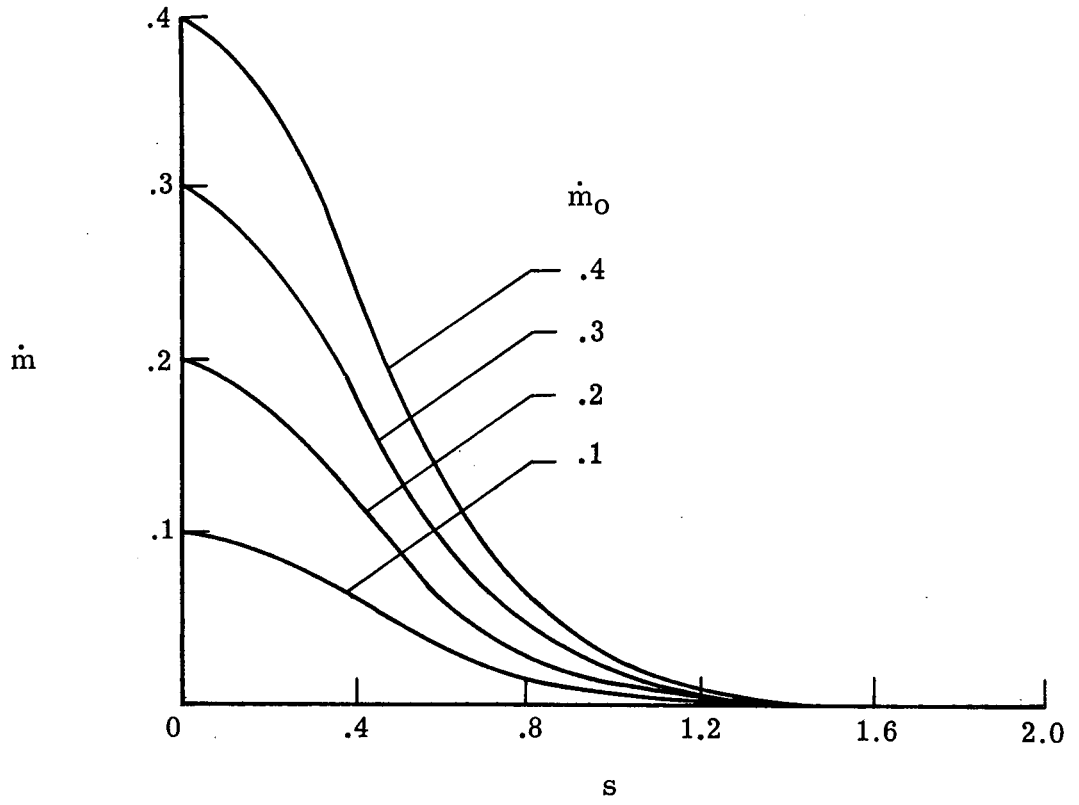


Figure 29.- Nondimensional mass injection distributions.

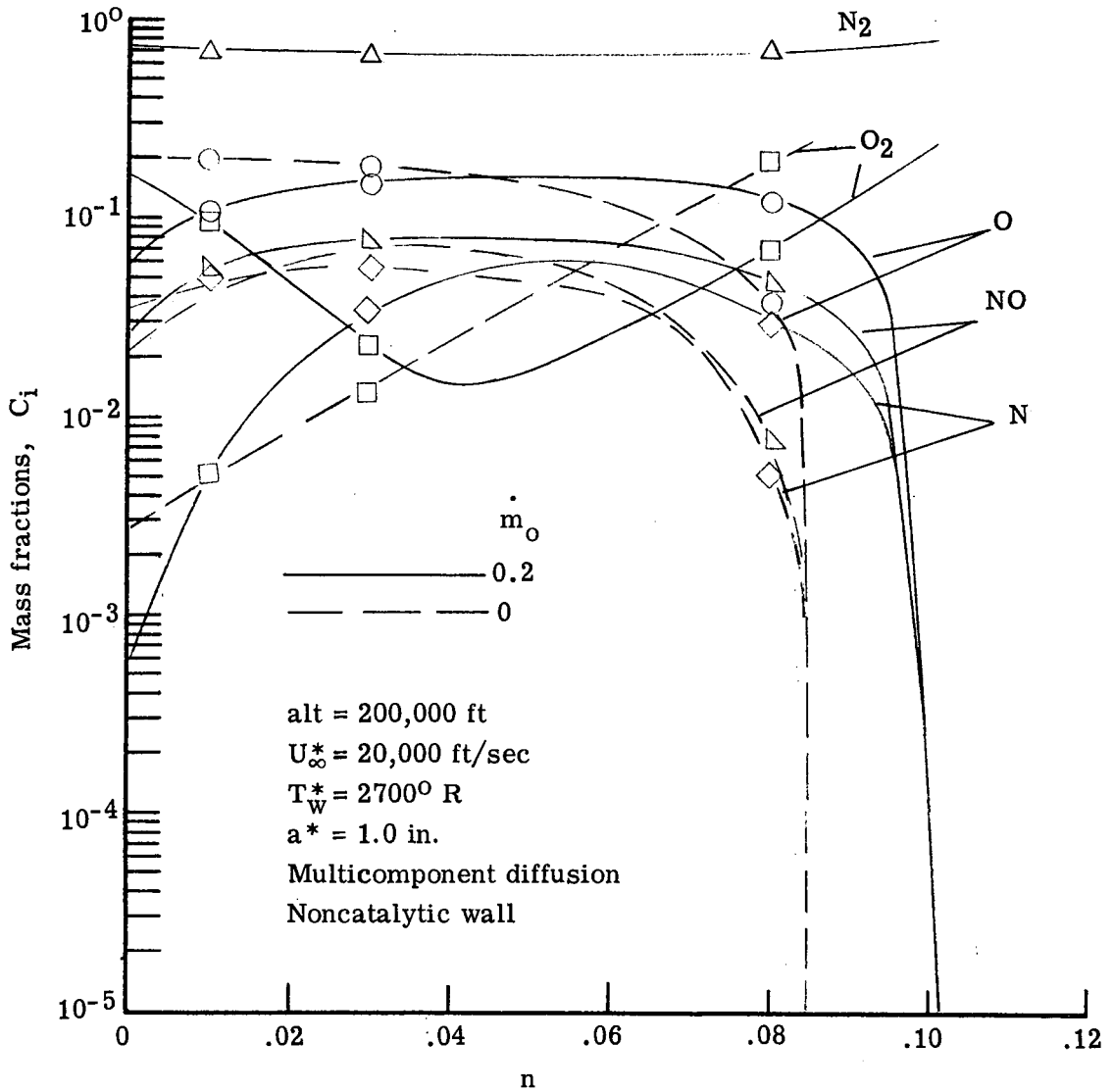
(a) $s = 0.0$.

Figure 30.- Comparison of nonequilibrium species profiles with and without mass injection of equilibrium air.

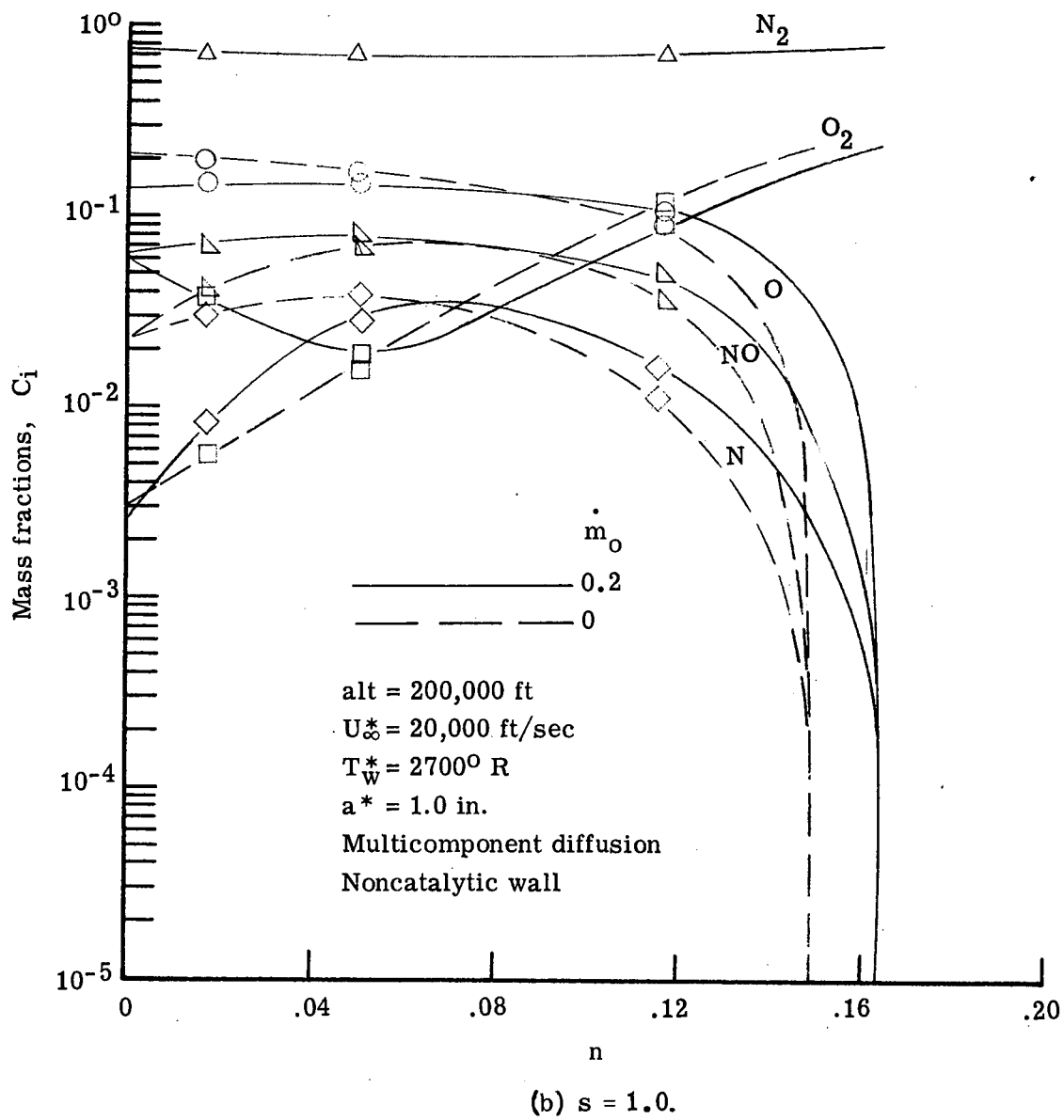


Figure 30.- Continued.

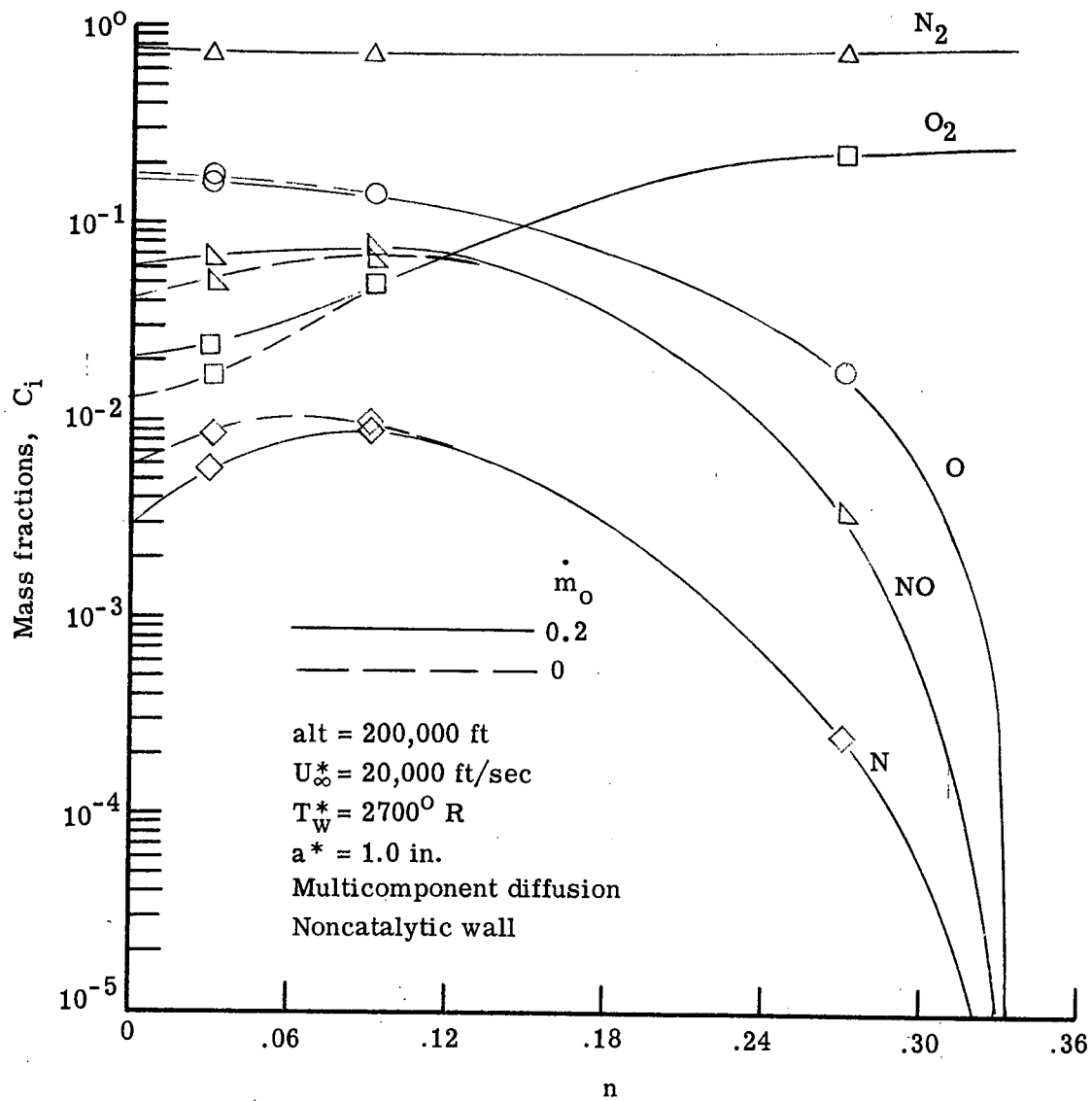
(c) $s = 3.0$.

Figure 30.- Concluded.

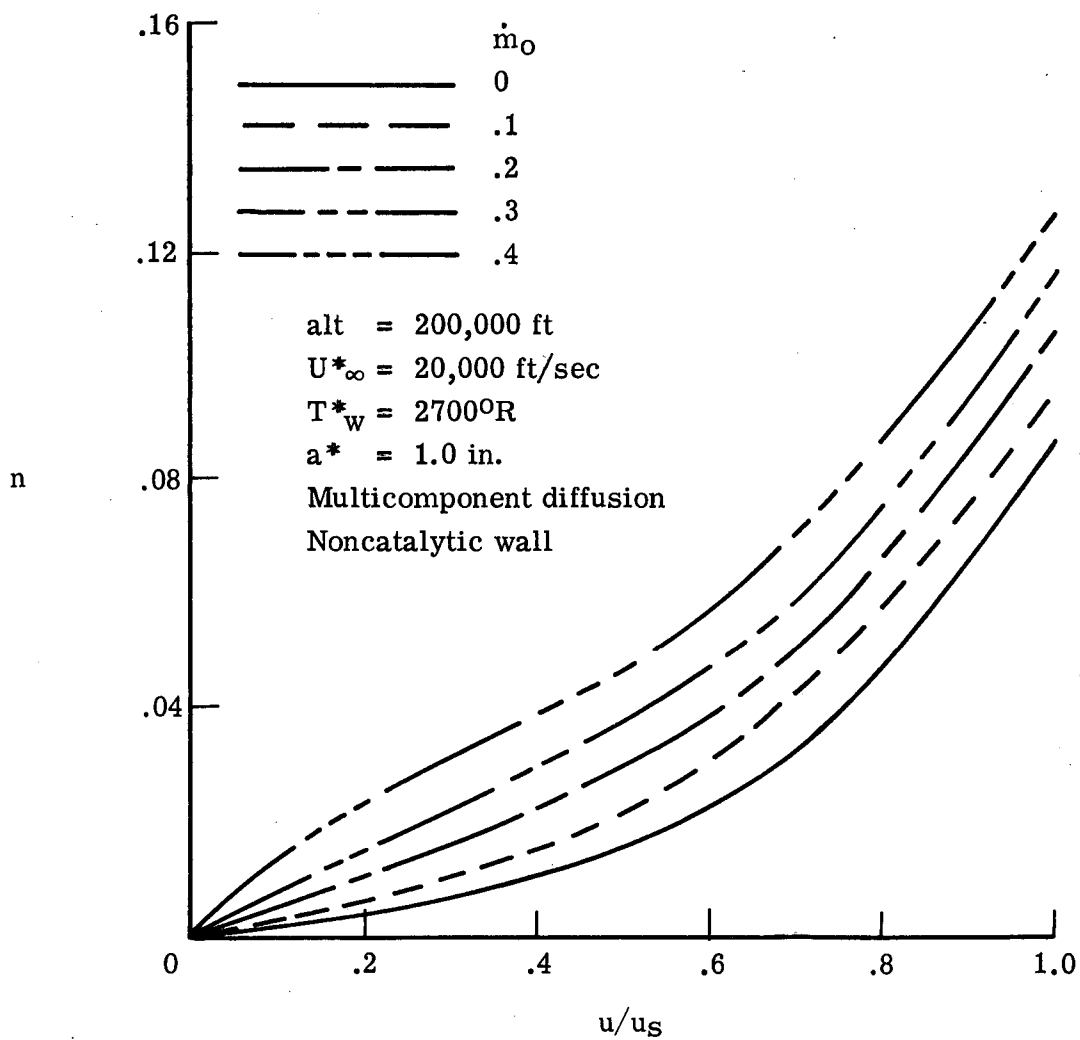


Figure 31.- Stagnation tangential velocity ratio profiles for different injection rates of equilibrium air into reacting non-equilibrium air.

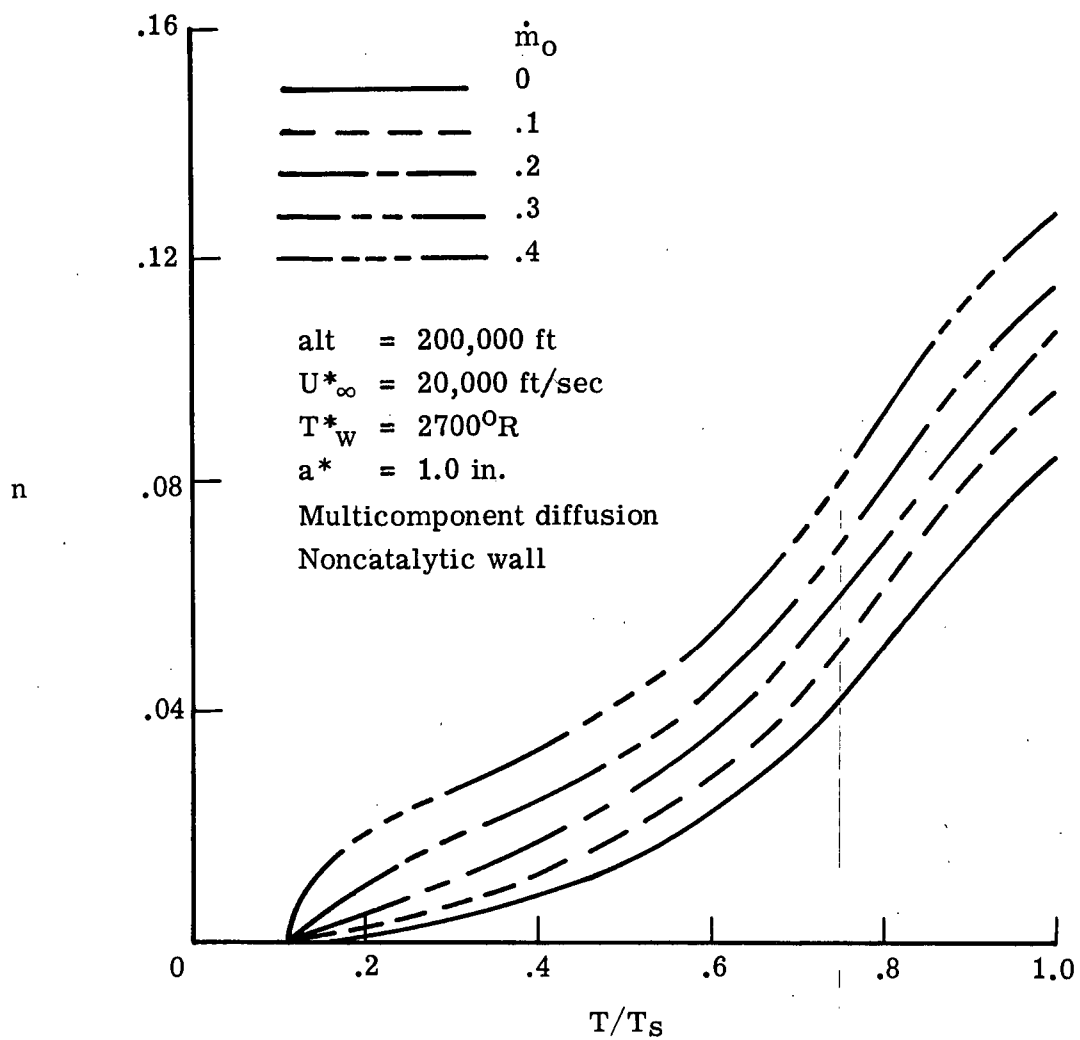


Figure 32.- Stagnation temperature profiles for different injection rates of equilibrium air into reacting nonequilibrium air.

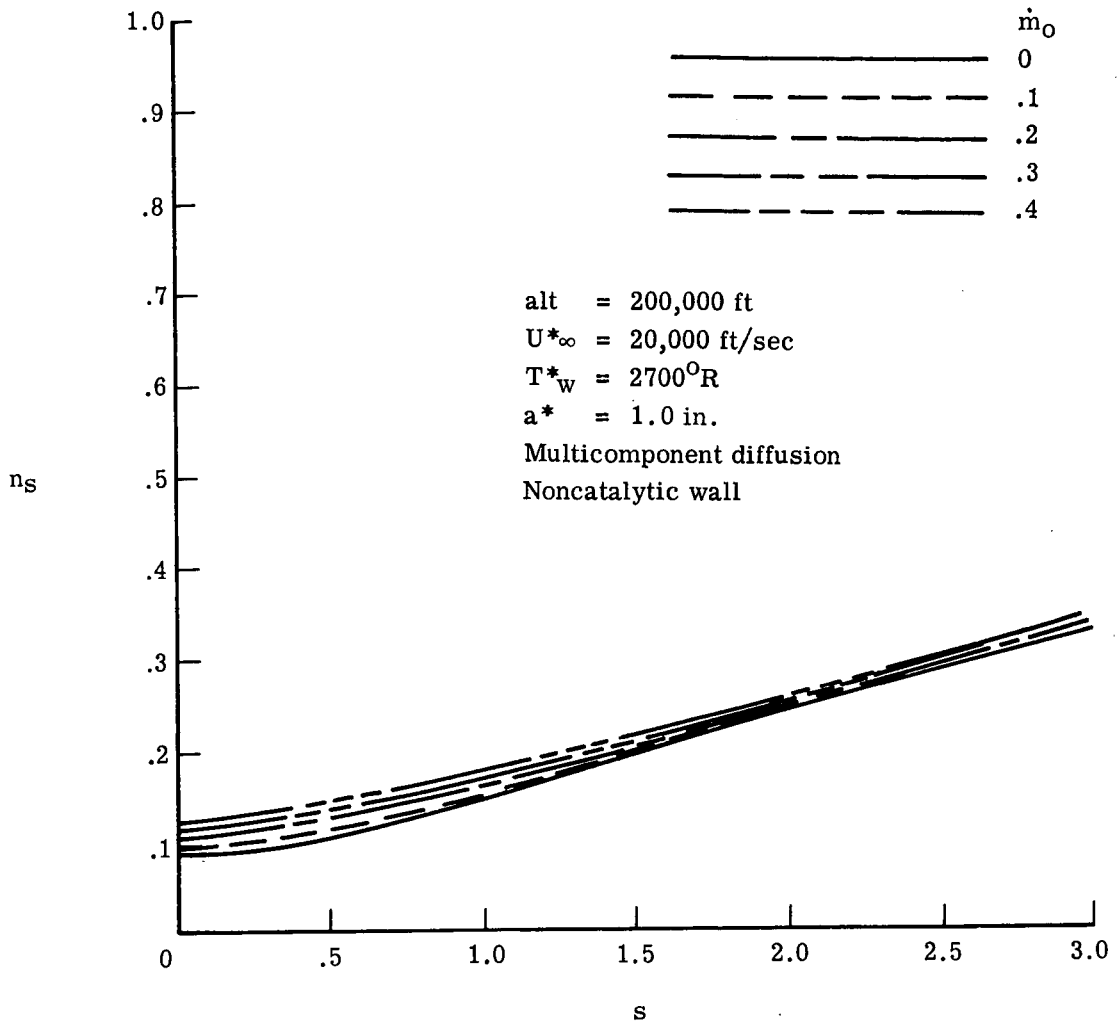


Figure 33.- Comparison of shock stand-off distances for different injection rates of equilibrium air into reacting nonequilibrium air.

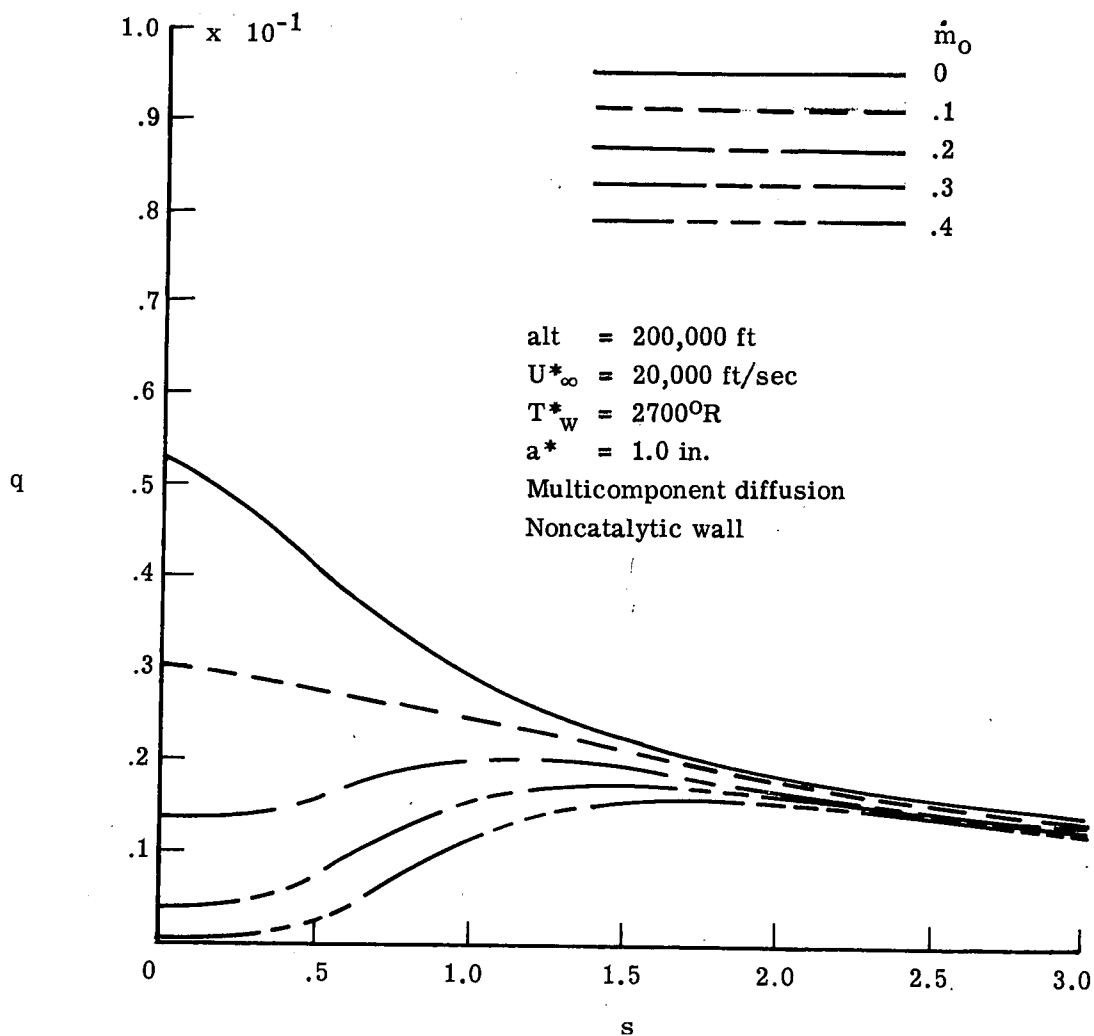


Figure 34.- Comparison of nondimensional heat transfer distributions for different injection rates of equilibrium air into reacting nonequilibrium air.

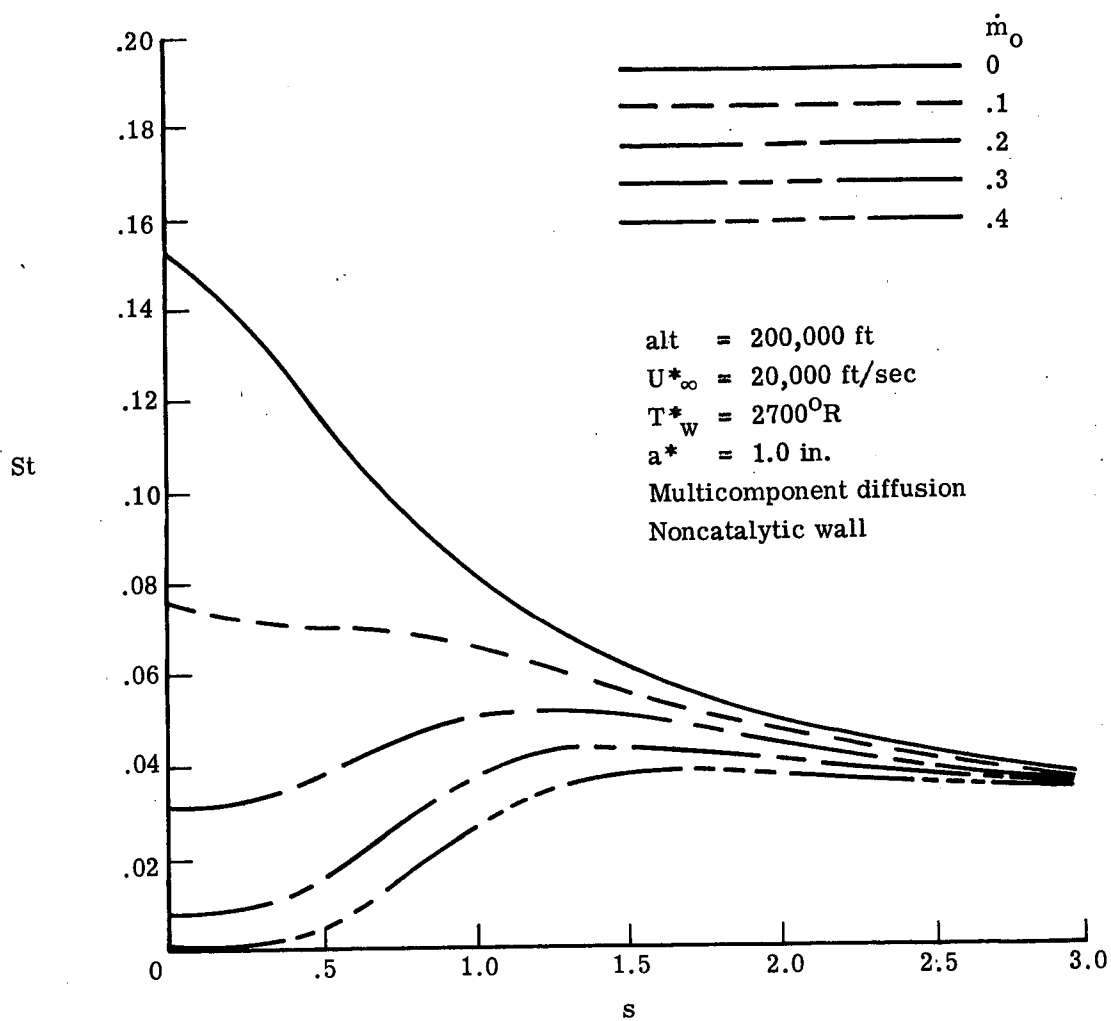


Figure 35.- Comparison of Stanton number distributions for different injection rates of equilibrium air into reacting non-equilibrium air.

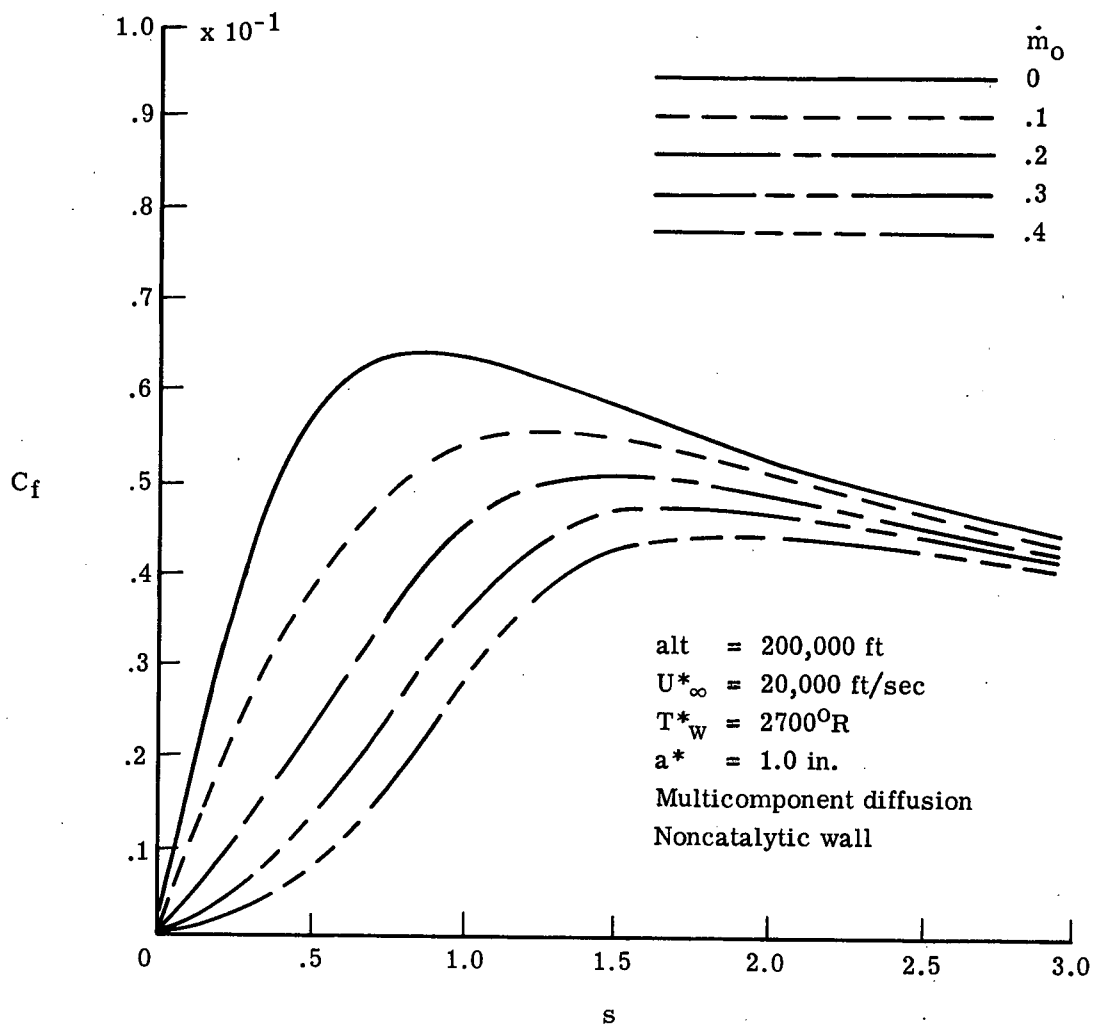


Figure 36.- Comparison of skin friction coefficient distributions for different injection rates of equilibrium air into reacting nonequilibrium air.

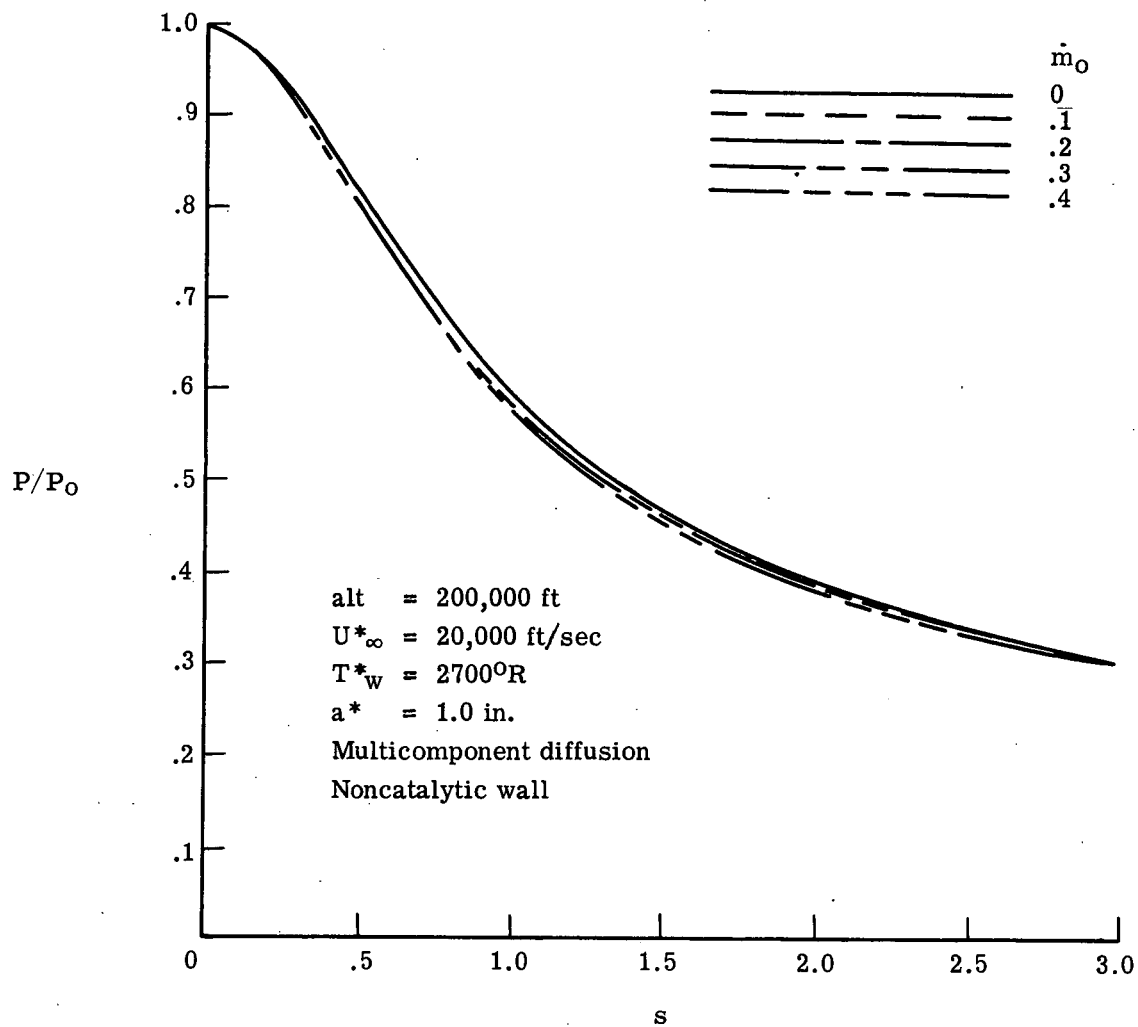


Figure 37.- Comparison of wall pressure ratio distributions for different injection rates of equilibrium air into reacting nonequilibrium air.

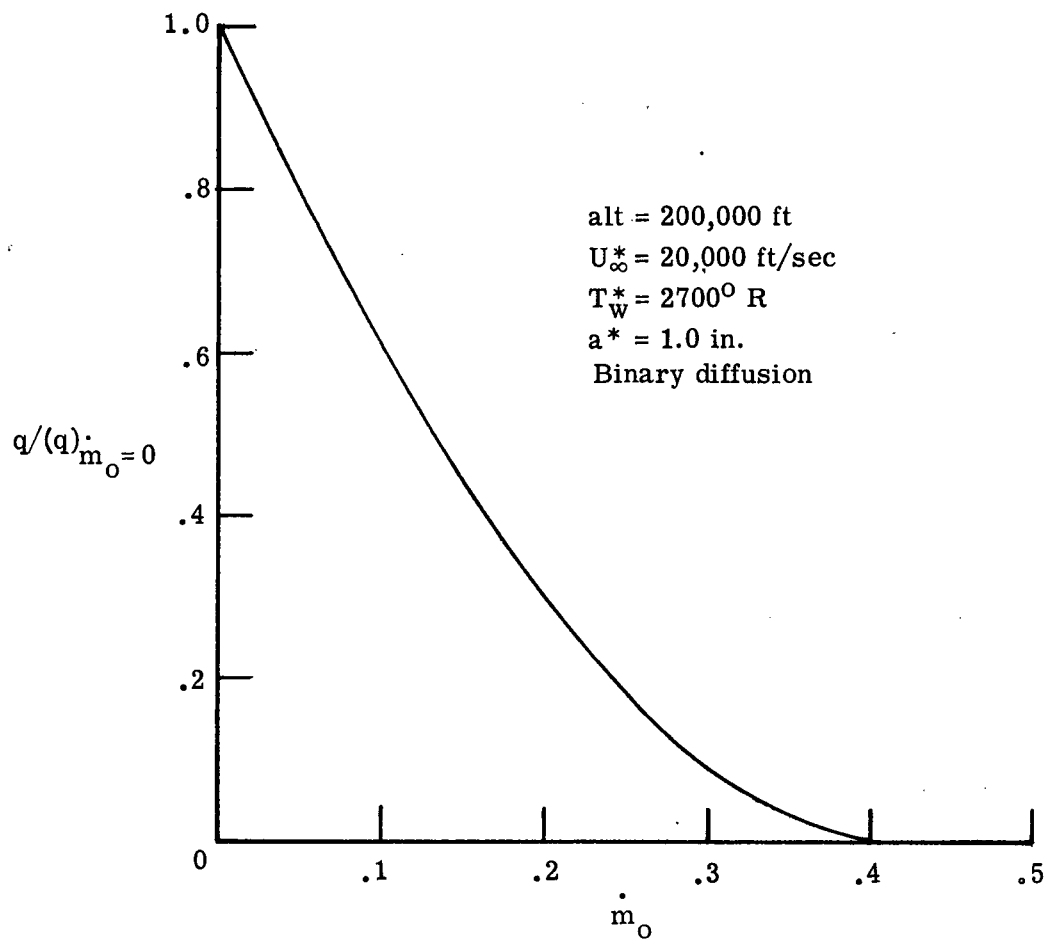


Figure 38.- Stagnation heat transfer as influenced by injecting equilibrium air into reacting equilibrium air.

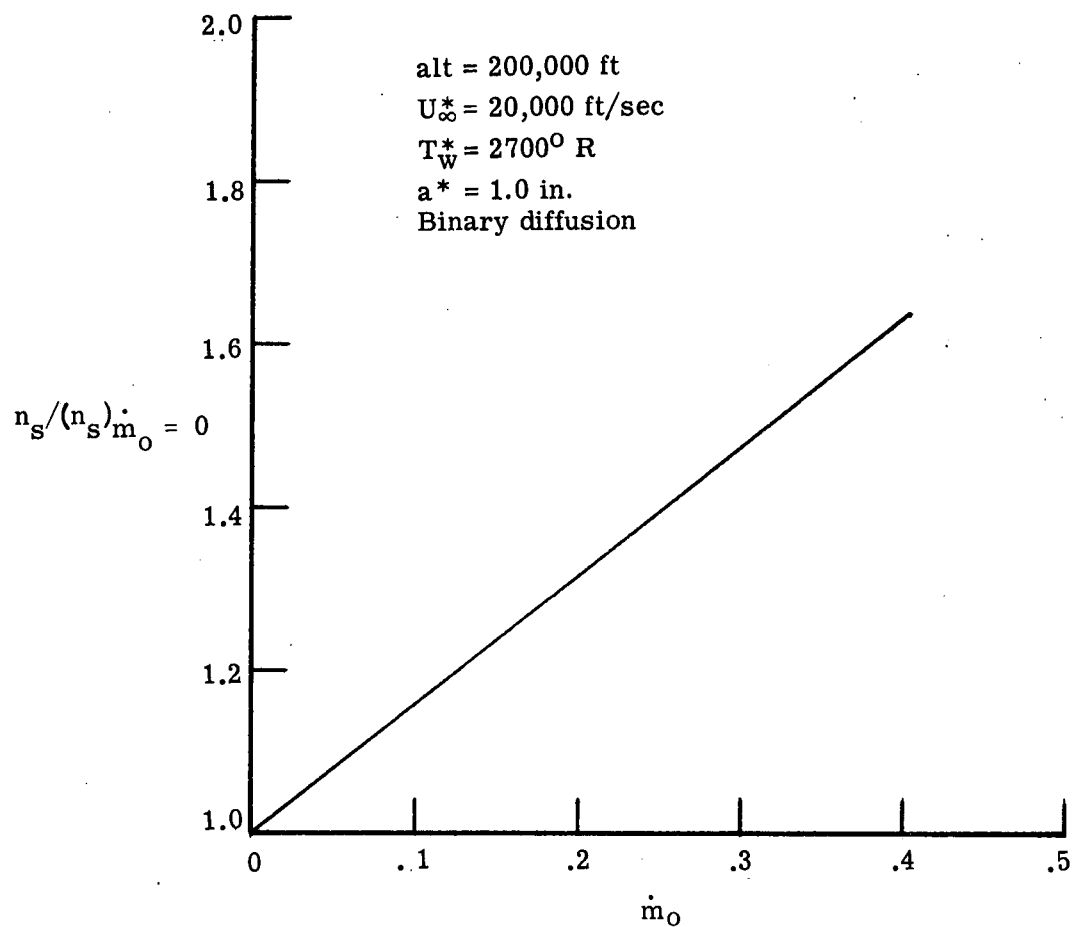


Figure 39.- Stagnation shock stand-off distance as influenced by injection of equilibrium air into reacting equilibrium air.

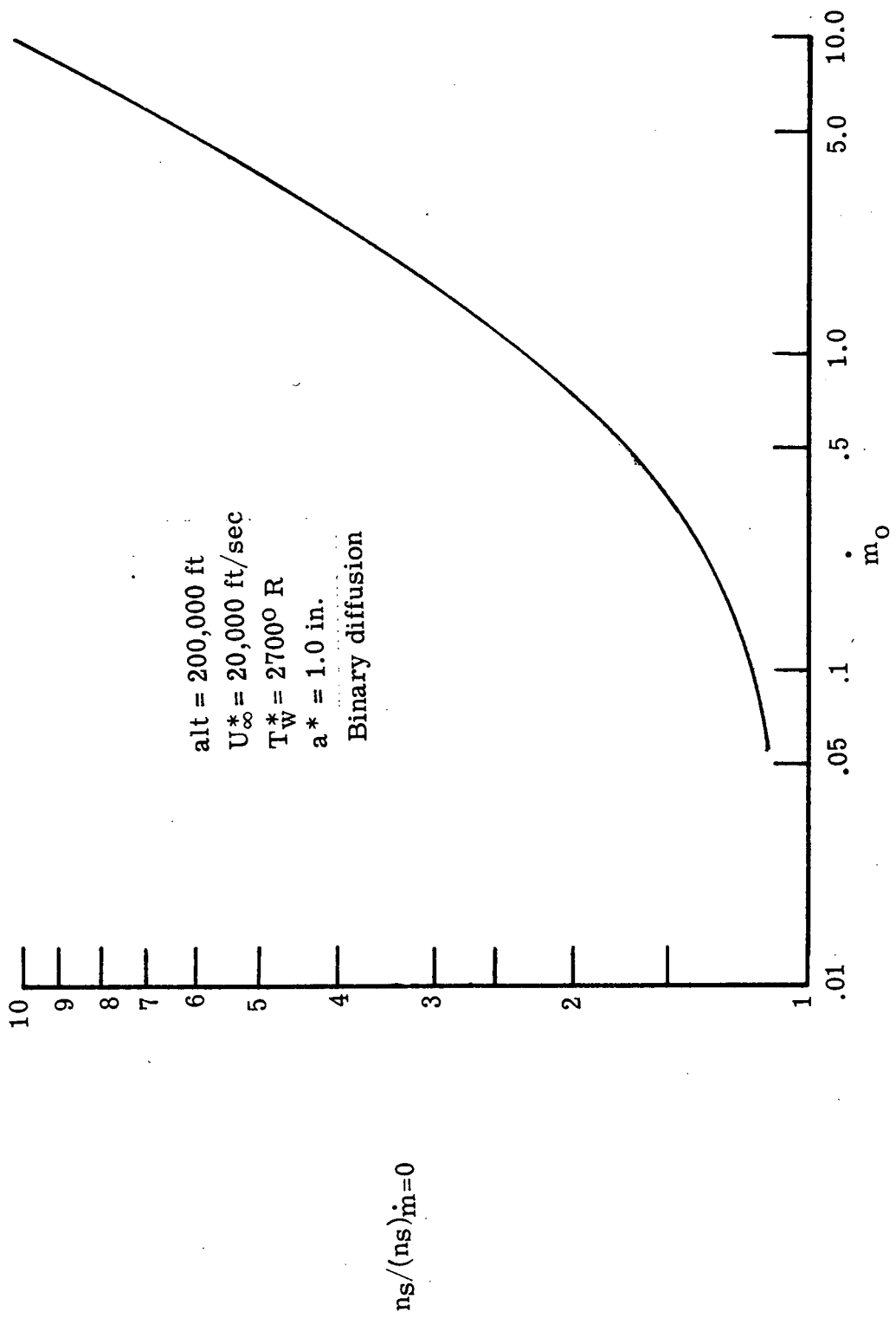


Figure 40.- Stagnation shock stand-off distance as influenced by large mass injection rates of equilibrium air into reacting equilibrium air.

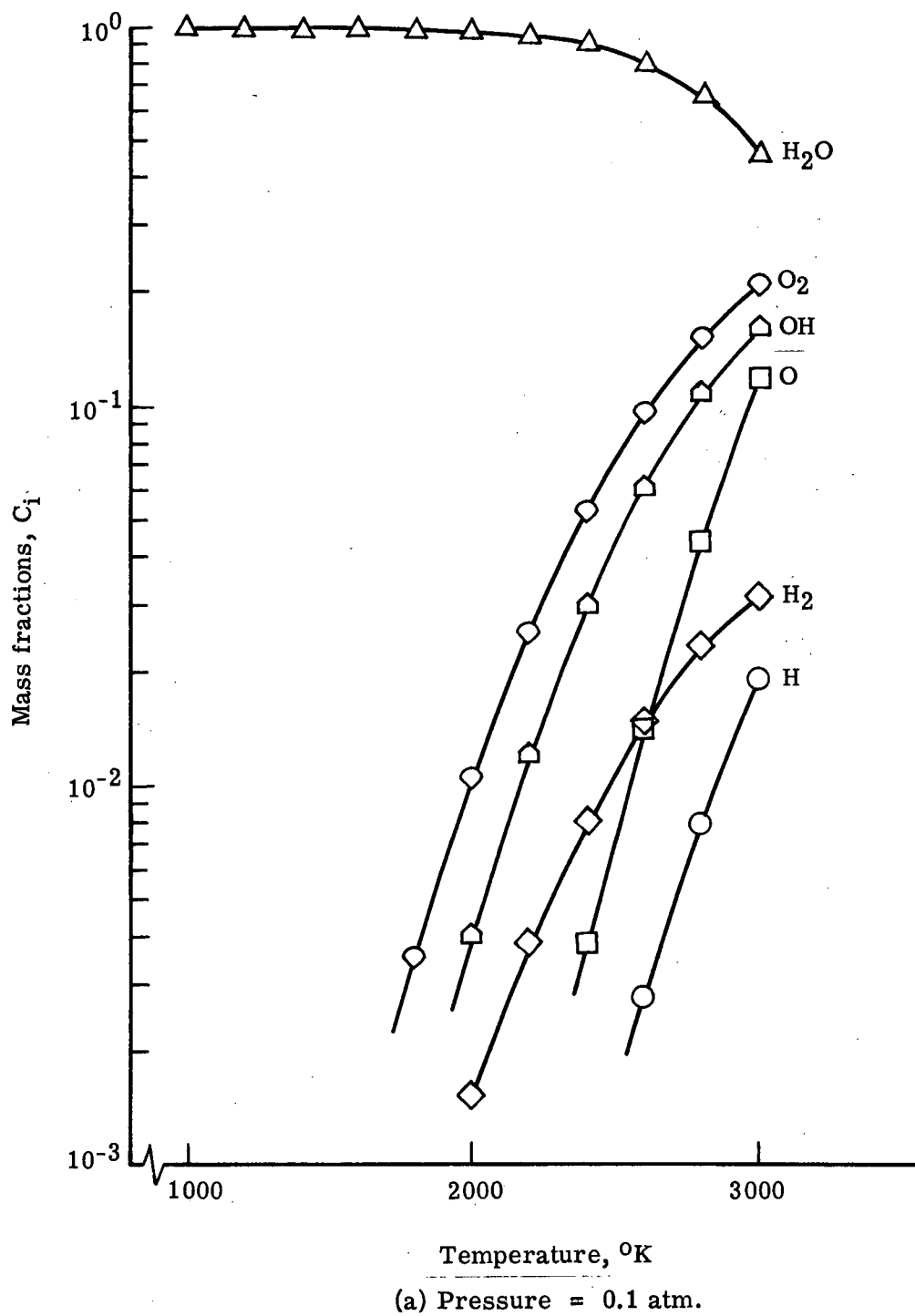


Figure 41.- Equilibrium composition of H_2O .

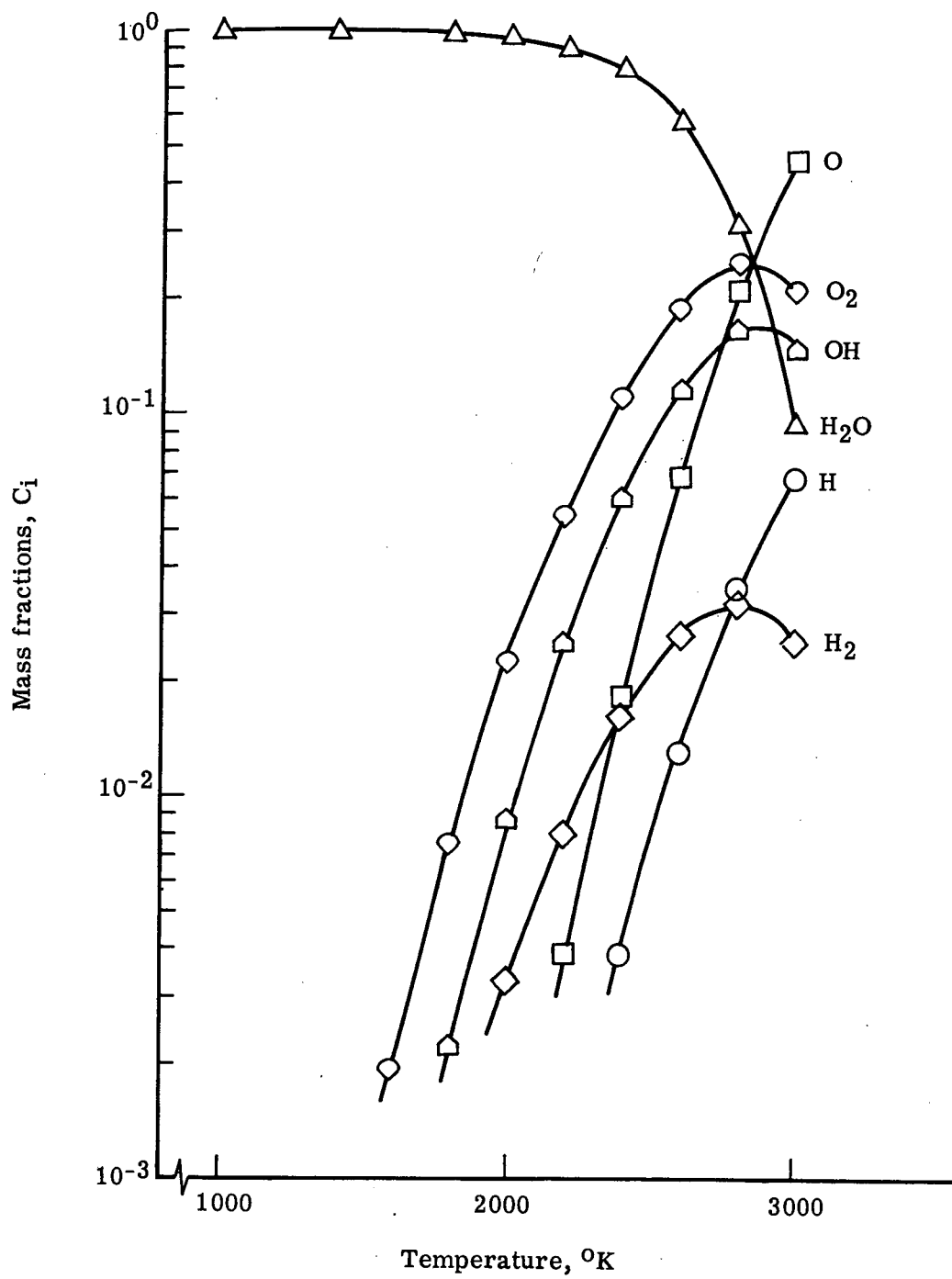


Figure 41.- Concluded.

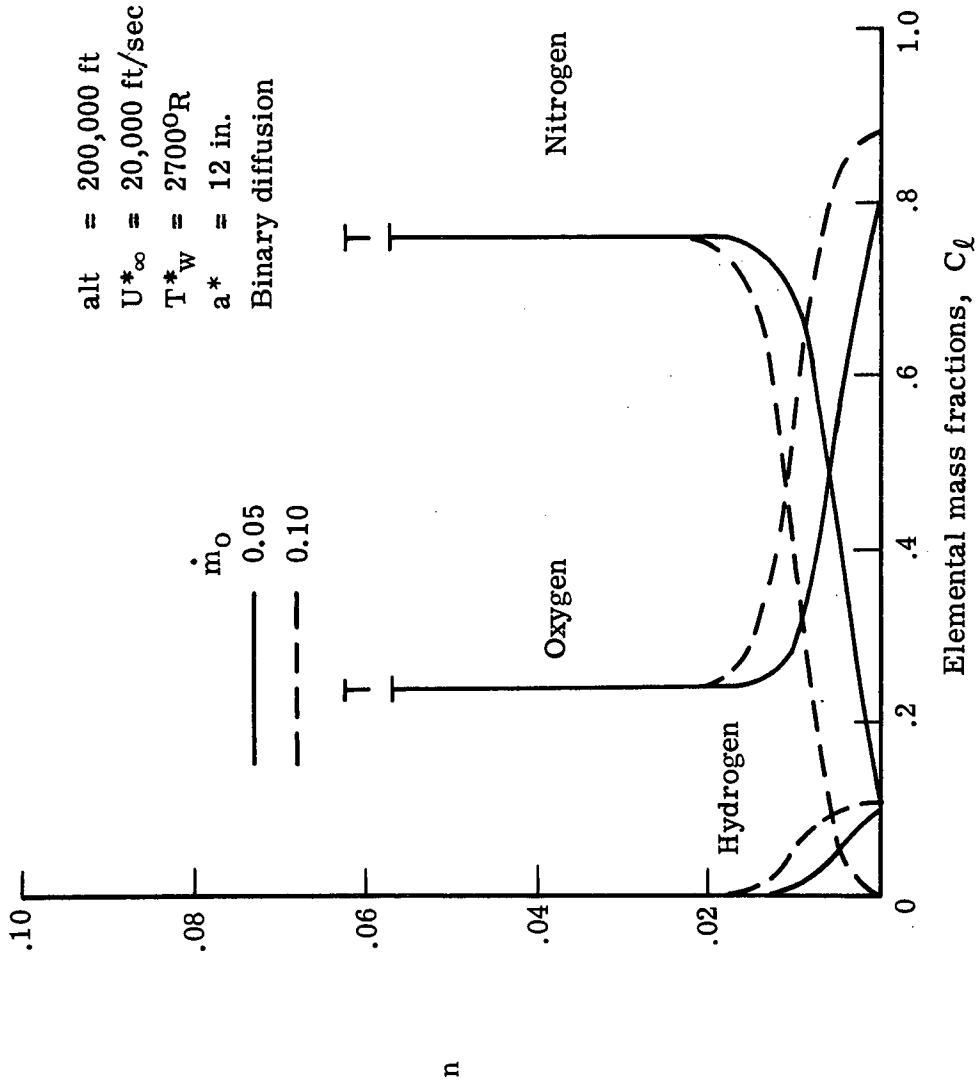


Figure 42.- Stagnation elemental profiles for injecting H_2O into equilibrium air.

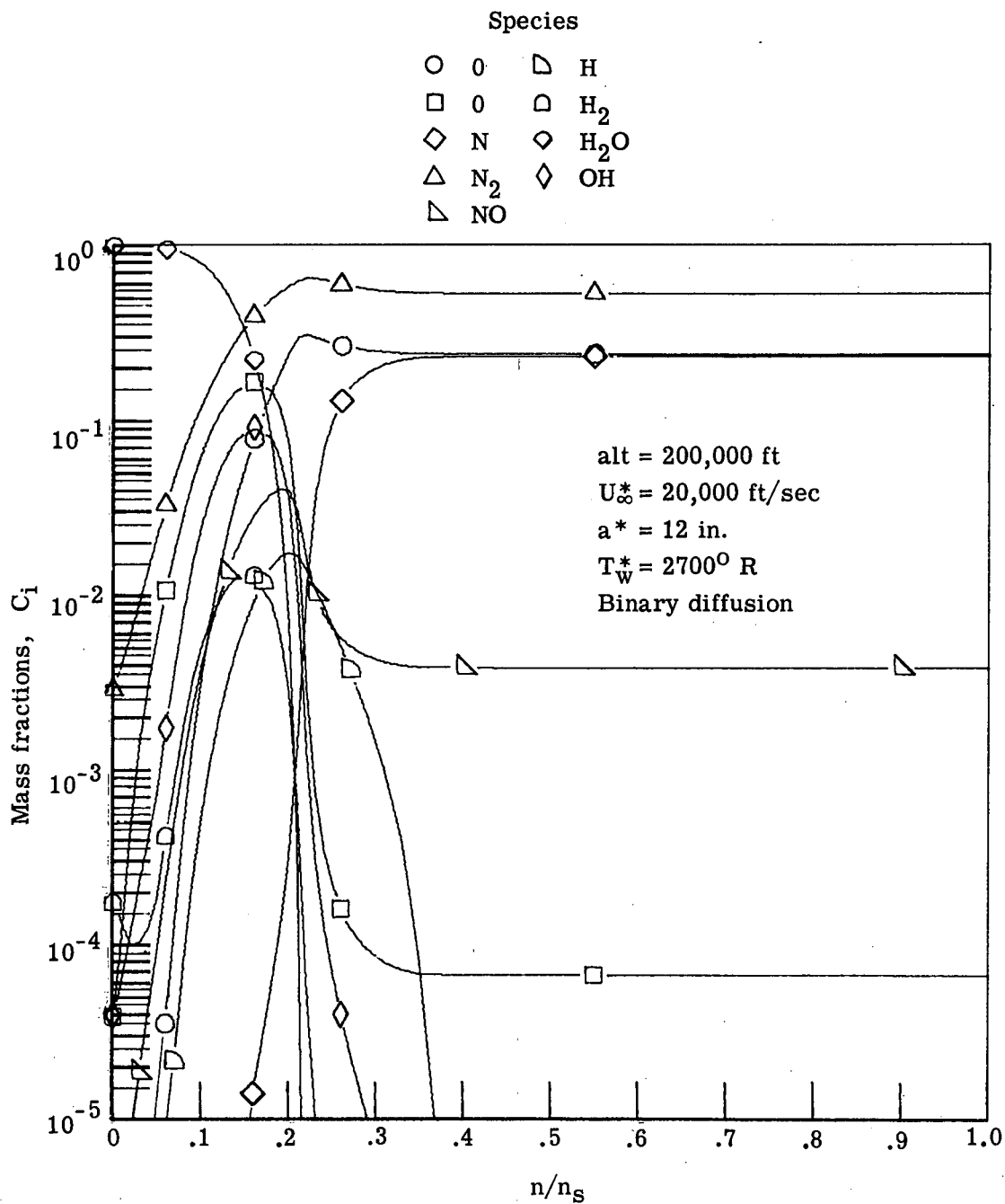


Figure 43.- Species profiles for a 0.1 injection rate of H₂O into equilibrium air.

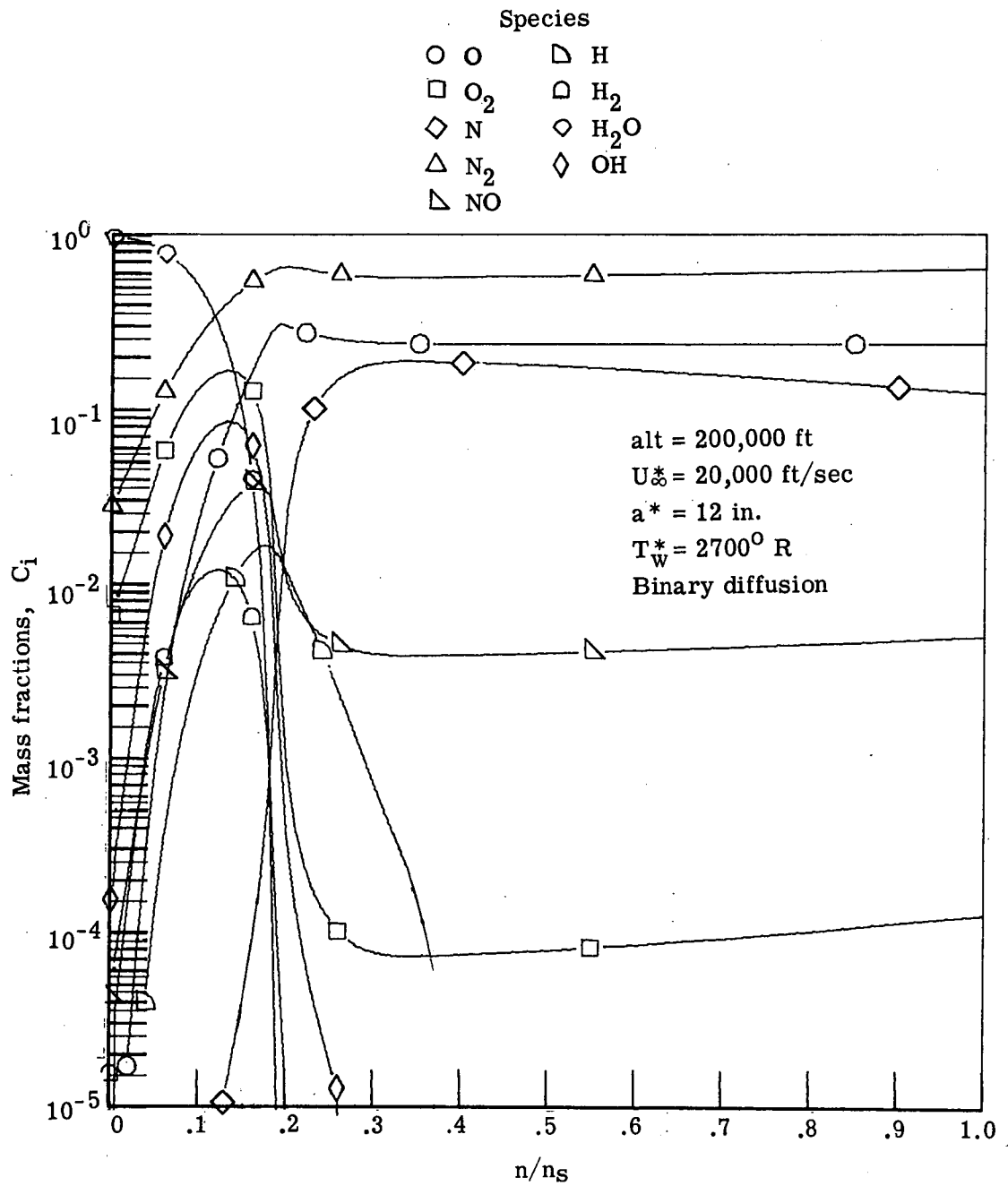
(b) $s = 0.4$.

Figure 43.- Continued.

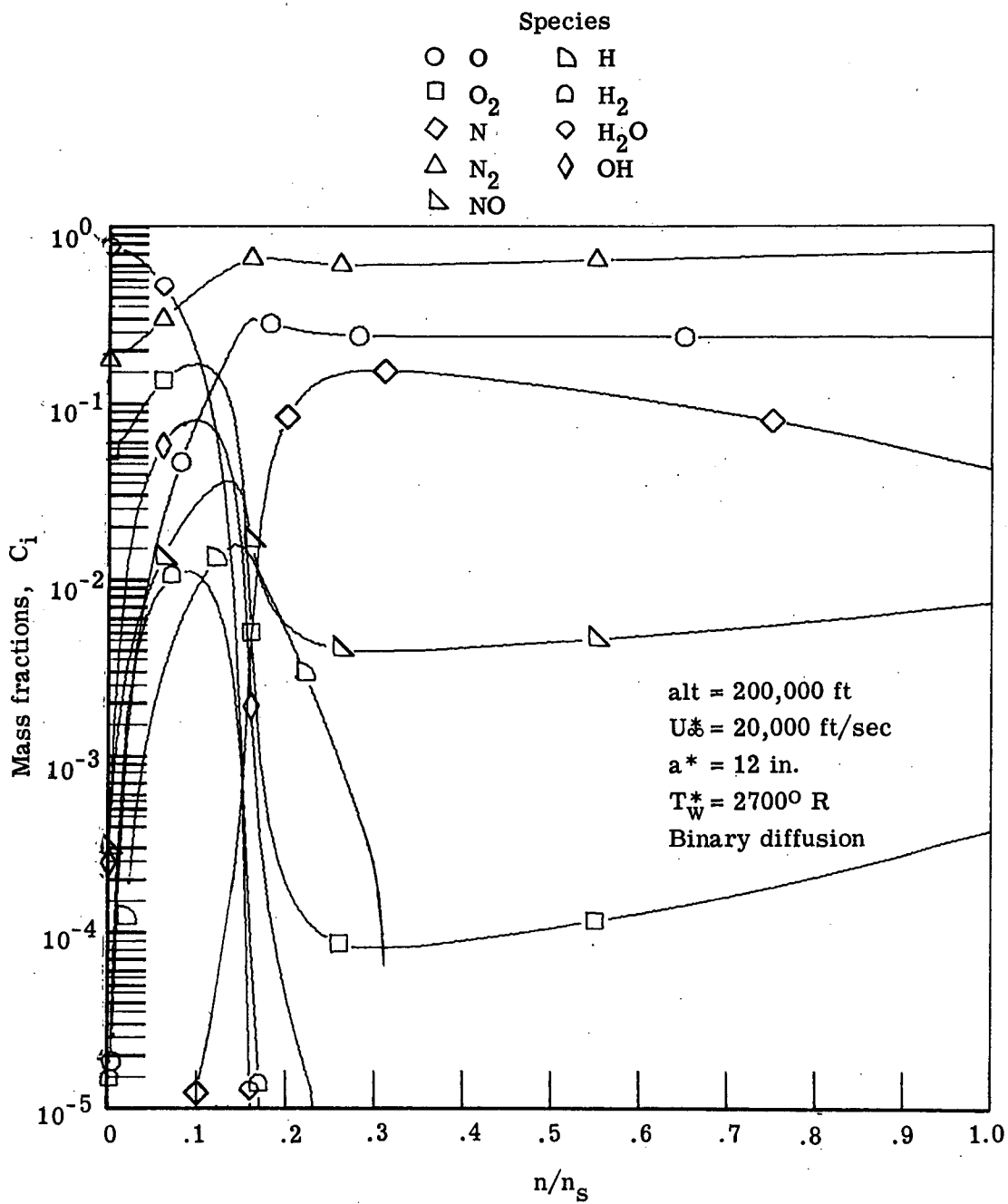


Figure 43.- Concluded.

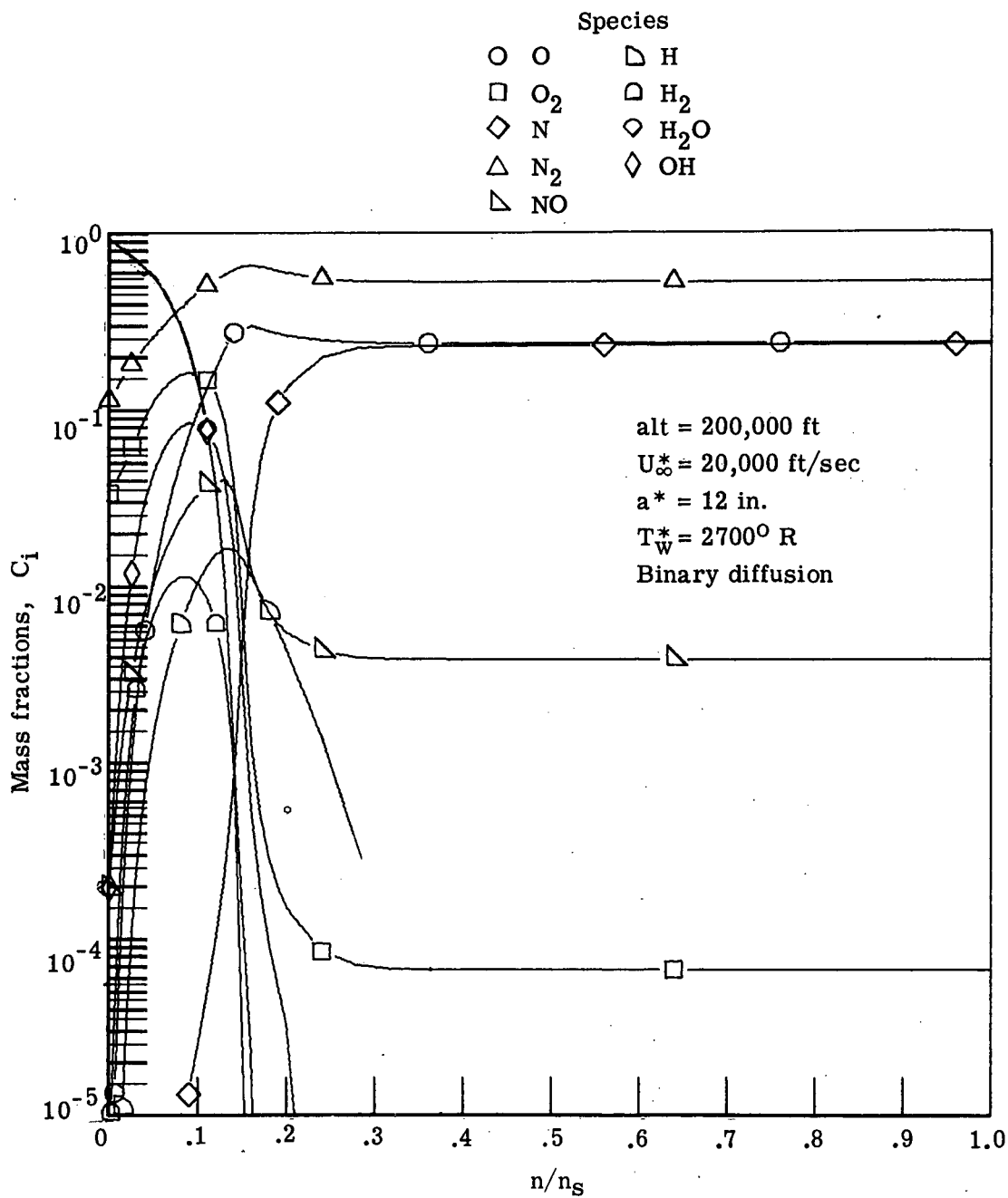
(a) $s = 0.0$.

Figure 44.- Species profiles for a 0.05 injection rate of H₂O into equilibrium air.

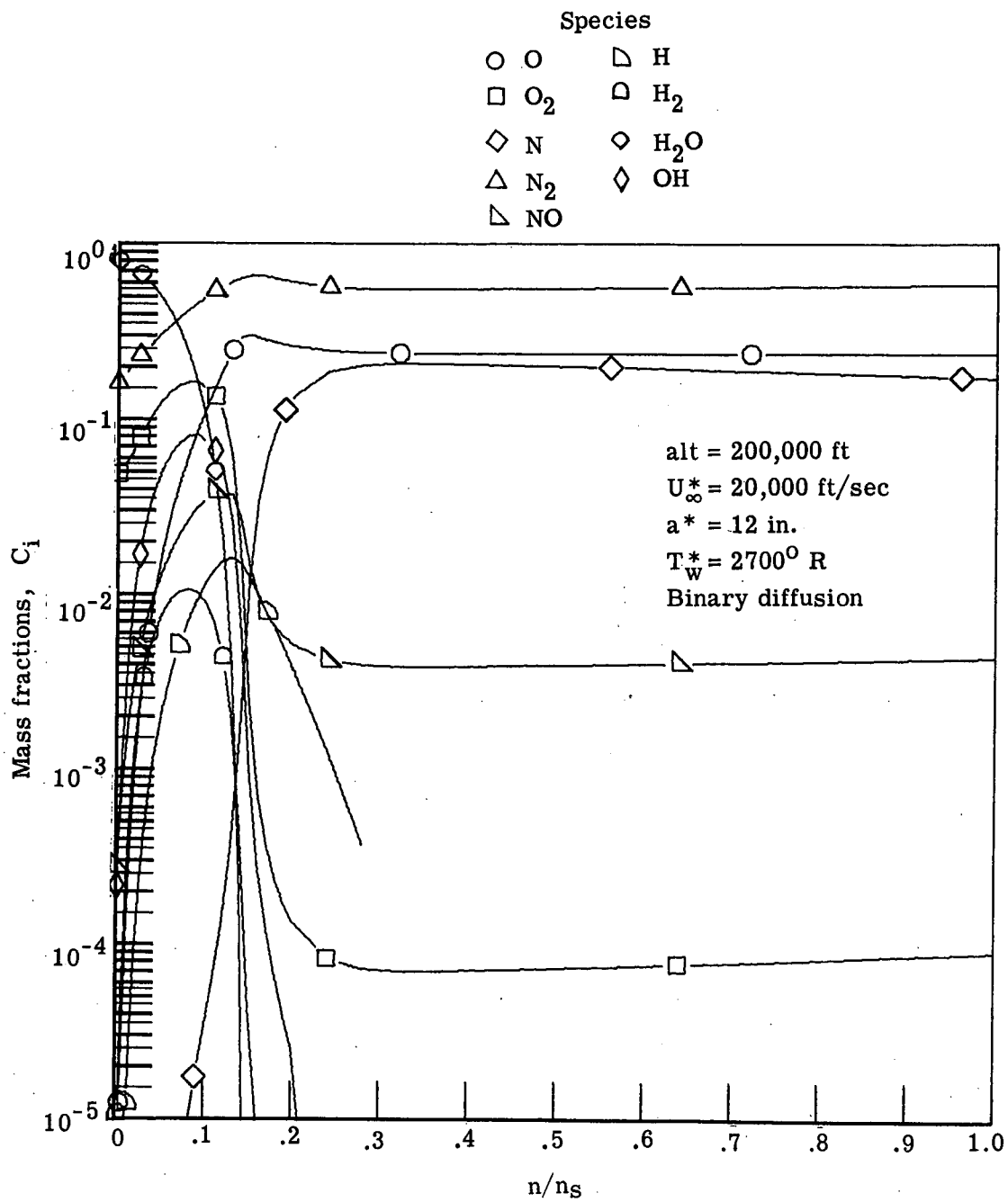
(b) $s = 0.4$.

Figure 44.- Continued.

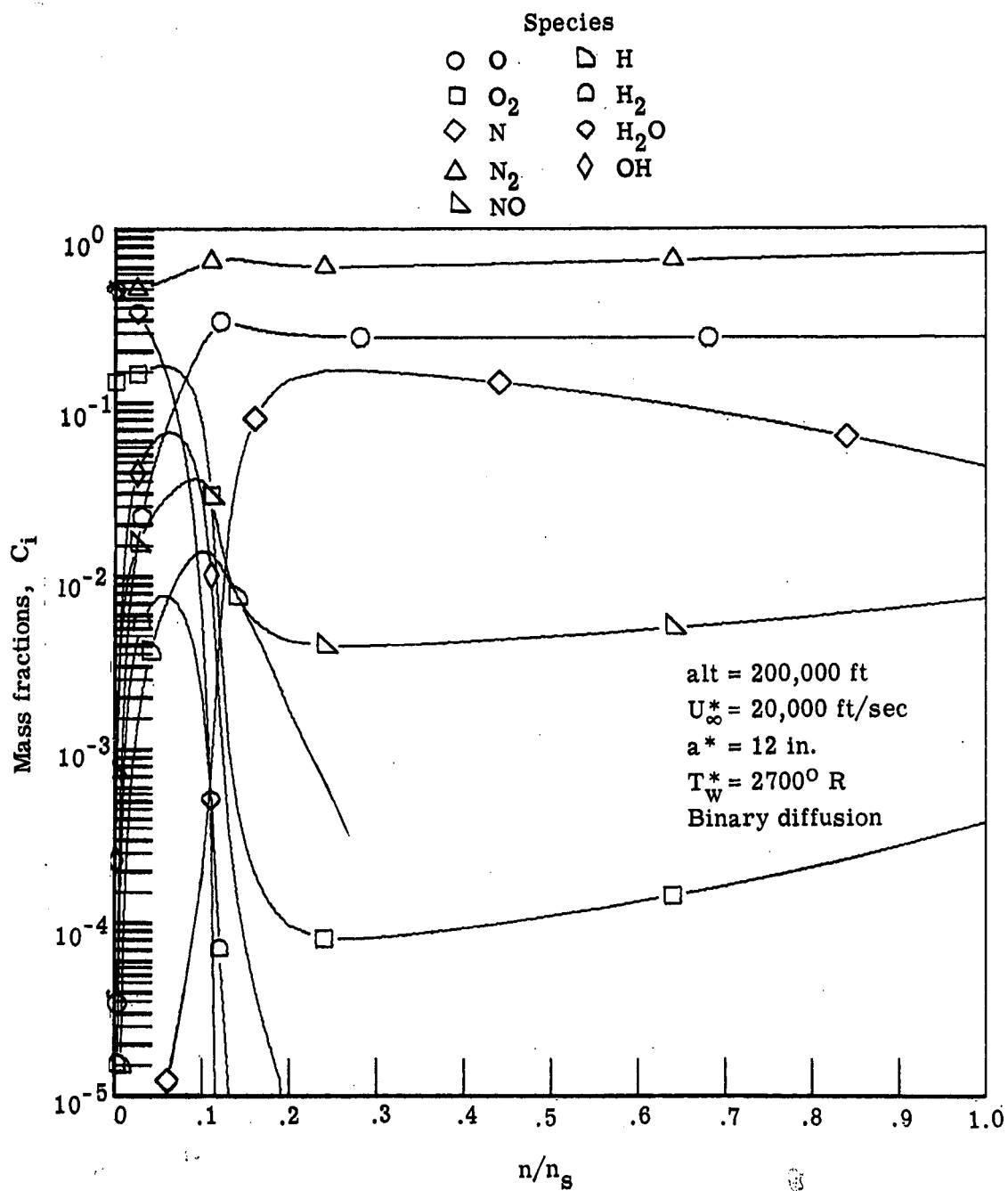
(c) $s = 1.0$.

Figure 44.- Concluded.

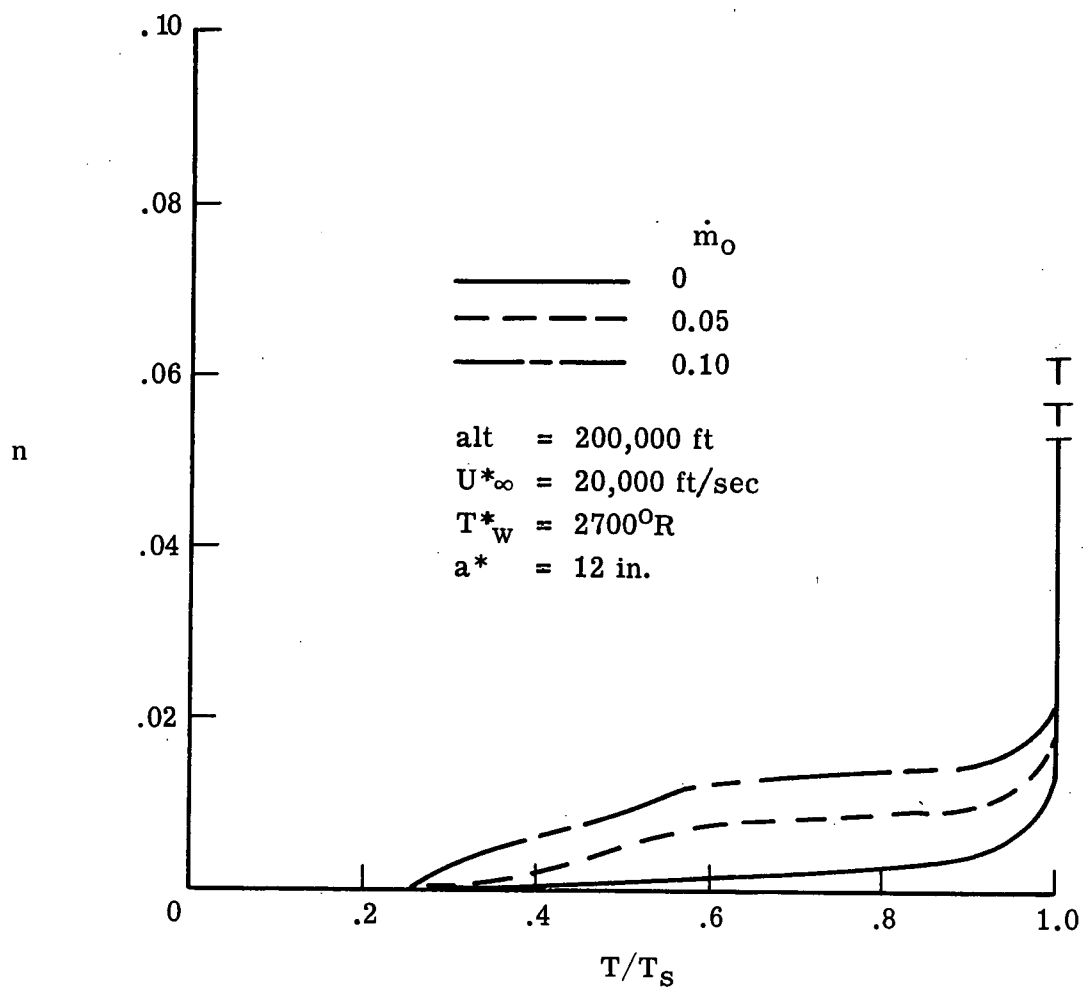


Figure 45.- Stagnation temperature profiles for different injection rates of H_2O into equilibrium air.

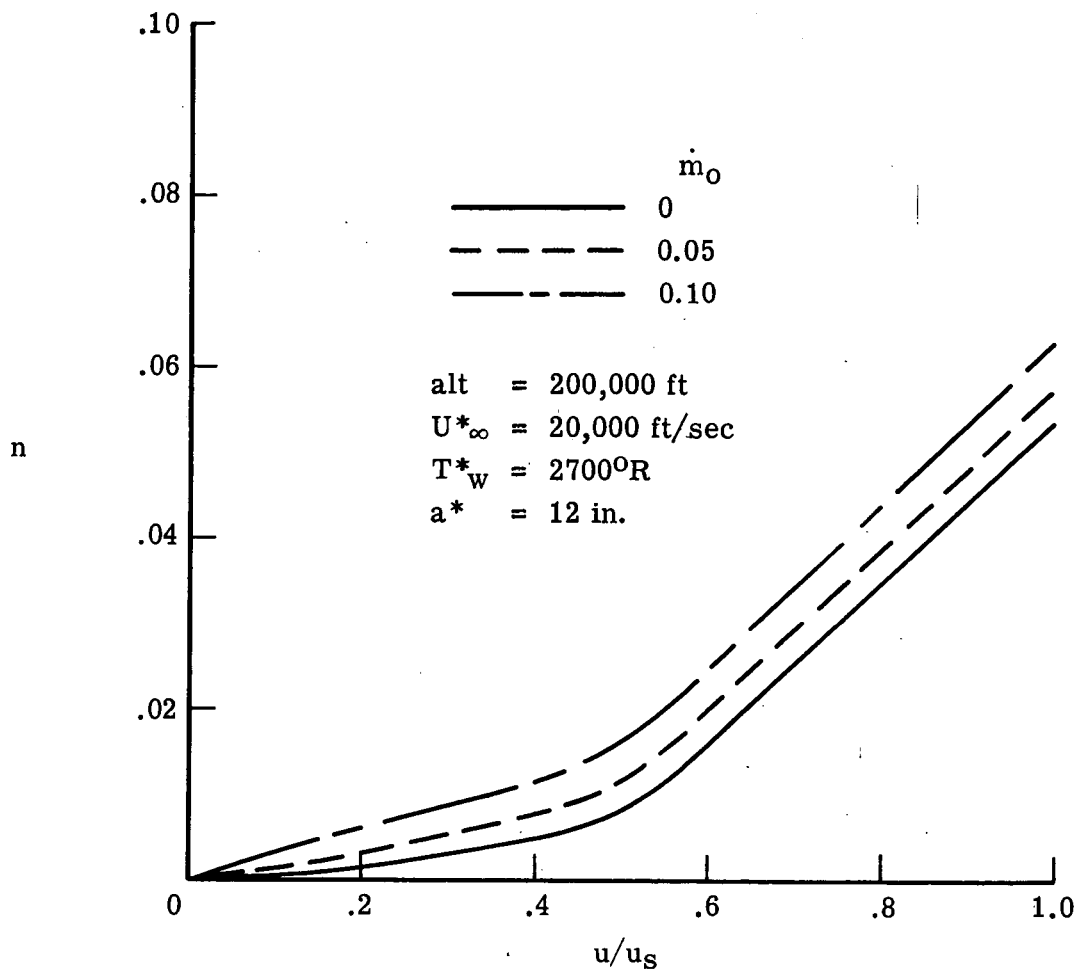


Figure 46.- Stagnation velocity profiles for different injection rates of H_2O into equilibrium air.

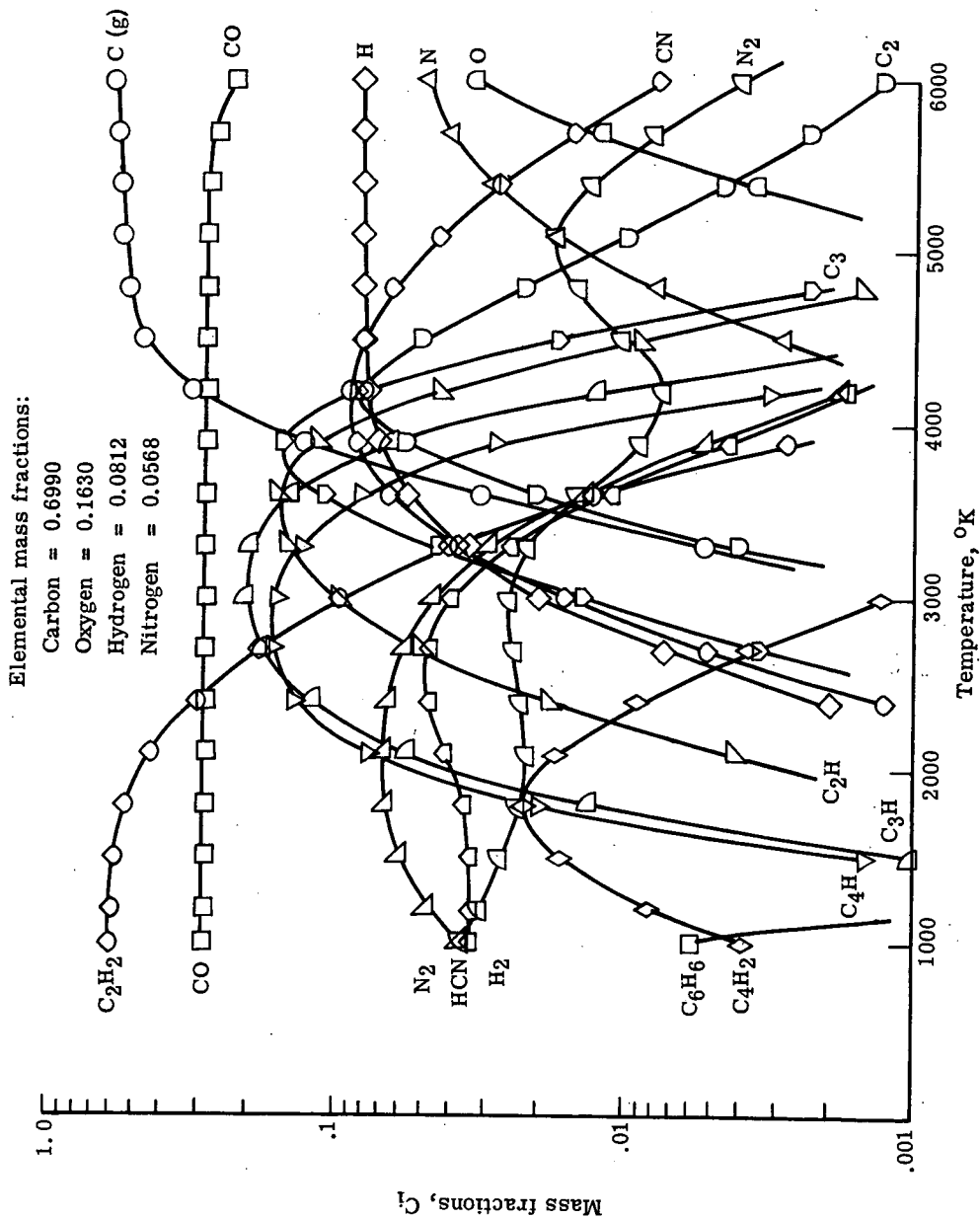


Figure 47.- Equilibrium composition of ablation products.

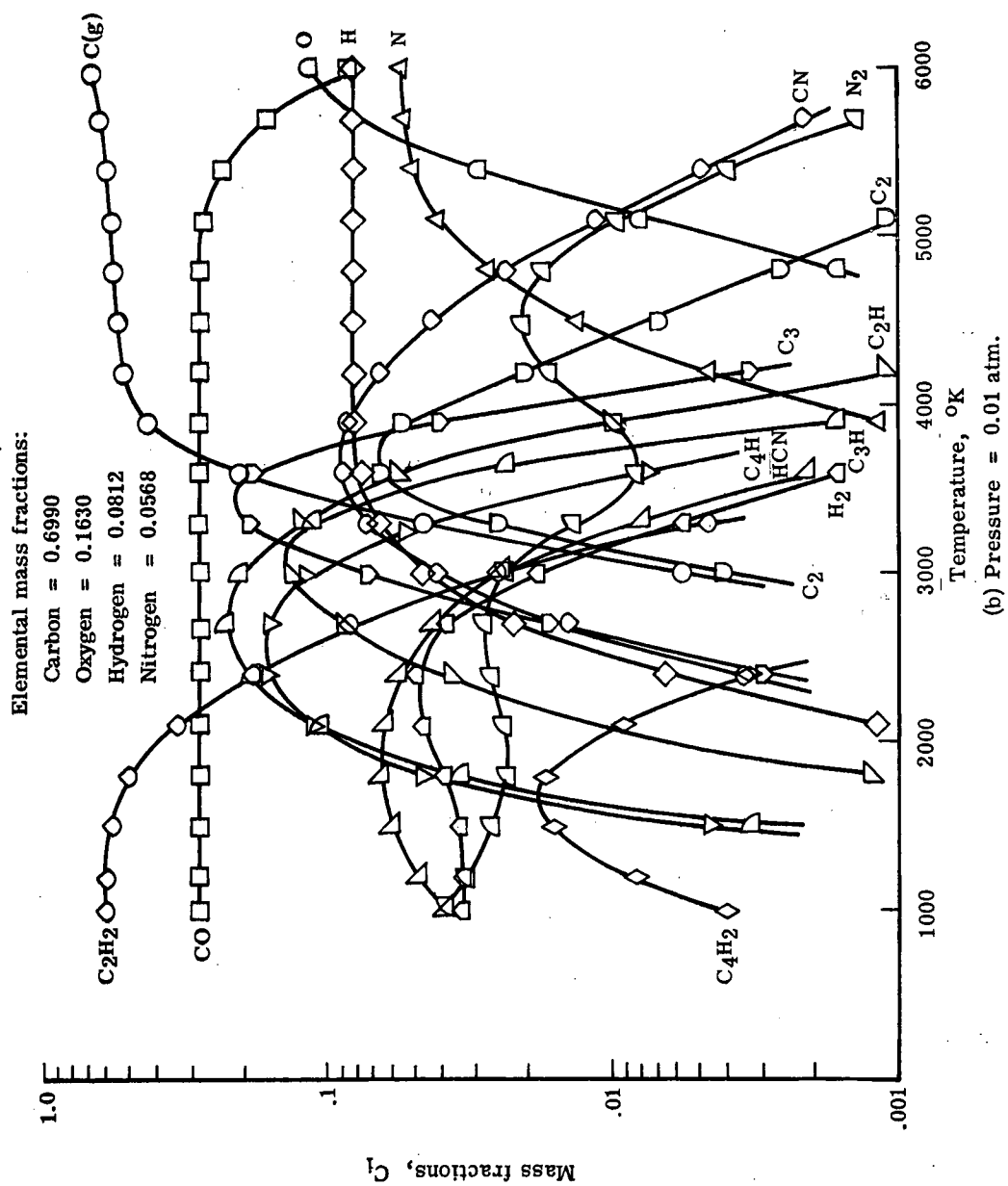


Figure 47.- Concluded.

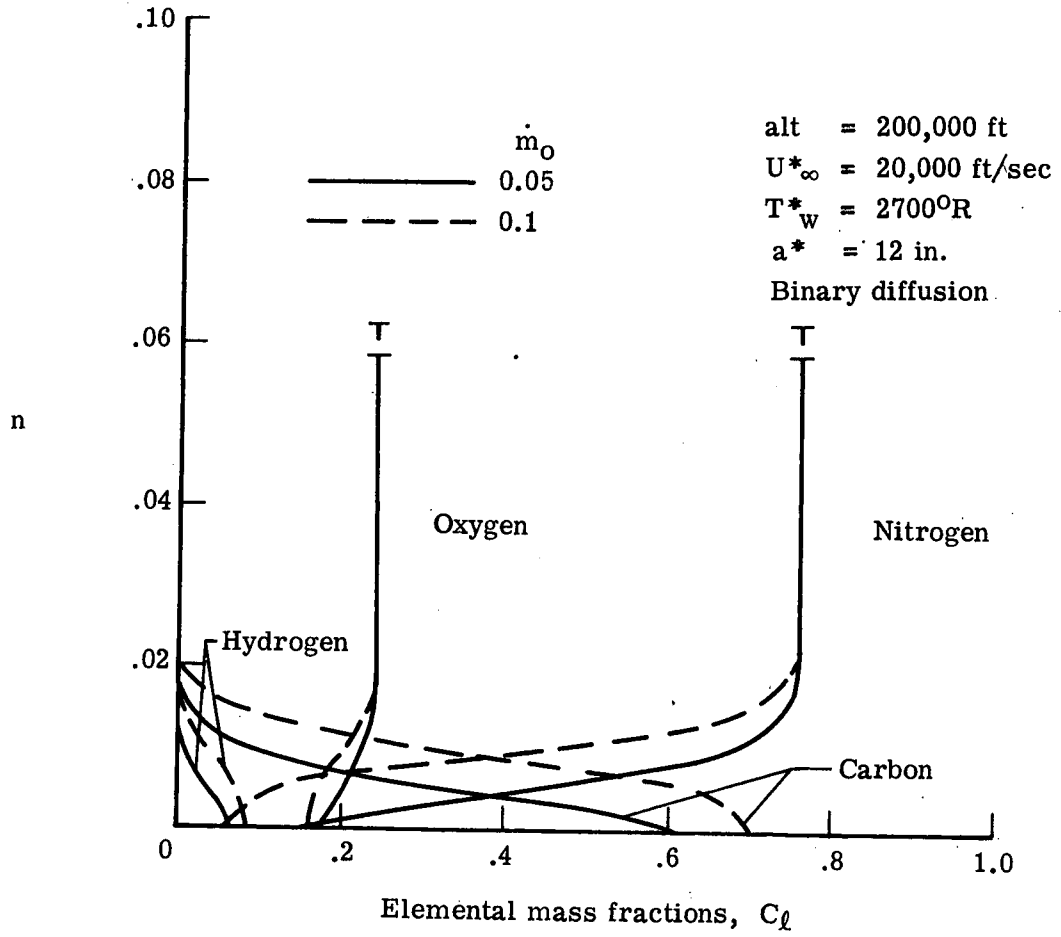


Figure 48.- Stagnation elemental profiles for injecting ablation species into equilibrium air.

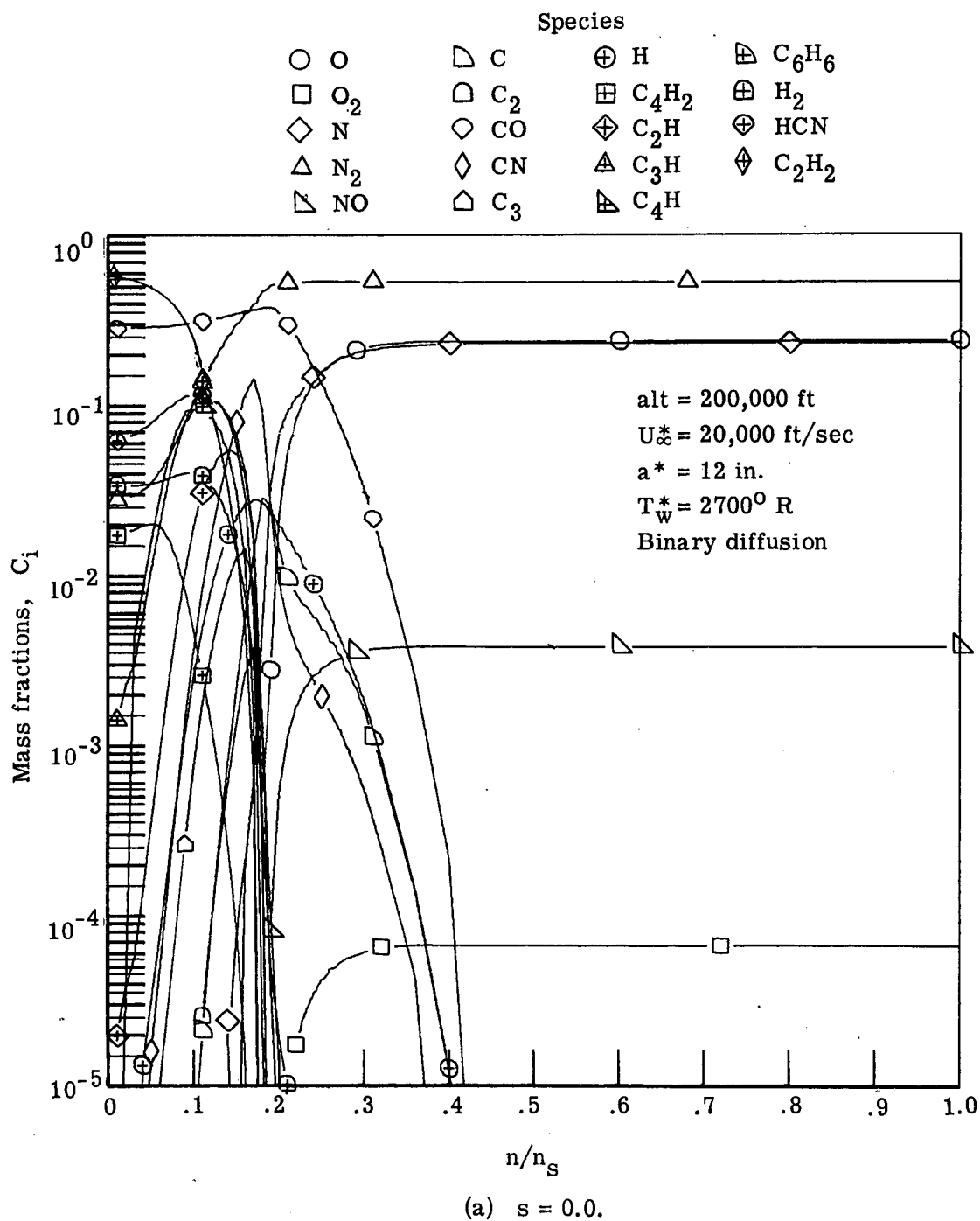


Figure 49.- Species profiles for a 0.1 injection rate of ablation species into equilibrium air.

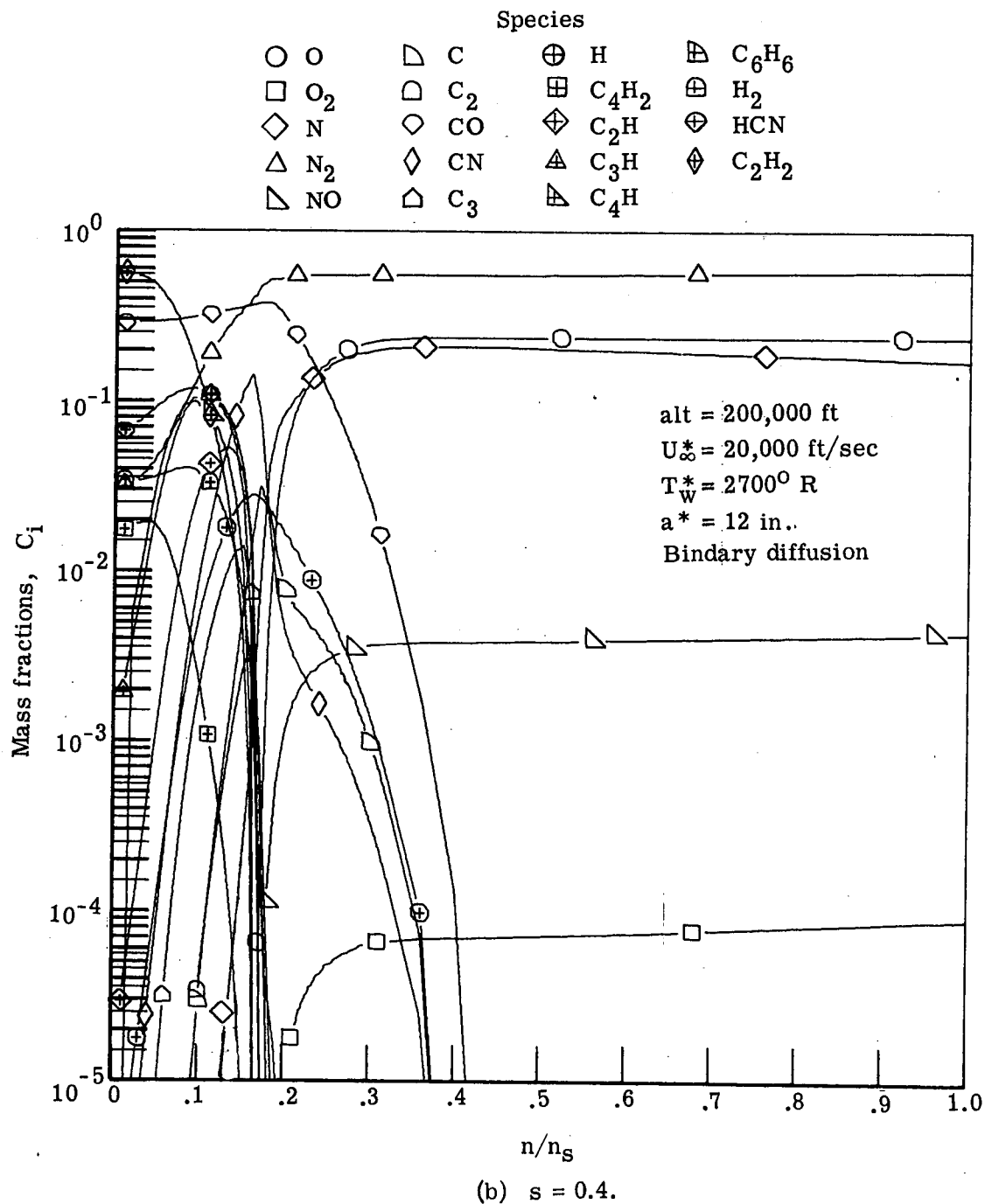


Figure 49.- Concluded.

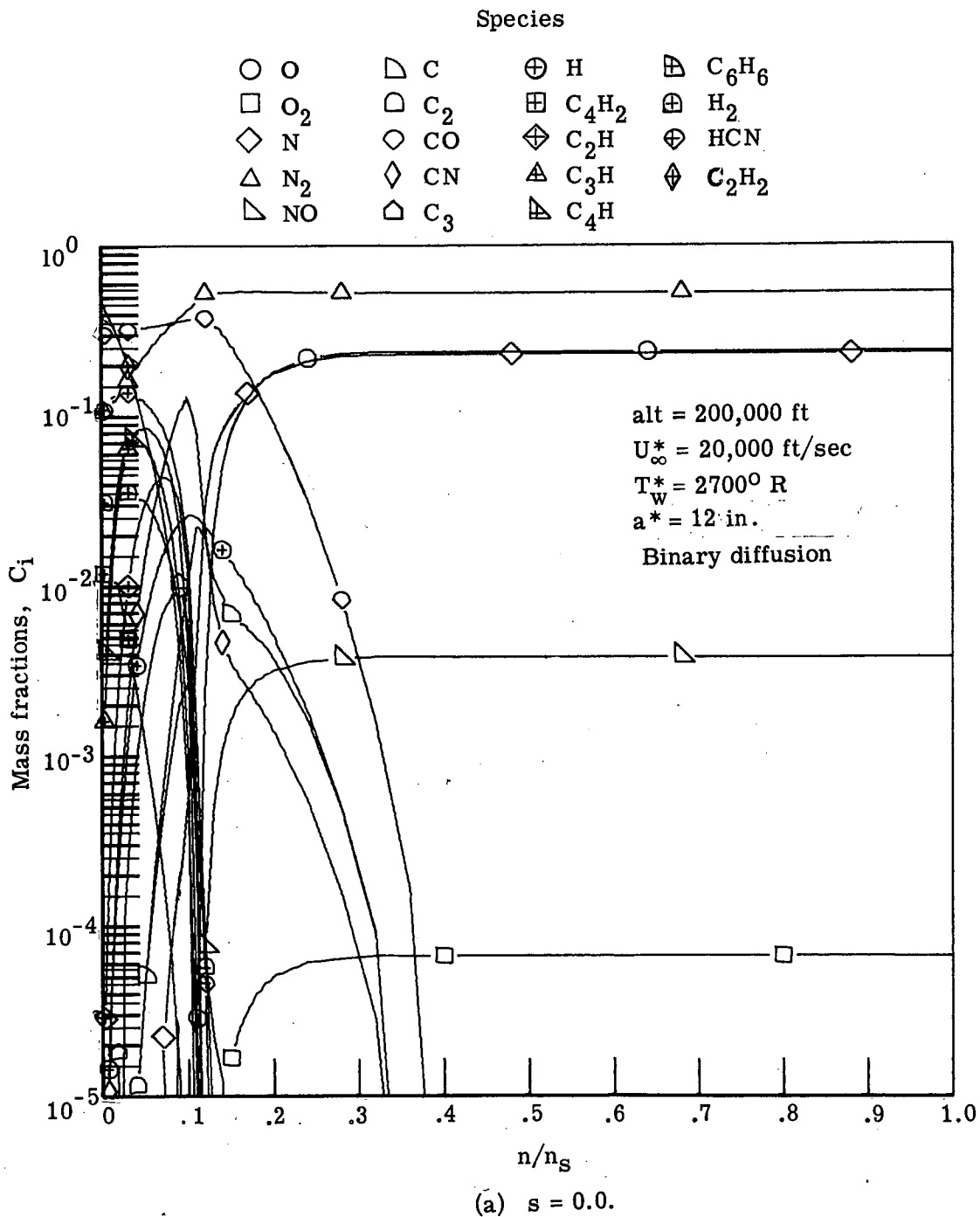


Figure 50.- Species profiles for a 0.05 injection rate of ablation species into equilibrium air.

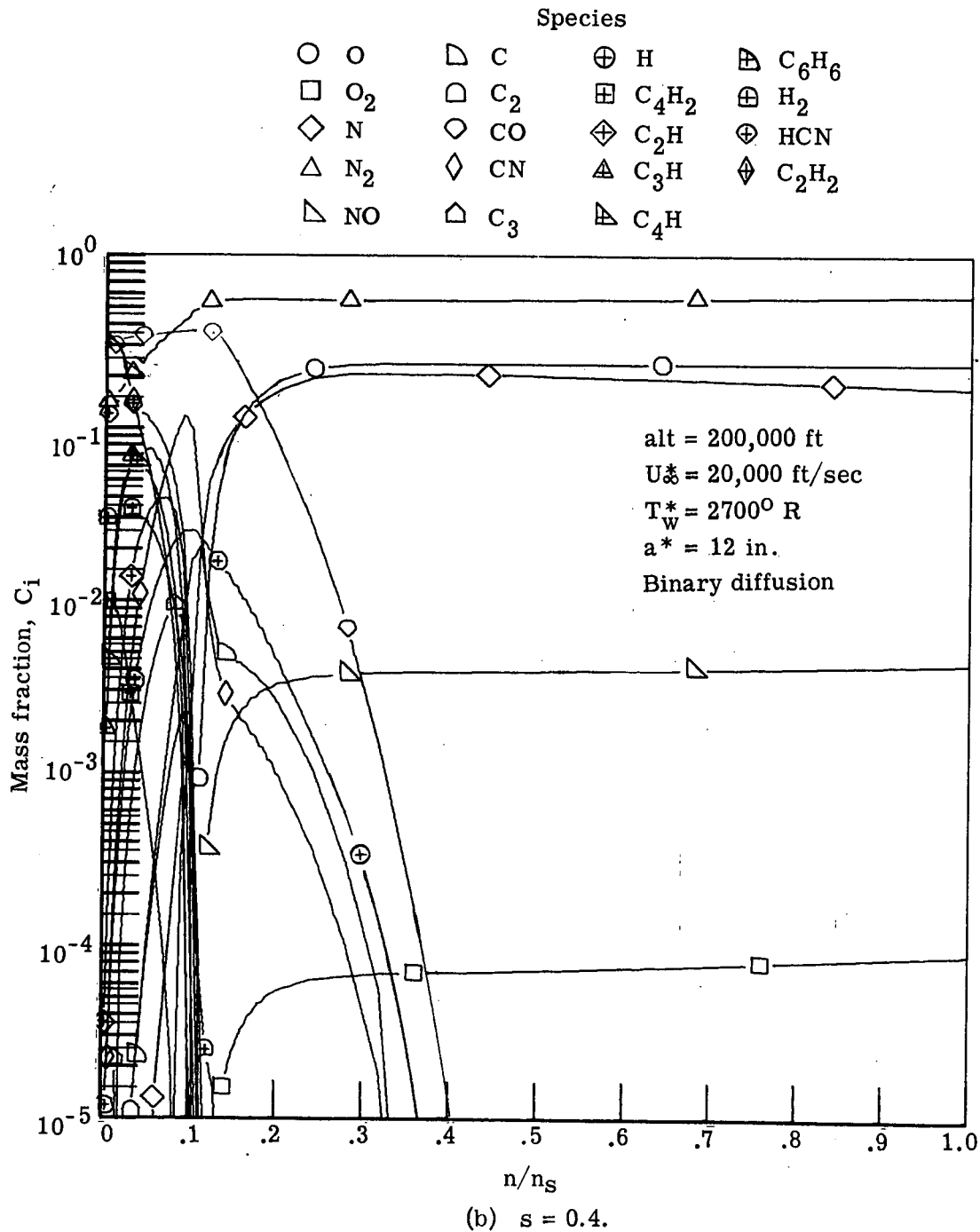


Figure 50.- Concluded.

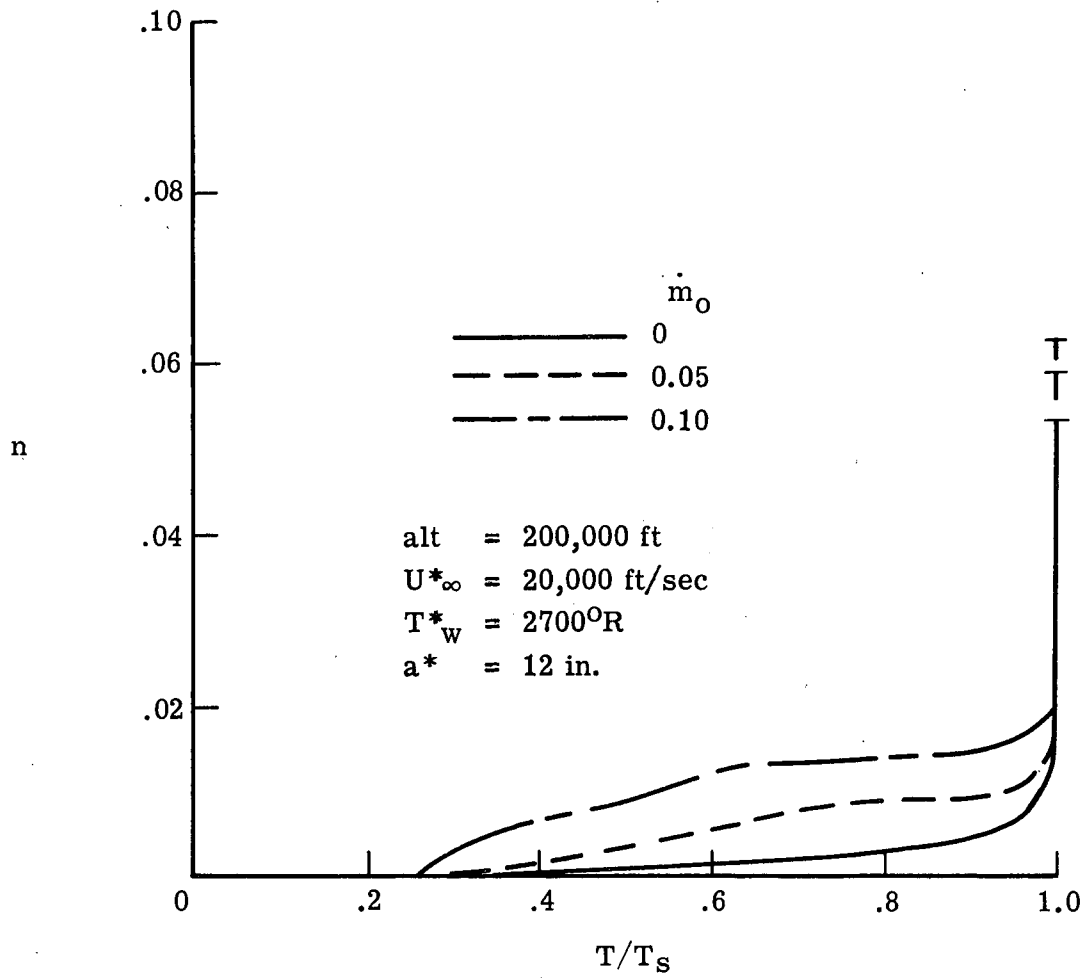


Figure 51.- Stagnation temperature profiles for different injection rates of ablation products.

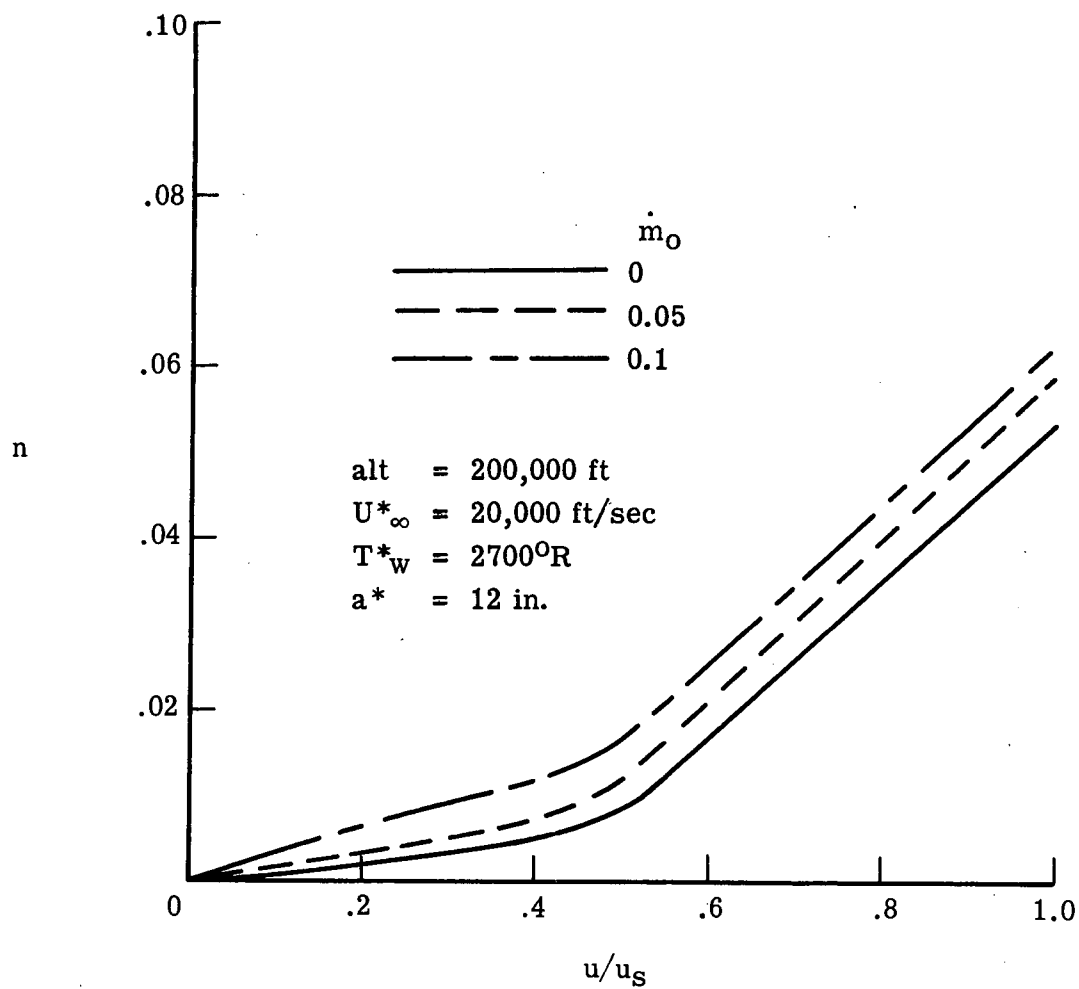


Figure 52.- Stagnation velocity profiles for different injection rates of ablation products.

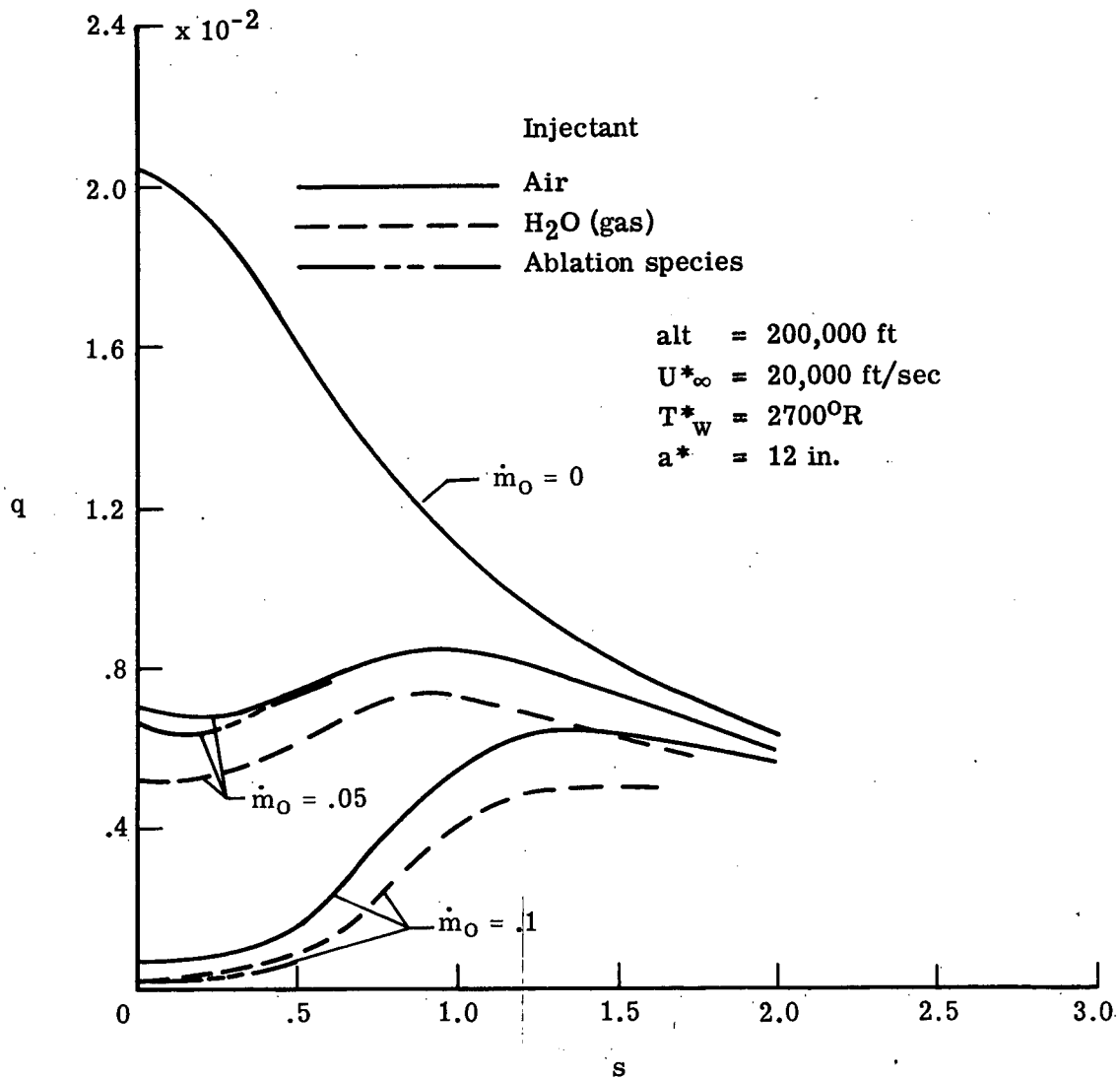


Figure 53.- Comparison of nondimensional heat transfer distributions for different injection rates of air, H_2O , and ablation species into equilibrium air.

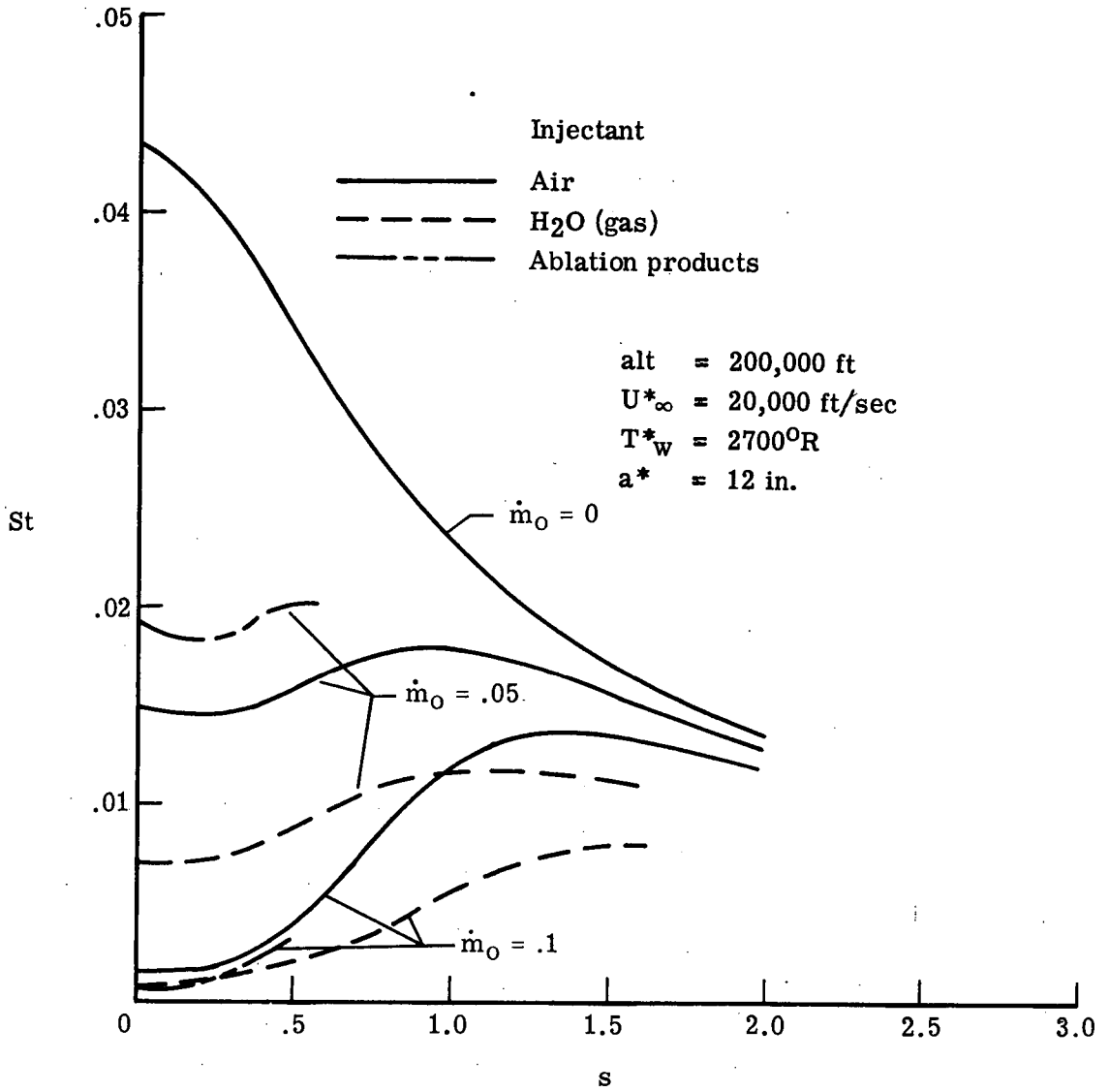


Figure 54.- Comparison of Stanton number distributions for different injection rates of air, H₂O, and ablation species into equilibrium air.

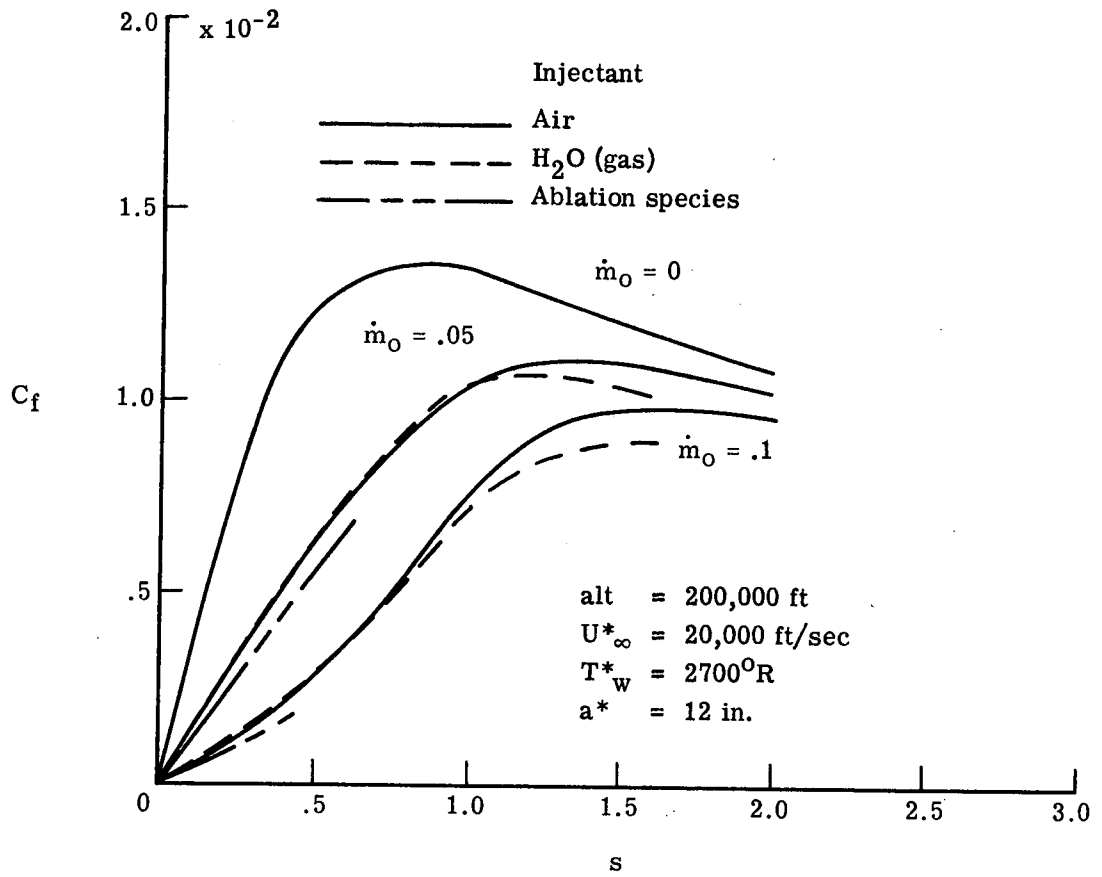


Figure 55.- Comparison of skin friction coefficient distributions for different injection rates of air, H_2O , and ablation species into equilibrium air.

VITA

The author was born in [REDACTED]

[REDACTED] After graduating from DeKalb County High School in 1958, he attended Tennessee Polytechnic Institute at Cookeville, Tennessee, and in August 1962 received a bachelor's degree in Engineering Science. Following graduation, he was employed by NASA at the Langley Research Center, Hampton, Virginia, where he is currently employed. He is presently assigned to the Thermal Analysis Section of the Thermal Protection Materials Branch in the Materials Division. Since joining NASA, he has earned a Master's Degree in Aerospace Engineering from the University of Virginia.

The author currently resides in Hampton, Virginia, with his wife, the former Nina R. Hibdon, and their three children, Reneè, Stanley, and Valerie.